

University College London

The Optical Inverse Problem in
Quantitative Photoacoustic Tomography

Lu An

A thesis submitted for the degree of
Doctor of Philosophy

Photoacoustic Imaging Group
Department of Medical Physics and Biomedical Engineering

March 2018

Declaration of Authorship

I, Lu An, confirm that the work presented in this thesis is my own. Where information has been derived from other sources, I confirm that this has been indicated in the thesis.

Signed: _____

Date: _____

Abstract

Photoacoustic tomography relies on the generation of ultrasound due to optical absorption to produce high resolution images with rich optical absorption-based contrast. In quantitative photoacoustic tomography, the aim is to estimate the concentration of the chromophores and thus provide functional information in addition to the structural images. This is a challenging task due to the unknown and spatially and spectrally varying light fluence within the tissue, which causes the photoacoustic images to be nonlinearly related to the chromophore concentrations. This thesis approaches this problem from two perspectives: Firstly, the conditions under which two linear quantification methods, linear spectroscopic inversion (SI) and independent component analysis (ICA), provide accurate results are investigated. Secondly, the statistical independence between the chromophores is used to improve the robustness and hence the usefulness of nonlinear model-based inversion methods in experimental settings. Using simulated images of a mouse brain, SI was shown to estimate the blood oxygenation within 5% error for a large range of imaging depths (0–9mm) and oxygenation levels (60–100%) if a large number of evenly spread wavelengths (>17) from the range 670–1000nm were used. Based on simulated and experimental images of tissue mimicking phantoms, ICA was shown to estimate the relative concentrations more accurately than SI when the spectral matrix is ill-conditioned and when the absorption of vessel-like features is approximately 0.5mm^{-1} , under the assumption that the chromophores are statistically independent and a first order fluence correction has been applied. To reduce the sensitivity of model-based inversion to model-mismatch, a measure of the statistical independence between the chromophores was included in the error functional in addition to the least-squares data error. By minimising the new error functional using a gradient-based optimisation algorithm, more accurate quantification was obtained for both simulated and experimentally acquired phantom images in the presence of experimental uncertainties.

Impact statement

The work in this thesis provides direct benefits for the photoacoustic imaging research community: The analyses on SI and ICA provide a better understanding of their limitations and enable the researchers to make more effective use of readily available linear quantification methods. This work is important because multiwavelength photoacoustic imaging systems are commercially available and linear methods – SI in particular, are commonly used in pre-clinical and more recently also clinical studies. The proposed method of incorporating the mutual information between the independent chromophores in the model-based inversion helps bringing potentially highly accurate nonlinear methods into practical use. This contributes towards accurate quantitative imaging of live animals in conditions where linear methods cannot provide sufficient accuracy. Hence, the outcomes of this thesis form steps towards realising the full capability of photoacoustic tomography as a quantitative, high resolution, functional and molecular imaging technique. This in turn could have benefits for the wider field of biomedical research as well as for clinical practice. The technique could provide a powerful tool for imaging small-animals in order to study disease progression, gene expression and drug delivery and response. It also has potential clinical applications, such as diagnosing breast cancer, skin diseases and tissue injuries.

Acknowledgements

First of all, I would like to thank my supervisor Dr Ben Cox for his guidance and support for this project. His patience, encouragement, his expertise in the subject combined with his ability to explain any complicated concept in a way that makes sense, and last but not least, his endless positive energy, have all been immensely helpful throughout the course of my studies. I am very thankful for the opportunity to work with Ben. I am also grateful to my second supervisor Prof Paul Beard for providing advice and insightful comments. Furthermore, I would like to thank Prof Simon Arridge for helpful discussions and suggestions for this work.

Thanks to all the members of the Photoacoustic Imaging Group for their help and encouragement. They created such a friendly and supportive atmosphere to work in. In particular I would like to thank Dr Edward Zhang, Dr James Guggenheim, Dr Olumide Ogunlade, Dr Roman Hochuli and Dr Thomas Allen for their assistance with the experiments, as well as for valuable ideas and suggestions shared over many cups of tea and biscuits. I also owe my thanks to Dr Emma Malone, Dr Felix Lucka, Dr Robert Ellwood and Dr Teedah Saratoon who provided computational algorithms and instrumentation that were crucial to this project. Special thanks to Dr Martina Fonseca, who I worked closely with – you have been so helpful in so many ways: sharing ideas, discussing literature, figuring things out in the labs – I am very glad to have you as my colleague and friend.

I am thankful to have made many new friends at UCL, including Callum Lamont, Clément Dupuy, Darije Čustović, Emma Hill, Greg Smith, Khoa Pham, Laura Dempsey, Luca Giannoni, Nico Chen, Reuben Hill, Sana Hannan, Simone Quaggia and Zuzana Kováčsová – thanks for making coming to work so much more entertaining with all the lunches together, tea breaks and evenings at the pub. In addition, I would like to thank my closest friends Martina Fonseca, Micheal Brown, Prashanthan Ganeswaran and Sara

Reis for all the long chats, frequent food adventures and many memorable trips during all the UCL years. Special thanks to Thore Bücking, who made thesis-writing not so bad at all. Thanks also to my top six housemates Adam Funnell and Daniel Elson.

I owe my sincere thanks to my parents, Wei An and Yingbo Jiang, for their support and encouragement and for being my inspiration.

It would not have been possible to complete this project without the support of my friends Isabella Söldner-Rembold and Jining Zhang, who despite living in different countries, were always there for me during the good times and the bad. Thanks for being so great.

At last, thanks to Caramel, the ginger cat who kept me company when I came home late.

Contents

1	Introduction	18
1.1	Biomedical photoacoustic imaging	19
1.2	Quantitative photoacoustic tomography and its challenges	20
1.3	Motivation, contributions and structure of the thesis	23
2	The forward problem and photoacoustic data acquisition	25
2.1	Light propagation in tissue	25
2.1.1	Absorption	26
2.1.2	Scattering	27
2.1.3	The radiative transfer equation	27
2.1.4	The diffusion approximation	29
2.1.5	The finite element method	30
2.1.6	The Monte Carlo method	31
2.2	Photoacoustic signal generation	32
2.3	Acoustic wave propagation	33
2.4	Photoacoustic image acquisition	34
2.4.1	Photoacoustic imaging modes	34
2.4.2	Tomographic scanning geometries	36
2.4.3	Photoacoustic sensors	37
3	The inverse problems in QPAT	39
3.1	Acoustic reconstruction	40
3.1.1	Practical limitations of the acoustic reconstruction	41
3.2	Chromophore quantification methods	44
3.2.1	Linear methods	44

3.2.1.1	Linear spectroscopic inversion	44
3.2.1.2	Linear unmixing methods	45
3.2.1.3	Fluence correction	45
3.2.1.4	Perturbation problem	47
3.2.2	Non-iterative nonlinear methods	48
3.2.2.1	Rearranging DA for absorption	48
3.2.2.2	Rearranging DA for absorption and scattering	49
3.2.3	Iterative nonlinear methods	49
3.2.3.1	Fixed point iteration	49
3.2.3.2	Methods based on optimisation (model-based inversion)	50
3.2.3.3	Implementations of model-based inversion	53
3.2.3.3.1	Multi-illumination	53
3.2.3.3.2	Multiwavelength	54
3.2.3.3.3	Monte Carlo implementations	55
3.2.3.3.4	One step method	56
3.2.3.4	Additional priors in model-based inversion	57
3.2.4	Quantification without fluence modelling	57
3.3	Discussion and remaining challenges	58
3.3.1	Limitations of linear methods	59
3.3.2	Challenges of nonlinear methods	59
3.3.3	Scattering	59
3.3.4	Grüneisen parameter	60
3.3.5	Practical considerations	60
3.4	Summary and outlook	61
4	Linear spectroscopic inversion	62
4.1	Introduction	62
4.2	Linear spectroscopic inversion for estimating sO_2	64
4.3	Numerically simulated images	67
4.4	Accuracy as a function of depth and sO_2	68
4.5	Smallest singular value and condition number	73
4.6	Spectral variation of the fluence	79
4.7	Error of the chromophore concentration ratio estimated using SI	81

4.8	Effect of the spectral range and number of wavelengths	83
4.9	Summary and discussion	87
4.10	Conclusion	89
5	Independent component analysis	90
5.1	Introduction	90
5.1.1	The use of ICA in QPAT	92
5.1.2	Aim and structure of the chapter	93
5.2	Statistical independence	94
5.2.1	Definition	94
5.2.2	Mutual information as a measure of statistical independence	95
5.2.3	Which chromophores are statistically independent?	96
5.3	Independent component analysis	99
5.3.1	Limitations of ICA	101
5.4	Generating multiwavelength photoacoustic images	102
5.4.1	Experimental photoacoustic image acquisition	102
5.4.1.1	The tissue mimicking phantom	103
5.4.1.2	Image acquisition	104
5.4.2	Numerically simulated photoacoustic images	106
5.4.3	Image reconstruction and fluence adjustment	108
5.4.4	Preprocessing for FastICA	109
5.5	Unmixing using ICA and SI	111
5.5.1	Accuracy as a function of absorption	112
5.5.2	Component selection	113
5.5.3	Experimental images and wavelength selection	115
5.6	Summary and discussion	118
5.7	Conclusion	120
6	Statistical independence in nonlinear model-based inversion	121
6.1	Model-based inversion for QPAT	122
6.2	Model-based inversion with statistical independence	124
6.2.1	Properties of the MI error term	125
6.2.2	Estimating the mutual information	126

6.2.3	The gradient of the mutual information	129
6.2.4	Implementation	130
6.2.4.1	FFT for fast computation of the kernel estimator	130
6.2.4.2	Estimation of the marginal PDF	131
6.2.4.3	Estimation of the entropy derivative	134
6.2.4.4	Estimation of the joint PDF	136
6.2.4.5	Estimation of the joint entropy derivative	138
6.3	Generating multiwavelength images of tissue mimicking phantoms	139
6.3.1	Experimentally acquired images	139
6.3.2	Numerically simulated images	142
6.4	Inverting for the chromophore concentrations	144
6.4.1	Effect of model-mismatch	145
6.4.2	Experimental results	146
6.5	Summary and discussion	149
6.6	Conclusion	151
7	Conclusions	152
	Appendices	157
	Appendix A Linear spectroscopic inversion with different spectral ranges	157
	Appendix B Linear spectroscopic inversion with a different phantom	160
	Appendix C Model-based inversion with mutual information for spatially overlapping chromophores	164

List of Figures

2.1	Absorption coefficient of oxyhaemoglobin, deoxyhaemoglobin, water and lipid.	26
2.2	Visible regions in arc and orthogonal sensor geometries.	36
3.1	Limited-view and full-view reconstructions compared to the true initial pressure.	43
4.1	Structure of the mouse brain phantom.	68
4.2	Absorption and scattering properties of the mouse brain phantom.	69
4.3	Simulated photoacoustic images of the mouse brain phantom.	69
4.4	Error in oxygenation using evenly spread wavelengths between 670nm and 1000nm.	70
4.5	Lowest errors in oxygenation obtained using random wavelength combinations.	72
4.6	The wavelength combinations which lead to the lowest errors in oxygenation.	73
4.7	Percentage of the randomly chosen wavelength combinations from the wavelength range 670–1000nm that result in oxygenation errors < 5%.	74
4.8	Error in oxygenation plotted against the smallest singular value of the spectral matrix.	77
4.9	Error in oxygenation plotted against the condition number of the spectral matrix.	78
4.10	Error in oxygenation as a function of the fluence variance.	80
4.11	Error in oxygenation calculated based on Eq. (4.22) for increasing number of wavelengths.	85
4.12	Error in oxygenation at a single voxel using increasing number of wavelengths.	86
5.1	The estimated concentrations of oxy- and deoxyhaemoglobin using 17 wavelengths.	91
5.2	Plot of $-\rho_{\mathbf{y}_k} \log \rho_{\mathbf{y}_k}$ as a function of the probability $\rho_{\mathbf{y}_k}$	96
5.3	Venn diagrams of entropy, joint entropy and mutual information.	97
5.4	Illustration of why the distribution of oxy- and deoxyhaemoglobin are unlikely to be statistically independent.	98
5.5	Experimental tube phantom.	103
5.6	Absorption and scattering properties of the experimental phantom.	104
5.7	Structure of the numerical tube phantom.	107
5.8	Experimental photoacoustic images of the tube phantom and the fluence adjustment.	109

5.9	Estimated spectra using ICA compared to the true spectra.	111
5.10	Errors of the unmixed components in three simulated case studies using ICA and SI.	114
5.11	Errors of the unmixed components when two, three or four principal components are further processed with ICA.	115
5.12	Errors of the unmixed components using different number of wavelengths.	116
5.13	Unmixed components from the experimental images when the six shortest wavelengths are used.	117
5.14	Condition number of the spectral matrix as a function of the number of wavelengths as the wavelengths are reduced from the longest.	118
6.1	Minimum of the error functional in an idealistic scenario, in the presence of model-mismatch and when the mutual information is used.	125
6.2	Illustration of the kernel density estimator.	128
6.3	Illustration of the re-sampling.	133
6.4	Illustration of the 1D interpolation.	134
6.5	Illustration of the convolutions of the kernel and the discretised concentration.	135
6.6	Illustration of the 2D interpolation.	137
6.7	Experimental set-up and phantom structure.	140
6.8	Absorption and scattering properties of the phantom.	141
6.9	A photograph of the experimental phantom.	141
6.10	2D cross-sectional slices of the 3D reconstructed experimental photoacoustic images.	143
6.11	Diagram of the 2D numerical phantom.	143
6.12	Errors in concentration as a function of errors in the beam diameter or the scattering amplitude in the inversion.	146
6.13	Estimated concentrations based on experimental images using error functionals with and without the mutual information term.	148
A.1	Error in oxygenation using evenly spread wavelengths between 650nm and 1000nm.	158
A.2	Error in oxygenation using evenly spread wavelengths between 690nm and 1000nm.	159
B.1	Structure of the blood vessel phantom.	160
B.2	Error in oxygenation for the blood vessel phantom using evenly spread wavelengths between 670nm and 1000nm.	162
B.3	Error in oxygenation at a single voxel using increasing number of wavelengths.	163
C.1	Estimated concentrations of overlapping chromophores using error functionals with and without the mutual information term.	166

List of Tables

- 4.1 Examples of publications where SI was used to estimate oxygenation based on *in vivo* photoacoustic images in the past three years (2015–2017). 63
- 6.1 The average estimated and true concentrations in gL^{-1} for each tube. . 147

Nomenclature

Abbreviations

AR-PAM	Acoustic resolution photoacoustic microscopy
BFGS	Broyden-Fletcher-Goldfarb-Shanno
BSS	Blind source separation
DA	Diffusion approximation
DOT	Diffuse optical tomography
EVD	Eigenvalue decomposition
FEM	Finite element method
FFT	Fast Fourier transforms
FPI	Fabry-Perot interferometer
ICA	Independent component analysis
MC	Monte Carlo
MI	Mutual information
OR-PAM	Optical resolution photoacoustic microscopy
PC	Principal component
PCA	Principal component analysis
PDF	Probability density function
PZT	Lead zirconate titanate
QPAT	Quantitative photoacoustic tomography
ROI	Region of interest
RTE	Radiative transfer equation
SI	Linear spectroscopic inversion
SNR	Signal to noise ratio
TV	Total variation

Symbols

α	Specific absorption coefficient
\sim	Estimation of a variable
\circ	Element-wise (Hadamard) product
δ	Error of the quantification
Γ	Grüneisen parameter
γ	Weight parameter
κ	Condition number of a matrix (in Chapter 4)
κ	Kernel function (in Chapter 6)
λ	Optical wavelength
\mathbf{F}	Flux vector
\mathcal{H}	Entropy
\mathcal{O}	Complexity of an equation
μ_a	Absorption coefficient
μ_s	Scattering coefficient
μ'_s	Reduced scattering coefficient
μ_{eff}	Effective attenuation coefficient
ν	Frequency of the photon
ϕ	Light fluence
ρ	Probability density function (PDF)
σ_{min}	Smallest singular value of a matrix
\star	1D convolution
$\star\star$	2D convolution
ε	Error functional
\dagger	Pseudo-inverse of a matrix
c	Chromophore concentration
c_s	Speed of sound
D	Optical diffusion coefficient
g	Anisotropy factor
H	Absorbed optical energy density

h	Kernel width (in Chapter 6)
h	Planck's constant (in Chapter 2)
Hb	Deoxyhaemoglobin
HbO_2	Oxyhaemoglobin
HbT	Total haemoglobin
J	Negentropy
K	Number of chromophores
L	Radiance or time integrated radiance
l	Mean free path
L_p	Directional photon density
M	Number of voxels
N	Number of wavelengths
p	Pressure
p_0	Initial pressure
p_{det}	Pressure measured at the tissue surface
q	Source of energy
q_0	Isotropic photon source
q_p	Source of photons
sO_2	Blood oxygenation
$\text{var}(\phi)$	Fluence variance

Chapter 1

Introduction

In a general sense, medical imaging refers to the techniques and processes for generating images of the internal structures in the body or providing information about the biological functions in living organisms. Medical imaging plays a crucial role in modern medicine, where it is used for diagnosing and monitoring diseases. It also has important pre-clinical applications, where it is used for drug development and studying pathological processes. A number of medical imaging modalities have been developed over the last century, including X-ray imaging, magnetic resonance imaging (MRI), single-photon emission computed tomography (SPECT), positron-emission tomography (PET), ultrasound imaging and optical imaging. Each imaging modality has unique sources of image contrast, and comes with its own intrinsic advantages and limitations, hence making them suitable for different fields of applications. Hybrid imaging modalities combine two or more imaging techniques to benefit from the advantages of the individual imaging techniques and/or to provide complimentary information. Biomedical photoacoustic imaging is a non-invasive hybrid imaging technique based on the generation of ultrasound waves due to the absorption of optical energy. It has the advantage of combining rich optical absorption based contrast which provides high specificity with the high resolution of ultrasound imaging, and it offers larger penetration depth than pure optical techniques relying on ballistic photons. Photoacoustic images can be obtained using endogenous contrast from optically absorbing tissue components such as blood, lipids, water and melanin, or exogenously administered contrast agents, such as near-infrared dyes and nanoparticles. By exploiting the spectral signature of the individual optical absorbers using light of different wavelengths, photoacoustic imaging

also has the potential to reveal the concentration of each absorber. This quantitative information would enable us to measure valuable parameters such as the blood oxygenation or map the distribution of certain biomarkers. Obtaining quantitatively accurate images is a challenging task because the photoacoustic signals are non-linearly related to the chromophore concentrations. This thesis provides an analysis of the accuracy of linear quantitative photoacoustic imaging methods and proposes a novel method based on statistical independence for improving the robustness of a nonlinear model-based quantification method for photoacoustic imaging.

1.1 Biomedical photoacoustic imaging

Photoacoustic imaging relies on the photoacoustic effect, which refers to the generation of sound due to the absorption of light. The photoacoustic effect was first discovered by Alexander Graham Bell in 1880 [1], but it had few applications before the development of lasers in the 1960s. In the following decades, a range of industrial and scientific applications of the photoacoustic effect for the analysis of solid and gas phase materials were developed. The photoacoustic effect was not exploited for biomedical imaging until the mid-1990s. In the last two decades, biomedical photoacoustic imaging has been a rapidly growing field of research, with significant development in the instrumentation, reconstruction algorithms and exogenous contrast agents. Today, compelling 3D photoacoustic images can be obtained *in vivo* and commercial imaging systems are available. The spatial resolution scales with depth and are typically $<10\mu\text{m}$ at depths of a few hundred micrometers, $<100\mu\text{m}$ at depths of a few millimetres and $<1\text{mm}$ at centimetre depths [2]. Photoacoustic imaging has been explored for a range of clinical applications, including breast imaging [3, 4], cardiovascular imaging [5, 6, 7], skin imaging [8, 9] and endoscopy [10, 11], as well as pre-clinical applications using endogenous contrast such as haemoglobin for imaging the vasculature in the mouse brain [12, 13, 14] and in tumour models [15, 16, 17], or exogenous contrast agents [18, 19] and reporter genes [20, 21] for molecular or cellular imaging.

The photoacoustic image acquisition involves illuminating the subject with pulsed radiation of nanoseconds duration. The optical energy is absorbed by the chromophores in the tissue and rapidly converted to heat energy, leading to a local rise in temperature and pressure. This pressure then propagates as an acoustic wave towards the surface

of the tissue where it is detected by ultrasound sensors. The photoacoustic image is formed by reconstructing the distribution of the initial pressure rise using the time-resolved recordings of the acoustic waves. This provides a qualitative structural image of the chromophores. A quantitative image of the chromophore concentrations can be obtained by acquiring multiple images using excitation light with different wavelengths and applying spectroscopic analysis. This is known as quantitative photoacoustic imaging and will be described in the next section.

1.2 Quantitative photoacoustic tomography and its challenges

Quantitative photoacoustic tomography (QPAT) [22] aims to provide functional information about the tissue by estimating the concentration of the chromophores that give rise to the photoacoustic signals detected at different optical wavelengths. The key endogenous chromophores of interest for quantitative photoacoustic tomography are oxy- and deoxyhaemoglobin, because their concentration ratio defines the blood oxygenation, sO_2 :

$$sO_2 = \frac{c_{HbO_2}}{c_{HbO_2} + c_{Hb}}, \quad (1.1)$$

where c_{HbO_2} and c_{Hb} denote the concentrations of oxy- and deoxyhaemoglobin respectively. The potential capability of using photoacoustic imaging to non-invasively map the sO_2 with high spatial resolution has high clinical relevance, because the sO_2 is an extremely important physiological parameter. For example, it has large impact on cancer diagnosis and treatment, because sO_2 is related to angiogenesis and hypermetabolism, which are well-known indicators of cancer, and it also affects the effectiveness of chemo- and radiotherapies in cancer treatments [23]. The measurement of sO_2 is also useful for other pre-clinical and clinical applications such as treating burns [24] and wounds [25,26] and monitoring brain injuries or imaging activities in the brain [12,27].

Other applications of QPAT for endogenous chromophores may include identifying and quantifying lipids for cardiovascular imaging of plaques [5,28,29,30], and measuring the melanin content for the diagnoses of skin diseases such as melanomas [31,32].

In addition to quantifying endogenous chromophores, QPAT could also be used for contrast-enhanced photoacoustic molecular imaging applications, where the detection

and quantification of the local accumulation of genetically encoded probes and extrinsically administered contrast agents [33] can provide information on biological processes, drug delivery, disease development and treatment response.

The quantification of the chromophore concentrations may be achieved to different extents:

- **Identification** of the chromophores could be achieved using spectral decomposition methods. The aim is to generate separate images of the locations of the individual chromophores. This does not provide information about the quantity of each chromophore but may still be useful for some applications [5, 34].
- **The concentration ratio** of two chromophores at the same location is mainly relevant for measuring the sO_2 [35, 36], which is related to the concentration ratio of oxyhaemoglobin and deoxyhaemoglobin. There are two factors which make estimating the ratio less challenging than estimating the absolute concentrations: Firstly, the scaling factors, such as the system calibration and the thermoelastic efficiency, do not need to be known or estimated as they will cancel out. Secondly, the concentration of each chromophore does not necessarily need to be accurate with respect to other spatial locations for the ratio to be correct. The concentration ratio is the quantity of interest in Chapter 4.
- **The relative concentration** will be used in this thesis to refer to chromophore concentration in arbitrary units. This also does not require knowing the system calibration factor, but unlike the concentration ratio estimation, it requires accurate estimation of the concentration of each chromophore with respect to other spatial locations. We distinguish between two types of relative concentrations: 1) The chromophore concentrations are estimated to the same (uncalibrated) scale [37, 38]. 2) Each chromophore concentration is estimated to a different scale [39, 40]. In type 2), the estimated chromophore concentration is still consistent across an image, but the concentration of one chromophore cannot be compared to another chromophore. This type of relative concentration will be estimated in Chapter 5.
- **The absolute concentration** is the most challenging quantity to estimate [41, 42]. Estimating the concentrations in the correct units (for example in gL^{-1}) requires a calibration of the imaging system and knowing the thermoelastic efficiency.

The absolute concentrations will be estimated in Chapter 6.

All types of quantification described above require that the significant chromophores have unique absorption spectra. This makes it possible to resolve the contribution from different chromophores using multiwavelength images. However, the photoacoustic image is not a direct representation of the absorption coefficient, but a reconstruction of the initial pressure, which is a product of the thermoelastic efficiency, the absorption coefficient and the light fluence. The thermoelastic efficiency is wavelength independent and varies for different chromophores, but is in some cases dependent on the chromophore concentrations. The spatially and spectrally varying light fluence poses the main challenge for QPAT. The fluence is generally unknown because it depends on the scattering and absorption coefficients, which themselves depend on the chromophore concentrations. As a simple example, in the case where one blood vessel is located directly below another blood vessel, the fluence reaching the lower blood vessel will depend on the absorption and scattering of the upper blood vessel. Therefore, the spectral variation of the initial pressure in the lower blood vessel will be affected, or “coloured”, by the presence of the upper blood vessel. This is referred to as “spectral colouring”. In fact, since light can be scattered in any direction, the fluence at a location is not only affected by the optical features above that location, but also by the absorption and scattering in other illuminated regions in the tissue. That is to say, the absorbed optical energy density at the upper vessel may also be affected by the optical properties of the lower one, if the back-scattering is sufficiently strong.

There are various methods which attempt to account for the spectral colouring. The simplest ones involve dividing the multiwavelength photoacoustic images by an approximation of the fluence at each wavelength (Sec. 3.2.1.3). In this way, the effect of the fluence is approximately corrected for, such that the images represent a linear sum of chromophore concentrations that can be unmixed using the linear spectroscopic inversion, as in conventional optical spectroscopy. Some *in vivo* QPAT studies use this approach [43, 44], because it is fast and simple. In many other studies, the fluence is simply assumed to be constant, and no corrections for the spectral colouring are applied (for example Refs. [45, 46, 47]). Both of these solutions are approximate and provides accurate results only in certain circumstances. More complex nonlinear methods involve modelling the light fluence using light transport equations (Sec. 3.2.2–3.2.3). They pro-

vide more generally applicable solutions to the quantification problem. These methods are more difficult to implement, because they have high computational demand and can be sensitive to model-mismatch errors. Therefore, they have mostly been investigated in theoretical studies or using numerically simulated data.

1.3 Motivation, contributions and structure of the thesis

This thesis first outlines the theories describing the processes from the irradiation of the tissue to the quantification of the chromophore concentrations and reviews the existing chromophore quantification methods. Chapter 2 provides a brief overview of light propagation in tissue and the generation, propagation and detection of the photoacoustic signals. Chapter 3 describes the acoustic inverse problem, which deals with the reconstruction of the photoacoustic images from the measured signals, and the optical inverse problem, which involves estimating the chromophore concentrations from the multiwavelength photoacoustic images. As the optical inverse problem is the main focus of this thesis, a detailed review of the existing methods for the optical inversion is included in Chapter 3.

Following the theory and review chapters, the three key research outcomes are presented in Chapters 4, 5 and 6. The motivation and contribution of these chapters are described below:

As mentioned in the previous section, simple linear quantification methods are available and have been used in many *in vivo* studies to estimate the sO_2 or distinguish biomarkers from the background tissue. While these methods may be suitable in some circumstances, few efforts have been made to investigate under what conditions they are likely to provide accurate quantification. A better understanding of the limitations of these methods would allow us to use them in a more reliable manner. It would also help us avoid using more complicated nonlinear methods which are typically slower and more computationally intensive in cases where a simple linear method can provide sufficient accuracy. The first aim of the thesis is to analyse the accuracy of two linear methods: linear spectroscopic inversion and independent component analysis.

In Chapter 4, the accuracy of using linear spectroscopic inversion (SI) to estimate sO_2 is investigated as a function of depth, oxygenation level and number of wavelengths available. Numerically simulated photoacoustic images of a realistic 3D tissue phantom

are used for this study. The results in this chapter demonstrate that accurate sO_2 estimates can be obtained for a large range of depths and oxygenation levels, but this requires using a large number of wavelengths from a certain spectral range. It also provides an analysis of the optimal wavelength selection and the error of the estimated sO_2 .

Independent component analysis (ICA) is a linear unmixing method that has mainly been used to aid the visualisation of biomarkers by distinguishing them from the background tissue. In Chapter 5, both numerical and experimental tube phantom images were used to identify the conditions under which ICA provides accurate quantification. It was shown that ICA outperforms SI when the inversion is ill-conditioned, and that ICA is more robust to spectral colouring compared to SI. These results provide guidance for when ICA can be used instead of SI to obtain higher accuracy while retaining the simplicity of a linear method.

Chapters 4 and 5 enable us to make better use of linear methods. For cases where linear methods cannot provide sufficiently accurate results, we need to rely on more complex quantification methods such as the nonlinear model-based inversion scheme. This type of methods have the potential to provide accurate estimation of the absolute chromophore concentrations in complex tissue structures. However, in practical implementations, the quantification results may suffer from errors arising from model-mismatch. Chapter 6 proposes incorporating statistical independence as additional information in the nonlinear model-based inversion method to reduce quantification errors caused by inaccurate forward modelling of the fluence. This was shown to improve the robustness of the inversion scheme for statistically independent chromophores. Hence, the applicability and usefulness of model-based inversion schemes may potentially be increased for practical imaging studies.

Lastly, the overall conclusions of the thesis are presented in Chapter 7.

Chapter 2

The forward problem and photoacoustic data acquisition

In this chapter, firstly, the forward problem in photoacoustic imaging is described. The forward problem consists of three parts: the diffuse light distribution in tissue (optical forward problem, Sec. 2.1), the thermalisation of the optical energy which leads to the generation of the photoacoustic signal (Sec. 2.2), and the propagation of the acoustic waves in tissue (acoustic forward problem, Sec. 2.3). Secondly, the photoacoustic image acquisition process is presented in Sec. 2.4, where the advantages and limitations of different imaging modes, scanning geometries and the acoustic signal detection mechanisms are discussed.

2.1 Light propagation in tissue

When light propagates through the tissue, it may be absorbed or scattered by the molecules in the tissue. These two processes are described in Sec. 2.1.1 and 2.1.2 respectively. The distribution of the light in tissue as a result of the scattering and absorption events can be described using the radiative transfer equation (RTE), which is presented in Sec. 2.1.3. Section 2.1.4 presents an approximation of the RTE which is valid in the diffusive regime away from the light source or boundaries, known as the diffusion approximation.

2.1.1 Absorption

A molecule can absorb an incident photon if the photon energy matches the energy gap between two energy states of the molecule. The molecule is thus excited to the higher energy state. The likelihood of absorption occurring per unit length travelled by the photon is described by the absorption coefficient, μ_a . It defines the rate of decrease of the fluence ϕ as photons propagate along the direction x through a homogeneously absorbing and non-scattering medium, such that $\frac{\partial \phi}{\partial x} = -\mu_a \phi$. The absorption coefficient of a chromophore is given by the product of its specific absorption coefficient, α , and its concentration, c . If multiple absorbers are present in the tissue, the absorption coefficient is given by the sum of their individual absorptions, such that

$$\mu_a(\mathbf{r}, \lambda) = \sum_k \alpha_k(\lambda) c_k(\mathbf{r}) \quad (2.1)$$

at position \mathbf{r} and wavelength λ , where c_k and α_k are the concentration and the specific absorption coefficient of the k^{th} chromophore.

The absorption coefficients of examples of endogenous tissue chromophores are shown in Fig. 2.1. In photoacoustic imaging, the wavelength of the excitation light is typically chosen within the near-infrared window (650 to 1350nm). In this spectral range, the absorptions of water and blood are relatively low, and therefore light can penetrate into deeper depths in the tissue.

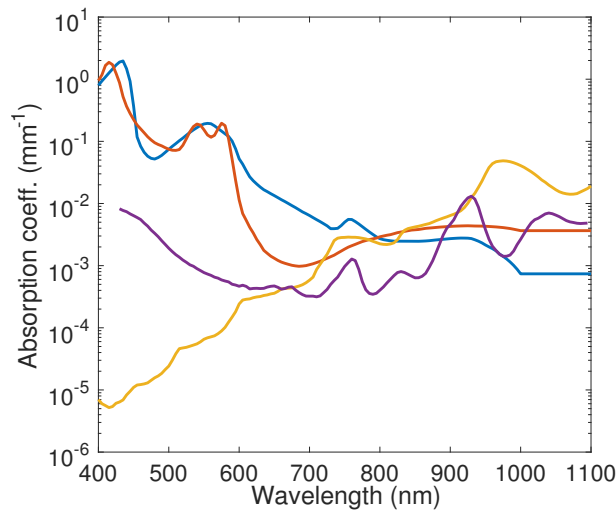


Figure 2.1: The absorption coefficient of oxyhaemoglobin (red) [48], deoxyhaemoglobin (blue) [48], water (purple) [49, 50] and lipid (yellow) [51].

2.1.2 Scattering

Scattering is the dominant type of light-matter interaction in soft tissue and refers to the process of the incoming photon being re-radiated by a molecule into a new direction. On a macroscopic level, scattering is caused by variations in the refractive index of the tissue. The dominant type of scattering in tissue is elastic scattering, where the photon energy does not change due to the scattering event. Similar to the absorption coefficient, the scattering coefficient, μ_s , describes the likelihood of scattering occurring. It is related to the decay of the fluence by $\frac{\partial \phi}{\partial x} = -\mu_s \phi$ in a homogeneous scattering and non-absorbing medium. The direction in which the photon is scattered depends on the size and shape of the particles in the tissue and the wavelength of the light. The probability of the photons coming from the direction $\hat{\mathbf{s}}$ being scattered into $\hat{\mathbf{s}}'$ is described by the scattering phase function, $\theta(\hat{\mathbf{s}}, \hat{\mathbf{s}}')$. Since the scattering phase function is a probability density function, its integral over all angles must be normalised to one:

$$\iint_{\mathbf{S}^2} \theta(\hat{\mathbf{s}}, \hat{\mathbf{s}}') d\hat{\mathbf{s}}' = 1. \quad (2.2)$$

2.1.3 The radiative transfer equation

Light propagation in matter can be described using Maxwell's electromagnetic equations, which fully accounts for the wave-like behaviour of light, such as diffraction and interference. However, due to the high level of heterogeneity in the optical properties of tissue, this analytical approach does not provide practically useful models for the light distribution in biological tissue. The radiative transfer equation (RTE) is a more feasible approach for describing light transport in tissue. The RTE was originally heuristically derived based on the conservation of energy, but it has since been shown that the RTE can also be derived from the Maxwell's equations [52, 53]. The light model based on the RTE neglects the wave-like properties of light and considers only the energy flow carried by the photons. The RTE can be derived by equating the change of the number of photons within a small volume to the difference between the number of photons entering and exiting the volume in a given direction at a given time:

$$\begin{aligned} (\Delta t \Delta V) \frac{\partial L_p}{\partial t} = & (c \Delta t \Delta V) \mu_s \int_{\mathbf{S}^2} \theta(\hat{\mathbf{s}}, \hat{\mathbf{s}}') L_p(\hat{\mathbf{s}}') d\hat{\mathbf{s}}' + (c \Delta t \Delta V) q_p \\ & - (c \Delta t \Delta V) \mu_a L_p - (c \Delta t \Delta V) \mu_s L_p - (c \Delta t \Delta V) \hat{\mathbf{s}} \cdot \nabla L_p \end{aligned} \quad (2.3)$$

where $c = 3 \times 10^8 \text{m/s}$ is the speed of photons and $L_p(\mathbf{r}, \hat{\mathbf{s}}, t)$ is the directional photon density, which is defined as the number of photons per unit volume travelling in direction $\hat{\mathbf{s}}$ at location \mathbf{r} and time t . The left hand side of Eq. (2.3) is the net change in the number of photons in volume ΔV and time Δt . The net change is due to the five contributing factors described by the terms on the right hand side of the equation: The first two terms represent the positive contributions due to photons travelling in other directions being scattered into the direction $\hat{\mathbf{s}}$ and the source of photons q_p . The remaining terms are negative contributions from the net outflow of photons due to the absorption of photons, the scattering of photons out of the direction $\hat{\mathbf{s}}$ and the gradient of the directional photon density. Equation (2.3) can also be expressed in terms of energy. The energy of a photon is given by $h\nu$, where ν is the frequency of the photon and h is Planck's constant, $h = 6.62 \times 10^{-34} \text{m}^2\text{kg/s}$. By multiplying both sides of the equation by $h\nu$ and dividing through by $c\Delta t\Delta V$, Eq. (2.3) becomes

$$\frac{1}{c} \frac{\partial L(\mathbf{r}, \hat{\mathbf{s}}, t)}{\partial t} = \mu_s(\mathbf{r}) \int_{\mathbf{S}^2} \theta(\hat{\mathbf{s}}, \hat{\mathbf{s}}') L(\mathbf{r}, \hat{\mathbf{s}}', t) d\hat{\mathbf{s}}' + q(\mathbf{r}, \hat{\mathbf{s}}, t) - (\hat{\mathbf{s}} \cdot \nabla + \mu_a(\mathbf{r}) + \mu_s(\mathbf{r})) L(\mathbf{r}, \hat{\mathbf{s}}, t). \quad (2.4)$$

where $L(\mathbf{r}, \hat{\mathbf{s}}, t) = h\nu c L_p(\mathbf{r}, \hat{\mathbf{s}}, t)$ is rate of energy flow per unit area per unit solid angle, known as the radiance, and $q = h\nu q_p$ is the source of energy.

Since the optical timescales are significantly shorter than the timescales for the acoustic propagation under stress confinement (Sec. 2.2), one can assume that the acoustic propagation does not start until all optical energy from a laser pulse has been absorbed. Therefore, the quantity of the interest in photoacoustic imaging is the total energy absorbed per unit volume. Hence, the time independent RTE can be applied, which is found by integrating Eq. (2.4) with respect to time:

$$(\hat{\mathbf{s}} \cdot \nabla + \mu_a(\mathbf{r}) + \mu_s(\mathbf{r})) L(\mathbf{r}, \hat{\mathbf{s}}) = \mu_s(\mathbf{r}) \int_{\mathbf{S}^2} \theta(\hat{\mathbf{s}}, \hat{\mathbf{s}}') L(\mathbf{r}, \hat{\mathbf{s}}') d\hat{\mathbf{s}}' + q(\mathbf{r}, \hat{\mathbf{s}}), \quad (2.5)$$

where $L(\mathbf{r}, \hat{\mathbf{s}})$ is the time-integrated radiance.

The RTE cannot be solved analytically except in a few restricted cases, such as in a medium consisting of optically homogeneous slabs. In all other cases, it needs to be solved numerically, which can be computationally intensive. To reduce the computational burden, in some cases, one can use the diffusion approximation to the RTE, which is described in the following section.

2.1.4 The diffusion approximation

The RTE can be simplified by expressing the radiance as a series of spherical harmonics. By truncating the series after n terms, we obtain the P_n approximations of the RTE. The diffusion approximation (DA) of the RTE is based on the P_1 approximation, where the angular dependence of the RTE is almost removed completely. The P_1 approximation consists of two coupled equations: one equation is obtained by integrating the RTE over all angles, and the other is obtained by multiplying the RTE by $\hat{\mathbf{s}}$ and then integrating over all angles. Using the time-independent RTE, these equations are given by [54]:

$$\nabla \cdot \mathbf{F} + \mu_a \phi = q_0 \quad (2.6)$$

$$\mathbf{F} = -D \nabla \phi \quad (2.7)$$

where \mathbf{F} is the flux vector defined by $\mathbf{F} = \int_{S^2} \hat{\mathbf{s}} L(\mathbf{r}, \hat{\mathbf{s}}) d\hat{\mathbf{s}}$, ϕ is the fluence defined by $\phi = \int_{S^2} L(\mathbf{r}, \hat{\mathbf{s}}) d\hat{\mathbf{s}}$, q_0 is the isotropic photon source given by $q_0 = \int_{S^2} q(\mathbf{r}, \hat{\mathbf{s}}) d\hat{\mathbf{s}}$ (the non-isotropic photon sources are considered negligible in this approximation), and D is the optical diffusion coefficient

$$D = \frac{1}{3(\mu_a + \mu'_s)}. \quad (2.8)$$

where $\mu'_s = \mu_s(1 - g)$ is the reduced scattering coefficient and g is the anisotropy factor, which is the average cosine of the angle between $\hat{\mathbf{s}}$ and $\hat{\mathbf{s}}'$. The anisotropy factor describes the mean direction of the scattering events in terms of the relative forward and backward scattering and can take values between -1 and 1. Positive values of g indicate that the forward scattering dominates, while negative values indicate strong backscattering. When $g = 0$, the scattering is isotropic. Biological tissues typically have $g \approx 0.8 - 0.98$ [55]. The DA is obtained by substituting Eq. (2.7) into Eq. (2.6) [54]:

$$(\mu_a - \nabla \cdot D \nabla) \phi = q_0. \quad (2.9)$$

The DA assumes that the radiance is nearly isotropic, or diffusive, which means that the light travels in all directions with almost equal probability. However, when collimated light enters the tissue, it is initially directional, and it does not become diffuse until after a few scattering events. Therefore, the DA is valid only in a highly scattering medium ($\mu'_s \gg \mu_a$) at a distance away from the light source and boundaries of the

medium. This distance is equal to one mean free path of the medium, given by $l = 1/(\mu_a + \mu_s(1 - g))$. Generic biological tissues typically have an average $l \approx 1\text{mm}$. The region well beyond this depth is referred to as the diffusive regime, where the DA can be used to accurately describe the light distribution. The superficial layer, where the photons retain some directionality of the light source, is known as the ballistic regime. Since the DA is not valid in the ballistic regime, it is more accurate to use the RTE for applications where the superficial layer is of interest. Alternatively, one can also use the δ -Eddington approximation [56], which includes an extra term in the scattering phase function that accounts for the forward scattering. In this approximation, the modelled fluence consists of both a scattered component and a collimated component. The latter has an exponential decay rate proportional to a modified transport coefficient. The δ -Eddington approximation is more accurate compared to DA for the ballistic regime.

In the special case of an optically homogeneous semi-infinite medium, the DA can be solved analytically using the free-space Green's function [57]. In a one dimensional case where the illumination source is an infinite plane wave, the solution is given by

$$\phi(z) = \phi_0 \exp(-\mu_{eff}z), \quad (2.10)$$

where z denotes the depth from the illuminated surface and μ_{eff} is the effective attenuation coefficient,

$$\mu_{eff} = \sqrt{3\mu_a(\mu_a + \mu'_s)}. \quad (2.11)$$

This 1D solution can be used as an approximation to provide a simple estimation of the fluence for quantitative photoacoustic imaging (Sec. 3.2.1.3).

However, in general, numerical methods are required for solving the DA for realistic tissues, as analytical solutions do not exist for arbitrary heterogeneous tissue structures. The finite element method and the Monte Carlo method are two commonly used numerical approaches for light modelling and they will be described briefly in the following sections.

2.1.5 The finite element method

The finite element method (FEM) can be used to provide approximate numerical solutions to partial differential equations. In the finite element model, the domain is

discretised into small pieces, known as elements, where the quantities of interest are continuous and often piecewise linear. The quantities of interest are calculated at the vertices of the elements, known as the nodes. Using this model, the fluence is approximated as [58]

$$\phi \approx \phi^h = \sum_i^{M_n} \phi_i \psi_i, \quad (2.12)$$

where ψ_i are the basis functions, ϕ_i are the nodal values of the fluence and M_n is the number of nodes. The solution in Eq. (2.12) must also be subject to boundary conditions.

In order to use FEM to solve the DA, Eq. (2.9) needs to be expressed in the integral form, also known as the variational formulation or the weak formulation. The derivation and the details of the formation are omitted here but can be found in Ref. [58]. The weak formulation leads to a linear equation which can be solved directly:

$$\mathbf{A}\phi^h = b, \quad (2.13)$$

where \mathbf{A} is the system matrix with the terms in the weak formulation of the DA and b is the source term.

2.1.6 The Monte Carlo method

The Monte Carlo (MC) method is a stochastic modelling method for light transport in tissue. In the MC method, the photons are modelled as energy packets which propagate through tissue by taking a series of incremental steps that form random walks. The length and direction of each step are randomly chosen but their probabilities are determined by the scattering properties of the tissue. At each step, some of the energy is deposited and the amount depends on the absorption coefficient. Each energy packet continues to travel through the medium until it leaves the volume or until all of the energy has been absorbed. The sum of the energy deposited by all energy packets forms a map of the distribution of the absorbed energy density.

The MC method is considered the gold standard modelling method for tissue optics, because as the number of energy packets in the simulation approaches infinity, the mapped absorbed energy density distribution approaches the true solution of the RTE.

2.2 Photoacoustic signal generation

The generation of the photoacoustic signals starts with the optical energy being absorbed by the chromophores in the tissue. The absorbed optical energy density, H , is given by

$$H(\mathbf{r}, \lambda) = \phi(\mathbf{r}, \lambda)\mu_a(\mathbf{r}, \lambda). \quad (2.14)$$

The absorption of optical energy excites the molecule to a higher energy state. The molecule then de-excites either through radiative decay (fluorescence or phosphorescence), or through non-radiative vibrational relaxation. It is the latter process that leads to photoacoustic signal generation. When a molecule undergoes vibrational relaxation, it collides with other molecules which raises their kinetic energy. If the time scale in which this occurs is so short that volume of the absorber does not have time to change, then the local pressure and temperature will increase. This localised pressure rise is the source of the photoacoustic signal and referred to as the initial acoustic pressure, p_0 . The increase in pressure can be assumed to be proportional to the absorbed optical energy density provided that the thermal and stress confinements hold. The thermal confinement requires the timescale at which the heat diffuses to be significantly longer than timescale of the optical heating, such that the thermal diffusion and acoustic propagation can be decoupled in the derivation of the photoacoustic wave equation. This requires that the laser pulse must be significantly shorter than the thermal relaxation time, which is typically tens or hundreds of milliseconds for blood vessels. The stress confinement sets a more stringent requirement for the duration of the laser pulse: it must be significantly shorter than the timescale at which the acoustic wave propagates across the absorber. When the stress confinement holds, the rate of change in pressure can be assumed to be dominated by conversion of optical energy and this conversion can be considered instantaneous. For blood vessels, this acoustic timescale, τ_{ac} , could be defined as the time required for the pressure wave to move across its vessel diameter, d , such that $\tau_{ac} = d/c_s$, where c_s is the speed of sound, and it is typically in the order of tens of nanoseconds. To satisfy the thermal and stress confinement conditions, laser pulses with nanoseconds duration are used for photoacoustic signal generation. Thus,

assuming that no radiative decay takes place, the initial pressure is related to H by

$$p_0(\mathbf{r}, \lambda) = \Gamma(\mathbf{r})H(\mathbf{r}, \lambda), \quad (2.15)$$

where Γ is the Grüneisen parameter, which represents the efficiency of the conversion of the heat energy to pressure, also known as the thermoelastic efficiency. The Grüneisen parameter is given by $\Gamma = \beta c_s^2 / C_p$ where β is the isobaric thermal expansion coefficient and C_p is the isobaric specific heat capacity.

The pressure propagates as an ultrasound wave away from the source and towards the tissue surface, where it can be detected by ultrasound sensors. The propagation of the acoustic waves in tissue is described in the next section.

2.3 Acoustic wave propagation

The acoustic wave propagation in the tissue can be described by a wave equation, which is derived from four coupled equations arising from the adiabatic equation of state and the conservation of mass, momentum and energy. These equations lead to the heat diffusion equation and acoustic wave equation, which can be decoupled, provided that thermal confinements hold, to give the photoacoustic wave equation [59]

$$\nabla^2 p(\mathbf{r}, t) - \frac{1}{c_s^2} \frac{\partial^2 p(\mathbf{r}, t)}{\partial t^2} = 0. \quad (2.16)$$

where $p(\mathbf{r}, t)$ denotes the pressure at location \mathbf{r} and time t . Equation (2.16) assumes that the medium is acoustically linear and non-attenuating, and that the stress confinement holds, such that the heating can be assumed to be instantaneous [59]. Solving the wave equation requires two initial conditions:

$$p(\mathbf{r}, t = 0) = p_0(\mathbf{r}) \quad (2.17)$$

and

$$\frac{\partial}{\partial t} p(\mathbf{r}, t = 0) = 0. \quad (2.18)$$

The first condition defines the initial pressure distribution and the second condition states that there is no motion of the tissue at $t = 0$. The solution to the wave equation

subject to the initial conditions can be given by Poisson's integral [60, 61]

$$p(\mathbf{r}, t) = \frac{1}{4\pi c_s} \frac{\partial}{\partial t} \int_{|\Delta\mathbf{r}|=c_s t} \frac{p_0(\mathbf{r} - \Delta\mathbf{r})}{c_s t} dS. \quad (2.19)$$

Equation (2.19) describes the pressure at location \mathbf{r} at time t as the sum of contributions from the sources located at a spherical surface S with radius $c_s t$ and centred at \mathbf{r} .

Analytical solutions for the acoustic forward problem have been derived for photoacoustic sources with specific geometries [62, 63, 64, 65]. Numerical methods are available for solving the time-domain model in Eq. (2.16) for sources with arbitrary distributions, such as the finite-difference [66, 67] and finite-element [68, 69] methods. Faster calculations can be achieved using k -space pseudo-spectral methods [59, 70], which take advantage of fast Fourier transforms (FFT). For example, in one k -space method the acoustic field can be calculated as [59]

$$p(\mathbf{r}, t) = \frac{1}{(2\pi)^3} \int p_0(\mathbf{k}) \cos(c_s k t) e^{i\mathbf{k}\cdot\mathbf{r}} d\mathbf{k}, \quad (2.20)$$

where $\mathbf{k} = (k_x, k_y, k_z)$ is the wavenumber vector and $p_0(\mathbf{k})$ is the 3D Fourier transform of the initial pressure given by

$$p_0(\mathbf{k}) = \int p_0(\mathbf{r}) e^{-i\mathbf{k}\cdot\mathbf{r}} d\mathbf{r}. \quad (2.21)$$

For given p_0 , the pressure field at a later time point can be calculated using Eqs. (2.21) and (2.20).

2.4 Photoacoustic image acquisition

The methods for tissue irradiation and signal detection depend on the imaging modes and scanning geometries, which will be described below in Sec. 2.4.1 and 2.4.2 respectively. The properties of the ultrasound sensors used in photoacoustic imaging are described in Sec. 2.4.3.

2.4.1 Photoacoustic imaging modes

Photoacoustic imaging has two main imaging modes: photoacoustic microscopy and photoacoustic tomography. In photoacoustic microscopy [71], the tissue surface is in-

terrogated point-by-point and the measured ultrasound time series are mapped into 1D depth-resolved initial pressures, known as A-lines, using the speed of sound. The 3D images are formed directly from the A-lines acquired at each point, without using a reconstruction algorithm. Photoacoustic microscopy is further separated into optical resolution photoacoustic microscopy (OR-PAM) and acoustic resolution photoacoustic microscopy (AR-PAM). In OR-PAM, the photoacoustic signal is generated using tightly focused laser beams. The lateral resolution is determined by the size of the optical-diffraction-limited beam focus, which depends on the wavelength and the numerical aperture of the focusing lens. Typically, using near-infrared wavelengths, the lateral resolution is in the order of a few micrometres. Since OR-PAM relies on optical focusing, the imaging depth is limited to one optical transport mean free path, which is typically only ~ 1 mm in biological tissue due to the high optical scattering. In this shallow region, obtaining quantitative estimates of the chromophore concentrations is relatively straightforward, since the photons are mainly ballistic and the spectral colouring is low. In AR-PAM, the focusing is achieved using focused ultrasound receivers, while excitation light is wide-field or weakly focused. The lateral resolution is determined by the size of the acoustic focus, which is larger than the optical focus in OR-PAM because the acoustic wavelength is longer. This typically results in a resolution of tens of micrometres. Since the imaging depth is not limited by the optical transport mean free path, it can reach several millimetres.

In photoacoustic tomography, expanded laser beams are used to provide wide-field illumination of the tissue. The acoustic waves are detected over a surface that is fully or partially surrounding the tissue, using an array of sensors or by mechanically scanning the detector. Image reconstruction algorithms are used to form an image of the initial pressure distribution based on the detected signals. The frequency-dependent ultrasound attenuation in tissue, which limits the maximum frequency of the detected acoustic wave, sets the fundamental limit for the highest achievable resolution in photoacoustic tomography. In practice, however, other factors such as the detector bandwidth, the aperture of the detecting surface, the spacing between the sensing elements and sound speed variations within the tissue can limit the spatial resolution.

2.4.2 Tomographic scanning geometries

The geometry of a tomographic scanning system determines the fraction of the photoacoustic wavefronts that will be detected. Therefore it has an effect on both the qualitative image reconstruction and the accuracy of the chromophore quantification. A perfect reconstruction of the structures in a region requires that any line that crosses a point in this region must intersect with the detector surface [72]. This is illustrated in Fig. 2.2, where the points marked with A can be reconstructed exactly, while reconstruction artefacts will be present at the points B because there are lines going through the points that do not meet the detector surface. Points A are said to be within the “visible region” in a scanning system, which are illustrated with grey in Fig. 2.2. The edges of structures outside the visible region can also be reconstructed perfectly if a line along the normal of the edge crosses the detector surface. Examples of this are shown at points C in Fig. 2.2.

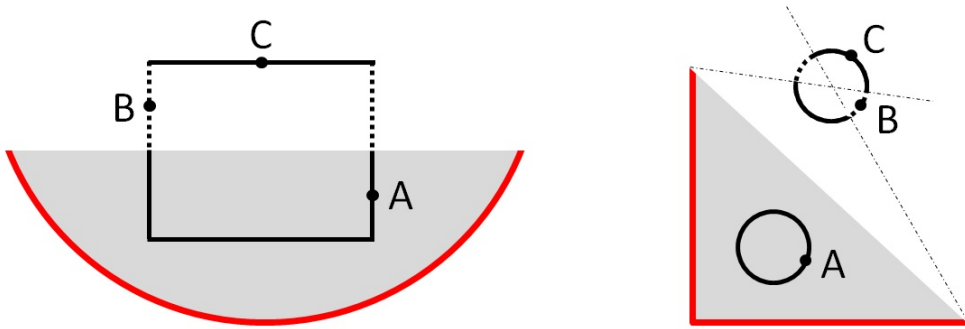


Figure 2.2: The visible region (gray) in arc (left) and orthogonal (right) sensor geometries. The sensor location is marked with red lines. The edges of the structures that can be reconstructed exactly are illustrated with solid lines, and the edges that will suffer from limited-view artefacts are illustrated with dashed lines.

In spherical photoacoustic scanning systems, the subject is fully enclosed within the detector surface and all the acoustic waves generated can be detected. Therefore, this detection geometry could in theory lead to a perfect reconstruction of the initial pressure distribution. Spherical scanning systems have been developed for whole-body small animal imaging [73], where the subject is rotated inside an arc of detector arrays to achieve signal detection over a spherical surface. Hemispherical scanners have been used in breast imaging [3, 74, 75], where the sensor elements are positioned in a bowl that can be rotated to decrease the spacing between the spatial sampling points. The cylindrical

scanning geometry [76] is commonly achieved by scanning arrays of detectors in a ring or an arc with partial angular coverage. Focused ultrasound transducers are commonly used in cylindrical scanners to avoid detecting out-of-plane signals in order to create a stack of 2D slice images of the subject. 3D images can be created by concatenating 2D slices acquired along the axial direction by moving the subject or the detector array. The drawback is that axial resolution is limited by the width of the acoustic focal plane. A simpler version of the cylindrical scanners is the circular scanning method, where a single transducer is mechanically moved around the subject along a circular path to detect the acoustic waves [77]. Both spherical and cylindrical/circular systems restrict the shape of the subject that can be imaged, since the subject needs to be enclosed or semi-enclosed. Hence, these systems are limited to imaging small animals or parts of the human body such as the breast or the fingers. Planar scanners [78] do not restrict the size of the subject as they only require access to one side of the tissue surface and are therefore more versatile. The disadvantage of planar sensors is the limited detection aperture which provides no visible region and leads to reconstruction artefacts.

2.4.3 Photoacoustic sensors

The most commonly used photoacoustic sensors are based on piezoelectric detectors, which have been well-developed for ultrasound imaging and have low cost of fabrication. Piezoelectric detectors based on polyvinylidene fluoride (PVDF) material can have up to tens of megahertz bandwidth, which is sufficient to capture the high frequency signals emitted from the smaller features in the superficial layers. However, the more commonly used lead zirconate titanate (PZT) detectors typically have narrower bandwidth. The main disadvantage of piezoelectric detectors is that their sensitivity reduces with element size. The element size must be small compared to the acoustic wavelength for two reasons: 1) The Nyquist criterion must be fulfilled to avoid aliasing, which requires that photoacoustic signals are spatially sampled at least every half an acoustic wavelength. 2) The acoustic reconstruction algorithms typically assume point detectors, which means that the element size should ideally be much smaller than the acoustic wavelength. Larger element size also leads to more spatial averaging, which results in increased angle-dependent sensitivity. It is difficult to fabricate piezoelectric detectors with sufficiently small element size while maintaining the required sensitivity. Another disadvantage is

that since piezoelectric detectors are not optically transparent, they may obstruct the delivery of the excitation light, which can be problematic for some imaging geometries. Interferometry based sensors [78, 79, 80, 81] can overcome these limitations. This type of sensors can allow for all-optical detection mechanism and typically have wideband, near-omni-directional detection capabilities. The sensor component can in some cases [78] be made transparent to the excitation beam, and hence provide a simple solution to the light delivery issue. Another advantage of interferometric sensors is that, unlike piezoelectric detectors, their sensitivity does not decrease as their element size decreases. One of the disadvantages of interferometry based sensors is that it is more challenging to achieve parallel detection which allows for faster scanning. However, recent developments in parallelising the scanning of the Fabry-Perot interferometer sensor have led to improved imaging speed [82] and dynamic imaging was enabled using compressed sensing [83, 84].

Chapter 3

The inverse problems in QPAT

Finding the chromophore concentrations from the measured photoacoustic signals requires solving two inverse problems: the acoustic inverse problem and the optical inverse problem. The acoustic inverse problem [85] involves reconstructing the initial pressure distribution from the acoustic time series measured at the tissue surface. The acoustic inverse problem has been researched extensively [85, 86, 87, 88, 89] and many reconstructions algorithms have been developed based on different mathematical approaches and assumptions about the detector geometry. While solving the acoustic inverse problem is a crucial pre-requisite for achieving quantitative photoacoustic imaging, it is not the main focus of this thesis, and therefore it will be summarised only briefly in Sec. 3.1.

This thesis focuses on the optical inverse problem, which is considered the remaining unsolved problem in QPAT. In fact, the term QPAT is often used to refer to the optical inverse problem only, under the assumption that the acoustic inverse problem has already been solved. In the optical inverse problem, the aim is to recover the concentration of the chromophores using the reconstructed initial pressure distribution at multiple wavelengths. It is a challenging problem to solve due to the unknown fluence distribution, the spatially varying Grüneisen parameter, the potentially large number of unknown variables to be estimated and the issue of non-unique solutions when both the scattering and absorption are unknown. Since the key contributions of this thesis are in the optical inverse problem, it will be described in detail and existing methods will be reviewed in Sec. 3.2.

3.1 Acoustic reconstruction

The acoustic reconstruction algorithms [85, 90, 91] can be broadly separated into four categories: time-domain methods (back-projection), frequency-domain methods, time-reversal methods and model-based optimisation methods.

The back-projection method is a simple and intuitive approach that was used to reconstruct the first photoacoustic images [92, 93]. The reconstruction is based on the solution to the wave equation in Eq. (2.19) and involves spreading the acoustic waves detected over a spherical surface to reconstruct the initial pressure distribution at each spatial location. The disadvantages of this method are the high computational cost and the fact that the reconstructed images contain circular reconstruction artefacts due to the approximate nature of the method. In the filtered back-projection method, a filtering step is performed before or after the back projection step. This process is analogous to back-projection reconstruction in X-ray computed tomography. The filtered back-projection method is able to reconstruct the photoacoustic images exactly for spherical [94], circular [95], ellipsoidal [96], cylindrical [88] and planar detectors [88].

In the frequency domain reconstruction method for a planar detector [86, 97], the measured pressure signals, $p_{det}(x, y, t)$, are Fourier transformed in 3D to give $p_{det}(k_x, k_y, \omega)$. Using the dispersion relation, the frequency component ω is mapped into k_z , resulting in $p_{det}(k_x, k_y, k_z)$. The inverse Fourier transform is then applied on $p_{det}(k_x, k_y, k_z)$ to obtain the initial pressure distribution $p_0(x, y, z)$. Fast Fourier transforms can be used to speed up the frequency domain reconstruction, making it significantly faster than the back-projection methods. Frequency domain reconstruction has also been developed for cubical [98], cylindrical [99] and spherical [100] detection geometries.

Time-reversal algorithms [101, 102] rely on the facts that 1) all acoustic waves generated within a finite volume will leave the volume to be captured by an enclosing detector surface after a sufficiently long time and 2) the wave equation is invariant when the direction of time is reversed. Hence, the forward acoustic model can be run backwards in time, such that the detected waves are emitted back into the image domain to form a reconstruction of the initial pressure at $t = 0$. Time-reversal algorithms are less restrictive compared to other algorithms as they do not rely on the assumption of specific detector geometries and can also, under some restrictions, account for heterogeneous acoustic properties [89]. Reconstruction based on time-reversal can be performed using

finite difference methods [102] or more efficiently using k -space pseudo-spectral methods [103]. More accurate reconstructions can be obtained for limited detection apertures using the iterative time-reversal method [104, 105], which is described in Sec. 6.3.1.

In model-based acoustic reconstruction methods [106], first, an initial reconstruction of the initial pressure distribution is generated. Then, a forward model is employed to calculate the acoustic signals at the detector surfaces. This is followed by iteratively adjusting the reconstruction of the initial pressure until the difference between the modelled and the measured acoustic signals is minimised, thus improving the accuracy of the reconstruction. Additional regularisation terms, for example Tikhonov [107, 108] or total variation regularisation [109], can be included in the minimisation scheme to increase the stability of the reconstruction. The main disadvantages of model-based reconstruction methods are that they are slow and memory intensive. Faster reconstruction could be achieved by multiplying the pseudo-inverse of a pre-calculated forward operator matrix with the vector of the measured acoustic signals for specific detector geometries [110]. However, due to the large size of the forward operator matrix, this is only feasible when the number of detector elements and the image size are small.

3.1.1 Practical limitations of the acoustic reconstruction

The acoustic reconstruction provides the initial pressure distribution that is used as input for the optical inversion¹. Therefore, the accuracy of the acoustic reconstruction impacts the estimation of the chromophore concentrations. Many theoretical QPAT studies assume that the acoustic reconstruction is perfect, such that the images represent p_0 exactly. However, in practice, errors in the acoustic reconstruction may arise due to many experimental issues. The most significant issues are discussed below:

Detection aperture Perfect reconstruction can only be achieved if all the acoustic waves generated were captured by the detectors. As discussed in Sec. 2.4.2, this is only possible with spherical scanners where the subject is enclosed within the detecting surface. In cylindrical and planar scanners, only a fraction of the acoustic waves generated are captured by the detectors. The effect of the finite detection aperture is illustrated

¹The exceptions are the quantitative reconstruction methods where the acoustic inversion is incorporated in an “one step” inversion, so that the chromophore concentrations are obtained directly from the pressure time series (Sec. 3.2.3.3).

using a numerical simulation in Fig. 3.1. The three circular insertions have the same initial pressure, p_0 , as shown in Fig. 3.1(a). Figure 3.1(b) shows the reconstructed p_0 using the photoacoustic signals recorded by a planar sensor at one side of the domain (limited-view). The sensor positions are marked with red lines. The limited-view reconstruction contains streak artefacts, and the edge of the circular insertions are not reconstructed accurately, leading to distorted shapes. Furthermore, the reconstruction of the initial pressure is higher for the bottom insertions, due to the fact that a larger fraction of the wave-front of the bottom insertion is captured by the sensor compared to the top insertion. These reconstruction errors are referred to as limited-view artefacts and it is clear that they will cause errors in the quantification. For comparison, Fig. 3.1(d) shows that an accurate reconstruction of p_0 can be obtained when the acoustic signals measured by detectors at all four sides of the domain are used (full-view). The limited-view artefacts of planar sensors can be reduced by placing a second orthogonal planar sensor to create a “V-shaped” scanner [111]. This configuration is described in more detail in Sec. 6.3.1.

Sensor properties The ideal photoacoustic sensor is a point-detector with omnidirectional response and infinite bandwidth. In practice, the data is often bandlimited to some extent. For example, the bandwidth of PZT transducers, which are commonly used, is typically limited to a few megahertz and their sensitivity is not equal for all frequencies. The finite size of the detection element and the related directional variations in their sensitivity may also contribute to errors in the image reconstruction.

Acoustic attenuation The attenuation of ultrasound in biological tissue is frequency dependent and often follows the experimentally determined power law: $a\omega^n$, where ω is the angular frequency of the ultrasound waves, a is the power law prefactor and n is the power law exponent. Both a and n vary depending on the tissue type. The loss of the high frequency components in the ultrasound signals limits the resolution in a depth dependent manner. To reduce the impact of the acoustic attenuation, Treeby *et al* proposed a time-reversal reconstruction method where the attenuation is compensated for by including a dispersion term in the reconstruction [89].

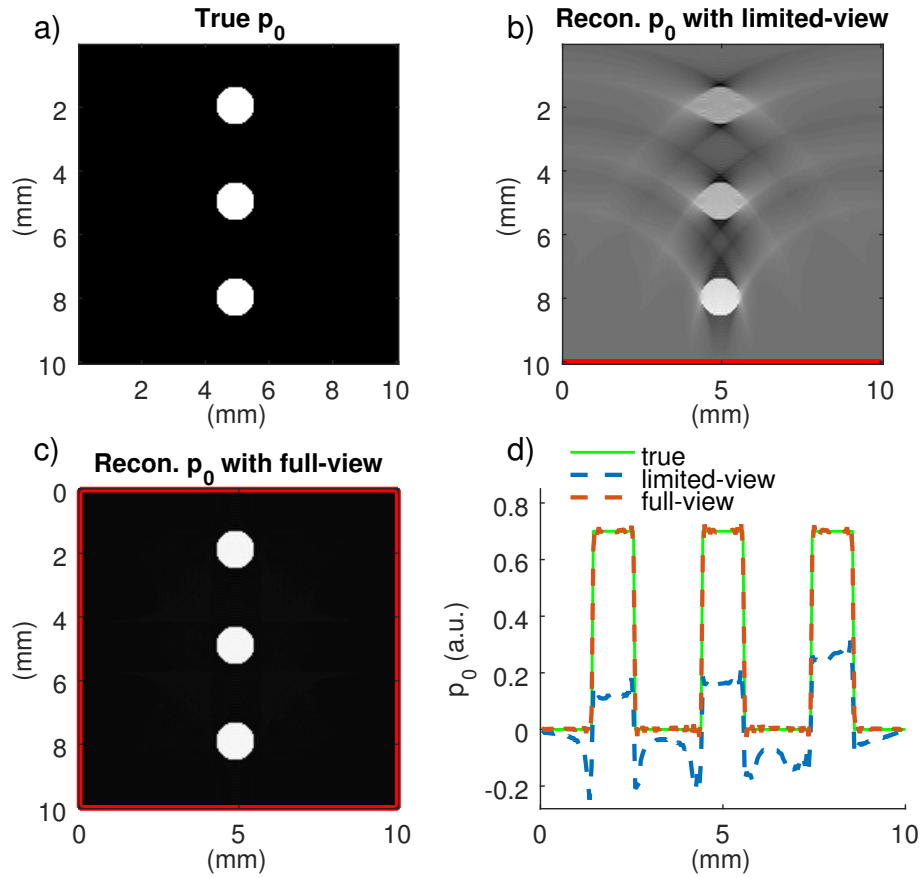


Figure 3.1: a) The true initial pressure. b) The limited-view reconstruction of the initial pressure, where the signals detected at only one side of the domain were used. The sensor locations are marked with red lines. c) The full view reconstruction, where the signals detected at all sides of the domain were used. d) The reconstructed initial pressure at a vertical line across the insertions using limited-view (blue dashed line) and full-view (red dashed line) compared to the true initial pressure (green solid line).

Heterogeneous sound speed The speed of sound in tissue is assumed to be spatially homogeneous in most reconstruction algorithms. However, in reality, the speed of sound may not be known accurately as it depends on the tissue type and may vary between 1400-1600m/s [112]. The spatially heterogeneous sound speed will, if unaccounted for, cause errors in the reconstruction and lead to blurry or distorted images. Reconstruction algorithms that allow for variable sound speed have been developed in Refs. [102, 113].

The above-mentioned issues need to be taken into consideration when choosing imaging systems, sensors and reconstruction algorithms, such that an accurate acoustic reconstruction can be produced. This is a crucial pre-requisite for obtaining accurate

quantitative estimates of the chromophore concentrations.

3.2 Chromophore quantification methods

The aim of QPAT is to estimate the chromophore concentrations, which requires solving the optical inverse problem in photoacoustic imaging [22]. If the fluence distribution was known, the solution would be trivial. Therefore the simplest QPAT methods involve using an estimation or measurement of the fluence to reduce the problem to a linear problem, which can be solved straightforwardly using linear methods (Sec. 3.2.1). In methods that do not require linearisation, the fluence is modelled based on light transport theory. The unknown optical parameters or chromophore concentrations can be solved for in a non-iterative manner (Sec. 3.2.2), or using iterative minimisation methods (Sec. 3.2.3). Methods that do not assume linearity, nor require fluence modelling, have also been developed (Sec. 3.2.4). Section 3.3 discusses the challenges that remain for achieving accurate quantification and the current state of QPAT is summarised in Sec. 3.4.

3.2.1 Linear methods

In linear methods, the reconstructed initial pressure distribution is assumed to be linearly related to the chromophore concentrations:

$$p_0(\mathbf{r}, \lambda) \propto \sum_k \alpha_k(\lambda) c_k(\mathbf{r}) \quad (3.1)$$

which means that any effect of the spectral colouring is ignored. In other words, it is assumed that the fluence has no spatial or spectral dependence. Quantification methods based on this linear model are described in the following sections. Methods for linearising the problem such that linear methods can be applied are also described.

3.2.1.1 Linear spectroscopic inversion

In linear spectroscopic inversion (SI), the concentrations are found by multiplying the pseudo-inverse of the matrix of the specific absorption coefficients by the multiwavelength images. SI is commonly used for estimating the sO_2 [35, 36, 46, 47, 114, 115] and

identifying biomarkers from the background tissue [43, 116, 117] in *in vivo* photoacoustic studies. The chromophore concentrations are estimated to a common scaling factor in SI. However, in the case of sO_2 measurements, the scaling factor cancels out since the sO_2 is defined by the ratio of the concentrations. SI is described in more detail in Sec. 4.2.

3.2.1.2 Linear unmixing methods

Here, the term “linear unmixing” will be used to refer to methods that are based on a linear model but primarily aim to separate, or “unmix”, the contributions from different chromophores in the multiwavelength photoacoustic images, rather than to provide an accurate quantification of the chromophore concentrations. In linear unmixing methods, the statistical properties of the chromophore distribution are exploited to separate the chromophores, and the *a priori* knowledge about the absorption spectra is either not used at all (blind unmixing) or used only to constrain/initialise the search (semi-blind unmixing). Linear unmixing methods include vertex component analysis [118], adaptive matched filter [119], principal component analysis (PCA) [120] and independence component analysis (ICA) [120, 121]. ICA is the subject of Chapter 5, where the algorithm and its applications will be described in detail.

3.2.1.3 Fluence correction

When applying the linear spectroscopic inversion or unmixing methods, it is assumed that the optical inverse problem has been linearised, even though the linearisation step is often not made explicit. Linearisation refers to approximating the nonlinear equation for the photoacoustic initial pressure in Eq. (2.15) by the linear equation in Eq. (3.1). Linearisation can be achieved either by simply assuming that the fluence is spatially and spectrally constant, or by dividing the photoacoustic images with an approximation of the fluence to partially correct for the fluence variations. A number of fluence correction methods which have different levels of accuracy are described below:

Correcting for an absorbing layer In a study of the vasculature in the mouse brain, Wang *et al* applied a correction for the absorption of the skin and skull layers using *in vitro* measurements [77]. Invasive *in vivo* measurements have also been performed, where

the attenuation of the skin layer was measured by inserting a thin sheet with known absorption properties under the skin [122, 123].

This type of correction can reduce the spectral colouring to some extent, provided that the absorption of the layer has been estimated accurately. However, it cannot fully remove the nonlinear effect of the fluence, because it can at best only account for the fluence distortion caused by the superficial layer. It neglects fluence variations due to the optical properties of the tissue underneath that layer, as well as the fact that the presence of the layer or the absorbing sheet changes the fluence in the surrounding tissue.

Other attempts to estimate the fluence include injecting the subject with a contrast agent of a known small concentration [124]. A linear equation for the concentration can be obtained using the images acquired before and after the injection, and the concentration of the contrast agent. This assumes that the fluence, the concentration of the endogenous chromophores, and the scaling parameters (including the Grüneisen parameter) do not change after the injection, and that the concentration of the contrast agent is known accurately. It is however unlikely that all assumptions can be fulfilled, because the distribution of the contrast agent is rarely known accurately, and for the change in the measured signal to be detectable, it is likely that the change in fluence is also significant.

Estimation based on a homogeneous medium The exponential decay given by Eq. (2.10) can be used as an estimation of the fluence, where the effective attenuation coefficient can be interpreted as a bulk average parameter for the tissue [44]. A similar correction can also be applied for imaging systems with circular illumination, in which case the fluence can be approximated as a radially symmetric function [125]. As described in Sec. 2.1.4, the exponential fluence model is exact for an optically homogeneous semi-infinite medium illuminated by an infinite plane wave. Clearly, practical imaging scenarios are unlikely to fully satisfy those assumptions. Therefore, the accuracy of the fluence correction depends on the level of homogeneity in the tissue, depth from the illuminated surface and the size of the illumination beam.

Non-invasive fluence measurements The simplest approach to non-invasively estimate the fluence involves using the photoacoustic image at one wavelength to correct for the fluence at other wavelengths [126]. A number of other studies have proposed using

measurements of the fluence at the surface of the tissue to estimate the internal fluence distribution. Ranasinghesagara *et al* [127] used diffuse reflectance measurements [128] of the back-scattered light to estimate the bulk average absorption and scattering coefficients of phantoms, which were used to calculate an approximate estimate of the fluence. The diffuse light was also measured by Yin *et al* [129] at different positions at the surface of a phantom and used as constraint for an iterative calculation of the fluence in a non-linear inversion (Sec. 3.2.2). The applications of the methods in Refs. [127] and [129] are limited to tissue regions with only small heterogeneities. In order to measure the fluence in tissues containing larger heterogeneous features, Bauer *et al* [130] used diffuse optical tomography (DOT). DOT can provide spatially resolved images of the absorption and scattering by using multiple light detectors at different locations. However, the higher frequency components of the fluence which arise due to abrupt changes in absorption at organ boundaries cannot be estimated accurately, because DOT has significantly lower resolution than photoacoustic imaging.

3.2.1.4 Perturbation problem

This group of methods takes advantage of the fact that the heterogeneous absorbing features in the tissue are often small, and can therefore be treated as perturbations in an optically homogeneous medium. This model was used by Ripoll and Ntziachristos [131] to recover small absorption perturbations. In this study, the fluence is assumed to be unchanged by the absorption perturbations, so that

$$\delta H = \delta\mu_a\phi_0, \quad (3.2)$$

where δH is the change in the absorbed energy density due to the absorption perturbation $\delta\mu_a$ and ϕ_0 is the unperturbed, or background, fluence. The background fluence is calculated based on the Green's function using the DA model. It is assumed that the scattering is homogeneous and known, and the unperturbed background absorption is also known. This method has similar disadvantages to when the fluence is corrected using the 1D exponential decay model, where errors may arise if the background optical properties are not known accurately and if the absorption perturbations are sufficiently large to cause significant changes in the fluence.

To reduce the errors for cases where the absorption perturbations are large, instead of

assuming unchanged fluence, the change in the fluence can be modelled as a perturbation on the background fluence, using the Born approximation method. The perturbed fluence can be modelled using the DA for perturbations in absorption only [132], or for perturbations in both the absorption and the scattering coefficients [133]. This leads to an expression for the change in the absorbed energy density that is linear with respect to the absorption perturbation, which can be inverted to recover $\delta\mu_a$. The quotient of images acquired with different illumination were used in the numerical implementations of the Born approximation method in Refs [132] and [133]. This has the advantage of cancelling out the Grüneisen parameter and system scaling factors. The disadvantage of the Born approximation method is that it is valid only for small changes in absorption and the optical properties of the background must be known accurately.

3.2.2 Non-iterative nonlinear methods

In general, linear methods are unlikely to be accurate when the tissue contains inhomogeneous optical features that are large or have optical properties that differ significantly from the background. Therefore, in these cases, it is necessary to use methods that are not based on a linear model. Two nonlinear methods that do not require iterative update, and instead rely on rearranging the diffusion equation are described below. One method assumes that the scattering is known (Sec. 3.2.2.1) and one assumes unknown scattering (Sec. 3.2.2.2). The Grüneisen parameter is assumed to be known in both methods.

3.2.2.1 Rearranging DA for absorption

Since the term $\phi\mu_a$ appears in the DA in Eq. (2.9), it can be replaced by the measured H , since $H = \phi\mu_a$ (assuming that Γ is known and has been divided out from the reconstructed images: $H = p_0/\Gamma$). In this way, the DA can be rewritten as [134]

$$(\nabla \cdot D\nabla)\phi = H - q_0. \quad (3.3)$$

Equation (3.3) can be solved numerically to find ϕ by assuming $\mu_a \ll \mu'_s$ such that $D \approx (3\mu'_s)^{-1}$. Hence, the absorption coefficient can be estimated by $\mu_a = p_0/(\Gamma\phi)$.

3.2.2.2 Rearranging DA for absorption and scattering

When scattering is unknown, the DA can be manipulated using two images acquired with different illumination patterns, $H_1 = \mu_a \phi_1$ and $H_2 = \mu_a \phi_2$, to give [135, 136]

$$\nabla \cdot \left(\frac{D\beta}{\mu_a^2} \right) = 0, \quad (3.4)$$

where β is the vector field

$$\beta = \mu_a^2 \phi_1^2 \nabla \left(\frac{\phi_2}{\phi_1} \right). \quad (3.5)$$

Two methods for solving Eq. (3.4) has been proposed in Refs [135, 136]. It was demonstrated using numerical simulations that a stable solution exists for suitably chosen illumination patterns (for example illuminating from different sides of the subject) [136]. The solution methods require μ_a to be non-zero everywhere and D must be known at the boundaries. Practical implementation of this method may be hindered by the sensitivity of the quotient term in Eq. (3.5) to noise in the images.

3.2.3 Iterative nonlinear methods

In this section, methods that use iterative updates to bring the unknown parameters closer to the true solution are described. These methods typically involve the forward modelling of the photoacoustic images and applying minimisation techniques.

3.2.3.1 Fixed point iteration

If the scattering is known, Eq. (2.14) can be rearranged such that the absorption coefficient can be written as a function of itself. Hence, a fixed point iteration can be used to recover μ_a [137]:

$$\mu_a^{(i+1)} = \frac{H^{meas}}{\phi^{(i)}(\mu_a^{(i)}, \mu_s) + \epsilon}, \quad (3.6)$$

where i denotes the i th iteration, H^{meas} denotes the measured H , ϵ is a small number that is included to ensure a non-zero denominator in the presence of noise and ϕ^i is estimated fluence at the i th iteration. The general procedure for estimating μ_a using the fixed point iteration is as follows: 1) Make an initial guess for the absorption, μ_a^0 . 2) Model the fluence based on μ_a^0 and the known scattering: $\phi^{(0)}(\mu_a^0, \mu_s)$. 3) Use Eq. (3.6) to calculate $\mu_a^{(i+1)}$. 4) Update the fluence using the new absorption

$\phi^{(i+1)}(\mu_a^{i+1}, \mu_s)$. 5) Iterate steps 3 and 4 until the difference between the measured and the modelled absorbed energy density, $\left|H^{meas} - \phi^{(i)}\mu_a^{(i)}\right|$, is smaller than a pre-defined tolerance threshold.

Using the DA as the light model, the fixed point iteration method has been applied to experimental data in a series of publications [138, 139, 140, 141, 142] aiming towards measuring the oxygenation in finger joints *in vivo*. The method was first demonstrated using 2D [138] and 3D [139] phantom images. The subsequent publications presented *in vivo* measurements [140] and comparing the blood oxygenation and total haemoglobin concentration of osteoarthritis patients with healthy volunteers [142].

The fixed point iteration scheme does not put restrictions on choice of light model and has also been implemented using the δ -Eddington approximation in Ref. [143] and the RTE in Refs. [144, 145].

3.2.3.2 Methods based on optimisation (model-based inversion)

Optimisation problems occur in many different fields and the aim, in a general sense, is to find the maximum or minimum of an objective function. In QPAT, optimisation can be used to solve inverse problems by iteratively updating the unknown parameters in a model of the initial pressure distribution until the difference between the modelled and the measured image data is minimised. For consistency with the literature, this method is referred to as “model-based” inversion in this thesis. Although, of course, all QPAT methods assume some model of light transport, either explicitly or implicitly (in the simplest case the fluence is assumed to be constant), except for the methods described in Sec. 3.2.4. In model-based inversion, the objective function, or error functional, ε , to be minimised can be written as

$$\underset{\mathbf{u}}{\operatorname{argmin}} \varepsilon(\mathbf{u}) = \frac{1}{2} \sum_{i=1}^I \sum_{n=1}^N \sum_{m=1}^M \left[p_{0,m,\lambda_n}^{model}(\mathbf{u}) - p_{0,m,\lambda_n}^{meas} \right]^2 + \mathcal{P}(\mathbf{u}), \quad (3.7)$$

where M is the total number of voxels, N is the total number of wavelengths, I is the total number of illuminations, and \mathbf{u} is the vector of the unknown variables, which may for example consist of the absorption and scattering coefficients at each voxel. The second term $\mathcal{P}(\mathbf{u})$ in Eq. (3.7) represents additional regularisers that penalise noise or artefacts. The most well-known regularisers are the Tikhonov regulariser [146], which increases the

smoothness of the estimated variables, and the total variation (TV) regulariser [147], which encourages the estimated variables to be piece-wise constant. Examples of applications of the Tikhonov and TV regularisers in QPAT can be found in Refs. [140, 148, 149] and [136, 150] respectively.

There is a large body of literature [151, 152, 153] on different approaches for updating the parameters in order to find the minimum of the error functional. The approaches can be categorised into two main groups: trust-region search methods and line-search methods. In trust region methods, the error functional is replaced by a function that is simpler but still an adequate approximation for a region close to the current set of variables, known as the “trust region”. Then a step direction which reduces the approximate function is chosen and the variables are updated with a step length within the trust-region.

In line-search methods, first, the step direction is determined based on the gradient information, and then the step size is computed by finding the minimum along the step direction. The most intuitive way to determine the step direction is to find the direction where the error function has the largest gradient (steepest descent). This is known as the gradient-descent method. The disadvantage of gradient-descent methods is that they can require many iterations before reaching the global minimum. Methods based on the Hessian matrix or its approximation, on the other hand, typically have faster convergence. These methods are briefly described below:

Newton’s method In Newton’s method, the step direction $\mathbf{s}^{(i)}$ at iteration i is given by

$$\mathbf{s}^{(i)} = -(\nabla^2 \varepsilon^{(i)})^{-1} \nabla \varepsilon^{(i)} \quad (3.8)$$

where $\nabla^2 \varepsilon^{(i)}$ is the Hessian matrix with the second derivatives (the notation should not be confused with the Laplace operator) and is given by

$$\nabla^2 \varepsilon = \begin{bmatrix} \frac{\partial^2 \varepsilon}{\partial \mathbf{u}_1} & \frac{\partial^2 \varepsilon}{\partial \mathbf{u}_1 \partial \mathbf{u}_2} & \cdots & \frac{\partial^2 \varepsilon}{\partial \mathbf{u}_1 \partial \mathbf{u}_L} \\ \frac{\partial^2 \varepsilon}{\partial \mathbf{u}_2 \partial \mathbf{u}_1} & \frac{\partial^2 \varepsilon}{\partial \mathbf{u}_2^2} & \cdots & \frac{\partial^2 \varepsilon}{\partial \mathbf{u}_2 \partial \mathbf{u}_L} \\ \vdots & \vdots & \ddots & \vdots \\ \frac{\partial^2 \varepsilon}{\partial \mathbf{u}_L \partial \mathbf{u}_1} & \frac{\partial^2 \varepsilon}{\partial \mathbf{u}_L \partial \mathbf{u}_2} & \cdots & \frac{\partial^2 \varepsilon}{\partial \mathbf{u}_L^2} \end{bmatrix} \quad (3.9)$$

where L denotes the number of unknown variables, and $\nabla\varepsilon^{(i)}$ is the gradient of the error functional given by

$$\nabla\varepsilon = \left[\frac{\partial\varepsilon}{\partial\mathbf{u}_1} \quad \frac{\partial\varepsilon}{\partial\mathbf{u}_2} \quad \cdots \quad \frac{\partial\varepsilon}{\partial\mathbf{u}_M} \right]^T. \quad (3.10)$$

The efficiency of the gradient calculations can be increased using the adjoint model (Sec. 6.4). The memory demand for storing the Hessian matrix can be extremely large, because the size of the Hessian matrix scales quadratically with the number of unknown variables L . Therefore, for the large scale inverse problem in QPAT, where the number of unknowns is in the order of 10^6 (because a high-resolution 3D photoacoustic image may have a voxel size of $100\mu\text{m}^3$, which means that for a 1cm^3 volume, the number of voxels equals 10^6), the practical implementation of Newton's method becomes difficult.

The Gauss-Newton method The cost of calculating the Hessian matrix can be reduced by approximating it with $\nabla^2\varepsilon \approx \mathbf{J}^T\mathbf{J}$, where \mathbf{J} is the Jacobian matrix with the partial derivative of p_0^{model} with respect to the unknown parameters. The Gauss-Newton method was implemented in Ref. [138] where μ_a was recovered from numerical and experimental phantoms, and in Ref. [154] where the chromophore concentrations were recovered from multiwavelength simulated 2D images.

Quasi-Newton methods Quasi-Newton methods are less memory intensive than both the Newton and Gauss-Newton method, because the Hessian matrix is approximated using only the gradients of the error functional. The Quasi-Newton methods have slower rate of convergence than the other methods, but the modest memory requirements makes them more attractive for applications in QPAT. Commonly used Quasi-Newton algorithms include the Broyden-Fletcher-Goldfarb-Shanno (BFGS) algorithm, the Davidon-Fletcher-Powell (DFP) formula, and the symmetric rank 1 (SR1) method. The methods are distinguished by different ways of approximating the Hessian and updating the unknown variables.

There are also optimisation methods that do not use any gradient information, such as the Nelder-Mead method, which was used in Ref. [155]. However, they have slower convergence rate and are not suitable for large scale inversions. The methods described above assume that the error functional is convex with respect to the unknown variables.

When the error functional is non-convex (for example the mutual information term in Eq. (6.3) in Sec. 6.2), search methods based on the gradient information may not lead to the optimal solution.

3.2.3.3 Implementations of model-based inversion

In the case where scattering is known, the absorption can be estimated from the reconstructed H at a single wavelength and illumination angle [137, 138, 144]. However, if both absorption and scattering are unknown, they cannot be uniquely reconstructed using a photoacoustic image acquired at a single wavelength and illumination angle [135]. That is to say, there are multiple combinations of absorption and scattering distributions that can give rise to the same photoacoustic image. This non-uniqueness problem can be overcome by using multi-illumination (Sec. 3.2.3.3.1) or multiwavelength imaging methods (Sec. 3.2.3.3.2). Implementations of model-based inversion using the Monte Carlo method are described in Sec. 3.2.3.3.3. Section 3.2.3.3.4 describes the one-step approach for recovering the optical parameters directly from the measured photoacoustic time series.

3.2.3.3.1 Multi-illumination The multi-illumination method uses images acquired with excitation light of the same wavelength but illuminating the subject from different angles or with different illumination patterns. The multi-illumination method has been applied by Gao *et al* [150] using the Bregman method in a model-based inversion based on the DA. The model-based inversion using multi-illumination has also been implemented using the RTE: Tarvainen *et al* [156] used the Gauss-Newton method to recover both the absorption and scattering coefficients based on 2D simulated multi-illumination images. Saratoon *et al* [157] demonstrated a more computationally efficient inversion using the quasi-Newton minimisation method and also included the acoustic reconstruction in the simulation.

In the multi-illumination method, the absorption coefficient is recovered at one single wavelength. It is then assumed that the method can be repeated for multiple wavelengths to obtain the absorption spectra, from which the concentrations can be found using a linear spectroscopic inversion.

A combination of multi-illumination and multiwavelength imaging, where the images

with different illumination patterns at different wavelengths were used simultaneously (as opposed to using multi-illumination images at each wavelength separately, which was suggested above) was proposed to simultaneously recover the absorption, the scattering and also the Grüneisen parameter. This method has been demonstrated using simulated images based on the DA [158] and the RTE [159], but not with experimental data.

3.2.3.3.2 Multiwavelength The non-uniqueness problem can also be removed by using images acquired using excitation light with different wavelengths. Cox *et al* [154] modelled the wavelength dependence of the scattering using the empirical formula

$$\mu'_s = a\lambda^{-b}, \quad (3.11)$$

where a is referred to as the scattering amplitude and b is an experimentally determined constant that varies for different types of tissues [160]. It was shown that the chromophore concentrations and the scattering amplitude can be uniquely recovered from multiwavelength images, provided that the wavelength dependence of both the scattering and the absorption are known [154].

The multiwavelength model-based inversion method was applied to experimental phantom images in a series of studies by Laufer *et al* [41, 155, 161]. The earliest publication [161] presented measurements of a blood-filled cuvette in which the fluence was modelled in 1D using the δ -Eddington approximation. The concentrations of oxy- and deoxyhaemoglobin and the scattering amplitude were estimated separately by fitting the modelled time series to the measured data. This was extended to a spatially resolved quantification of oxy- and deoxyhaemoglobin concentrations based on a 2D δ -Eddington model in Ref. [155]. Finally, in Ref. [41], an acoustic propagation model was included in the inversion such that the minimisation was performed on the reconstructed images rather than the acoustic time series, and the accuracy of the fluence model was improved by including a correction factor for the circular light beam. The concentrations of contrast agents in a tube phantom were quantified for segmented regions with piece-wise constant optical properties.

Since the publication of this series of papers, a number of other studies tackling the quantification problem using model-based inversion *in vivo* or in full 3D has been published. However, these studies did not rely on multiwavelength images to remove

non-uniqueness. Instead, it was avoided by either fixing [42] or restricting [162] the values the scattering take. Brochu *et al* [162] used the least squares minimisation approach as a means of estimating the fluence. This estimated fluence was then divided out from the images to correct for the spectral colouring. The inversion was performed on a per-2D-slice-basis using phantom images and *in vivo* mouse images acquired in a cylindrical scanner. The 2D δ -Eddington model was used as the light model and piecewise constant optical properties were assumed at organ level, which required manual segmentation. The main limitation of the study is the fact that the 2D model is unlikely to be accurate due to the complex 3D structures within the mouse.

In a recent publication, Fonseca *et al* [42] demonstrated a full 3D inversion based on the DA and assuming known scattering. The concentration ratio as well as the absolute chromophore concentrations were estimated on a voxel-by-voxel basis (no segmentation) in an experimental phantom. The study showed accurate results for the concentration ratio estimation. The estimation of the absolute chromophore concentrations contained larger errors, but promising improvement was observed once an additional scaling factor for the system calibration was added as an unknown variable in the minimisation.

The advantages of using the multiwavelength approach over the multi-illumination approach include [22]:

- In cases where there are images at more wavelengths than chromophores with unknown concentrations ($N > K$), the number of unknowns is smaller when chromophore concentrations are recovered directly ($L = KM$), than when the absorption is recovered at each wavelength ($L = NM$). This means that the computational burden may be less in the multiwavelength approach.
- The multi-illumination approach requires at least two images per wavelength to recover the absorption coefficient uniquely when scattering is unknown, while the multiwavelength approach only requires one image per wavelength. Hence, using the multiwavelength approach reduces the time required for image acquisition.

3.2.3.3.3 Monte Carlo implementations In all above mentioned studies, the model-based inversion was implemented using FEM. Monte Carlo (MC) implementations are less common, but have been published in Refs. [163, 164, 165, 166]. The MC

model is usually used to calculate the fluence rate, which is the radiance integrated over all angles, but the angle-dependent radiance is not stored for several reasons: the large memory demand, the fact that radiance is often not the quantity of interest and calculating radiance requires using more photons in the model compared to only calculating the fluence rate. Therefore, the functional gradient with respect to scattering cannot be calculated analytically. In Refs. [165, 166], a non-gradient based minimisation algorithm was used to find the concentration ratios in segmented regions with piecewise constant concentrations in 3D experimental phantom. In Refs. [163, 164], Hochuli *et al* used a harmonic angular basis to store the radiance field computed using a 2D MC model. This allowed the gradients to be calculated based on the harmonic angular basis, such that a gradient-descent minimisation algorithm could be used to estimate the absorption and scattering coefficients from simulated images with multiple illuminations.

3.2.3.3.4 One step method The model-based inversion scheme and its variations described above are based on the reconstructed images. It is also possible to perform a “one-step” inversion, where the optical parameters are recovered directly from the measured photoacoustic time series. This was implemented by Laufer *et al* in Ref. [161], as mentioned in Sec. 3.2.3.3.2. A different approach was proposed by Shao *et al* [167]. They used the Born approximation based on the DA to model the fluence and recovered the absorption and scattering from 2D simulated images illuminated from different angles. Another experimental demonstration of the one-step inversion using the DA was presented by Yuan *et al* [168]. In this study, the scattering was fixed and only the absorption coefficient was recovered. The one-step inversion has also been implemented in a simulation study using the RTE [148] to recover the absorption coefficient. In the above mentioned studies, the sound speed was fixed in the inversion. In Ref. [169] both the absorption coefficient and the sound speed were reconstructed simultaneously using eight illuminations, assuming known scattering. The one-step inversion has also been solved using a Bayesian approach (see Sec. 3.2.3.4) in Ref. [170], where reconstructions of the absorption and scattering were demonstrated also for limited-view settings.

3.2.3.4 Additional priors in model-based inversion

The Bayesian approach was used in Ref. [171], which allowed the statistical properties of the noise to be explicitly included in the model-based inversion, leading to improved reconstructions of the absorption and scattering. Pulkkinen *et al* [172] extended the Bayesian quantitative reconstruction method to be used for multiwavelength images. They used two illuminations at three wavelengths (six measurements in total) to estimate the chromophore concentrations, the scattering and the Grüneisen parameter. However, implementing the Bayesian approach for high resolution 3D images is challenging due to the high computational and memory demands.

Malone *et al* [173] proposed a reconstruction-classification method which uses the prior knowledge that the optical parameters belong to a few classes to improve their estimates. The algorithm alternates between solving the conventional least-squared minimisation problem, and a segmentation problem (the classification step). Both 2D and 3D simulations were used to demonstrate improved estimates of the absorption and scattering.

In these studies [171, 172, 173], the improvement of the estimate of the scattering is more significant than for the absorption. This may be due to the fact that the scattering is typically recovered less accurately than the absorption in conventional model-based inversion. The reasons for this are discussed in Sec. 3.3.3.

3.2.4 Quantification without fluence modelling

Accurately inverting for the chromophore concentrations by modelling the fluence is not a straightforward task. Therefore, a number of methods that avoid using experimental measurements or modelling strategies to account for the fluence have been developed and are described below.

Rosenthal *et al* [174] presented a quantification method based on the assumption that the fluence is slowly varying in space due to diffusion, while the map of the absorption coefficient has high spatial frequency components as it changes abruptly at organ or vessel boundaries. These spatial characteristics are exploited to decompose the image into two components describing the light fluence and the absorption coefficient respectively, using sparse representations in two suitable sets of elementary functions.

Tzoumas *et al* [175] proposed representing the fluence in the unknown and hetero-

geneous tissue as a linear superposition of a few reference fluence base spectra, which were generated by applying principal component analysis (PCA) on 1470 simulated fluence distributions. The weight for each base fluence spectrum and the oxy- and deoxyhaemoglobin concentrations at each voxel were estimated using a constrained optimisation scheme that finds the closest match between the modelled and the measured image intensity.

Choi *et al* [176] attempted to avoid the effect of the local fluence variations by measuring the superimposed “differential” photoacoustic signal generated by two square wave modulated light sources with different wavelengths. The ratio of the amplitude of the two excitation signals and their phase difference can be adjusted to give the photoacoustic signal high sensitivity towards small changes in sO_2 .

3.3 Discussion and remaining challenges

The complexity and computational intensity vary greatly between different inversion techniques. If only the location of the chromophores or the concentration ratios are of interest, the quantification task becomes relatively easy, and it may be possible to obtain sufficiently accurate results with a simple approximation of the fluence. However, if the goal is to estimate the concentrations accurately in absolute units in complex tissue structures, it is likely that more sophisticated methods of accounting for the fluence are required. Also, it is more challenging to obtain accurate quantification when more parameters are unknown. For example, when the Grüneisen parameter and the scattering coefficient are unknown, more images from different illumination pattern and/or wavelengths are required to remove non-uniqueness. Furthermore, the computational and memory demands often scale with the number of unknown variables. This means that inverting for segmented regions with piece-wise constant optical parameters is significantly less challenging than obtaining quantification on a voxel-by-voxel basis. With these issues in mind, it is important to identify which type of quantification and what level of accuracy are required for each particular application, such that an appropriate quantification method can be chosen.

To conclude this chapter, the main challenges of QPAT are discussed below and a brief summary of the current state of QPAT is provided in Sec. 3.4

3.3.1 Limitations of linear methods

The linear model in Eq. (3.1) is an approximation of the nonlinear relationship between the photoacoustic initial pressure and the chromophore concentrations (Eq. (2.15)). This approximation may be accurate under some circumstances, for example where spatial variations in optical parameters are low such that the fluence is nearly constant or can be approximated with a simple exponential decay. However, it is unlikely that linear methods can provide accurate quantification in a general sense. Despite the lack of rigorous assessment of their accuracy, linear methods have been used extensively in *in vivo* preclinical studies. Furthermore, methods such as SI and ICA cannot provide absolute quantification and are unable to account for the Grüneisen parameter.

3.3.2 Challenges of nonlinear methods

In theory, the nonlinear model-based inversion method can be used to obtain accurate recovery of the chromophore concentrations for arbitrary tissue structure and hence provides a generally applicable solution to the QPAT problem. However, nonlinear methods are more complex to implement algorithmically and its practical applications for 3D *in vivo* images may be challenging due to a number of issues, including:

- The number of unknowns typically exceeds one million when estimating the chromophore concentrations on a voxel-by-voxel basis in high resolution 3D photoacoustic images. The extensive computational memory demands of the large scale of the inversion may be prohibitive for practical implementations.
- Model-mismatch may arise due to the approximations in the fluence model, particularly when the DA model or 2D fluence models are used, and uncertainty in the model parameters (which are typically determined experimentally). This is discussed in more detail in Sec. 6.1.

The issues of the unknown scattering and Grüneisen parameter can also affect the practical applicability of nonlinear methods and are discussed below.

3.3.3 Scattering

In some QPAT studies, the scattering coefficient is assumed to be known. While this makes the inversion easier to implement, it can also lead to quantification errors when

the assumed values of the scattering coefficient are erroneous. For example, Jetzfellner *et al* [177] showed that the absorption estimations in the fixed point iteration may diverge if the scattering is wrong. The effect of errors in the “known” scattering has also been demonstrated for model-based minimisation schemes [178].

To avoid these errors, the scattering can instead be incorporated as an unknown variable in the inversion, as discussed in Sec. 3.2.3.3, and unique solutions can be found under certain conditions. However, the photoacoustic images are only weakly dependent on the scattering coefficient, because the initial pressure is only indirectly affected by the scattering coefficient through its effect on the fluence distribution. This causes slow rate of convergence for the scattering and the estimation of the scattering is typically poorer than the absorption.

3.3.4 Grüneisen parameter

The vast majority of the inversion methods require that the Grüneisen parameter is known. A few exceptions include the methods based on multi-illumination at multiple wavelengths in Refs. [158] and [159], and the Born approximation method where the Grüneisen parameter cancels out from the quotient images [132, 133]. In Refs. [41, 42], the Grüneisen parameter was incorporated as a parameter that is dependent on the chromophore concentrations. In *in vivo* applications of QPAT, on the other hand, the Grüneisen parameter is commonly assumed to be a spatially constant scaling factor. This is likely to lead to quantification errors since the Grüneisen parameter may vary by more than a factor of four for difference tissue types [179] and may not be known *a priori*.

3.3.5 Practical considerations

Many nonlinear methods are demonstrated in numerical simulation using images of H , with the assumption that the Grüneisen parameter and the system calibrations factor are known, and that the acoustic reconstruction is perfect. The system calibration factor could be estimated using calibrated sensors, such that the measured photoacoustic signals can be converted to have units of Pascals [41, 42]. However, the assumption of perfect acoustic reconstruction is unlikely to hold, due to limited-view artefacts, inhomogeneous sound speeds and the limited bandwidth of the sensors, which may

distort or blur the images as well as create artefacts, as discussed in Sec. 3.1.1.

It is also worth noting that many of the publications presenting the nonlinear methods demonstrate the recovery of the absorption coefficient at a single wavelength, even though the key quantity of interest is the chromophore concentrations. In theory, the methods can be applied to each wavelength individually to estimate the absorption spectra, from which the concentrations can be calculated. However, this has rarely been demonstrated experimentally (except in [142, 162]). All other experimental estimations of the chromophore concentrations using nonlinear methods have used multiwavelength images (with a single illumination) to estimate the chromophore concentrations directly [41, 42, 155].

3.4 Summary and outlook

The QPAT problem has been tackled from different perspectives by various research groups, but a generally applicable method for recovering the chromophore concentrations has not yet been found. Most *in vivo* studies use simplified fluence models or *ad hoc* experimental measurements of the fluence to linearise the problem in order to calculate the concentrations with SI, which is likely to lead to inaccuracies if the tissue has a complex and inhomogeneous structure. Fluence modelling using light transport equations has been incorporated in iterative nonlinear inversion schemes, which can provide more accurate quantification, but are challenging to implement for *in vivo* images. Other quantification strategies require additional elements such as light modulation or generating spectral libraries, which increases the complexity of the methods.

There are large gaps between the mathematical literature with numerical simulations, the few validated experimental demonstrations and practical *in vivo* applications (which continue to ignore most theoretical literature). This thesis aims to bridge this gap by 1) identifying the circumstances under which simple linear methods can provide accurate estimation of the chromophore concentrations, in order to better understand their accuracy and limitations such that they can be used with more confidence, and 2) improving the robustness of model-based inversion under experimental conditions, in order to encourage the transition of theoretical methods into practical use.

Chapter 4

Linear spectroscopic inversion

4.1 Introduction

The linear spectroscopic inversion (SI) is a simple QPAT method which uses the (pseudo) inverse of the matrix of the specific absorption spectra (the spectral matrix) to find the relative chromophore concentrations. The estimation of the concentrations of oxy- and deoxyhaemoglobin are of particular interest as their ratio is related to the blood oxygenation, sO_2 .

SI is a standard method in conventional spectroscopy, where the concentrations can be calculated straightforwardly from the absorption of the material at different wavelengths. In photoacoustic tomography, however, the measured signals are not linearly related to the absorption coefficient, because of the spectral colouring by the fluence. Therefore, using SI is likely to lead to errors in the estimation of sO_2 for photoacoustic tomography [155, 180]. Despite this, SI has been frequently used in *in vivo* imaging studies, as shown in Table 4.1, which presents a non-exhaustive list of publications using SI to measure sO_2 based on *in vivo* photoacoustic images in the last three years. The publications include clinical and pre-clinical studies of the oxygenation in for example tumour models, the placenta and the skin, either with or without employing approximate fluence correction methods. In many publications, only two wavelengths are used for the SI, and while some use 4–8 wavelengths, only rarely are more than 10 wavelengths used.

The analysis in this chapter is motivated by two reasons: Firstly, since SI is very commonly used for estimating sO_2 in QPAT by many research groups, it is important

Table 4.1: Examples of publications where SI was used to estimate sO_2 based on *in vivo* photoacoustic images in the past three years (2015–2017). Many of these recent publications used the commercially available Vevo LAZR scanner (VisualSonics, Toronto, ON, Canada) [181]. (These references are indicated with the superscript ^v.)

Ref.	N	Wavelengths	Fluence correction	Application
[182] ^v	2	[750, 850]	No	Placenta
[183] ^v	2	[750, 850]	No	Placenta
[114] ^v	2	[750, 850]	No	Tumour
[35]	2	[765, 796]	Yes	Human finger joint
[184]	2	[756, 797]	No	Tumour
[45] ^v	2	[750, 850]	No	Tumour
[185] ^v	2	[750, 850]	No	Tumour
[186] ^v	2	[750, 850]	No	Tumour
[187]	2	[576, 584]	No	Human finger joint
[188] ^v	2	[750, 850]	No	Tumour
[189] ^v	2	[750, 850]	No	Femoral artery
[190] ^v	2	[750, 850]	No	Tumour
[115]	4	[520, 540, 560, 650]	Yes	Skin
[47]	5	[780:10:820]	Yes	Placenta
[46]	8	[720:20:860]	No	Tumour
[36]	15	between 700 and 880	No	Tumour
[191]	25	[710:10:950]	No	Tumour

to assess its accuracy. Secondly, if SI can be shown to be accurate, it would be a very attractive approach because it is extremely simple, fast and computationally inexpensive.

In a numerical study of a single blood vessel, Hochuli *et al* [192] found that using SI with certain pairs of wavelengths can provide accurate sO_2 estimates, but the optimal wavelength pairs vary for different depths from the illumination source and sO_2 levels. Therefore it is difficult to choose an optimal pair of wavelengths that will reliably result in accurate estimations without knowing true sO_2 in advance. The first aim of this chapter is to investigate whether similar observations hold in a more complex and realistic numerical phantom and whether using more than two wavelengths can lead to accurate estimates for a large range of depths and sO_2 levels.

The remainder of the chapter aims to better understand the error associated with estimating sO_2 using SI with multiple wavelengths. It would be intuitive to assume

that using more wavelengths over a broad spectral range would lead to more accurate results. This assumption is valid in linear problems where ill-conditioning and the noise in the data are the main potential sources of error. However, since the spectral colouring causes bias in SI for QPAT, further investigation is required to determine whether it is more advantageous to use more wavelengths, or fewer wavelengths selected from a spectral range where the spectral colouring is low.

Finding the wavelength combination for SI that leads to the smallest errors is challenging, as there are many possible combinations (for example, choosing 25 out of 51 wavelengths gives ${}^{51}C_{25} = 2.5 \times 10^{14}$ unique combinations). Maximising the smallest singular value of the spectral matrix [193], or minimising the condition number of the spectral matrix [194] have previously been suggested as methods of selecting wavelengths. The suitability of these methods will also be investigated in this chapter.

Numerically simulated multiwavelength photoacoustic images of a mouse brain with skin and skull intact will be used to study the accuracy of SI for estimating the sO_2 in this chapter. The chapter is structured as the following: Section 4.2 presents the linear model using matrix notation and the SI for sO_2 . Section 4.3 describes the numerical phantom and forward simulation. The average accuracy of the sO_2 estimation is presented for different depth layers and true sO_2 levels using an increasing number of wavelengths in Sec. 4.4. The correlations between the sO_2 and the condition number, smallest singular value and the change in fluence between wavelengths are investigated in Sec. 4.5 and 4.6. The behaviour of the error in the estimated sO_2 is explained using the equation for SI in Sec. 4.7. Section 4.8 discusses how the number of wavelengths used in the inversion affects the accuracy. Lastly, the findings are summarised in Sec. 4.9 and the conclusions are presented in Sec. 4.10

4.2 Linear spectroscopic inversion for estimating sO_2

As described in Sec. 2.2, the initial pressure is given by

$$p_0(\mathbf{r}, \lambda) = \Gamma(\mathbf{r})\phi(\mathbf{r}, \lambda) \sum_k \alpha_k(\lambda)c_k(\mathbf{r}). \quad (4.1)$$

Assuming that the acoustic reconstruction is perfect and the system calibration factor is equal to one, such that the reconstructed image represents the distribution of p_0 exactly,

a set of photoacoustic images with M voxels acquired at N wavelengths, whose contrast originate from K chromophores, can be described using matrix notation as

$$\mathbf{P} = \mathbf{\Phi} \circ (\mathbf{A} (\mathbf{\Gamma} \circ \mathbf{C})), \quad (4.2)$$

where \circ denotes the element-wise (Hadamard) product, \mathbf{P} is a $(N \times M)$ matrix with each row corresponding to a reconstruction of the initial pressures at one of the wavelengths,

$$\mathbf{P} = \begin{bmatrix} p_{0,\lambda_1,m_1} & p_{0,\lambda_1,m_2} & \cdots & p_{0,\lambda_1,m_M} \\ p_{0,\lambda_2,m_1} & p_{0,\lambda_2,m_2} & & \\ \vdots & & \ddots & \vdots \\ p_{0,\lambda_N,m_1} & & \cdots & p_{0,\lambda_N,m_M} \end{bmatrix}, \quad (4.3)$$

$\mathbf{\Phi}$ is the $(N \times M)$ fluence matrix with each row representing the spatially varying fluence at one of the wavelengths,

$$\mathbf{\Phi} = \begin{bmatrix} \phi_{\lambda_1,m_1} & \phi_{\lambda_1,m_2} & \cdots & \phi_{\lambda_1,m_M} \\ \phi_{\lambda_2,m_1} & \phi_{\lambda_2,m_2} & & \\ \vdots & & \ddots & \vdots \\ \phi_{\lambda_N,m_1} & & \cdots & \phi_{\lambda_N,m_M} \end{bmatrix}, \quad (4.4)$$

\mathbf{A} is the $(N \times K)$ mixing matrix with each column representing the wavelength dependent specific absorption coefficient of one of the chromophores,

$$\mathbf{A} = \begin{bmatrix} \alpha_{c_1,\lambda_1} & \alpha_{c_2,\lambda_1} & \cdots & \alpha_{c_K,\lambda_1} \\ \alpha_{c_1,\lambda_2} & \alpha_{c_2,\lambda_2} & & \\ \vdots & & \ddots & \vdots \\ \alpha_{c_1,\lambda_N} & & \cdots & \alpha_{c_K,\lambda_N} \end{bmatrix}, \quad (4.5)$$

\mathbf{C} is the $(K \times M)$ concentrations matrix with each row representing the concentration distribution of one of the chromophores,

$$\mathbf{C} = \begin{bmatrix} c_{1,m_1} & c_{1,m_2} & \cdots & c_{1,m_M} \\ c_{2,m_1} & c_{2,m_2} & & \\ \vdots & & \ddots & \vdots \\ c_{K,m_1} & & \cdots & c_{K,m_M} \end{bmatrix}, \quad (4.6)$$

and $\mathbf{\Gamma}$ is a $(K \times M)$ matrix where all rows are identical and equal to the spatially varying Grüneisen parameter,

$$\mathbf{\Gamma} = \begin{bmatrix} \Gamma_{m_1} & \Gamma_{m_2} & \cdots & \Gamma_{m_M} \\ \Gamma_{m_1} & \Gamma_{m_2} & \cdots & \Gamma_{m_M} \\ \vdots & \vdots & & \vdots \\ \Gamma_{m_1} & \Gamma_{m_2} & \cdots & \Gamma_{m_M} \end{bmatrix}. \quad (4.7)$$

In this thesis, the matrices are written with upper case bold letters, the vectors are denoted with lower case bold letters and the matrix and vector elements are denoted with normal lower case letters.

Equation (4.2) is nonlinear, due to the spectrally and spatially varying fluence matrix. An approximation to linearity can be achieved by dividing \mathbf{P} element-wise by an approximate estimate of the fluence, $\check{\Phi}$, such that

$$\frac{\mathbf{P}}{\check{\Phi}} = \check{\mathbf{P}} \approx \mathbf{A}(\mathbf{\Gamma} \circ \mathbf{C}). \quad (4.8)$$

where breve symbol ($\check{}$) is used to denote the estimation of a variable. As Table 4.1 shows, many recent *in vivo* studies do not apply any fluence correction, which means that the fluence is assumed to be spatially and spectrally constant. This is the equivalent to using the identity matrix, \mathbf{I} , as the approximate estimate of the fluence, such that $\check{\Phi} = \mathbf{I}$. To access the accuracy of SI under this condition, $\check{\Phi} = \mathbf{I}$ is used for all inversions with SI in this chapter. Based on the linear model in Eq. (4.8), the linear spectroscopic inversion (SI) can be applied. In SI, the chromophore concentrations are estimated using the pseudo-inverse of the spectral matrix, \mathbf{A}^\dagger :

$$\mathbf{A}^\dagger \check{\mathbf{P}} \approx \mathbf{\Gamma} \circ \mathbf{C}, \quad (4.9)$$

LI cannot separate Γ from the concentrations because Γ is wavelength independent and scales with the concentrations.

For the estimation of the sO_2 , one may assume that oxy- and deoxyhaemoglobin are the only chromophores present, such that \mathbf{C} consists only of the concentrations of oxy- and deoxyhaemoglobin, c_{HbO_2} and c_{Hb} . The blood oxygen saturation, sO_2 is given by

$$sO_2 = \frac{c_{HbO_2}}{c_{HbO_2} + c_{Hb}}. \quad (4.10)$$

4.3 Numerically simulated images

The 3D numerical phantom was generated based on the segmentation of a μ CT vascular cast of a mouse brain ¹ with $2.5\mu\text{m}$ resolution and dimensions of $9.1 \times 10.5 \times 13.8 \text{mm}^3$. The resolution was down-sampled to $125\mu\text{m}$ to create a phantom with $73 \times 87 \times 110$ voxels. Skull and skin layers were added to the phantom by dilating the volume by $500\mu\text{m}$ in all directions. These thicknesses were chosen based on Refs. [195, 196]. The maximum projection images of the phantom structure from the z, x, and y dimensions are shown in Fig. 4.1.

The blood vessels in the mouse brain are distinguished into background and foreground vessels, as indicated in Fig. 4.1. The total haemoglobin concentrations of both the background and foreground blood vessel are 150gL^{-1} . The foreground vessels are the regions of interest and their sO_2 was varied from 60% to 100% in steps of 10% in five sets of simulations. The background vessels have a sO_2 of 80% for all data sets. The absorption coefficients of oxy- and deoxyhaemoglobin [48] and water [50] are shown in Fig. 4.2(a). The absorption spectra of the skin and the skull are taken from Refs. [197] and [198, 199] respectively, which are based on measurements of human samples. The optical properties of the background tissue are based on the cortical tissue in rat brains, which has 5.65gL^{-1} total haemoglobin concentration with $sO_2 = 60.7\%$ [200] and water fraction of 45% [201]. The absorption spectra of the skin layer, the skull and the background tissue are shown in Fig. 4.2(b). The scattering amplitude and wavelength dependence for the different types of tissues are shown in Fig. 4.2(c) [160].

The light source was defined as a radially-symmetric Gaussian beam with a $1/e$

¹The mouse brain μ CT data was kindly provided by Simon Walker-Samuel (Centre for Advanced Biomedical Imaging, University College London) and segmented by Roman Hochuli (Photoacoustic Imaging Group, University College London).

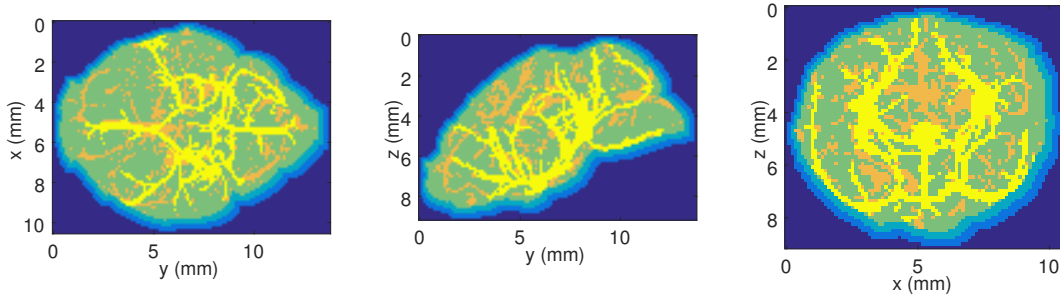


Figure 4.1: Maximum intensity projection plots of the structure of the mouse brain phantom. The different colours indicate the skin (blue), the skull (turquoise), the background brain tissue (green), the background blood vessels (orange) and the foreground blood vessels (yellow). The cerebrospinal fluid (CSF) between the skull and the brain tissue has not been included in this phantom. However, since the CSF does not significantly absorb or scatter light, it has a relatively small effect on the spectral colouring.

radius of 5mm incident on the x-y plane. The fluence distribution was simulated for 51 wavelengths between 500 and 1000nm with 10nm spacing based on the DA using the MATLAB software Toast++ [202]. The acoustic reconstruction is assumed to be perfect and the Grüneisen parameter, which cancels out in the ratio that defines the sO_2 , is assumed to be spatially constant and equal to one. Under these assumptions, the reconstructed initial pressure is equal to the absorbed optical energy density. The maximum intensity projection of the simulated images of the initial pressure are shown at the wavelengths 500, 650 and 1000nm in Fig. 4.3. A zero-mean Gaussian noise with variance equal to 0.5kPa (the incident excitation light was assumed to be 0.2mJ/mm²) was added to the images.

4.4 Accuracy as a function of depth and sO_2

SI was performed with an increasing number of evenly spread wavelengths from a fixed spectral range to investigate the accuracy of SI using multiple wavelengths for different depths from the illumination source and various sO_2 levels. Since oxy- and deoxyhaemoglobin are the only absorbers present in the foreground blood vessels, all inversions in this chapter use a spectral matrix consisting of the specific absorption spectra of oxy- and deoxyhaemoglobin only, such that the SI only inverts for those two chromophores.

The number of wavelengths used in each inversion is denoted by N and the minimum and maximum wavelengths are denoted by λ_{min} and λ_{max} . The error of the sO_2

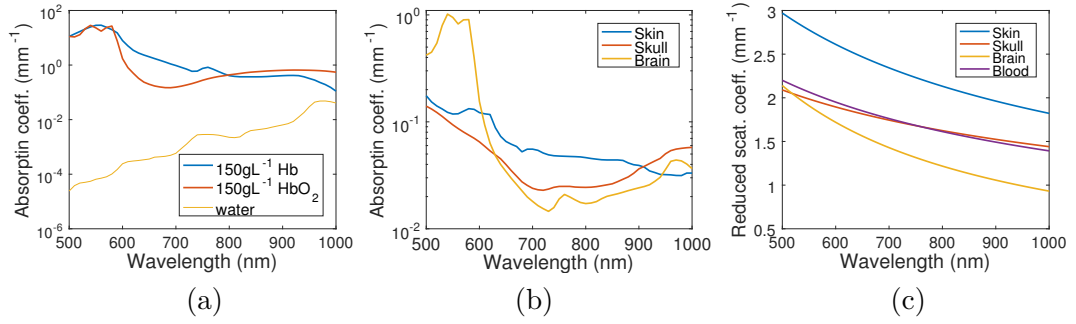


Figure 4.2: (a) The absorption coefficient of 150gL^{-1} deoxyhaemoglobin (blue) [48], oxyhaemoglobin (red) [48] and water (yellow) [50] shown using logarithmic scale. (b) The absorption coefficient of the skin (blue) [197], skull (red) [198, 199] and background tissue (yellow) also in logarithmic scale. (c) The reduced scattering coefficient of skin (blue), skull (red), background brain tissue (yellow) and blood (purple), taken from Ref. [160]

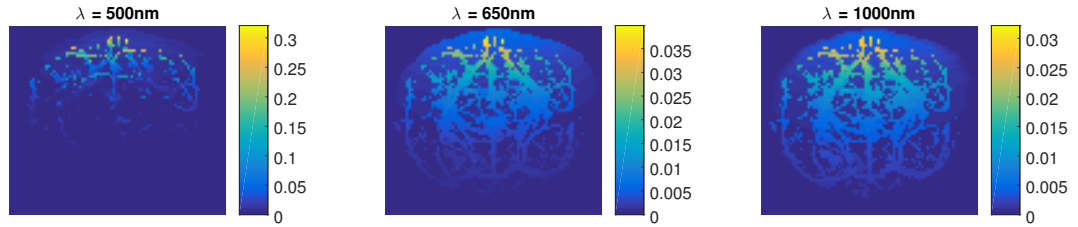


Figure 4.3: The maximum intensity projection of the simulated photoacoustic images at 500, 650 and 1000nm. The initial pressure is higher for 500nm as the absorption of the oxy- and deoxyhaemoglobin is approximately an order of magnitude higher than at 650 and 1000nm. The initial pressure reduces with depth, because the fluence is lower further away from the light source at the top of the domain.

estimation, δ_{sO_2} , is defined as the absolute difference between the estimated sO_2 and the true sO_2 . The δ_{sO_2} was calculated for nine inversions with $N = 2, 3, 5, 8, 12, 17, 23, 28$ and 34 for each of the five true sO_2 levels. The λ_{min} and λ_{max} were fixed at 670nm and 1000nm for all inversions. The other wavelengths were chosen to be as evenly spread as possible from the simulated set of wavelengths within this range. The mouse brain was divided into five equally thick depth layers and the average δ_{sO_2} was calculated for the foreground vessel in each layer. The δ_{sO_2} is shown using a colourscale in Figure 4.4, where the depth layers are indicated in the y-axis and the true sO_2 levels are indicated in the x-axis. Each plot represents the inversion using a different N . When N is relatively small, the average δ_{sO_2} is shown to be higher for large depths and low sO_2 levels. Comparing the different plots shows that for this spectral range, increasing N leads to

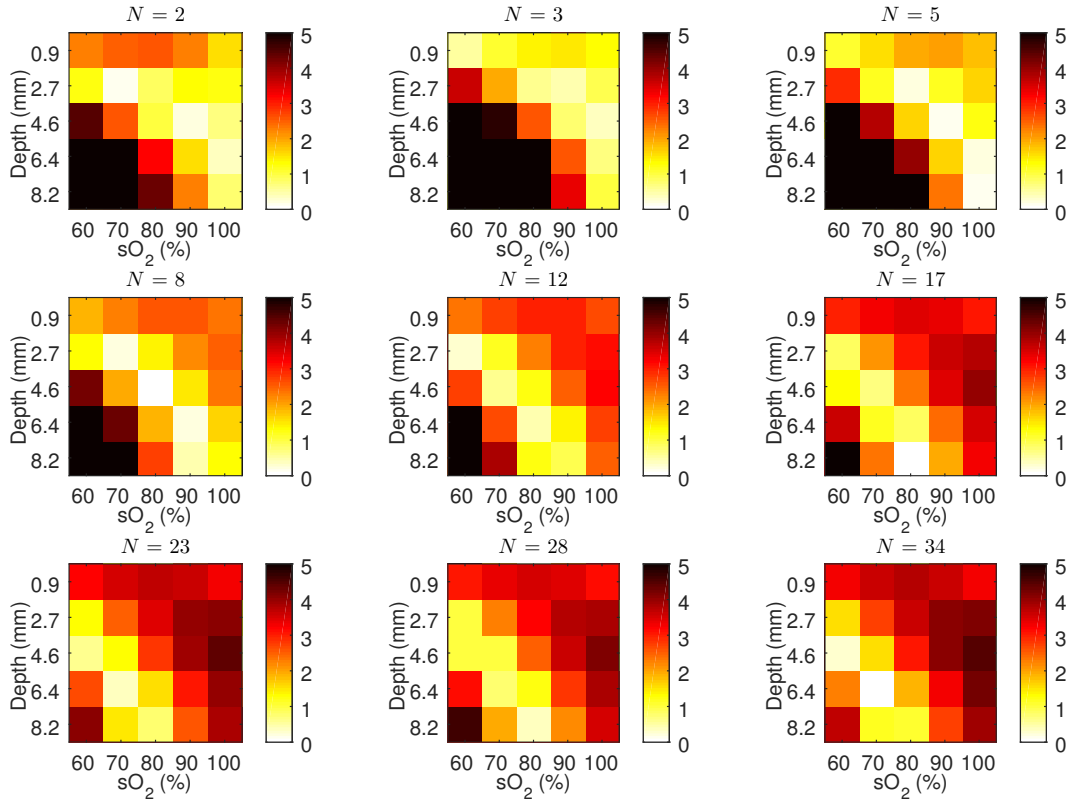


Figure 4.4: The average error, δ_{sO_2} , at the foreground vessel shown using a colourscale indicating the average absolute difference between the estimated and the true sO_2 (in units of percentage). The depth layers are indicated in the y-axis and the five sO_2 levels are shown along the x-axis. The errors higher than 5% are indicated with black pixels.

smaller average δ_{sO_2} for the deeper depths and lower sO_2 , but increases δ_{sO_2} slightly for the shallower depths and higher sO_2 . When $N \geq 17$, average $\delta_{sO_2} < 5\%$, where % refers to percentage points, was achieved for the whole range of depths up 9.1mm and for all five sO_2 levels.

The results in Fig. 4.4 are based on SI using the spectral range 670–1000nm. If a shorter λ_{min} of 650nm is used instead, lower average δ_{sO_2} can be achieved for the superficial layers and high sO_2 , but the errors for the deeper depths and lower sO_2 are significantly increased (data shown in Fig. A.1 in Appendix A). This may be caused by the lower SNR and larger changes in fluence between the wavelengths, which is due to the increase of the absorption of blood when the wavelength is decreased to 650nm. Using a longer λ_{min} of 690nm leads to the opposite trend, where the deeper layers and lower true sO_2 have lower errors, and higher errors are seen for the shallow depths and high true sO_2 (data shown in Fig. A.2 in Appendix A). The variations in the error depending

on spectral range suggest that there may be different wavelength combinations that lead to accurate estimates for each depth layer and true sO_2 .

To find combinations of wavelengths that give more accurate estimates of the sO_2 , SI was performed with a maximum of 10^5 random unique combinations of wavelengths chosen from [500:10:1000]nm (but not necessarily using 500nm and 1000nm as λ_{min} and λ_{max}) for each N . Figure 4.5 shows the lowest average δ_{sO_2} that was obtained out of all the wavelength combinations for each depth layer and true sO_2 . The results show that there exist wavelength combinations that provide very accurate estimates of sO_2 for the whole range of depths and sO_2 levels with δ_{sO_2} close to zero. For $N = 34$, the lowest average δ_{sO_2} is shown to increase. This may seem counter-intuitive given the previous results with evenly spread wavelengths, where large N generally led to lower errors. It can be explained by the fact that using fewer wavelengths allows more room for selection of the more optimal wavelength combination, while higher N forces the inversion to use a larger range of wavelengths.

In general, the lowest δ_{sO_2} shown in Fig. 4.5 are obtained using different wavelength combinations for each depth and sO_2 . These optimal wavelength combinations are shown in Fig. 4.6. The y-axis of each plot indicates N , and x-axis shows the wavelength. The bright yellow pixels indicate the wavelengths included in the wavelength combination that resulted in the lowest δ_{sO_2} , for a particular depth range and sO_2 . For example, for the depth layer at 2.7mm, true sO_2 level of 90% and $N = 2$, the best wavelength combination was 650 and 960nm. The results show that including the shorter wavelengths below 650nm is unlikely to lead to the lowest errors when N is small, particularly for the shallower layers. Two vertical dark blue gaps appears near 550nm and 600nm, which suggests using wavelengths close to these values is unlikely to result in the most accurate sO_2 estimates. In general, the optimal wavelength combinations have a scattered appearance and no wavelength combination gives the best results for all depths and the full range of sO_2 .

Figure 4.6 shows the wavelength combinations that provide the most accurate estimates of the sO_2 , but there are many other combinations that also result in low errors. Therefore, one may be interested in the probability of choosing a “good” wavelength combination, i.e. one that leads to low errors, if the wavelengths were chosen randomly. Figure 4.7 shows the percentage of 10^5 randomly selected wavelength combinations that

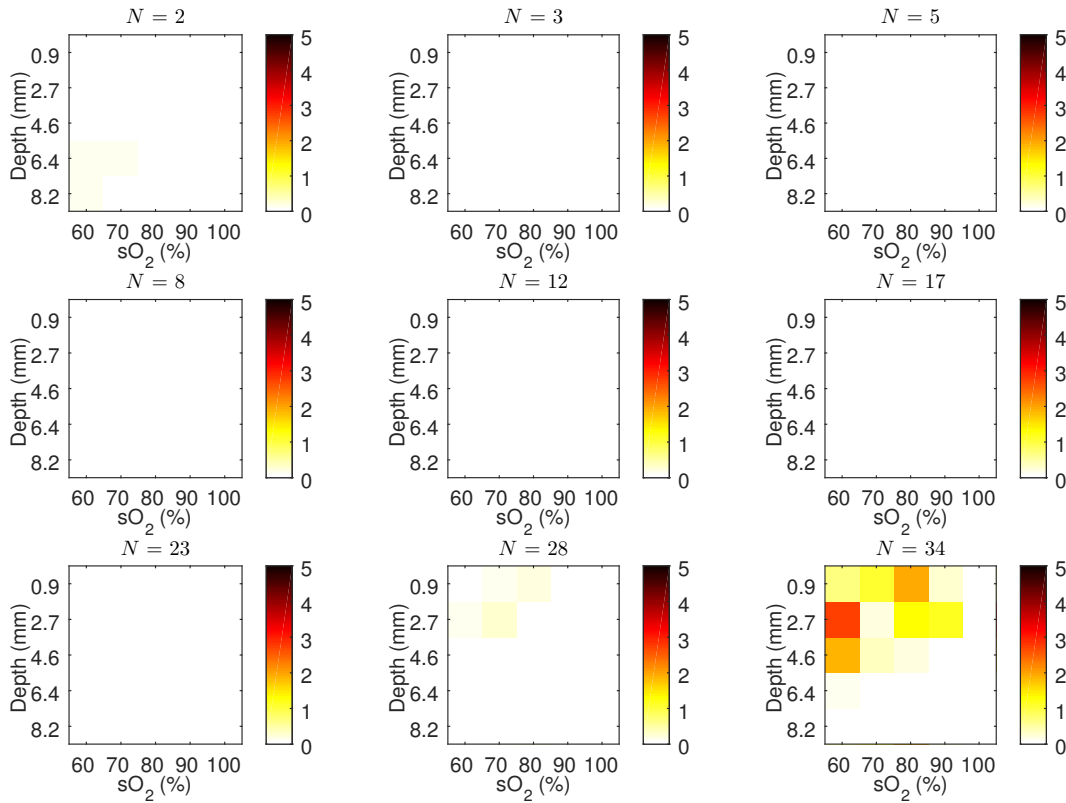


Figure 4.5: The lowest average δ_{sO_2} obtained from SI by picking the best from 10^5 random wavelength combinations chosen from $[500:10:1000]$ nm. The bright colours indicate that the very low average δ_{sO_2} can be achieved. (Most of the plots appear white because the average δ_{sO_2} are typically in the order of 0.001–0.01%.) Higher average δ_{sO_2} are seen for $N = 34$, due to less flexibility in avoiding the unfavourable wavelengths.

resulted in average $\delta_{sO_2} < 5\%$ when chosen from $[670:10:1000]$ nm. Comparing Fig. 4.4 with Fig. 4.7 shows that for cases where evenly spread wavelengths resulted in large errors, the likelihood of obtaining accurate sO_2 estimates with a random choice of wavelength combination is also low. This suggests that, if the optimal wavelengths are unknown, using as many evenly spread wavelengths as possible between 670nm and 1000nm is the most suitable method for obtaining accurate estimates of sO_2 . However, in *in vivo* applications, it may not be practically feasible to acquire images with a large number of wavelengths.

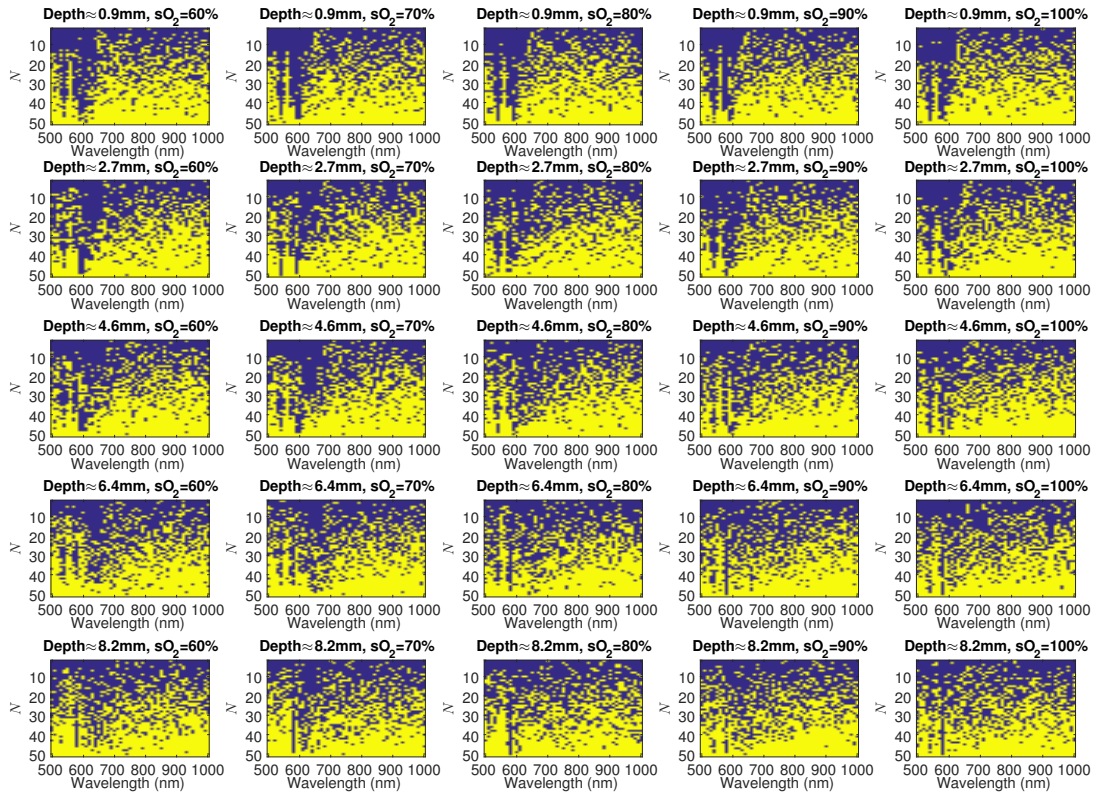


Figure 4.6: The wavelength combinations which lead to the lowest δ_{sO_2} . The x-axis shows the wavelength and the y-axis indicates N . The yellow pixels indicate the wavelengths that were used in the inversion which results in the lowest δ_{sO_2} . Each plot shows the results for a specific depth layer and sO_2 level.

4.5 Smallest singular value and condition number

The previous section showed that a large number of evenly spread wavelengths are required to achieve $\delta_{sO_2} < 5\%$ if the wavelengths are selected within a certain range. However, if the optimal wavelength combinations were known, we could use lower N to achieve accurate results. Unfortunately, finding the optimal wavelength combinations is not straight-forward, as there are many possible combinations and no clear patterns emerge for the optimal wavelengths in Fig. 4.6. This section investigates to what extent the conditioning of the inversion can be used as an indicator for the accuracy of SI for different wavelength combinations.

The condition number, κ , of the spectral matrix is defined as the ratio between the largest and the smallest singular value of the matrix, $\kappa = \sigma_{max}/\sigma_{min}$. The linear system is ill-conditioned if κ is large, which indicates that the inversion is unstable. This means

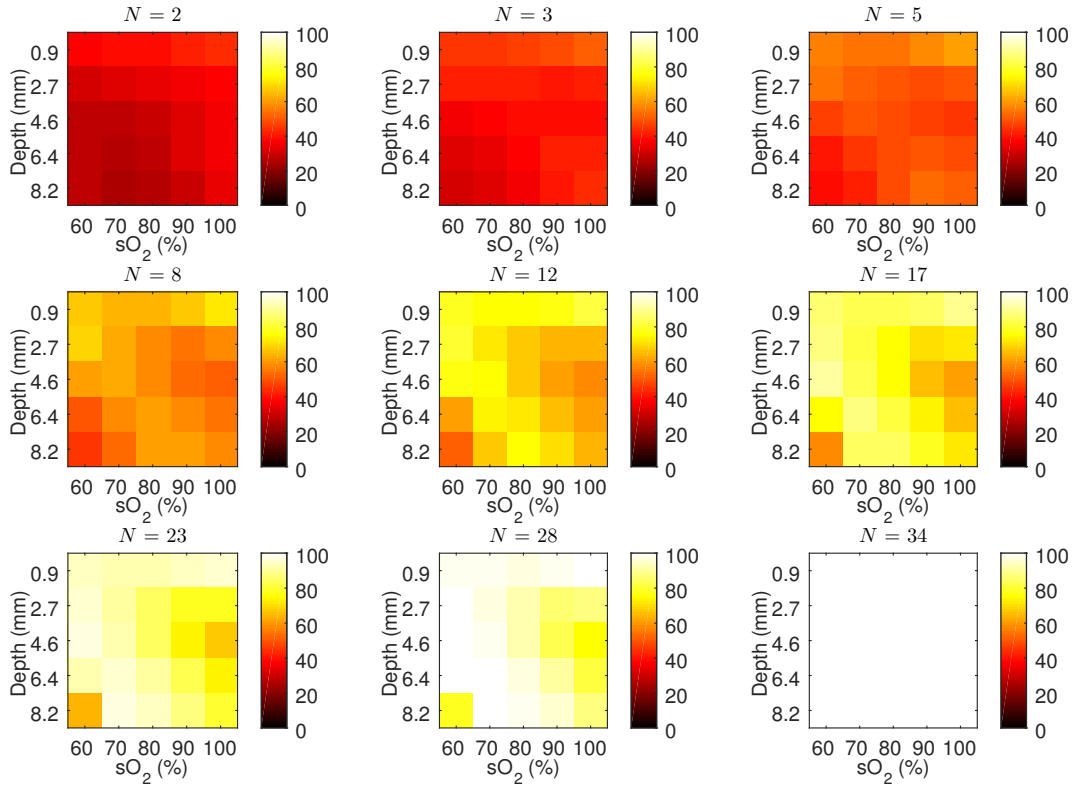


Figure 4.7: The percentage of the randomly chosen wavelength combinations from the wavelength range 670–1000nm that result in the average $\delta_{sO_2} < 5\%$ is indicated by the colours of the pixels. The likelihood of obtaining average $\delta_{sO_2} < 5\%$ are higher for higher N .

that small perturbations in the multiwavelength image data lead to large changes in the estimated concentrations. Xiao *et al* [194] showed that lower κ correlates with more accurate estimates of the chromophore concentration using SI. Luke *et al* [193] suggested choosing wavelengths that maximise the smallest singular value of the spectral matrix, σ_{min} . In a subsequent publication [203], Luke *et al* showed that this led to smaller errors than using wavelength combinations that minimise κ .

The κ and σ_{min} as well as the δ_{sO_2} were evaluated for a large number of wavelength combinations in order to investigate the relationship between these quantities. A maximum of two hundred unique wavelength combinations were randomly chosen from [500:10:1000]nm for each λ_{min} and the possible N . (Higher λ_{min} allows only for lower N . For example, if $\lambda_{min} = 990$ nm, only $N = 2$ is possible and [990, 1000]nm is the only possible wavelength combination.) SI was used to invert for the oxy- and deoxyhaemoglobin concentrations for each of the wavelength combinations using the simulated

images based on $sO_2 = 90\%$. The δ_{sO_2} was found for a single voxel in the foreground blood vessel at a depth of 4.5mm and near the centre of the x-y plane. The κ and σ_{min} were calculated for the spectral matrix with the specific absorption spectra of oxy- and deoxyhaemoglobin for the chosen wavelengths.

Figure 4.8 shows δ_{sO_2} plotted against the smallest singular value, σ_{min} . Each data point in the scatter plots represents one inversion with a unique combination of randomly chosen wavelengths. The results using $N = 2, 5, 20$ and 35 are shown in different rows. The colour of each data point indicate the λ_{min} used for in that inversion. The left column of plots uses a logarithmic scale to display the full range of δ_{sO_2} and σ_{min} obtained for all inversions. The right column of plots zooms in on the data points with lower δ_{sO_2} and σ_{min} using a linear scale, in order to show the trends in the error range that is of most interest for potential applications. The results show that the data points with the lowest δ_{sO_2} typically have $\lambda_{min} \approx 650\text{nm}$, and do not have the largest σ_{min} . As seen in the logarithmic plots, the wavelength combinations resulting in data points with the largest σ_{min} are bluer (shorter λ_{min}) and have extremely high δ_{sO_2} . This demonstrates that, contrary to what previous studies suggested, choosing wavelengths solely based on maximising σ_{min} is unlikely to lead to accurate sO_2 estimates. The right column of plots further highlights that σ_{min} does not correlate with δ_{sO_2} for the wavelength combinations that result in $\delta_{sO_2} < 25\%$.

The relationship between δ_{sO_2} and the condition number κ is shown in Fig. 4.9. Similarly to the Fig. 4.8, the left and right columns of plots use logarithmic and linear scales respectively, and the colours of the data points represent λ_{min} . Overall, κ is shown to correlate better with δ_{sO_2} compared to σ_{min} , as the data points with high κ are generally associated with high δ_{sO_2} : The clusters of bluer data points with high δ_{sO_2} are shown to have high κ in the left column of plots. When the δ_{sO_2} decreases as the λ_{min} decreases to $\approx 650\text{nm}$, κ generally also decreases. The increase in δ_{sO_2} for $\lambda_{min} < 650\text{nm}$ is correlated with an increase in κ . The bottom right plot ($N = 35$) shows clusters of data points that follow a linear trend, where increasing κ leads to increasing δ_{sO_2} . However, when N is smaller, this trend is less clear for $\delta_{sO_2} < 25\%$, as a large range of δ_{sO_2} can be seen for similar values of κ in the linear plots. For $N = 2$ (top right plot), while δ_{sO_2} is relatively low for the lowest κ , it is clear that the smallest δ_{sO_2} do not occur at the minimum κ . These results suggest that while minimising κ of the spectral

matrix is useful for eliminating wavelength combinations that result in extremely high δ_{sO_2} , it does not minimise the δ_{sO_2} for the range of accuracies that are of key interest ($\delta_{sO_2} < 25\%$) unless N is very large.

The results in this section suggest that, for some wavelength combinations, ill-conditioning of the spectral matrix is not the main source of error for estimating sO_2 using SI. The next section investigates the impact of the spectral colouring on the accuracy by presenting the relationship between the spectral variance of the fluence and the δ_{sO_2} .

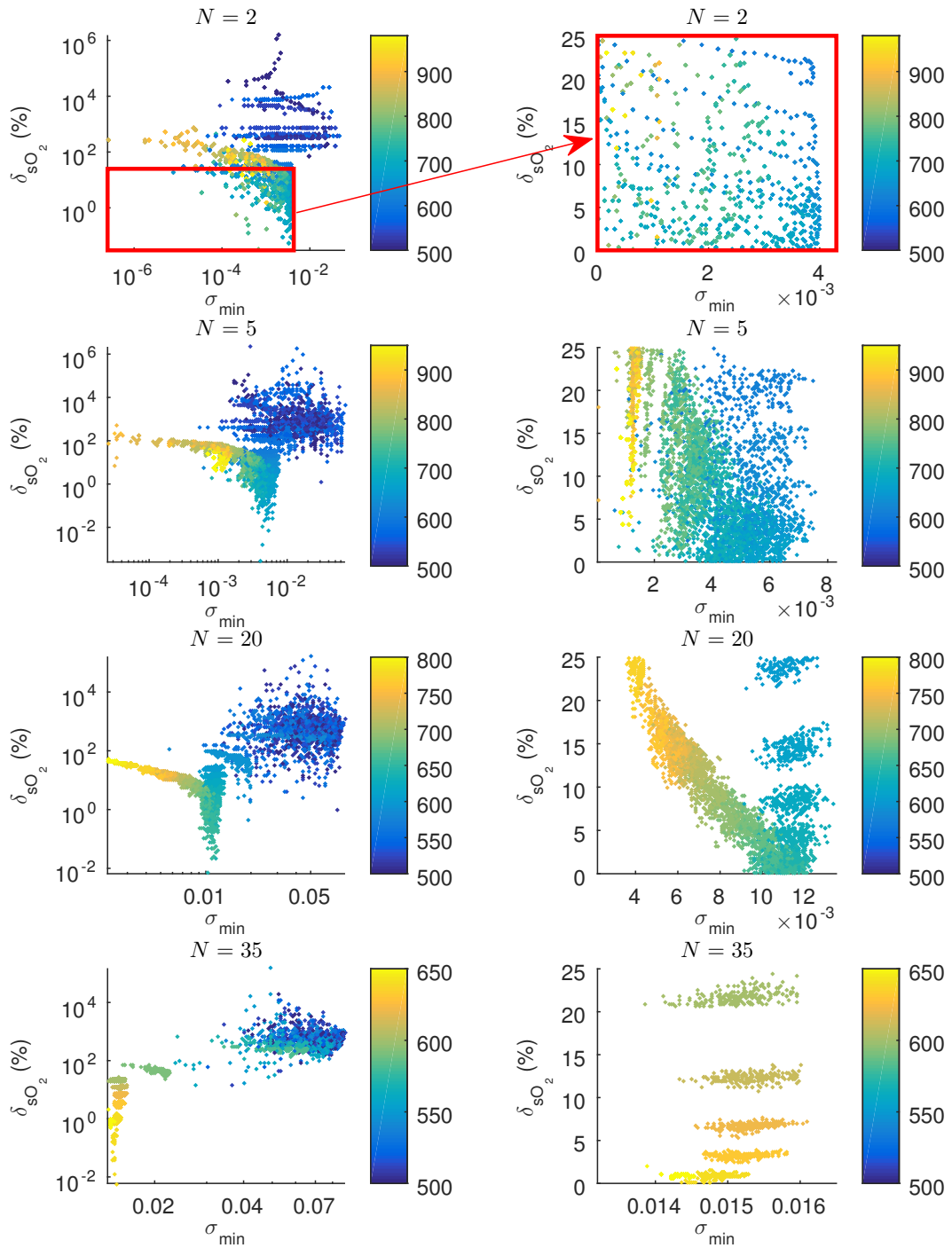


Figure 4.8: The error of the sO_2 estimate, δ_{sO_2} , at a single voxel at a depth of 4.5mm plotted against the smallest singular value of the spectral matrix, σ_{min} . Each data point represents the result from a unique combination of N wavelengths. The colour indicates the smallest wavelength used in the inversion (in nm). The left column of plots uses a logarithmic scale and the right column shows a smaller range using a linear scale. The corresponding regions of the logarithmic and linear plots are marked with red rectangles in the top row of the plots. The data show that increasing σ_{min} does not result in lower δ_{sO_2} .

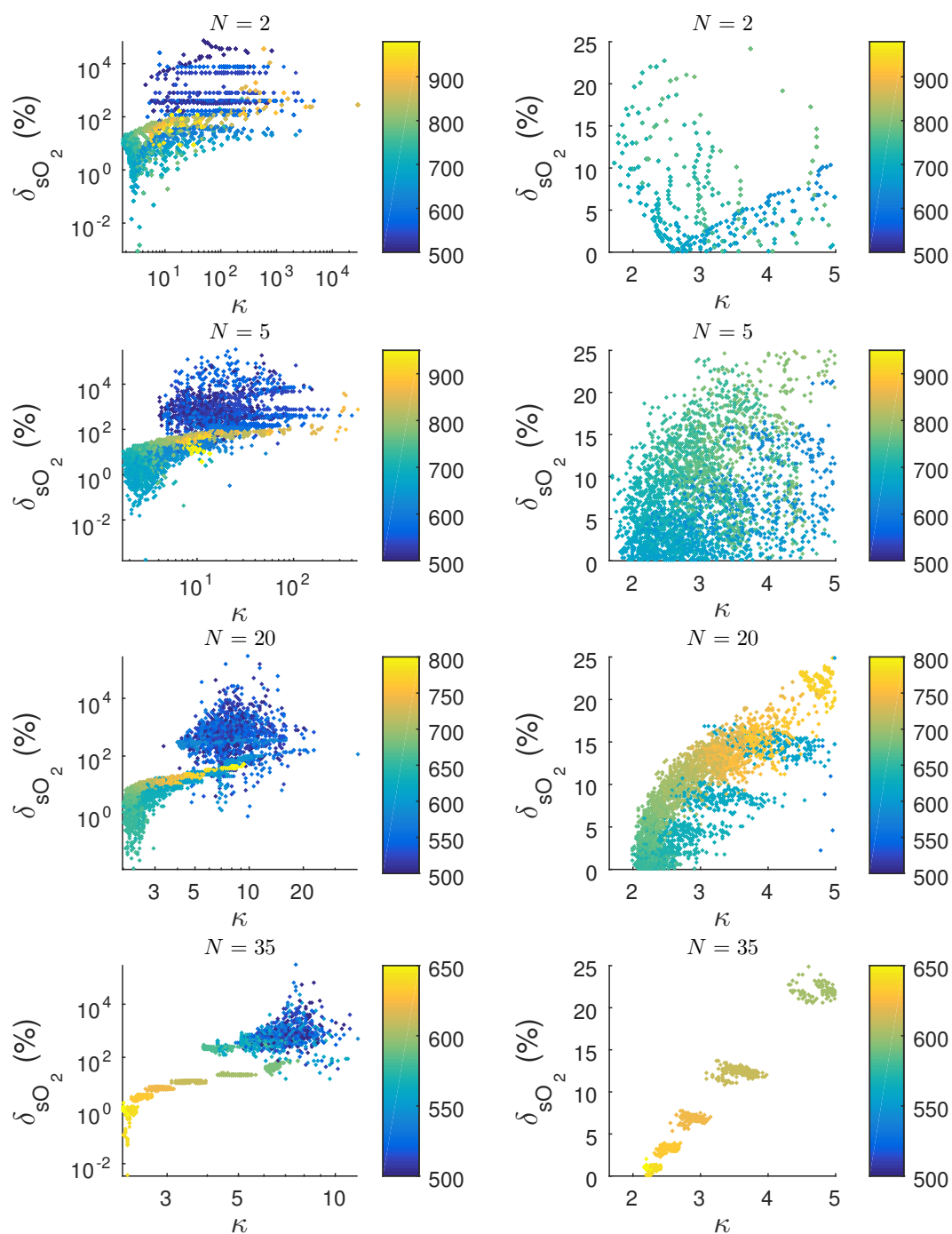


Figure 4.9: The error of the sO_2 estimate, δ_{sO_2} , plotted against the condition number, κ , of the spectral matrix. High condition numbers are correlated with extremely large errors. However, minimising the condition number does not necessarily result in the smallest error, except for cases where N is large.

4.6 Spectral variation of the fluence

Here, the fluence variance, $\text{var}(\phi)$, will be used as an indication of the level of spectral colouring. The fluence variance at one voxel can be defined as

$$\text{var}(\phi) = \frac{1}{N-1} \sum_{n=1}^N (\phi_{\lambda_n} - \mu_\phi)^2, \quad (4.11)$$

where the fluence at that voxel at different wavelengths is denoted by $\phi = [\phi_{\lambda_1}, \phi_{\lambda_2}, \dots, \phi_{\lambda_N}]$ and μ_ϕ is the mean of ϕ . In this numerically simulated study, the fluence is known from the modelling using DA based on the true absorption and scattering coefficients. Therefore, $\text{var}(\phi)$ can be used to investigate how the changes in fluence affects the accuracy of the sO_2 estimation. However, of course, it is not possible to use $\text{var}(\phi)$ to select the optimal wavelengths in a practical experiment, where the fluence distribution is unknown.

The $\text{var}(\phi)$ was calculated for the same wavelength combinations and voxel as in Sec. 4.5 and plotted in Fig. 4.10 against δ_{sO_2} using logarithmic scale (left column) and linear scale (right column) for different N (rows) with colours indicating λ_{min} . The plots in the bottom row show that for $N = 35$, decreasing $\text{var}(\phi)$ is generally seen to correspond to lower δ_{sO_2} for the full range of values of δ_{sO_2} . This is expected as larger changes in the fluence between wavelengths cause more spectral colouring, hence reducing the accuracy of SI. The relationship between the δ_{sO_2} and $\text{var}(\phi)$ is less straightforward for lower N , as shown in the plots in the top three rows. The data points with $\lambda_{min} < 650\text{nm}$ and large $\text{var}(\phi)$ generally have high δ_{sO_2} , as expected. However, a large range of δ_{sO_2} can be seen for similar $\text{var}(\phi)$ in both the logarithmic and linear plots. For $\delta_{sO_2} < 25\%$, lower $\text{var}(\phi)$ typically correspond to lower δ_{sO_2} for *the same* λ_{min} . However, in general, smaller $\text{var}(\phi)$ does not necessarily correspond to lower δ_{sO_2} . This is somewhat surprising as spectral colouring is the main source of error for SI when the inversion is well-conditioned. To explain this error trend, further investigation is presented in the next section.

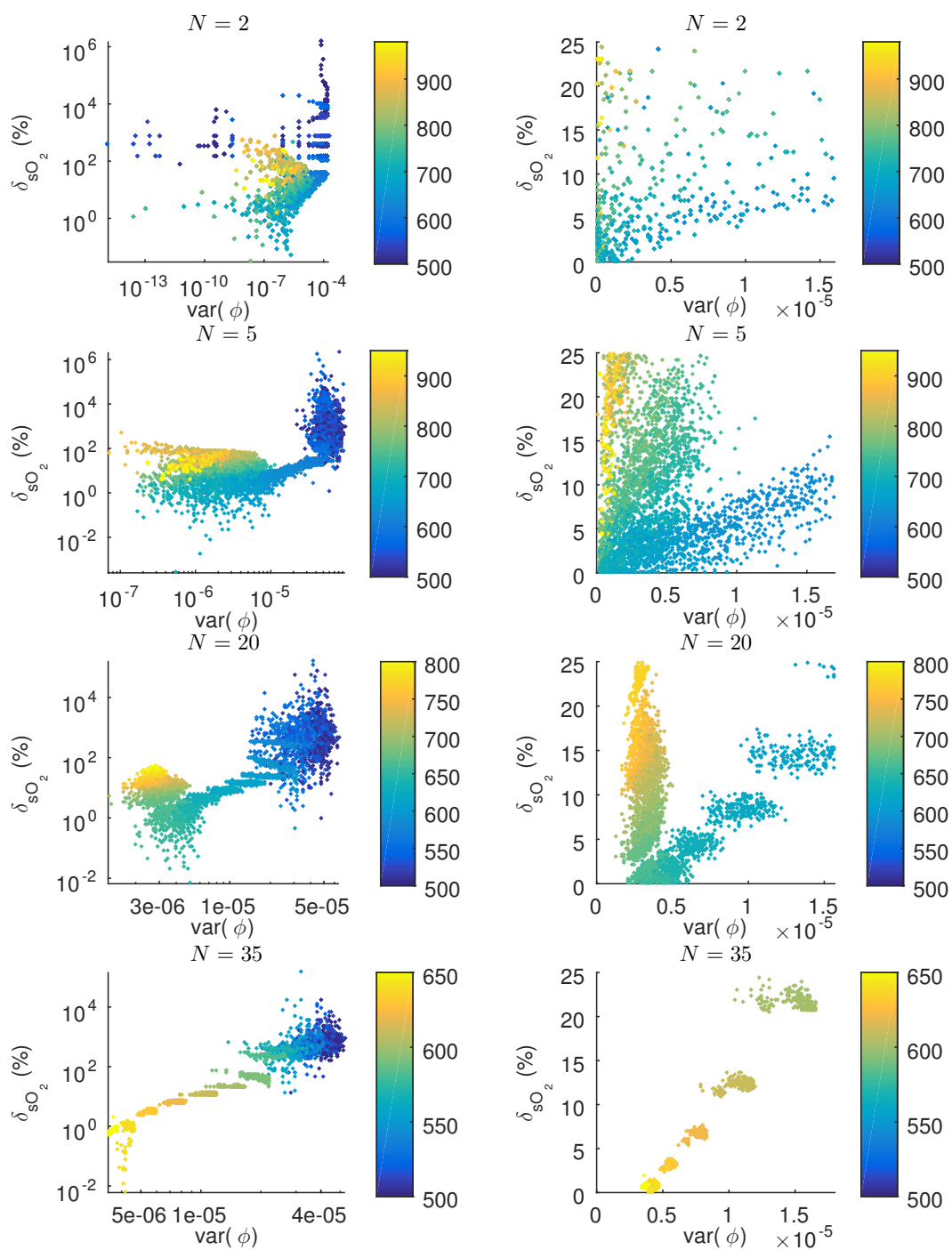


Figure 4.10: The error of the sO_2 estimate as a function of the fluence variance. When the fluence variance is very large, the errors are generally also large. However, the fluence variance does not correlate with the error for the lower error range, as the right column of plots show that when $\delta_{sO_2} < 25\%$, different errors can be seen for the same fluence variance for $N \leq 20$.

4.7 Error of the chromophore concentration ratio estimated using SI

The previous Sections 4.5 and 4.6 show that while there are some correlations between the δ_{sO_2} and κ or $\text{var}(\phi)$, the error does not fully depend on these quantities. To investigate the cause of the δ_{sO_2} , an analysis of the mathematical expression for the SI is provided in this section.

The initial pressure is given in matrix form in Eq. (4.2). Assuming that Γ and the system calibration factor are equal to one, and the only chromophores present are oxy- and deoxyhaemoglobin, then the initial pressure at one single voxel at N wavelengths is given by

$$\begin{bmatrix} p_{0,\lambda_1} \\ p_{0,\lambda_2} \\ \vdots \\ p_{0,\lambda_N} \end{bmatrix} = \begin{bmatrix} \phi_{\lambda_1} & 0 & \cdots & 0 \\ 0 & \phi_{\lambda_2} & & \\ \vdots & & \ddots & \vdots \\ 0 & & \cdots & \phi_{\lambda_N} \end{bmatrix} \begin{bmatrix} \alpha_{HbO_2,\lambda_1} & \alpha_{Hb,\lambda_1} \\ \alpha_{HbO_2,\lambda_2} & \alpha_{Hb,\lambda_2} \\ \vdots & \vdots \\ \alpha_{HbO_2,\lambda_N} & \alpha_{Hb,\lambda_N} \end{bmatrix} \begin{bmatrix} c_{HbO_2} \\ c_{Hb} \end{bmatrix}, \quad (4.12)$$

and the SI for the chromophore concentrations is given by

$$\begin{bmatrix} c_{HbO_2} \\ c_{Hb} \end{bmatrix} = \begin{bmatrix} \alpha_{HbO_2,\lambda_1} & \alpha_{Hb,\lambda_1} \\ \alpha_{HbO_2,\lambda_2} & \alpha_{Hb,\lambda_2} \\ \vdots & \vdots \\ \alpha_{HbO_2,\lambda_N} & \alpha_{Hb,\lambda_N} \end{bmatrix}^\dagger \begin{bmatrix} 1/\phi_{\lambda_1} & 0 & \cdots & 0 \\ 0 & 1/\phi_{\lambda_2} & & \\ \vdots & & \ddots & \vdots \\ 0 & & \cdots & 1/\phi_{\lambda_N} \end{bmatrix} \begin{bmatrix} p_{0,\lambda_1} \\ p_{0,\lambda_2} \\ \vdots \\ p_{0,\lambda_N} \end{bmatrix}. \quad (4.13)$$

Performing SI without correcting for the fluence is equal to assuming that the fluence matrix is equal to the identity matrix. The estimated concentrations is then given by

$$\begin{bmatrix} \check{c}_{HbO_2} \\ \check{c}_{Hb} \end{bmatrix} = \begin{bmatrix} \alpha_{HbO_2,\lambda_1} & \alpha_{Hb,\lambda_1} \\ \alpha_{HbO_2,\lambda_2} & \alpha_{Hb,\lambda_2} \\ \vdots & \vdots \\ \alpha_{HbO_2,\lambda_N} & \alpha_{Hb,\lambda_N} \end{bmatrix}^\dagger \begin{bmatrix} p_{0,\lambda_1} \\ p_{0,\lambda_2} \\ \vdots \\ p_{0,\lambda_N} \end{bmatrix}, \quad (4.14)$$

where the breve symbol ($\check{}$) denotes that the quantity is an estimation. By rewriting the elements of the pseudo-inverse of the spectral matrix using $x_{i,j}$, where i denotes the

row and j denotes the column, and using $p_{0,\lambda_n} = \phi_{\lambda_n} \mu_{a,\lambda_n}$, Eq. (4.14) can be written as

$$\begin{bmatrix} \check{c}_{HbO_2} \\ \check{c}_{Hb} \end{bmatrix} = \begin{bmatrix} x_{1,1} & x_{1,2} & \cdots & x_{1,N} \\ x_{2,1} & x_{2,2} & \cdots & x_{2,N} \end{bmatrix} \begin{bmatrix} \phi_{\lambda_1} \mu_{a,\lambda_1} \\ \phi_{\lambda_2} \mu_{a,\lambda_2} \\ \vdots \\ \phi_{\lambda_N} \mu_{a,\lambda_N} \end{bmatrix}. \quad (4.15)$$

The fluence at each wavelength, ϕ_{λ_n} , can be written as the fluence at the first wavelength, ϕ_{λ_1} , plus the difference between wavelength n and the first wavelength, $\delta\phi_{\lambda_n} = \phi_{\lambda_1} - \phi_{\lambda_n}$, such that Eq. (4.15) becomes

$$\begin{bmatrix} \check{c}_{HbO_2} \\ \check{c}_{Hb} \end{bmatrix} = \begin{bmatrix} x_{1,1} & x_{1,2} & \cdots & x_{1,N} \\ x_{2,1} & x_{2,2} & \cdots & x_{2,N} \end{bmatrix} \begin{bmatrix} \phi_{\lambda_1} \mu_{a,\lambda_1} \\ (\phi_{\lambda_1} + \delta\phi_{\lambda_2}) \mu_{a,\lambda_2} \\ \vdots \\ (\phi_{\lambda_1} + \delta\phi_{\lambda_N}) \mu_{a,\lambda_N} \end{bmatrix}. \quad (4.16)$$

Based on Eq. (4.16), the expression for \check{c}_{HbO_2} is

$$\check{c}_{HbO_2} = x_{1,1} \phi_{\lambda_1} \mu_{a,\lambda_1} + x_{1,2} (\phi_{\lambda_1} + \delta\phi_{\lambda_2}) \mu_{a,\lambda_2} + \dots + x_{1,N} (\phi_{\lambda_1} + \delta\phi_{\lambda_N}) \mu_{a,\lambda_N}. \quad (4.17)$$

Multiplying out the brackets and dividing both sides of the equation by ϕ_{λ_1} , gives

$$\frac{\check{c}_{HbO_2}}{\phi_{\lambda_1}} = (x_{1,1} \mu_{a,\lambda_1} + x_{1,2} \mu_{a,\lambda_2} + \dots + x_{1,N} \mu_{a,\lambda_N}) + (x_{1,2} \Delta\phi_{\lambda_2} \mu_{a,\lambda_2} + \dots + x_{1,N} \Delta\phi_{\lambda_N} \mu_{a,\lambda_N}), \quad (4.18)$$

where $\Delta\phi_{\lambda_n} = \delta\phi_{\lambda_n} / \phi_{\lambda_1}$. The first bracket is equal to the true concentration c_{HbO_2} , so Eq. (4.18) can be simplified to

$$\frac{\check{c}_{HbO_2}}{\phi_{\lambda_1}} = c_{HbO_2} + (x_{1,2} \Delta\phi_{\lambda_2} \mu_{a,\lambda_2} + \dots + x_{1,N} \Delta\phi_{\lambda_N} \mu_{a,\lambda_N}). \quad (4.19)$$

Similarly, the expression for \check{c}_{Hb} is given by

$$\frac{\check{c}_{Hb}}{\phi_{\lambda_1}} = c_{Hb} + (x_{2,2} \Delta\phi_{\lambda_2} \mu_{a,\lambda_2} + \dots + x_{2,N} \Delta\phi_{\lambda_N} \mu_{a,\lambda_N}). \quad (4.20)$$

Finally, since sO_2 is related to the ratio between the oxy- and deoxyhaemoglobin con-

centrations, we use Eqs. (4.19) and (4.20) to obtain

$$\frac{\check{c}_{HbO_2}}{\check{c}_{Hb}} = \frac{c_{HbO_2} + (x_{1,2}\Delta\phi_{\lambda_2}\mu_{a,\lambda_2} + \dots + x_{1,N}\Delta\phi_{\lambda_N}\mu_{a,\lambda_N})}{c_{Hb} + (x_{2,2}\Delta\phi_{\lambda_2}\mu_{a,\lambda_2} + \dots + x_{2,N}\Delta\phi_{\lambda_N}\mu_{a,\lambda_N})}. \quad (4.21)$$

The first wavelength λ_1 has been used to define $\Delta\phi_{\lambda_n} = \frac{\phi_{\lambda_1} - \phi_{\lambda_n}}{\phi_{\lambda_1}}$ in Eq. (4.21). However, of course, this choice of wavelength is arbitrary and does not change the estimated concentration ratio.

It is clear from Eq. (4.21) that when there are no changes in fluence between the wavelengths, the terms within the brackets are equal to zero and hence the estimated concentration ratio is equal to the true concentration ratio. The equation also shows that when there is a change in fluence between the wavelengths, the error is not simply dependent on the amplitude of the change in fluence, but a combination of terms involving the inverse of the spectral matrix, the absorption coefficient and the change in fluence. In the next section, Eq. (4.21) will be used to investigate how N and the spectral range affect the errors.

4.8 Effect of the spectral range and number of wavelengths

The results in Sections 4.5 and 4.6 show that data points with higher N and $\lambda_{min} \approx 670\text{nm}$ are likely to have lower δ_{sO_2} . To further investigate the effect of N and λ_{min} on the accuracy, instead of using randomly selected wavelength combinations, the inversions in this section use as evenly spread wavelengths as possible.

To isolate the effect of the spectral fluence variation on Eq. (4.21), we first examine the behaviour of Eq. (4.21) for different N and λ_{min} when the fluence is nearly constant. Assuming that the fluence at a single voxel is the same for all wavelengths except the first one, such that $\Delta\phi_{\lambda_2} = \Delta\phi_{\lambda_3} = \dots = \Delta\phi_{\lambda_N}$, and dividing Eq. (4.21) by $\Delta\phi_{\lambda_2}$, the estimated ratio becomes

$$\frac{\check{c}_{HbO_2}}{\check{c}_{Hb}} = \frac{\frac{c_{HbO_2}}{\Delta\phi_{\lambda_2}} + (x_{1,2}\mu_{a,\lambda_2} + \dots + x_{1,N}\mu_{a,\lambda_N})}{\frac{c_{Hb}}{\Delta\phi_{\lambda_2}} + (x_{2,2}\mu_{a,\lambda_2} + \dots + x_{2,N}\mu_{a,\lambda_N})}. \quad (4.22)$$

The terms within the bracket in this equation are equal to the true concentrations minus $x_{1,1}\mu_{a,\lambda_1}$ or $x_{2,1}\mu_{a,\lambda_1}$. Therefore, in this scenario, as N increases, the missing terms $x_{1,1}\mu_{a,\lambda_1}$ or $x_{2,1}\mu_{a,\lambda_1}$ have smaller effect, and the sum of the terms within the

bracket converge to c_{HbO_2} or c_{Hb} . To illustrate this effect, Eq. (4.22) is evaluated for evenly spread wavelengths with different N and λ_{min} . The sO_2 is then calculated using

$$sO_2 = \frac{\frac{\check{c}_{HbO_2}}{\check{c}_{Hb}}}{\frac{\check{c}_{HbO_2}}{\check{c}_{Hb}} + 1}. \quad (4.23)$$

The results are shown in Fig. 4.11. The spectral range is fixed in each plot, which means that all data points in each plot have the same λ_{min} (as indicated in the plot title) and λ_{max} (which is 1000nm for all data points). As N increases (x-axis), as evenly spread wavelengths as possible are added between the fixed λ_{min} and λ_{max} from the set of 51 wavelengths. For example, the wavelength combination for $\lambda_{min} = 650\text{nm}$ and $N = 4$ is [650, 770, 880, 1000]nm. For each wavelength combination, Eq. (4.22) is evaluated for different $\Delta\phi_{\lambda_2}$, which is indicated by the colour of the data points. The results show that for all λ_{min} , the estimated sO_2 converges to a constant value as more wavelengths are added, and the smaller the $\Delta\phi_{\lambda_2}$, the closer the convergence is to the true sO_2 .

Of course, in reality, the fluence is unlikely to be constant for nearly all wavelengths. Next we evaluate Eq. (4.21) using the fluence changes calculated from the simulated fluence distribution based on the DA. This is equivalent to simply performing SI on the noise-free simulated images of p_0 . The estimated sO_2 for the single voxel at a depth of 4.5mm is plotted in Fig. 4.12, where the colours represent the fluence variance, $\text{var}(\phi)$. The true $sO_2 = 90\%$, as indicated with the dotted red lines. The results show that when $\lambda_{min} \geq 590\text{nm}$, the $\text{var}(\phi)$ is generally smaller, and increasing N leads to the sO_2 estimate converging to a constant value, in a similar way as in Fig. 4.11 when the fluence was nearly constant. Interestingly, increasing N generally leads to lower estimation of sO_2 . For this particular voxel, using $\lambda_{min} = 650\text{nm}$ led to the most accurate estimate when N is increased. When $\lambda_{min} > 650\text{nm}$, increasing N leads to underestimation of the sO_2 . However, using $\lambda_{min} = 680\text{nm}$ is shown to achieve high accuracy with small N . When $\lambda_{min} < 590\text{nm}$, the trend of the estimated sO_2 is different from in Fig. 4.11, due to the large changes in fluence when the shorter wavelengths are included. In Fig. 4.12, the estimated sO_2 differs from the true value significantly and do not converge to a constant value when N increases for $\lambda_{min} < 590\text{nm}$.

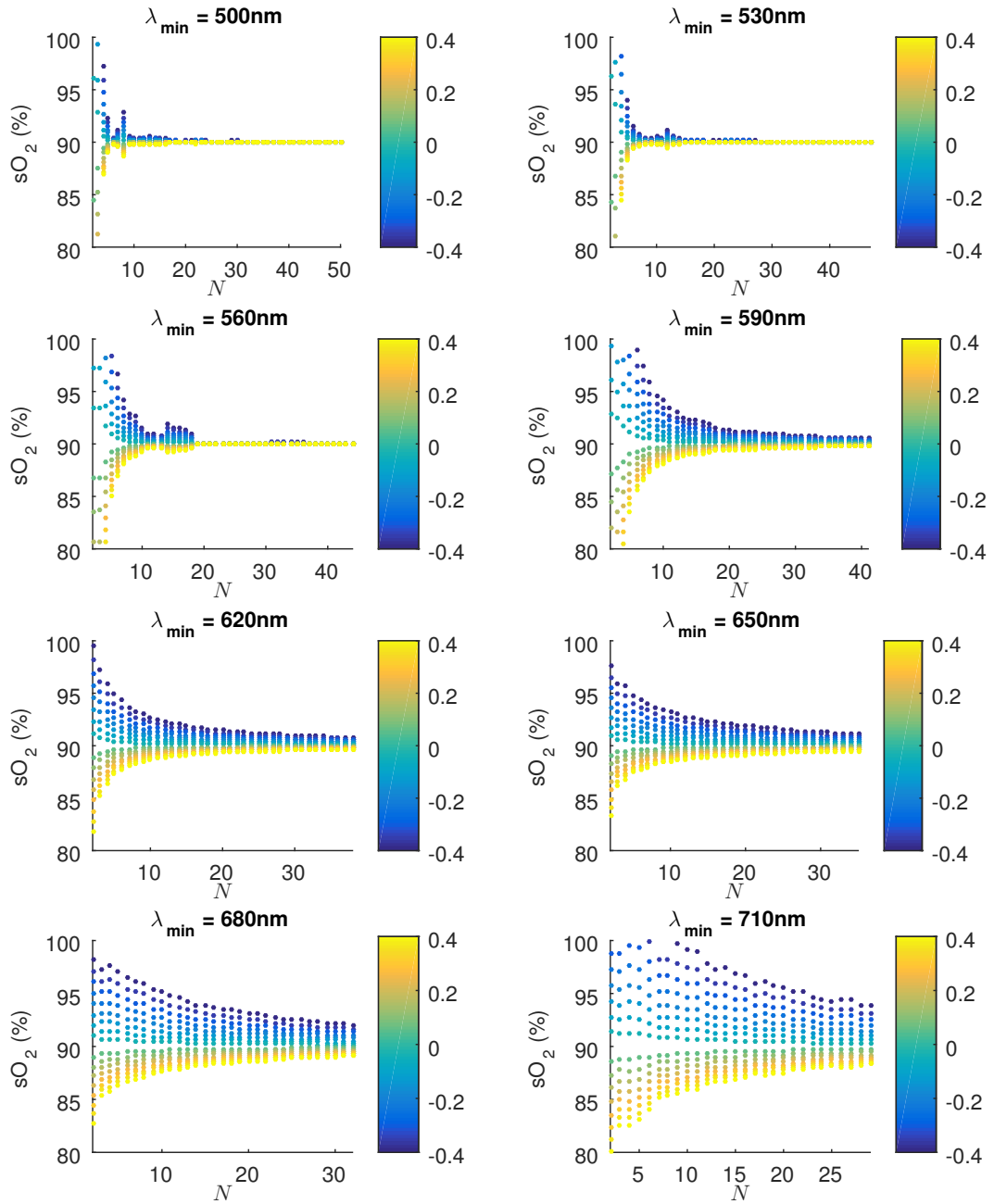


Figure 4.11: The sO_2 calculated based on Eq. (4.22) with different $\Delta\phi_{\lambda_2}$ (colour) and increasing N (x-axis) for equally spaced wavelengths between λ_{\min} (plot title) and λ_{\max} ($=1000\text{nm}$). The true sO_2 is equal to 90%. The estimated sO_2 is shown to converge to a constant value when N increases.

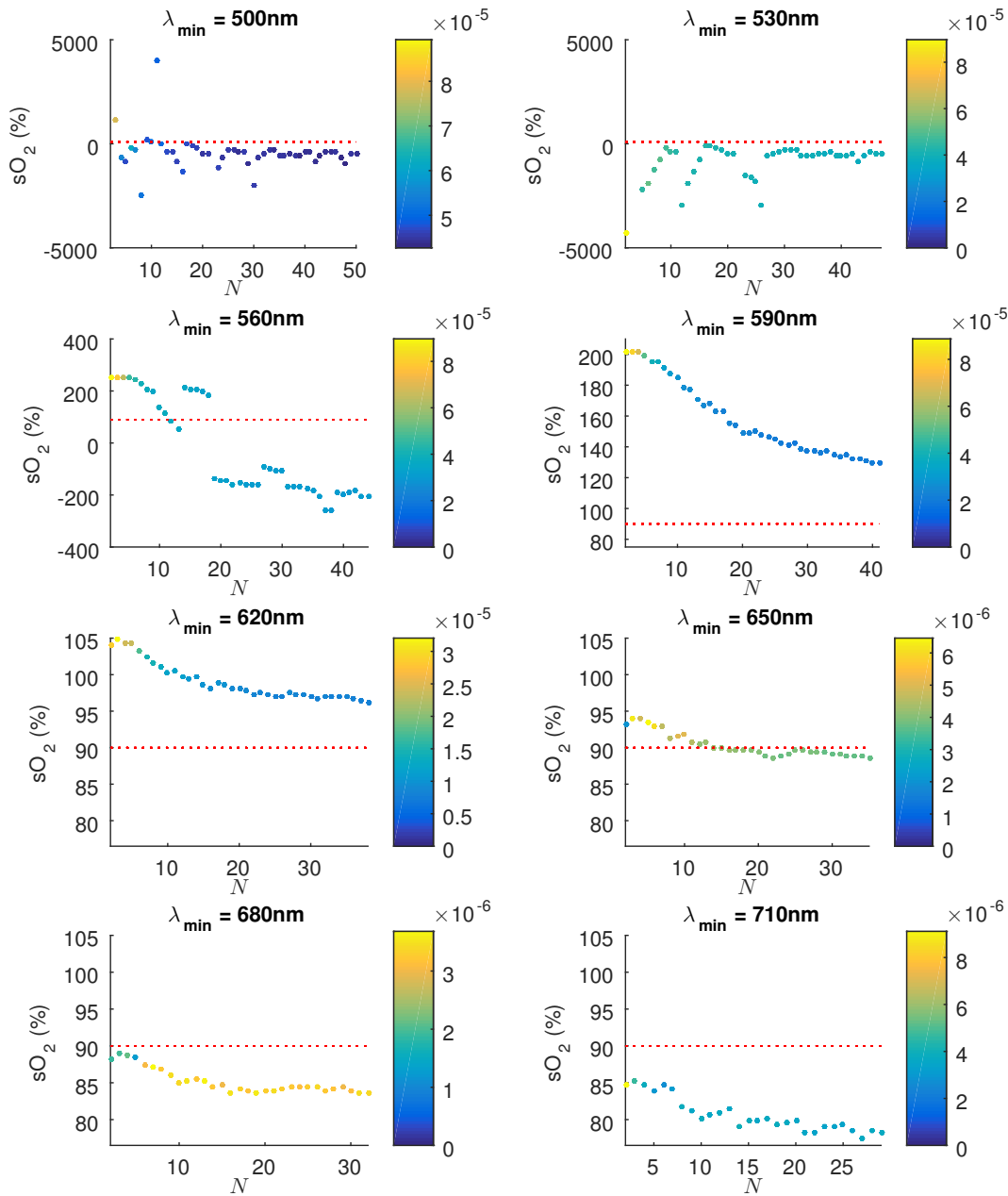


Figure 4.12: The estimated sO_2 at a single voxel at a depth of 4.5mm using evenly spread wavelengths with fixed λ_{max} and different λ_{min} for each plot. The colour of the data points indicate the fluence variance at that voxel. The true sO_2 is 90% (indicated with dotted line). The plots show that, increasing N leads to the estimated sO_2 converging relatively smoothly to a lower value provided that $\lambda_{min} \geq 590$ nm. For $\lambda_{min} = 650$ nm, the convergent value is close to the true sO_2 . Accurate sO_2 estimates were also achieved with lower N when $\lambda_{min} = 680$ nm.

4.9 Summary and discussion

In this chapter, numerically simulated photoacoustic images of a mouse brain were used to investigate the accuracy of estimating sO_2 with SI. The errors were analysed with respect to a number of parameters: the depth from the light source, the true sO_2 level, the smallest singular number of the spectral matrix, the condition number of the spectral matrix, the spectral variance of the fluence, the number of wavelengths and the shortest wavelength used in the inversion. The results demonstrated that using $N = 17$ or more evenly spread wavelengths between 670nm and 1000nm can lead to accurate sO_2 estimates with $\delta_{sO_2} < 5\%$ for depths up to approximately 9mm and sO_2 levels between 60% and 100%. It was also shown that there exist wavelength combinations with fewer wavelengths ($N < 17$) that lead to extremely low errors for different depth ranges and sO_2 levels. It was shown that using randomly chosen wavelength combinations is unlikely to lead to more accurate results than using evenly spread wavelengths for the spectral range 670–1000nm. Choosing wavelength combinations that maximise the σ_{min} of the spectral matrix has previously been suggested as a method to obtain the most accurate estimates of the chromophore concentrations. However, the results from this chapter demonstrate that δ_{sO_2} does not correlate with σ_{min} . Minimising κ of the spectral matrix was shown to be useful for eliminating wavelength combinations that result in extremely large δ_{sO_2} , but it does not necessarily lead to the lowest errors when the δ_{sO_2} is smaller than 25%. The δ_{sO_2} was also shown to be related to, but not linearly dependent on, the variance of the fluence. This was explained by the fact that the δ_{sO_2} is due to a combination of terms including the inverse of the specific absorption spectra, the absorption coefficient and the spectral changes in fluence. Finally, it was shown that increasing the number of wavelengths used in the inversion leads to the estimated sO_2 converging to a constant value provided that the change in fluence is relatively small. Including wavelengths shorter than 590nm in the inversion leads to significantly larger spectral variation in the fluence, and hence results in extremely large δ_{sO_2} and the estimated sO_2 does not converge smoothly to a constant value when N is increased.

The results in this chapter are based on simulated images of a realistic mouse brain phantom. However, given the diffuse nature of light in highly scattering biological tissue, the precise structure of the blood vessels is unlikely to have a large impact on the quantification results. To provide an indication of the generalisability of the

results, the analysis was repeated for a second numerical phantom, which consisted of horizontally aligned blood filled tubes arranged in a vertical line and submerged a tissue-like background. Details of this phantom and the results can be found in Appendix B. The structure of this phantom represents a scenario where a larger amount of spectral colouring is likely to be present compared to the mouse brain phantom, because the tubes are aligned in a vertical line. As a result, the average δ_{sO_2} was found to be higher for deeper depths and lower true sO_2 compared to the mouse brain phantom. However, the increase is $<5\%$ for the comparable depths and true sO_2 levels. The error trends are similar to the mouse brain phantom, where the errors generally increase with depth, decrease with higher true sO_2 , and decrease with larger N in the spectral range 670–1000nm. This indicates that the accuracy of the SI is not highly dependent on the specific structures of the blood vessel of similar diameters. Given that the spectral colouring is typically lower in realistic tissues than this tube phantom, these results provide an indication for the lowest accuracy that can be expected when imaging vasculature of similar diameters. However, this does not suggest that SI is a generally applicable method for estimating sO_2 in any arbitrary tissue structures. For example, it is likely to result in larger errors in blood vessels with large diameters and in the presence of large and/or highly absorbing features, such as fluorescent probes or targeted contrast agents. In these cases, the spectral colouring is likely to be more severe, leading to poorer sO_2 estimates.

Simple approximate fluence correction methods have been used to reduce the spectral colouring before performing SI in some studies. Typically the fluence is assumed to be exponentially decaying with increasing distance away from the light source and the rate of the decay is calculated based on average optical properties of the tissue. It has been shown that applying the exponential fluence correction method can lead to improved accuracy of the sO_2 estimation [180]. This type of fluence correction has not been used for the analysis in this chapter, because its accuracy depends on numerous other factors, such as the level of spatial homogeneity of the optical properties in the tissue and how accurately the optical properties are estimated. If an appropriate approximate fluence correction has been applied, it is possible that lower errors can be achieved for wider range of depths and/or sO_2 levels, or with fewer wavelengths.

4.10 Conclusion

In conclusion, this chapter demonstrates that it is difficult to predict precisely the optimal wavelengths for estimating sO_2 using SI, due to the fact that the errors depend on a combination the absorption spectra and its inverse, as well as the changes in fluence. However, it may be possible to achieve accurate estimation of the sO_2 with $\delta_{sO_2} < 5\%$ using 17 or more evenly spread wavelengths between 670nm and 1000nm for a large range of depths from the light source and sO_2 levels in the vasculature of a mouse brain.

Chapter 5

Independent component analysis

The previous chapter showed that SI can be used to estimate sO_2 relatively accurately in a range of scenarios. However, it is important to recall that sO_2 only requires the estimation of the concentration ratio, which is a comparatively easy quantity to estimate, because it does not require the concentrations to be estimated correctly with respect to other spatial locations. Therefore, the errors are caused only by the spectral variation of the fluence, while the spatial variation of the fluence does not affect the sO_2 estimate. Figure 5.1 shows a typical result of SI where, even though the sO_2 is accurately estimated, the estimated concentrations of oxy- and deoxyhaemoglobin (in arbitrary units) are inaccurate. In cases where the spatial distribution of the concentrations are of interest rather than the ratio, more accurate quantification methods are required. Independent component analysis (ICA) is an alternative linear QPAT method that is attractive for *in vivo* studies, because it can, under certain conditions, potentially provide quantification with higher accuracy than SI without adding extra degrees of complexity or significant computational burden. Instead of using the known absorption spectra, ICA exploits the statistical properties of the chromophore distributions in order to estimate their concentrations. In this chapter, we investigate the accuracy of ICA under different circumstances and compare the results to the accuracy of SI.

5.1 Introduction

The statistical properties of multidimensional data can be utilised in blind source separation (BSS) methods. The general aim of BSS is to find the sources that give rise

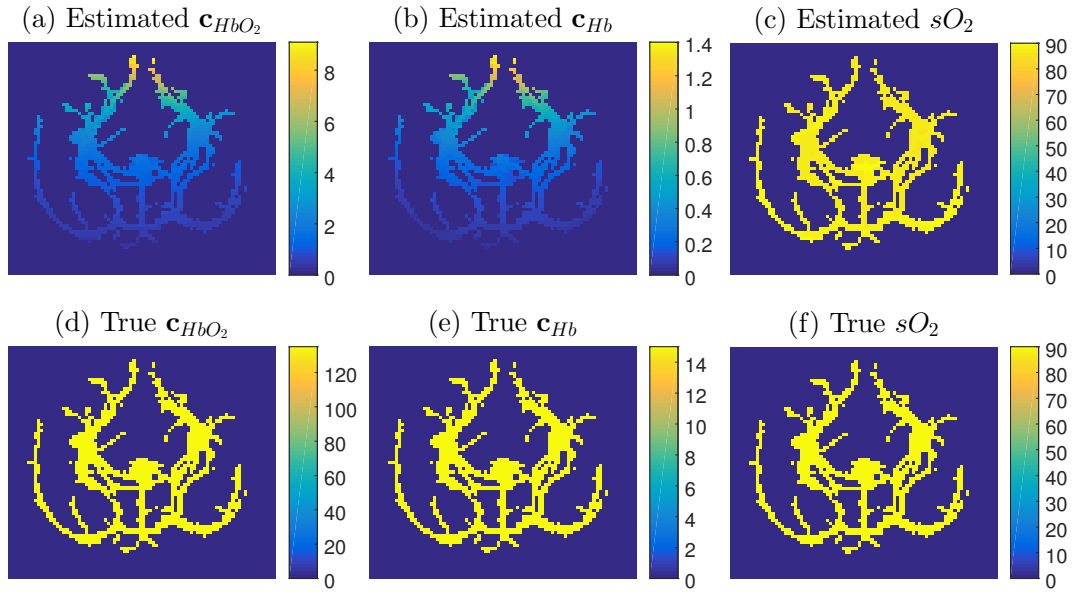


Figure 5.1: Maximal intensity projections of the SI results from Chapter 4 using 17 wavelengths with $\lambda_{min} = 670\text{nm}$ and $\lambda_{max} = 1000\text{nm}$. The estimated concentrations for oxy- and deoxyhaemoglobin in the foreground vessels are shown with arbitrary units in (a) and (b), respectively. By comparing to the true concentrations shown in (d) and (e), it is clear that the estimated concentrations are inaccurate as they decrease significantly with depth, while the true concentrations are constant inside the foreground vessels. Despite the fact that the estimated concentrations are inaccurate with respect to other spatial locations, the estimated sO_2 , which is shown in percentages in (c), is relatively accurate. The true sO_2 is 90% in the foreground vessels, as shown in (f).

to the observed signals which are mixtures of the original source signals. The “blindness” refers to the fact that the information about the mixing process is unavailable. BSS is frequently used in signal processing for telecommunications, speech recognition systems and biomedical applications [204]. For spectroscopic imaging applications of BSS, the “sources” are the concentrations of each chromophore that provide the image contrast, and the image acquired at each wavelength is an “observation” of the sources mixed in different portions due to the unique spectrally varying optical properties of the chromophores. In linear BSS, it is assumed that the observed signals are linearly related to the sources. In the context of photoacoustic imaging, this is equivalent to stating that the images are directly proportional to a weighted sum of the chromophore concentrations.

Independent component analysis (ICA) is a linear BSS method that can be used to decompose the multiwavelength image data into components representing the individual

chromophores. This is achieved by exploiting the fact that the distribution of certain chromophores can be assumed to be statistically independent of each other. In ICA, the matrix with the specific absorption coefficients, which is referred to as the mixing matrix, is assumed to be unknown, and the chromophore concentrations are found by searching for the mixing matrix that corresponds to the most independent chromophores. ICA has the advantages of being fast, easy to implement and computationally inexpensive compared to model-based inversion methods, and may potentially provide more accurate results than SI.

5.1.1 The use of ICA in QPAT

ICA was first proposed for unmixing chromophores in photoacoustic imaging by Glatz *et al* [120]. They showed that ICA is able to separate fluorescent dyes from the background tissue with less crosstalk of the components than SI and principal component analysis (PCA) using *ex vivo* multiwavelength photoacoustic images of a nude mouse with insertions of indocyanine green (ICG) and cyanine 7 (Cy7).

Subsequently, ICA has been applied in a number of *in vivo* photoacoustic imaging studies. In Ref. [39], ICA was used to separate a contrast agent which was targeted to cells undergoing apoptosis from the background tissue in mouse tumour models. The results demonstrated that the probe accumulated in the blood vessels surrounding the tumours, which correlated well with *ex vivo* epifluorescence images and cryo slices. ICA has also been used in imaging of myocardial infarction in murine models [40]. Two days after the infarction was induced, 2D multiwavelength images of the heart region of the mice were acquired before and after the injection of a contrast agent which binds to selectin – a cell adhesive molecule that is expected to accumulate at injured tissues. A component representing the contrast agent was obtained by applying ICA on the multi-wavelength images, which showed that the concentration of the contrast agent was higher at the infarcted tissue regions. This result was shown to be consistent with histological analysis of the heart tissue. Furthermore, in an imaging study of reporter-genes, Deliolanis *et al* [205] used ICA to separate three components representing oxyhaemoglobin, deoxyhaemoglobin and a fluorescent protein from *in vivo* multiwavelength photoacoustic images of a mouse brain.

In all above-mentioned studies, the main purpose of applying ICA was to aid the

visualisation of the probe by distinguishing it from the background tissue. Despite presenting images of the separated chromophores with normalised scales for concentration, the quantitative accuracy of the estimated chromophore concentration was not discussed. The unmixing results were validated through *ex vivo* fluorescence imaging or histology techniques, which do not provide quantitatively accurate representations of the *in vivo* probe concentrations. It is also worth noting that in Ref. [205], ICA was used to separate oxy- and deoxyhaemoglobin, despite the fact that they are unlikely to be independent chromophores (see Sec. 5.3.1).

Dean-Ben *et al* [121] presented a study with focus on the quantitative accuracy of ICA. The analysis in this study uses the logarithm of the photoacoustic images, so that the initial pressure is represented as a sum of the fluence and the absorption coefficient rather than a product. Numerically simulated images, images of an experimental tissue mimicking phantom and *ex vivo* mouse images with insertion of contrast agents with overlapping absorption spectra were used to show that applying ICA on the logarithm of the images provided more accurate quantification than standard ICA. However, this method requires that the chromophore concentration in the background tissue is homogeneous since the components of interest are represented as a ratio to the background chromophore concentration.

5.1.2 Aim and structure of the chapter

ICA has been proposed as a fast and simple method of unmixing multiwavelength photoacoustic images and shows some promise of providing improved accuracy compared to other linear methods. However, despite having been applied in several *in vivo* studies, the quantitative accuracy of ICA has not been rigorously assessed for photoacoustic imaging. Therefore, the aim of this chapter is to investigate the conditions required for ICA to provide quantitatively accurate unmixing, which required an approximate fluence correction step. Simulated multiwavelength photoacoustic images are used to assess the robustness of ICA against inaccuracies in the fluence correction and demonstrate the effect of retaining different numbers of dimensions as a pre-processing step to ICA. The results of ICA are also compared to SI for experimentally acquired images of a tissue mimicking phantom. Furthermore, the performances of ICA and SI are analysed using the experimental images with a varying number of wavelengths. We demonstrate

both the advantages of ICA and its limitations, by including examples of cases where it provides accurate quantification, as well as cases where it breaks down.

Section 5.2 provides the definition of statistical independence and explains how it can be measured using mutual information. It also shows examples of statistically independent chromophores. Section 5.3 outlines the principles of ICA and describes a widely used ICA algorithm known as FastICA [206]. Section 5.4 describes the experimental image acquisition of a tissue mimicking phantom and the generation of the numerically simulated images. The accuracy of unmixing the experimental and numerical images using ICA and SI are presented in Sec. 5.5. Section 5.6 summarises and discusses the findings. The conclusions of this chapter are presented in Sec. 5.7.

5.2 Statistical independence

5.2.1 Definition

The mathematical definition of statistical independence states that two random variables, \mathbf{y}_1 and \mathbf{y}_2 , are statistically independent if their joint probability density function (PDF), $\rho_{\mathbf{y}_1, \mathbf{y}_2}(y_1, y_2)$, is the product of their marginal PDFs, $\rho_{\mathbf{y}_1}(y_1)$ and $\rho_{\mathbf{y}_2}(y_2)$, such that [207]

$$\rho_{\mathbf{y}_1, \mathbf{y}_2}(y_1, y_2) = \rho_{\mathbf{y}_1}(y_1)\rho_{\mathbf{y}_2}(y_2), \quad (5.1)$$

where y_1 and y_2 denote possible values of \mathbf{y}_1 and \mathbf{y}_2 . More intuitively, this definition means that two events, A and B, are independent of each other if the probability of A occurring does not in any way influence the probability of B occurring. In QPAT, two chromophores are considered independent if the knowledge of the concentration of one chromophore at a location does not affect the estimate of the other chromophore's concentration at the same location. For example, if a contrast agent is independent of the blood, then the estimation of the contrast agent concentration at a voxel does not in any way predict the blood concentration at that voxel. As a counter example, oxy- and deoxyhaemoglobin are typically *not* independent chromophores: if a voxel is found to contain a high concentration of deoxyhaemoglobin, then the likelihood that a high concentration of oxyhaemoglobin will be found at the same voxel increases, as the voxel is likely to represent a blood vessel.

5.2.2 Mutual information as a measure of statistical independence

The degree of independence between variables can be measured using the mutual information (MI). MI is an estimate of the amount of information one variable provides on another variable. Variables with higher statistical independence have lower MI, which means that they contain less information about each other. MI can also be understood as an estimation of how much the observation of one random variable reduces the uncertainty of the value of other variables. The MI, I , between \mathbf{y}_1 and \mathbf{y}_2 is given by

$$I(\mathbf{y}_1, \mathbf{y}_2) = \mathcal{H}(\mathbf{y}_1) + \mathcal{H}(\mathbf{y}_2) - \mathcal{H}(\mathbf{y}_1, \mathbf{y}_2), \quad (5.2)$$

where $\mathcal{H}(\mathbf{y}_k)$ and $\mathcal{H}(\mathbf{y}_1, \mathbf{y}_2)$ are the entropy and the joint entropy of \mathbf{y}_1 and \mathbf{y}_2 respectively. Entropy is a key concept in information theory: it measures the amount of information provided by the observation of a random variable and it is defined by

$$\mathcal{H}(\mathbf{y}_k) = - \int_{y_k} \rho_{\mathbf{y}_k}(y_k) \log \rho_{\mathbf{y}_k}(y_k) dy_k, \quad (5.3)$$

where $k = 1$ or 2 . All logarithms in Chapter 5 and 6 are in base 2 unless otherwise stated. The behaviour of \mathcal{H} for different probability distributions can be understood from a plot of $-\rho_{\mathbf{y}_k} \log \rho_{\mathbf{y}_k}$ for $0 < \rho_{\mathbf{y}_k} < 1$, which is shown in Fig. 5.2. This plot shows that $-\rho_{\mathbf{y}_k} \log \rho_{\mathbf{y}_k}$ is small for probabilities close to 0 and 1. If the variable \mathbf{y}_k almost always takes the same value, then the probabilities for most values would be close to 0, except for one value that has a probability close to 1. This means that $-\rho_{\mathbf{y}_k} \log \rho_{\mathbf{y}_k}$ will be small for all values, and hence the variable will have a small entropy. However, if the values that the variable take are less predictable, then the probabilities are more equal and more likely to be midway between 0 and 1. In this case the entropy would be higher, which indicates that the variable is less predictable and therefore contains more information. Similarly, the joint entropy measures the amount of information provided by the simultaneous observation of a set of variables, and is defined as

$$\mathcal{H}(\mathbf{y}_1, \mathbf{y}_2) = - \int_{y_1} \int_{y_2} \rho_{\mathbf{y}_1, \mathbf{y}_2}(y_1, y_2) \log \rho_{\mathbf{y}_1, \mathbf{y}_2}(y_1, y_2) dy_1 dy_2. \quad (5.4)$$

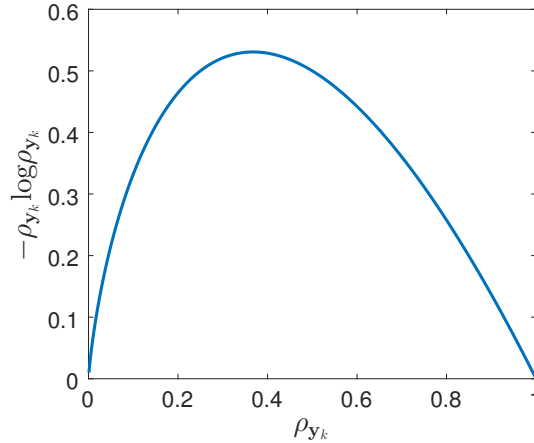


Figure 5.2: When the probabilities are close to 0 or 1, the variable is more predictable, and the value of $-\rho_{\mathbf{y}_k} \log \rho_{\mathbf{y}_k}$ is small, resulting in small entropy. The value of $-\rho_{\mathbf{y}_k} \log \rho_{\mathbf{y}_k}$ is larger for probabilities far from 0 or 1, which means that the variable is less predictable, and results in larger entropy.

The MI can also be calculated for multiple random variables using

$$I(\mathbf{y}_1, \mathbf{y}_2, \dots, \mathbf{y}_K) = \sum_{k=1}^K \mathcal{H}(\mathbf{y}_k) - \mathcal{H}(\mathbf{y}_1, \mathbf{y}_2, \dots, \mathbf{y}_K). \quad (5.5)$$

The concept of MI is illustrated with Venn diagrams in Fig. 5.3. The blue and red circles represent the entropy of \mathbf{y}_1 and \mathbf{y}_2 respectively, and the area within the purple curves is their joint entropy. The left diagram shows a case where the overlap of the entropies, or information contents, of \mathbf{y}_1 and \mathbf{y}_2 is large, which means that \mathbf{y}_1 and \mathbf{y}_2 have large MI, and therefore low independence. In the right diagram, their information contents do not overlap as much. As a consequence, the variables are more independent, which means that when \mathbf{y}_1 is known, there is still large uncertainty in what values \mathbf{y}_2 might take.

5.2.3 Which chromophores are statistically independent?

It should be made clear that ICA, or any other technique relying on statistical independence, is unlikely to be able to estimate the sO_2 , because, as mentioned above, the distribution of oxy- and deoxyhaemoglobin are unlikely to be statistically independent. This is illustrated in Fig. 5.4, which shows four hypothetical examples of the chromophore concentration distributions along a line profile across some volume. Ex-

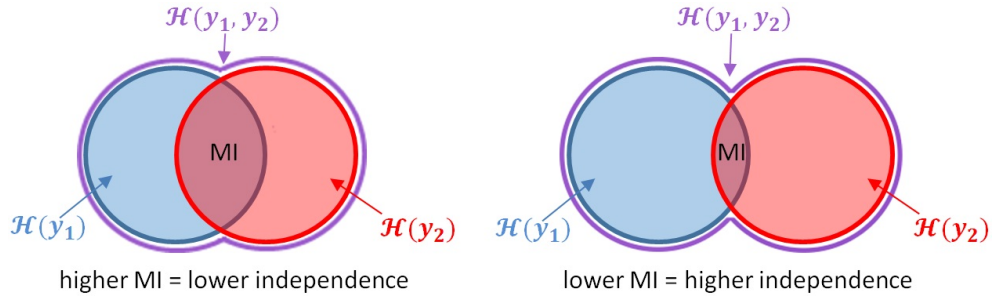


Figure 5.3: The blue and red regions represent the entropies of \mathbf{y}_1 and \mathbf{y}_2 respectively. The area within the purple curves represents the joint entropy of \mathbf{y}_1 and \mathbf{y}_2 . The MI is in the overlapping regions of blue and red. The left diagram illustrates higher MI and therefore lower statistical independence compared to the right diagram.

ample A simulates a possible distribution of oxy- and deoxyhaemoglobin concentrations, c_{HbO_2} and c_{Hb} , along a line across nine blood vessels with the same total haemoglobin concentration, $c_{HbT} = 150\text{gL}^{-1}$, and varying sO_2 . In this case, if it is given that the c_{HbO_2} is 140gL^{-1} at a location, then there is a 100% chance that the c_{Hb} is 10gL^{-1} at the same location, due to the fixed c_{HbT} . This means that no uncertainty remains for c_{Hb} once c_{HbO_2} is known. These chromophores are therefore completely dependent on each other. In Example B, both the c_{HbT} and sO_2 vary for the different blood vessels. In this scenario, wherever $c_{HbO_2} = 140\text{gL}^{-1}$, the chances of c_{Hb} being 10, 20 or 30gL^{-1} are 33.3% each. This remaining uncertainty means that in this example, oxy- and deoxyhaemoglobin are more independent of each other. Example C shows a case where a contrast agent has been injected inside blood vessels. The independence between the contrast agent and oxy- or deoxyhaemoglobin is comparable to the chromophores in Example B, where some independence can be observed. Example D represents a scenario where a contrast agent is distributed both outside and inside some blood vessels and is therefore highly independent of oxy- and deoxyhaemoglobin.

In order to apply QPAT methods based on statistical independence, one must have the prior knowledge that the chromophore distributions are expected to be statistically independent. Examples of statistically independent chromophores in cases of practical interest include:

- Contrast agents that accumulate in areas unrelated to the blood distribution, such as in lymphatic vessels and lymph nodes [208].

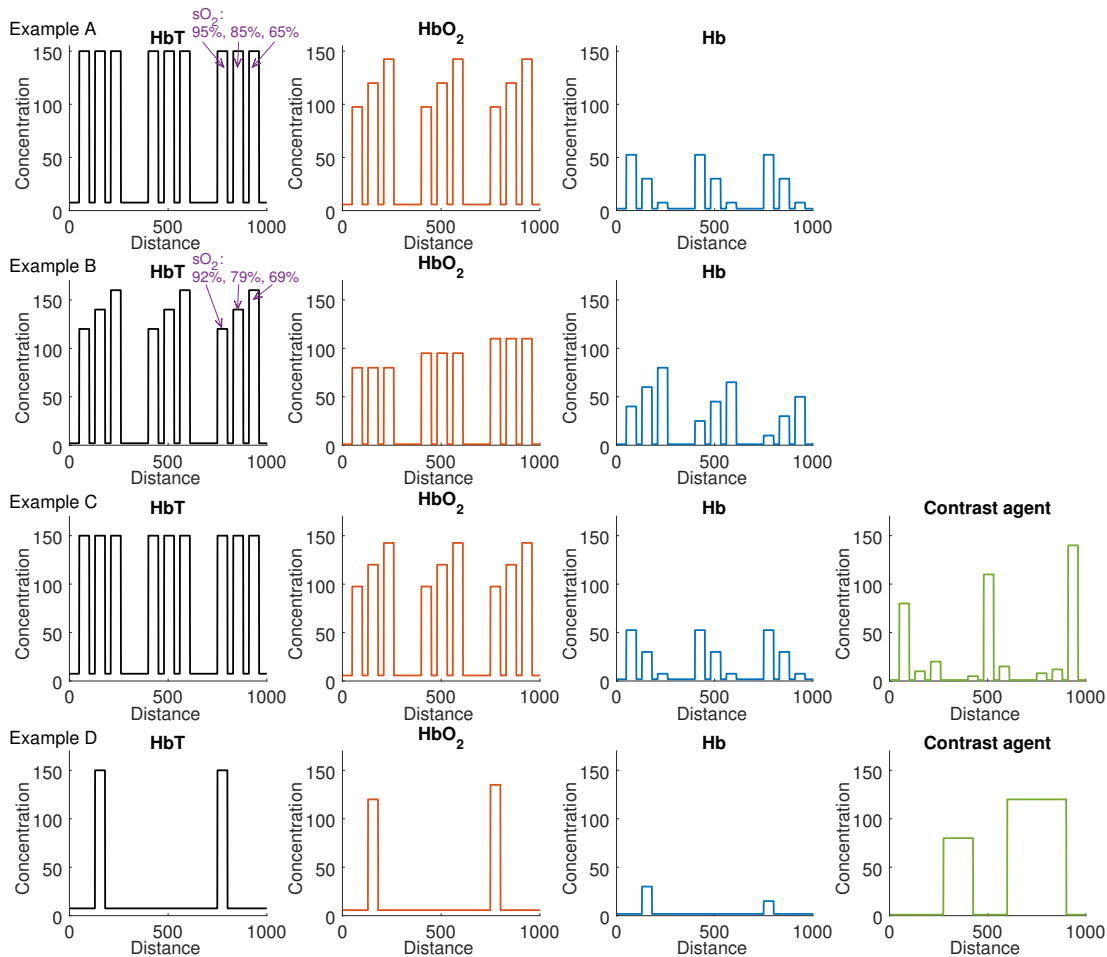


Figure 5.4: The plots show the concentrations of total haemoglobin (HbT), oxyhaemoglobin (HbO₂), deoxyhaemoglobin (Hb) and a contrast agent along a hypothetical 1D cross sections of blood vessels. The sO_2 for some vessels are indicated with arrows. Example A shows completely dependent oxy- and deoxyhaemoglobin distributions, because each value of oxyhaemoglobin corresponds to only one possible outcome of deoxyhaemoglobin. Example B shows more independent oxy- and deoxyhaemoglobin distributions, where each value of oxyhaemoglobin corresponds to three possible outcomes of deoxyhaemoglobin. Example C includes a contrast agent injected in the blood vessels. The contrast agent is somewhat independent from the oxy- and deoxyhaemoglobin distributions. Example D shows a contrast agent that is distributed independently from the oxy- and deoxyhaemoglobin.

- Certain cells that have been genetically modified to express optical absorbers, such as genetically encoded fluorescent proteins [43] or tyrosinase-expressing cells [209], can be found at locations independent from other absorbers.
- Imaging probes that are targeted to disease-specific receptors whose spatial distribution is unrelated to that of the blood and the background tissue [39, 40].

5.3 Independent component analysis

ICA is a blind unmixing method based on a linear model, and it can be used to separate independent components from the multiwavelength photoacoustic images. The matrix form of the equation describing the initial pressure is given in Eq. (4.2), and is restated here for convenience

$$\mathbf{P} = \mathbf{\Phi} \circ (\mathbf{A} (\mathbf{\Gamma} \circ \mathbf{C})), \quad (5.6)$$

where \circ denotes an element-wise (Hadamard) product. To linearise this equation, one can divide it with an approximate estimate of the fluence, $\check{\mathbf{P}}$, such that (Eq. (4.8))

$$\frac{\mathbf{P}}{\check{\mathbf{P}}} = \check{\mathbf{P}} \approx \mathbf{A} (\mathbf{\Gamma} \circ \mathbf{C}). \quad (5.7)$$

where breve symbol ($\check{}$) is used to denote the estimation of a variable. In SI, the pseudo-inverse of the mixing matrix \mathbf{A} is used to find the chromophore concentrations. In ICA, on the other hand, the mixing matrix is assumed to be unknown. Instead, ICA aims to decompose the multiwavelength photoacoustic images into the source components, which represent the individual chromophores, based on the assumption that the source components are statistically independent of each other. This is achieved by searching for a mixing matrix, \mathbf{W} , whose inverse can be multiplied by the matrix with the mixed signals to give the matrix of the source components, \mathbf{S} :

$$\mathbf{W}^\dagger \check{\mathbf{P}} = \mathbf{S}, \quad (5.8)$$

where the rows of \mathbf{S} have maximal mutual statistical independence. The unmixed component in each row of \mathbf{S} corresponds to one of the chromophores, such that $\mathbf{S} \approx \mathbf{\Gamma} \circ \mathbf{C}$, provided that the true spatial distributions of the chromophore concentrations are in-

dependent. Similarly to SI, ICA is unable to separate $\mathbf{\Gamma}$ from the concentrations.

The source components could be estimated by finding a mixing matrix that will minimise the MI between the chromophores. However, using MI as the independence measure involves calculating the PDFs of the variables, which is a non-trivial procedure (Sec. 6.2.2 and 6.2.4). The widely known ICA algorithm named FastICA [206] uses instead a simple independence measure based on the Central Limit Theorem. The Central Limit Theorem states that the probability distribution of the sum of multiple independent random variables will always be more Gaussian than the probability distribution of any one of the independent random variables alone. It follows from the Central Limit Theorem that a linear combination of the mixed signals with the weight vector \mathbf{w} , $\mathbf{y} = \mathbf{w}^T \check{\mathbf{P}}$, will be the least Gaussian when this combination actually equals one of the sources components. The aim is therefore to find the optimal \mathbf{w} that maximises the non-Gaussianity of $\mathbf{w}^T \check{\mathbf{P}}$. This \mathbf{w} is then equal to one of the columns of \mathbf{W} , and hence \mathbf{W} can be constructed by finding \mathbf{w} for each of the independent components.

A suitable measure of Gaussianity is required to determine whether maximum non-Gaussianity has been reached. Gaussianity is related to information content and it can be shown that a Gaussian distributed variable has the highest entropy among all other random variables with equal variance [210, 211]. Entropy can therefore be used as a measure of non-Gaussianity. In practice, however, it is more convenient to use negentropy, J , which is a normalised form of entropy. Negentropy is always positive and is zero for Gaussian distributions, and it is defined as

$$J(\mathbf{y}_k) = \mathcal{H}(\mathbf{y}_{Gauss}) - \mathcal{H}(\mathbf{y}_k), \quad (5.9)$$

where \mathbf{y}_{Gauss} is a Gaussian random variable that has the identical covariance matrix as \mathbf{y}_k . To avoid having to calculate \mathcal{H} which requires estimating the PDFs, FastICA uses an approximation of negentropy, given by:

$$J(\mathbf{y}_k) \propto [E\{G(\mathbf{y}_k)\} - E\{G(\nu)\}]^2, \quad (5.10)$$

where $E\{\cdot\}$ denotes the expectation value, ν is a Gaussian variable with zero mean and unit variance, \mathbf{y}_k is the variable of interest which is also assumed to have zero mean and unit variance, and G is a non-quadratic function. A suitable choice of G has been

shown to be $G(u) = \frac{1}{a} \log[\cosh(au)]$, where $1 \leq a \leq 2$ is a constant [206]. This function for G will be used for all calculations this chapter.

In summary, an individual independent component has a more non-Gaussian distribution than a mixture of multiple independent components, and the non-Gaussianity of a component can be measured using negentropy. Thus, FastICA finds the independent components by searching for the \mathbf{w} that results in maximum $J(\mathbf{w}^T \check{\mathbf{P}})$ in a fixed point iteration scheme. To find multiple independent components, the algorithm is run for multiple weight vectors $\mathbf{w}_1, \dots, \mathbf{w}_K$, with a decorrelation step for the outputs after each iteration.

5.3.1 Limitations of ICA

The obvious main limitation of ICA is that it can only be applied to chromophores that are known to be statistically independent of each other. As previously mentioned, this means that it is not suitable to use ICA to separate oxy- and deoxyhaemoglobin. However, it can still be a valuable tool for a range of other QPAT applications where the chromophores are expected to be independent (as discussed in Sec. 5.2.3).

Furthermore, ICA does not recover the concentrations for different chromophores to a common scale because the magnitude of each independent source is unknown. It is clear from the ICA model in Eq. (5.8) that since neither of \mathbf{W} and \mathbf{S} are fixed, the magnitude of each source can be arbitrarily changed by multiplying any row in \mathbf{S} and dividing the corresponding column in \mathbf{W} with the same constant. This means that while the relative concentration to other spatial locations for each chromophore can be recovered, the concentration of one chromophore cannot be compared to that of another chromophore. In other words, each chromophore concentration is estimated to a different scale, and therefore the concentration ratio between two chromophores cannot be recovered (Sec. 1.2). Section 5.6 discusses the possibility of overcoming this ambiguity by using the known absorption spectra.

Another limitation of ICA is that the order of the estimated independent components is arbitrary. The components are typically identified manually to the corresponding chromophores, using prior knowledge of the expected results. In this chapter, the components are identified using the known absorption spectra.

Lastly, ICA cannot unmix Gaussian sources because their probability distribution

is symmetric and hence lack information on the direction of the mixing matrix. Therefore ICA requires the values of the chromophore concentrations to have a probability distribution that is as non-Gaussian as possible.

5.4 Generating multiwavelength photoacoustic images

If the fluence was estimated exactly, such that $\check{\Phi} = \Phi$, the approximate model in Eq. (5.7) would be an exact equality and, if the chromophore distributions were independent, both ICA and SI would achieve accurate unmixing of the chromophores, such that the outputs of both inversions are exactly equal to $\Gamma \circ \mathbf{C}$. In practice however, $\check{\Phi}$ is only an approximation of Φ , and both methods will lead to errors. Both experimental and numerically simulated multiwavelength photoacoustic images of tissue mimicking phantoms were generated to investigate the accuracy of ICA for various levels of absorption and heterogeneity in the tissue structure, as well as the effect of dimension reduction and wavelength selection, in order to understand the extent to which ICA can be used as a reliable quantification method. The same data sets are also unmixed with SI for comparison. The experimental and numerical phantoms were designed such that the following criteria were satisfied:

1. The spatial distributions of the chromophores are independent, so that when the fluence adjustment is perfect, ICA results in accurate unmixing.
2. The specific absorption spectra of the chosen chromophores are such that the mixing matrix \mathbf{A} is full rank, so that when the fluence adjustment is perfect, SI also results in accurate unmixing.

Hence, using these phantoms, it is possible to see how the inaccuracies in an approximate fluence adjustment affect the performance of the unmixing methods.

5.4.1 Experimental photoacoustic image acquisition

A liquid tissue mimicking phantom containing capillary tubes was imaged at multiple wavelengths in a photoacoustic imaging system based on the planar Fabry-Perot polymer film interferometer sensor. The phantom design and the imaging system are described below.

5.4.1.1 The tissue mimicking phantom

Eight capillary tubes (Paradigm Optics, Morcap 83) with an inner diameter of $590\mu\text{m}$ and wall thickness of $66.5\mu\text{m}$ were used to construct the tissue mimicking phantom. The tubes were arranged horizontally in two vertical lines as indicated in Fig. 5.5, which shows a cross-section of the phantom in the experimental set-up. The left column of tubes were filled with four different concentrations of copper(II) chloride dihydrate ($\text{CuCl}_2 \cdot 2\text{H}_2\text{O}$) dissolved in deionised water. The concentrations were in the ratios 1:2:3:4, where the uppermost tube had the lowest concentration of 5.2gL^{-1} while the bottom tube had the highest concentration of 20.8gL^{-1} . The right column of tubes were filled with solutions of nickel(II) chloride hexahydrate ($\text{NiCl}_2 \cdot 6\text{H}_2\text{O}$), also with concentration ratio of 1:2:3:4. These contrast agents simulate different absorbers in the tissue and their specific absorption coefficients are shown in Fig. 5.6(a). For brevity, the copper(II) chloride dihydrate and nickel(II) chloride hexahydrate will be referred to as CuCl_2 and NiCl_2 . Since the specific absorption coefficient of NiCl_2 is approximately one order of magnitude lower than that of CuCl_2 (see Fig. 5.6(a)), the concentrations of NiCl_2 were set to be approximately ten times higher than CuCl_2 to give similar optical absorption. Therefore, the uppermost and bottom tubes in the right column had NiCl_2 concentrations of 55.1gL^{-1} and 220.3gL^{-1} respectively. The average absorption of all tubes was 0.25mm^{-1} at 810nm .

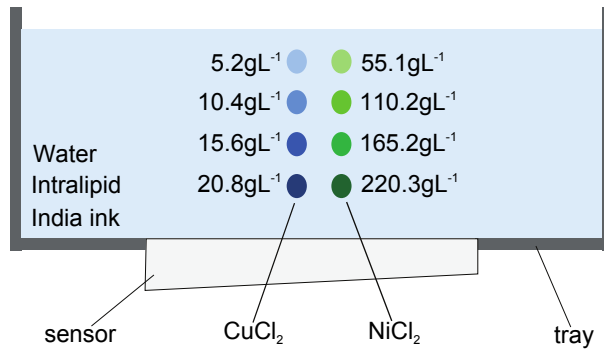


Figure 5.5: A cross-section of the experimental phantom which consisted of eight tubes filled with different concentrations of CuCl_2 (left column) and NiCl_2 (right column). The centre of the tubes were positioned at depths 1.0mm, 2.7mm, 4.4mm and 6.1mm in a scattering and absorbing background solution of water, 1% (w/v) Intralipid and India ink. The distance between the water surface where the phantom was illuminated and the acoustic sensor at the bottom of the tray was 7.3mm.

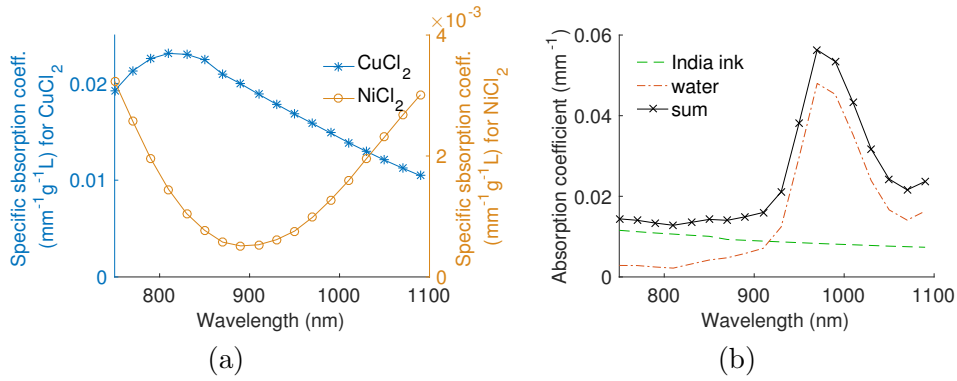


Figure 5.6: (a) The specific absorption coefficient of CuCl₂ (asterisks) is approximately one order of magnitude larger than that of NiCl₂ (circles). (b) The crosses indicate the absorption of the background solution, which is the sum of the absorption coefficients of water (dash and dotted curve) and India ink (dashed curve). The absorption of the Intralipid is negligible in this wavelength range. The absorption spectra of CuCl₂, NiCl₂ and India ink are based on spectrophotometer measurements (Lambda 750S, Perkin Elmer), and the absorption spectra of water was published by Kou *et al* [50]. Reprinted with permission from Ref. [212].

The tubes were submerged at depths between 1.0mm and 6.1mm in a background solution containing India ink (951 black, Winsor & Newton) and 1% (w/v) Intralipid diluted in deionized water, such that they provide an absorption of approximately 0.013mm⁻¹ at 810nm and a scattering coefficient of approximately 1mm⁻¹, which are comparable to realistic values in soft tissue [160]. The Grüneisen parameter of CuCl₂ and NiCl₂ are both known to scale with their concentrations such that

$$\Gamma_i = \Gamma_{H_2O}(1 + \beta_i c_i), \quad i = \text{CuCl}_2 \text{ or } \text{NiCl}_2 \quad (5.11)$$

where the β_i coefficients are $5.80 \times 10^{-3}\text{Lg}^{-1}$ and $2.25 \times 10^{-3}\text{Lg}^{-1}$ for CuCl₂ or NiCl₂ respectively [213], c_i denotes the concentrations of CuCl₂ or NiCl₂, and Γ_{H_2O} is the Grüneisen parameter of water, which is 0.12Lg^{-1} at 22°C [214].

5.4.1.2 Image acquisition

The image acquisition system relies on a planar Fabry-Perot interferometer (FPI) sensor [78] for ultrasound detection. As discussed in Sec. 2.4.3, the FPI sensor has the advantages of being transparent to the excitation light and its sensitivity does not decrease with smaller detecting element size. The FPI is formed by two dielectric dichroic

mirrors, between which a Parylene C polymer spacer is sandwiched. The FPI is supported on a wedged polymethylmethacrylate (PMMA) backing stub. When an ultrasound wave generated in the phantom propagates to the sensor, it modulates the optical thickness of the FPI, leading to a small optical phase shift, and hence changes its optical reflectivity. Thus, by scanning the surface of the FPI with an interrogation laser and recording the reflected intensity, a time varying spatial mapping of the photoacoustic signals is generated. The sensor interrogation beam has an energy of approximately 10mW and is provided by a fibre-coupled tunable continuous wave (CW) laser. It is focused onto the FPI at normal incidence, and directed by a pair of galvanometer mirrors to surface-scan the sensor point-by-point. The sensitivity of the sensor is maximised by tuning the wavelength of the interrogation beam to the point of maximum slope of the interferometer transfer function, which describes the reflectivity of the sensor as a function of the optical phase shift. Provided that this optimal wavelength is used, the phase shift generated by the acoustic modulations of the optical thickness of the FPI is linearly converted to a corresponding change in the reflected light intensity. The optimal interrogation wavelength is position dependent because the optical thickness of the FPI is not spatially homogeneous. Therefore, the tuning procedure is performed for each scanning point and the optimal wavelengths are stored for the image acquisition.

The excitation light source is a tunable optical parametric oscillator (OPO) system (SpitLight 600 OPO, InnoLas Laser GmbH), which produces laser pulses of 6ns duration and at a repetition rate of 30Hz. The idler output of the laser was coupled into an optical fibre and the beam was homogenised by forcing sharp turns in the fibre. The tip of the fibre was positioned vertically above the phantom, creating a beam diameter of approximately 10mm at the surface of the phantom. The pulse energy at the tip of the fibre was measured to be 7-13mJ depending on wavelength. A small fraction of the excitation light was reflected into an integrating sphere with a photodiode to measure the fluctuations of pulse-to-pulse laser energy during image acquisition, which was used to normalise the measured photoacoustic signals.

The image acquisition procedure is as follows: the interrogation laser tunes to the optimal wavelength for the first scanning point, and starts recording the reflected beam intensity when it is triggered by the firing of the excitation laser pulse. It then moves to the next scanning point and tunes to the corresponding optimal wavelength. This is

repeated until all points along a 20mm line with $10\mu\text{m}$ step size have been interrogated, such that 2D images of the cross-section of the tubes can be reconstructed. The images were acquired at 18 equally spaced wavelengths between 750nm and 1090nm.

5.4.2 Numerically simulated photoacoustic images

Using the same structure and chromophores as the experimental phantom, a total of 37 sets of simulated 2D multiwavelength photoacoustic images were generated to assess the performance of ICA for different levels of absorption. The structure of the numerical phantom is shown in Fig. 5.7. The main differences to the experimental phantom are the absence of the tube walls and the fact that the India ink and Intralipid are also present within the tubes. The concentration ratios of 1:2:3:4 between the tubes in each column, as well as the tenfold ratio between the CuCl_2 and NiCl_2 concentrations were kept constant for all simulated data sets, while the absolute concentrations of CuCl_2 and NiCl_2 were varied in different ways in three case studies:

Case I consists of 15 data sets, where the concentrations inside the tubes were increased such that the average absorption coefficient of all tubes increased from 0.05mm^{-1} to 0.75mm^{-1} at 810nm in equal steps. The ink concentration was kept constant for all data sets such that its absorption coefficient is the same as shown in Fig. 5.6(b).

Case II consists of 11 data sets, where the concentration of the ink was increased such that the absorption coefficient of the background solution at 810nm was increased from 0.003mm^{-1} to 0.20mm^{-1} . The CuCl_2 and NiCl_2 concentrations inside the tubes were kept constant at the same values as the experimental phantom, such that the average absorption of the tubes was 0.25mm^{-1} at 810nm.

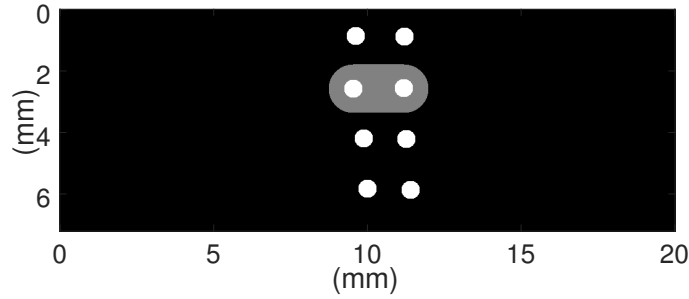


Figure 5.7: The structure of the numerical phantom. The white circular regions represent the tubes and the gray region represents the additional region with increasing CuCl_2 concentration in Case III.

Case III aims to investigate the impact of spatially inhomogeneous absorption in the background. A region containing CuCl_2 which surrounded two of the tubes was included, as shown in Fig. 5.7. The CuCl_2 concentration in this region was increased such that its absorption coefficient was increased from 0.015mm^{-1} to 0.362mm^{-1} at 810nm in 11 data sets. The concentrations of the chromophores outside this additional region were kept constant at the same values as the experimental phantom.

The absorption coefficient was calculated for the same 18 wavelengths as the experimental phantom for each data set based on the chromophore concentrations and their known specific absorption coefficients. The reduced scattering coefficient was kept the same as the experimental phantom for all data sets. Based on the distribution of the absorption and reduced scattering coefficients, the fluence was modelled based on the DA using FEM with the MATLAB software package TOAST++ [202] for a 10mm wide Gaussian light source at the top of the phantom. The computational mesh consists of square elements with a $20\mu\text{m}$ spacing, creating a domain size of $7.4 \times 20.0\text{mm}^2$ for the simulated images. The initial pressure was found by multiplying the modelled fluence by the optical absorption coefficient and the Grüneisen parameter.

The photoacoustic wave propagation from the initial pressure distribution was modelled using the MATLAB toolbox *k*-Wave [70] based on a *k*-space pseudospectral method (Sec. 2.3). The time varying photoacoustic pressure was recorded at the bottom edge of the numerical phantom.

5.4.3 Image reconstruction and fluence adjustment

Both the experimental and simulated images were reconstructed using the time-reversal method [89] (Sec. 3.1) which back-propagates the recorded time series of the photoacoustic pressure into the image domain to form an image of the initial pressure. Gaussian noise with standard deviation equal to 3% of the peak intensity of data set in Case I with the same concentrations as the experimental phantom were added to all simulated images. An approximate fluence adjustment was performed by dividing the reconstructions of the initial pressure by the estimation of the fluence, $\check{\Phi}$. The simple exponential decay fluence model in Eq. 2.10 was chosen as $\check{\Phi}$, such that

$$\check{\Phi}(z, \lambda) = \Phi_0 \exp(-\mu_{eff}(\lambda)z), \quad (5.12)$$

where z is the depth from the illuminated surface, Φ_0 is the known fluence at the illuminated surface, μ_{eff} is the effective absorption coefficient given by $\mu_{eff} = \sqrt{3\mu_a(\mu_a + \mu'_s)}$, and where the μ_a and μ'_s are assumed to be known and equal to that of the background solution. As discussed in Sec. 2.1.4, this 1D fluence model is derived from the DA based on the simplifying assumptions that the medium is a semi-infinite optically homogeneous slab illuminated by infinitely wide plane waves. The exponential fluence adjustment is chosen in this study because it can be applied straightforwardly in practice for *in vivo* photoacoustic images, with μ_{eff} estimated as an average parameter for the tissue. The fluence correction step is necessary for obtaining accurate estimates of the relative chromophore concentrations, but it is important to emphasise that it is still an approximate method and does not fully remove the fluence distortion.

The fluence adjustment amplifies the noise in the regions away from the light source where the values of $\check{\Phi}$ are small. To avoid this, a 6.5×6.5 mm region of interest in the fluence adjusted experimental images was decomposed using ICA and SI. Figure 5.8 shows the raw experimental images (top row), the fluence estimations (middle row) and the fluence adjusted images (bottom row). The raw images at 750nm and 1090nm show higher intensity for the right column of tubes containing NiCl_2 , while the image acquired at 810nm shows higher intensity for the left column of tubes containing CuCl_2 . These trends are expected based on the specific absorption coefficients of the chromophores. The streak artefacts extending from the tubes, the distortion of the circular shapes

of the tubes and the pixels with negative values are limited-view artefacts. They are caused by the limited detection aperture of the planar sensor detection geometry, where only the solid angle subtended by the edges of the detection line of the acoustic wave front is captured. The bottom row of figures show that after the fluence adjustment, the image intensity at the tubes increases with depth, which is expected as the chromophore concentrations are higher inside the deeper tubes. The negative values in the images lack physical meaning, and were therefore set to zero before further processing.

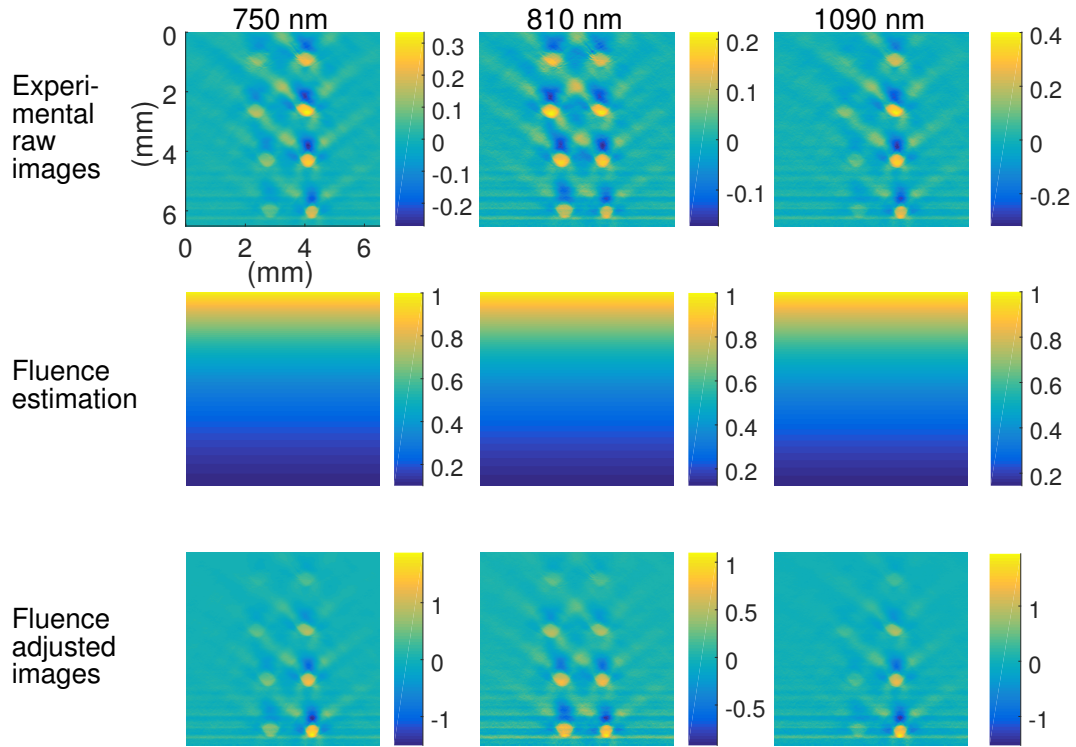


Figure 5.8: The experimental photoacoustic images of the tube phantom acquired at three different wavelengths (top row), the fluence estimations based on the 1D exponential decay (middle row), and the fluence adjusted photoacoustic images (bottom row). The fluence adjusted images are more similar to the expected absorption coefficients than the raw images.

5.4.4 Preprocessing for FastICA

The FastICA algorithm requires further pre-processing of the multiwavelength fluence adjusted images before unmixing.

Mean subtraction The first preprocessing step is to centre the data around zero by subtracting the mean of all images. The mean subtraction is necessary because the Gaussianity measure in Eq. (5.10) is based on the assumption that the data have zero-mean and unit variance. The unit variance requirement is fulfilled in the next preprocessing step. Due to the mean-subtraction, the estimated \mathbf{S} in Eq. (5.8) will also have zero-mean. To recover the mean, \mathbf{WM} is added back to the unmixed sources \mathbf{S} , where \mathbf{M} represents the mean matrix that was initially subtracted.

Whitening The data is said to be whitened when the images at different wavelengths are uncorrelated with each other and each have variances of one. To whiten the data, we first find the eigenvalue decomposition (EVD) of the covariance matrix, $E\{\check{\mathbf{P}}\check{\mathbf{P}}^T\}$. The EVD is given by $E\{\check{\mathbf{P}}\check{\mathbf{P}}^T\} = \mathbf{Q}\mathbf{D}\mathbf{Q}^T$, where \mathbf{Q} is the $(N \times N)$ square matrix whose columns are the eigenvectors of $E\{\check{\mathbf{P}}\check{\mathbf{P}}^T\}$, and \mathbf{D} is a diagonal matrix whose diagonal elements are the eigenvalues d_n so that $\mathbf{D} = \text{diag}(d_1, d_2, \dots, d_N)$. The matrix \mathbf{Q} is the decorrelation matrix, and it is used in principal component analysis (PCA) to find the decorrelated data, which are known as the principal components (PC) and given by $\mathbf{Q}^T\check{\mathbf{P}}$. The variances of the PCs are not uniform. In fact, the covariance matrix of decorrelated data is equal to a diagonal matrix where the diagonal entries are equal to the eigenvalues d_1, d_2, \dots, d_N . Therefore, the matrix of eigenvalues \mathbf{D} can be used to scale the data such that the variances are unity. The whitening process is thus given by

$$\tilde{\mathbf{P}} = \mathbf{D}^{-1/2}\mathbf{Q}^T\check{\mathbf{P}}, \quad (5.13)$$

where $\tilde{\mathbf{P}}$ denotes the whitened data and $\mathbf{D}^{-1/2} = \text{diag}(d_1^{-1/2}, d_2^{-1/2}, \dots, d_N^{-1/2})$. Essentially, the whitening process involves first performing PCA, which decorrelates the measured images, and then scaling the decorrelated components to have unit variance.

Dimension reduction The ICA algorithm will attempt to find as many independent components as the number of measurements, N . However, in photoacoustic imaging, it is common that there are more multiwavelength images available than the number of chromophores, i.e. $N > K$. As a result, many of the estimated components will represent mainly noise. To avoid this, the dimensions of the data are reduced prior to the unmixing by discarding the PCs with small eigenvalues. This is achieved by retaining

the first L entries in \mathbf{D} and columns in \mathbf{Q} , such that the dimensions are reduced at the same time as the whitening is performed in Eq. (5.13). In this chapter, L is set to three unless stated otherwise, such that FastICA will decompose the data into three independent components.

5.5 Unmixing using ICA and SI

The fluence corrected and pre-processed multiwavelength image data are the input to the FastICA algorithm, and the output is \mathbf{S} , which represents the estimated values of the Grüneisen parameter multiplied by the concentrations, $\mathbf{S} \approx \mathbf{\Gamma} \circ \mathbf{C}$. As mentioned in Sec. 5.3.1, the ordering of the estimated independent components is arbitrary. However, the estimated spectra in the mixing matrix resemble the true absorption spectra (an example is shown in Fig. 5.9). Therefore, the output components are identified to the corresponding chromophores by calculating the sum of squared differences between the normalised columns in the estimated mixing matrix and the normalised known absorption spectra of the chromophores of interest.

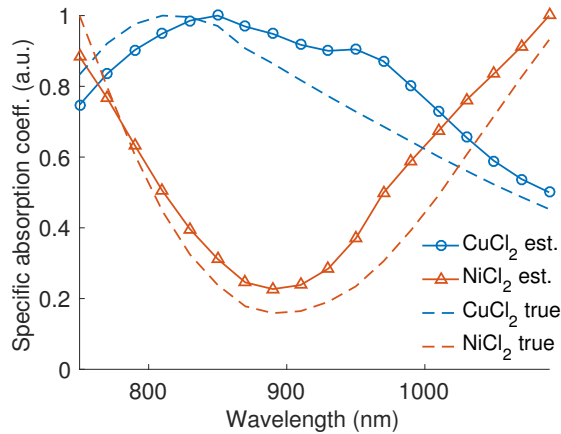


Figure 5.9: The estimated spectra in \mathbf{W} for CuCl_2 (circles) and NiCl_2 (triangles) are shown with solid curves for a data set in Case I where the average absorption of the tubes at 810nm is 0.4mm^{-1} . The estimated spectra resemble the true spectra of these chromophores, which are shown with dashed curves.

The fluence corrected (but not pre-processed) images $\check{\mathbf{P}}$ were also unmixed using SI, based on the known specific absorption spectra of CuCl_2 , NiCl_2 and the background solution, for the purpose of comparison with the ICA results.

5.5.1 Accuracy as a function of absorption

In this section, the fluence adjusted simulated photoacoustic images were unmixed using ICA and SI to analyse their accuracy for various levels of absorption. The unmixed components were normalised to their average value at the tube with the highest concentration of the relevant chromophore. The normalised components were compared to the expected normalised components, which are the true concentrations of the relevant chromophores multiplied by the Grüneisen parameter. The absolute difference between the estimated and expected normalised components at each pixel defines the error map. Three types of errors are defined based on the error maps to provide a quantitative assessment of the accuracy of the unmixing methods:

1. The concentration error, δ_c , is defined as the average error at the pixels in the tubes where the chromophore of interest is present.
2. The average error at the tubes where the relevant chromophore is absent is defined as the “false positive” error, δ_f .
3. The background error, δ_b , is the average error outside the eight tubes.

For example, in the estimated CuCl_2 component, δ_c is the average error at the left column of tubes, δ_f is the average error at the right column of tubes and δ_b is the average error outside the tubes. For Case III, the error at the additional region is included in the definition of δ_c and δ_f .

The errors were calculated for each data set in the three Cases. The three types of errors are plotted in Fig. 5.10 as functions of the average absorption of the tubes at 810nm, μ_a^{tubes} , for Case I (top row), the absorption of the background solution at 810nm, μ_a^{bkg} , for Case II (middle row), and the absorption of the additional region at 810nm, μ_a^{add} , for Case III (bottom row). The errors of ICA and SI are shown with dots and asterisks respectively.

In Case I, the δ_c error for SI increases with μ_a^{tubes} at a nearly constant rate for the whole range of absorptions between 0.05mm^{-1} and 0.75mm^{-1} . This is expected as the estimated fluence is based on an optically homogeneous region, and therefore the accuracy of $\check{\Phi}$ is reduced for increasing μ_a^{tubes} . The δ_f and δ_b of SI errors remain below 7% for this entire range of absorption. All three types of errors for ICA are

$>10\%$ for $\mu_a^{tubes} < 0.15\text{mm}^{-1}$ in Case I. The large errors at low absorption may be due to the lower SNR, which leads to the first three PC containing a smaller fraction of the total variance of the data (see Sec. 5.5.2). When μ_a^{tubes} is increased beyond 0.15mm^{-1} , the errors of ICA are comparable to SI for the data points with relatively low μ_a^{tubes} . As μ_a^{tubes} is further increased, ICA results in smaller δ_c than SI. However, when $\mu_a^{tubes} > 0.55\text{mm}^{-1}$, the performance of ICA abruptly deteriorates as the errors increase to large values beyond the scale of the plots. This is because beyond this threshold, the accuracy of the fluence estimation is sufficiently low to lead to non-linearities so severe that the independent components found by ICA cannot be correctly identified to the relevant chromophores based on the estimated absorption spectra, hence resulting in a significant increase in errors. This absorption level is comparable to that of blood, which is 0.46mm^{-1} at 810nm [160] (assuming a total haemoglobin concentration of 150gL^{-1} and 100% oxygenation). The blue circles show the errors that would have been obtained if the correct components were manually selected. This manual selection may not be possible in practical applications because prior knowledge of the expected chromophore distribution may not be available.

In Case II, accurate unmixing with all three types of errors $\lesssim 10\%$ were obtained for $\mu_a^{bkg} < 0.06\text{mm}^{-1}$ at 810nm using ICA, and $< 0.10\text{mm}^{-1}$ using SI. When μ_a^{bkg} is increased further, the errors for both unmixing methods increase rapidly. However, these thresholds are significantly higher than the absorption coefficient of the common types of biological tissue, which is typically $\approx 0.01\text{mm}^{-1}$ at 810nm [160].

The performance of both ICA and SI is dependent on the accuracy of the fluence adjustment, which in this study is mainly determined by the level of spatial inhomogeneity in the optical properties of the phantom. This is highlighted by the fact that both methods fail to produce accurate results in the presence of the additional region with increasing concentration of CuCl_2 in Case III, where the errors increase with μ_a^{add} .

5.5.2 Component selection

The thresholds above which the independent components cannot be identified to the correct chromophores can potentially be shifted towards higher absorption levels if the multiwavelength image data are decomposed into fewer independent components. This can be realised by keeping fewer PCs in the preprocessing stage to reduce the dimensions

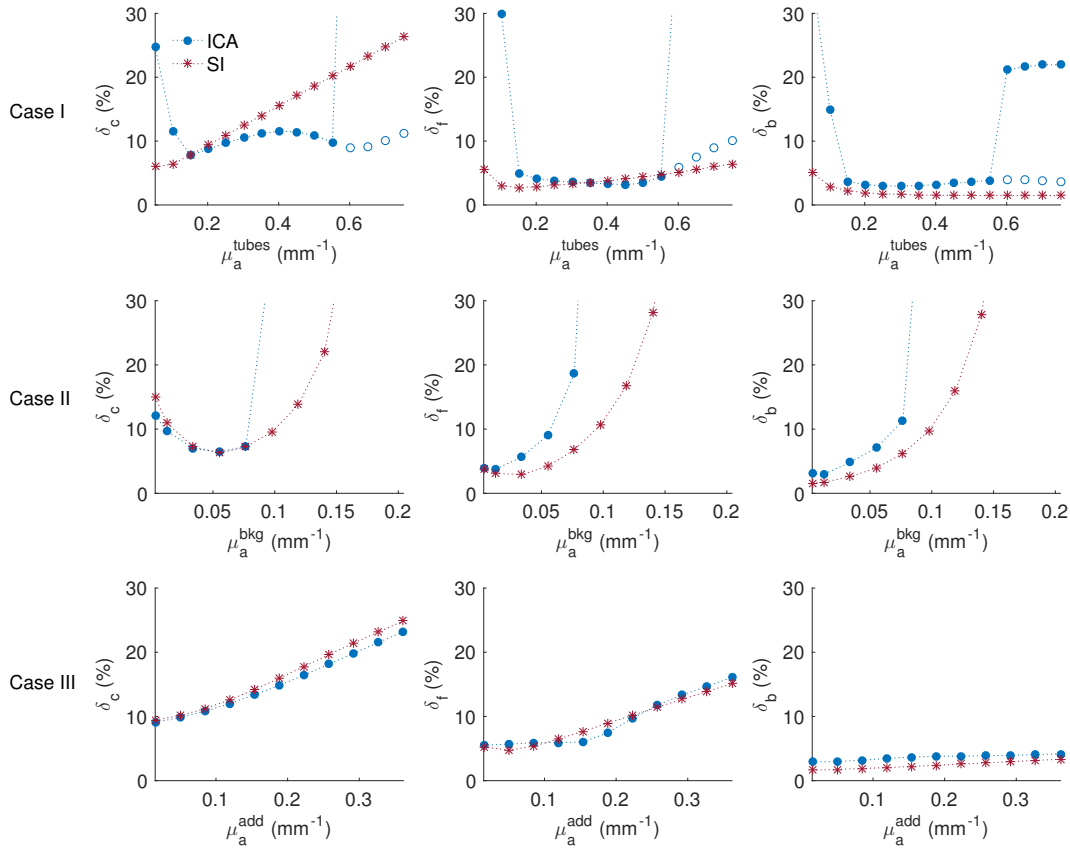


Figure 5.10: The left, centre and right columns of plots show the δ_c , δ_f and δ_b errors respectively for the chromophore components unmixed from the simulated images from Case I (top row), Case II (middle row) and Case III (bottom row) using ICA (dots) and SI (asterisks). The x-axis indicates the average absorption of the eight tubes for Case I, the absorption of the background solution for Case II, and the absorption of the additional region with CuCl_2 for Case III, all at 810nm. For Case I, the δ_c error for ICA is $\lesssim 10\%$ for μ_a^{tubes} between 0.15mm^{-1} and 0.55mm^{-1} , while the δ_c error for SI increases approximately constantly with μ_a^{tubes} . The circles indicate the ICA errors for manual selection of the corresponding components. Case II shows that the errors associated with ICA and SI are both relatively low for physiologically realistic range of absorption in the background tissue. The δ_c and δ_f errors in Case III increase with the absorption in the additional region for both ICA and SI.

of the data.

Figure 5.11 shows the δ_c , δ_f and δ_b errors from unmixing the images in Case I with ICA using two, three or four PCs. The results show that if only two PCs were processed with ICA, the unmixed independent components can be correctly identified as CuCl_2 or NiCl_2 for the full range of absorption levels investigated in Case I, and no abrupt increase in error is observed. However, using only two PCs also results in larger unmixing errors for the higher absorption levels. When four PCs are used, the error trends are similar to using three PCs, but a slight lower shift of the range of the absorption in which ICA results in accurate unmixing is observed. This shift may be explained by the fact that, when the main features in the image have lower contrast, a smaller fraction of the total variance of the data is included in the first three PCs.

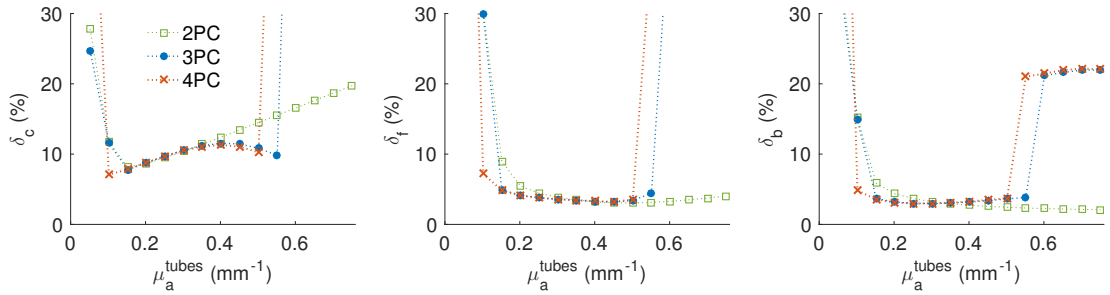


Figure 5.11: The δ_c , δ_f and δ_b errors of the unmixed components when two, three or four PC are further processed with ICA. Using two PC (squares) results in larger δ_c for higher absorption, but no abrupt increase in errors is observed. The range of absorption in which ICA leads to accurate unmixing is shifted to lower absorption when four PC (crosses) is used instead of three (dots).

5.5.3 Experimental images and wavelength selection

The experimental images were acquired at 18 wavelengths ($N = 18$) over a spectral range where the absorption spectra of the chromophores have distinct features. However, in *in vivo* imaging applications, it may be necessary to reduce N , and some chromophores in the tissue may have flatter and/or less unique absorption spectra. To simulate such a scenario, ICA and SI were applied on images of smaller sets of wavelengths where N was reduced by removing the images of the longest wavelengths, such that in the final inversion (the inversion with the fewest wavelengths) only the images at the wavelengths 750, 770 and 790nm were used. Of course, when reducing the number of wavelengths in practice, one would choose wavelengths that are more spread out for these particular

chromophores. Here, the wavelengths were removed from the longest to investigate how the unmixing methods deal with poorly conditioned absorption spectra. The unmixed components were normalised and the errors δ_c , δ_f and δ_b are found in same way as for the simulated images.

The three types of errors are plotted as a function of N used in ICA and SI in Fig. 5.12. When the full set of 18 wavelengths are used, both methods result in accurate unmixing with the δ_c , δ_f and δ_b errors equal to 11%, 4% and 3% for ICA, and 10%, 5% and 3% for SI. This result is in agreement with the simulated data which showed high accuracy for lower absorption levels for both ICA and SI. The high accuracy is maintained for the inversions using $N > 10$. When N is further reduced, the accuracy of SI rapidly deteriorates, while the errors associated with ICA remain relatively low. An example of the unmixed components is shown in Fig. 5.13, where $N = 6$. Both the CuCl_2 and NiCl_2 components are estimated accurately with ICA. SI, on the other hand, is able to unmix the NiCl_2 component with relatively low errors, but its estimate of the CuCl_2 component is noisy and contains large errors.

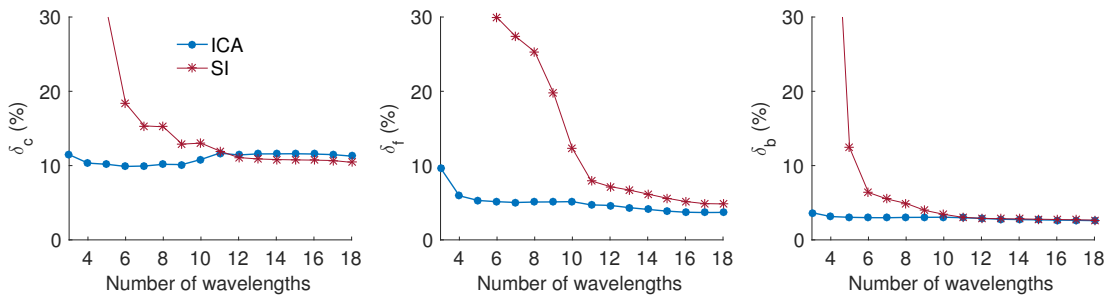


Figure 5.12: The δ_c , δ_f and δ_b errors of the unmixed components using different number of wavelengths for ICA and SI. The SI errors increase significantly when less than 10 wavelengths are used, while the errors of ICA remain relatively low.

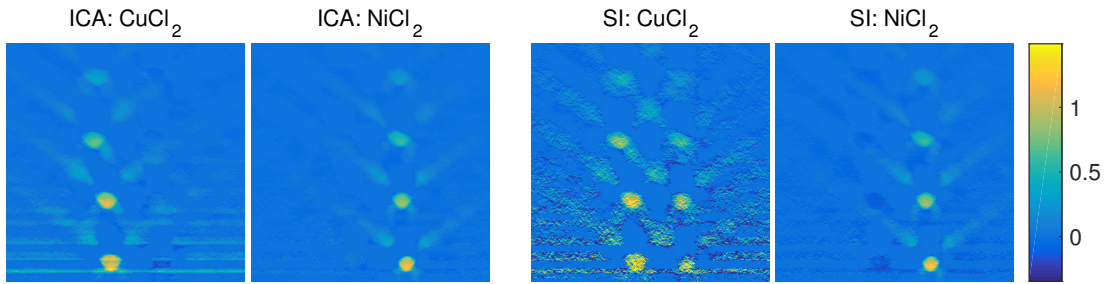


Figure 5.13: The estimated components corresponding to CuCl_2 and NiCl_2 using ICA and SI when the six shortest wavelengths are used. The components are normalised to the average of the estimated concentration at bottom tube containing the relevant chromophore. The CuCl_2 component estimated using SI contains large cross-talk errors, while both components are estimated relatively accurately with ICA.

Two key factors are likely to affect the unmixing results when the longer wavelengths are removed. Firstly, due to the spectral variation in the absorption of the contrast agents in the tubes and the background solution, the fluence correction is more accurate for some wavelength combinations than others. This results in variations in the accuracy of SI when certain wavelengths are excluded. Secondly, the condition number of the known mixing matrix increases by several orders of magnitude when $N < 5$, as shown in Fig. 5.14. Therefore, the fact that the inversion is more ill-conditioned is likely to be the dominant cause of the large errors of SI for the inversions where $N < 5$. However, both these factors affect ICA less significantly. As shown with the simulated image data in Sec. 5.5.1, ICA is more robust against non-linearities caused by poor fluence correction, and therefore the errors of ICA remains low when wavelength range changes. Furthermore, the low errors of ICA when $N < 5$ suggest that unmixing based on statistical independence can potentially be used to obtain accurate separation of the chromophores when SI performs poorly due to the ill-conditioning of the mixing matrix. This is possible because ICA does not rely on the known spectra for unmixing, and can therefore tolerate ill-conditioning better than SI.

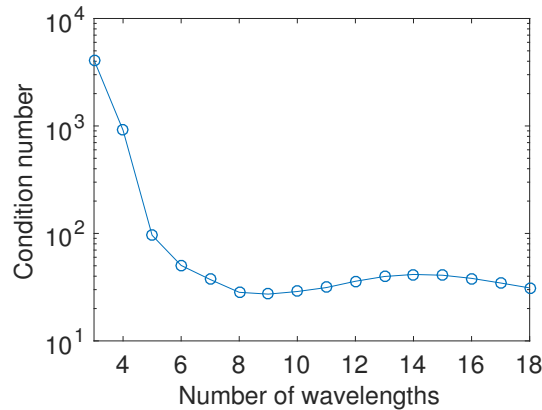


Figure 5.14: The condition number of the matrix \mathbf{A} with the known specific absorption spectra as a function of number of wavelengths as the wavelengths are reduced from the longest.

5.6 Summary and discussion

This study demonstrates that ICA can be used to unmix the chromophores to a useful degree of accuracy under certain conditions, provided that a simple exponential fluence correction, which is straightforwardly applicable in practice, has been performed. Experimental and numerical phantoms were designed for which the assumptions underlying both ICA (statistical independence) and SI (full rank molar absorption coefficient matrix) were true. Either approach would therefore give accurate results for a perfect fluence correction. When using the approximate, but practical, fluence correction (Eq. (5.12)), it was shown that ICA results in smaller unmixing errors compared to SI in two circumstances: Firstly, when the absorption level of the contrast agents is approximately $0.4\text{--}0.5\text{mm}^{-1}$, ICA is more robust against non-linearities caused by inaccurate fluence estimation than SI, because it allows the mixing matrix to vary in order to produce the most independent components. Secondly, when the mixing matrix with the known absorption spectra is more ill-conditioned, ICA provides significantly more accurate results as it avoids using the fixed mixing matrix by searching for the chromophore components based on their statistical independence instead. This may be useful for applications where the chromophore of interest has relatively flat/featureless absorption spectrum, for example the tyrosinase-expressing cells in Ref. [209].

When the average absorption of the features of interest is higher than a certain threshold (which in this particular phantom is at 0.55mm^{-1}), leading to greater dif-

ferences between the estimated and the true fluence, the errors of ICA were shown to abruptly increase as the output components corresponding to the chromophores of interest could not be identified by comparing the estimated spectra with the known. This suggests that, with sufficient SNR, ICA can provide accurate unmixing for absorptions up to a threshold. The threshold will likely be dependent on the absorption spectra, the spatial structure of the chromophores and the accuracy of the fluence adjustment. Given the potential presence of these upper absorption thresholds under which ICA provides relatively low errors, it would be ideal to use lower concentrations of contrast agents. This would require the imaging system to have high sensitivity in order to obtain sufficient SNR.

ICA is a suitable unmixing method that is robust to the small errors in the fluence correction that are unavoidable in practical scenarios, provided that the chromophores are known to be mutually statistically independent. This assumption is valid for the chromophores in the phantoms used in this study, and in applications such as unmixing some exogenous contrast agents from the tissue in the background. However, the independence criterion is not always fulfilled for all tissue chromophores, hence limiting the range of applications of ICA.

The number of components that will be estimated is fixed in SI and determined by the dimensions of the spectral matrix, which is equal to the number of chromophores. This study showed that in ICA, it is not straightforward to choose how many independent components the multiwavelength images should be decomposed into. Since larger dimensionality leads to difficulty in identifying the components as chromophores, one should ideally retain the minimum number of PC that contains a sufficient fraction of the total variance to explain the data well. In this study, PC representing $>75\%$ of the variance needed to be kept for further processing with ICA to provide accurate results. However, there are no general guidelines based on theoretical principles for the optimal choice of dimension reduction.

As discussed in Sec. 5.3.1, the magnitude of the independent components estimated using ICA is arbitrary because both \mathbf{W} and \mathbf{S} are unknown. However, some prior knowledge often exists for the absorption spectra of the chromophores. These known specific absorption spectra can potentially be used to fix the magnitude of the independent components, such that the relative concentration between different chromophores

are scaled correctly, and hence reducing ambiguities of ICA. One simple approximate scaling method would be to divide the estimated independent components by a scaling factor equal to the ratio between the mean of each estimated spectrum and the corresponding known spectrum.

5.7 Conclusion

In conclusion, ICA offers a fast and simple alternative to unmixing multiwavelength photoacoustic images into components representing individual chromophores, provided that the spatial distributions of the chromophore concentrations are statistically independent. When a first order fluence adjustment has been applied, and the absorption is within certain ranges and relatively spatially homogeneous, ICA can provide accurate quantification of the relative chromophore concentrations. The results of ICA depend on the choice of dimensions retained in the pre-processing step, as accurate results require that the components can be identified as the correct chromophores. It was shown that ICA outperforms SI when mixing matrix is ill-conditioned, and that ICA is more robust to errors in the fluence correction compared to SI.

Chapter 6

Statistical independence in nonlinear model-based inversion

While both SI and ICA can under certain circumstances separate the contributions from individual chromophores, neither of the methods provides a complete solution to the general quantitative problem in photoacoustic imaging. SI can estimate the concentration ratio accurately for oxy- and deoxyhaemoglobin, provided that the wavelengths are suitably chosen. To obtain accurate concentrations relative to other spatial locations, both SI and ICA rely on linearisation, which typically requires that the optical properties are close to spatially homogeneous. For cases where simple approximate fluence models cannot provide a sufficiently accurate fluence correction, more sophisticated inversion methods that incorporate an accurate fluence model are required. These methods are typically computationally more demanding and are less robust to experimental errors compared to simple linear methods, and therefore not commonly used in *in vivo* imaging studies. In this chapter, we propose incorporating a measure of the statistical independence of the chromophore concentrations in a nonlinear model-based inversion scheme. This aims to exploit the intrinsic statistical property of the chromophores in order to reduce the model-mismatch errors in experimental settings, and hence improve the practical applicability of the model-based inversion method.

Section 6.1 outlines the principles of model-based inversion and explains why they are challenging to implement in practice. Section 6.2 presents the proposed model-based inversion scheme where the statistical independence is incorporated. It describes properties of the mutual information (MI) term in the error functional (Sec. 6.2.1), the kernel

estimator for the MI (Sec. 6.2.2), the gradient of the MI with respect to the chromophore concentrations (Sec. 6.2.3) and the implementation of the calculations (Sec. 6.2.4). Section 6.3 describes the generation of the experimental and numerical simulated multi-wavelength images of tissue mimicking phantoms. The result of the quantification using model-based inversion with MI is presented and compared to the standard model-based inversion in Sec. 6.4. Section 6.5 discusses the results and conclusions are presented in Sec. 6.6.

The journal article in Ref. [221] (DOI: [10.1364/BOE.8.005297](https://doi.org/10.1364/BOE.8.005297)) has been modified and adapted to form parts of this chapter, with reprint permission under [CC BY 4.0 License](https://creativecommons.org/licenses/by/4.0/).

6.1 Model-based inversion for QPAT

Nonlinear model-based inversion was introduced in Sec. 3.2.3.2. The key steps are repeated below and the challenges of the practical implementations are discussed.

The first step in the model-based inversion method is to make an initial guess for the unknown variables, which are represented with the vector \mathbf{u} . We focus on the multiwavelength case (Sec. 3.2.3.3.2), where the unknown variables are typically the chromophore concentrations and the scattering amplitude, such that $\mathbf{u} = [\mathbf{c}_1, \dots, \mathbf{c}_{K_t}, \mathbf{a}]$. The total number of chromophores is denoted with K_t (the subscript t is used to distinguish from the number of statistically independent chromophores, which is denoted with K in this chapter). The unknown quantities \mathbf{c}_k and \mathbf{a} are vectors with each element representing a voxel, such that $\mathbf{c}_k = [c_{k,1}, c_{k,2}, \dots, c_{k,M}]$ and $\mathbf{a} = [a_1, \dots, a_M]$, where M denotes the total number of voxels. The absorption coefficient and the scattering coefficient are calculated based on the initial guess and using $\mu_a = \sum_k \alpha_k c_k$ (Eq. (2.1)) and $\mu'_s = a\lambda^{-b}$ (Eq. (3.11)), where α_k is the specific absorption spectra and b is the wavelength dependence of the scattering. Both α_k and b are assumed to be known. The fluence, ϕ , is then modelled using the DA or the RTE for the distribution of the absorption coefficient and the scattering coefficient. Using the modelled fluence, the absorption coefficient and the Grüneisen parameter, Γ , the modelled initial pressure $p_{0,m,\lambda_n}^{model}$ at voxel m and wavelength λ_n is calculated using (Sec. 2.2)

$$p_{0,m,\lambda_n}^{model} = S\Gamma_m \phi_{m,\lambda_n} \mu_{a,m,\lambda_n}, \quad (6.1)$$

where S is the system calibration factor that depends on the acoustic response of the sensors, which can typically be assumed to be spatially homogeneous and independent of the optical wavelength. The data error to be minimised, ε_d , is defined as the sum of squared differences between the modelled and the measured initial pressure, p_{0,m,λ_n}^{meas} , such that

$$\underset{\mathbf{u}}{\operatorname{argmin}} \varepsilon_d(\mathbf{u}) = \frac{1}{2} \sum_{n=1}^N \sum_{m=1}^M \left[p_{0,m,\lambda_n}^{model}(\mathbf{u}) - p_{0,m,\lambda_n}^{meas} \right]^2, \quad (6.2)$$

where the total number wavelengths is denoted by N . By iteratively updating the values of the unknown variables until ε_d is minimised, accurate quantification can be achieved in an idealised scenario for arbitrary tissue structures. Thus, in theory, the model-based inversion scheme can be used as a general method for recovering the chromophore concentrations in QPAT with relatively little prior information or other restrictive assumptions. However, as discussed in Sec. 3.3.2, the practical implementation of model-based inversion for experimentally acquired images faces challenges including the large computational demand and the presence of model-mismatch errors. In this chapter, we tackle the latter issue of model-mismatch. It refers to the inaccurate forward modelling of $p_{0,m,\lambda_n}^{model}$ which leads to the minimum of the data error occurring at erroneous values of the unknown parameters, and hence results in inaccurate quantification. Model-mismatch can arise due to a number of reasons:

- The DA has been extensively used as the fluence model in nonlinear inversion studies, even though it does not accurately represent the fluence distribution at regions close to the illuminated surface or near the boundaries of the domain.
- Some studies are based on 2D fluence models, even though light propagation in biological tissue occurs in 3D and most biological tissues contain complex 3D structures that extend out of any 2D plane, leading to modelling errors.
- Even when 3D fluence models are employed, due to computational memory restrictions, the modelled domain may be limited to a region of interest smaller than the size of the illuminated region. Therefore, there may be backscattering from outside the domain that is neglected in the model, which may lead to errors.
- There may be inaccuracies in the fixed parameters in the forward model, such as the size and the position of the excitation beam, the absorption spectra and

scattering properties, which are typically determined experimentally.

Most of the above-mentioned problems are practical issues that arise only in experimental settings and are often not taken into account in theoretical or numerical studies of the model-based inversion. Therefore, the model-mismatch may be one of the main issues that contribute to fact that model-based inversion is not commonly implemented in experimental studies. In order to make model-based inversion more applicable for experimental images, we propose reducing the errors due to model-mismatch by exploiting the intrinsic statistical properties of the chromophore distributions which do not depend on the forward model. This approach is described in the next section.

6.2 Model-based inversion with statistical independence

The concept of utilising the statistical independence between the chromophores to improve the accuracy of model-based inversion in the presence of model-mismatch is illustrated in Fig. 6.1. In the idealised scenario, where the model is perfectly accurate, the minimum of the error functional consisting of the data error only (Eq. (6.2)) occurs at the true solution, as shown in Fig. 6.1(a). Figure 6.1(b) illustrates that the presence of experimental uncertainties in the model parameters and other inaccuracies in the fluence model causes the minimum of the error functional to shift away from the true solution, and occurs instead at an erroneous solution. Unlike the data error, the statistical independence is a property of the distribution of the chromophores alone, rather than a function of the forward modelling. Therefore, the errors in the fluence model due to the issues mentioned in the previous section do not affect the MI between the chromophore concentrations, which will always have a minimum at the true solution, provided that the chromophores are statistically independent. The MI of the independent chromophores is illustrated in red in Fig. 6.1(c). Hence, by including a term representing the MI between the independent chromophores in the error functional, the quantification errors can be reduced. The new minimisation problem using an error functional, ε_{d+MI} , consisting of both the data error and the MI is given by

$$\underset{\mathbf{u}}{\operatorname{argmin}} \varepsilon_{d+MI}(\mathbf{u}) = \frac{1}{2} \sum_{n=1}^N \sum_{m=1}^M \left[p_{0,m,\lambda_n}^{\text{model}}(\mathbf{u}) - p_{0,m,\lambda_n}^{\text{meas}} \right]^2 + \gamma \check{I}(\mathbf{c}_1, \dots, \mathbf{c}_K), \quad (6.3)$$

where γ is the weight parameter for the MI. The new error functional in Eq. (6.3) is illustrated with blue dashed curve in Fig. 6.1(c), and its minimum occurs closer to the true solution than the data error in Eq. (6.2).

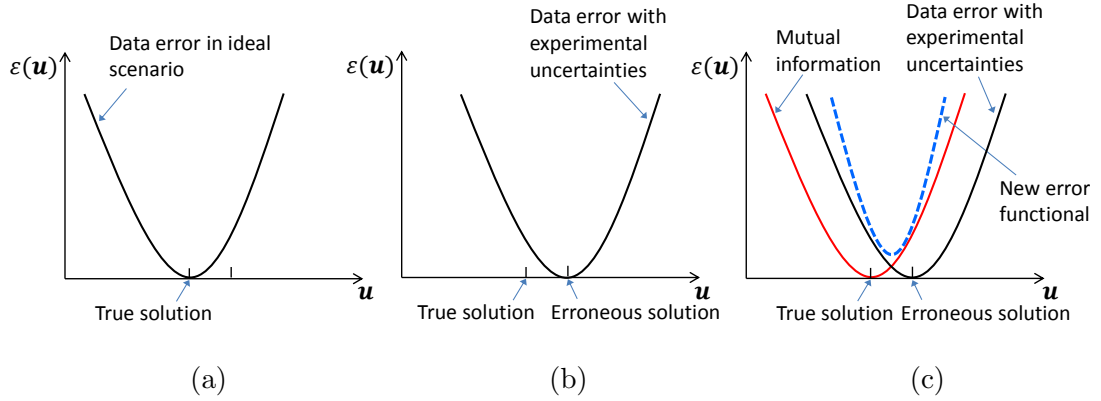


Figure 6.1: (a) The minimum of the data error occurs at the true solution in an idealistic scenario. (b) In the presence of model-mismatch, the minimum shifts toward an erroneous solution. (c) The minimum of the MI is independent of the forward modelling and occurs at the true solution provided that the chromophores are independent (red curve). A new error functional (dashed blue curve) is created by combining the data error and the MI and it has a minimum closer to the true solution compared to the data error alone.

6.2.1 Properties of the MI error term

It is important to understand the differences between the use of statistical independence in ICA, which is a linear unmixing method, and in model-based inversion, which is a nonlinear optimisation scheme. In ICA, the unknown mixing spectra are iteratively updated, and the statistical independence is calculated between the output components, which represents the chromophores whose concentrations are calculated based on the estimated mixing spectra and the linear model in Eq. (5.7). This means that the MI (or other measures of statistical independence) is minimised under the restriction of the linear model – the aim is to find the most independent components that can be linearly unmixed from a given set of measured data. In the model-based inversion using Eq. (6.3), the unknown parameters to be updated are the chromophore concentrations themselves, between which the MI is calculated. Therefore, unlike in ICA, the input into the MI estimation is not restricted by the measured data in any way and may take any value. The measured data is only used in the data error term. Consequently, if the error

functional in Eq. (6.3) consisted only of the MI term, the minimisation could result in spatially homogeneous concentrations which have no information whatsoever and hence also zero MI. It is therefore important to have a suitable weight balance between the terms.

Unlike the data error term, the MI term in the error functional is non-convex and contains many local minima. The local minima exist for the MI term because there are many ways two spatially varying variables can be statistically independent of each other. The true solution occurs at a local minimum that may not necessarily be the global minimum of the MI term. For example, the initial guess of the chromophore concentrations for the model-based inversion is often chosen to be some spatially homogeneous values. This initial guess may have lower MI than the true concentrations in many cases. Nevertheless, the local minima can be avoided with the presence of the data error term, which brings the solution towards to the correct minimum.

6.2.2 Estimating the mutual information

In FastICA, the statistical independence was measured using negentropy, which can be estimated straightforwardly using Eq. (5.9). The use of negentropy was justified based on the Central Limit Theorem, which assumes that the components are linear mixtures of the independent components. In the model-based inversion, however, the input chromophore concentrations for each iteration may take any value that minimise the error functional and are not restricted to being linear sums of the true concentrations. Therefore, MI is used as the independence measure in Eq. (6.3) instead of negentropy.

As indicated in Eq. (5.2), MI depends on the entropy and the joint entropy of the variables, which involves calculating the marginal and joint PDFs. We consider the concentrations of K independent chromophores, $\mathbf{c}_1, \dots, \mathbf{c}_K$, as continuous random variables with the PDFs $\rho_{\mathbf{c}_1}, \dots, \rho_{\mathbf{c}_K}$. The values of the concentration of the k th chromophore at different voxels, $[c_{k,1}, \dots, c_{k,M}]$, are considered the instantiations or “observations” of the random variable. The total number of observations is equal to the number of voxels M . Since the true PDFs of the chromophore concentrations are in general unknown, they need to be estimated based on the observations. The simplest method of estimating the PDF is using the histogram-based approach. The histogram consists of a number of bins that cover the whole range of values that the data points of \mathbf{c}_k take and the probability

density at the centre of each bin is approximated as the fraction of the data points that falls within the relevant bin. Hence, the histogram estimation of the probability density of \mathbf{c}_k at the value ξ_{k,q_k} is given by

$$\check{\rho}_{\mathbf{c}_k}(\xi_{k,q_k}) = \frac{1}{Mh_{hist}} \times (\text{nr. of elements in } \mathbf{c}_k \text{ in the same bin as } \xi_{k,q_k}) \quad (6.4)$$

where h_{hist} is the width of the bins and the subscript q_k is the index of the value at which the PDF is evaluated. The histogram method is useful simple way of estimating the PDFs. However, the gradient of the histogram estimation of the PDF is everywhere zero, except at the edges of each bin, where it is infinite. It is therefore not a suitable estimator for MI in gradient-based optimisations.

To overcome this issue, the kernel estimator, also known as the Parzen window estimator, is used as an alternative method of estimating the PDF. Conceptually, the kernel density estimation method involves placing a smoothly varying spread of values, or kernel, on the value of each data point. Figure 6.2 illustrates this with the random variable \mathbf{y} , which only has seven data points. The data points are $\mathbf{y} = [3, 6, 9.3, 10, 10.4, 12.5, 15]$. The shape of the weights are determined by the kernel function, which in this example is a Gaussian function, as shown with dashed curves. The PDF is estimated as the sum of these weights, as indicated by the solid black curve in Fig. 6.2.

The kernel estimation of the PDF and the joint PDF are given by [215]

$$\check{\rho}_{\mathbf{c}_k}(\xi_{k,q_k}) = \frac{1}{M} \sum_{m=1}^M \kappa(\xi_{k,q_k} - c_{k,m}) \quad (6.5)$$

and

$$\check{\rho}_{\mathbf{c}_1, \dots, \mathbf{c}_K}(\xi_{1,q_1}, \dots, \xi_{K,q_K}) = \frac{1}{M} \sum_{m=1}^M \prod_{k=1}^K \kappa(\xi_{k,q_k} - c_{k,m}), \quad (6.6)$$

where ξ_{k,q_k} is the value at which the PDF is estimated, $c_{k,m}$ are the data points and κ is the kernel function. The kernel function must satisfy

$$\kappa(x) \geq 0 \quad (6.7)$$

and

$$\int_{-\infty}^{\infty} \kappa(x) dx = 1, \quad (6.8)$$

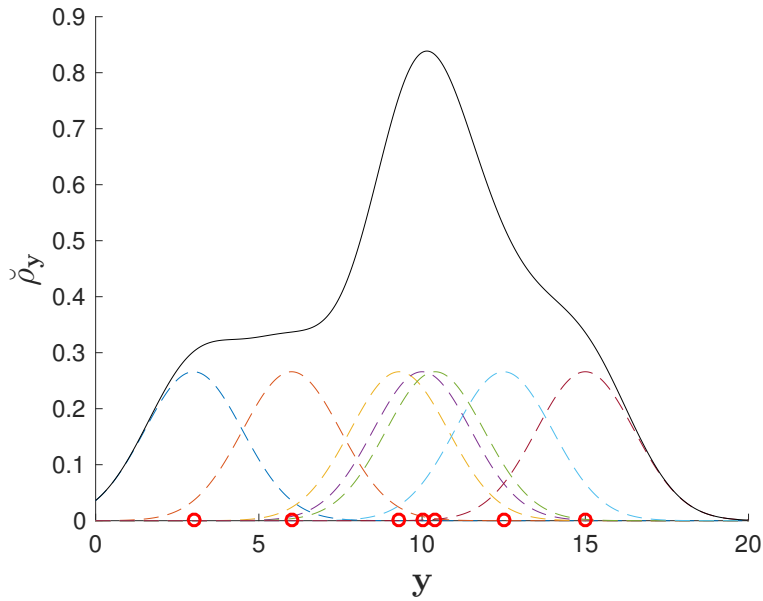


Figure 6.2: The circles indicate the data points of \mathbf{y} , the dashed curves indicate the kernels weights for each data point, and the solid curve is equal to the sum of the kernels, which is the estimation of the PDF of \mathbf{y} , $\check{\rho}_y$.

to ensure that the estimated PDF is non-negative and integrates to one. The motivation for using the kernel density estimator instead of a simple histogram approximation is that the former ensures continuity and differentiability of the estimated PDFs, provided that a continuous and differentiable kernel function is used. To satisfy those criteria, the Gaussian kernel is chosen for this study:

$$\kappa(x) = \frac{1}{h\sqrt{2\pi}} \exp(-x^2/2h^2), \quad (6.9)$$

where h is the kernel width, also known as the smoothing parameter or bandwidth. If the kernel width used is too large, $\kappa(\xi_{k,q_k} - c_{k,m})$ changes slowly with ξ_{k,q_k} , and the resultant PDF is a superposition of broad and slowly varying functions, which lacks resolution. A too small window width, on the other hand, will cause the kernels to become “spiky” with high amplitude centred on each possible outcome of \mathbf{c}_k . This leads to a noisy estimate of the PDF. It was shown by Silverman [215] that the optimal window width for data that follows Gaussian distribution is given by

$$h = \left(\frac{4}{3M} \right)^{\frac{1}{5}} \sigma \approx 1.06\sigma M^{-\frac{1}{5}}, \quad (6.10)$$

where σ is the standard deviation of the data.

To estimate the entropies of the chromophore concentrations, the PDF is evaluated at a set of discrete equally spaced points denoted by $\boldsymbol{\xi}_k = [\xi_{k,1}, \xi_{k,2}, \dots, \xi_{k,Q}]$, where Q is the total number of points (see Sec. 6.2.4 for details of the implementation). The integral in the definition of the entropy and the joint entropy for continuous variables in Eq. (5.3) and (5.4) can be approximated as a sum using the trapezium rule, such that

$$\check{\mathcal{H}}(\mathbf{c}_k) = - \sum_{q_k=1}^Q \check{\rho}_{\mathbf{c}_k}(\xi_{k,q_k}) \log \check{\rho}_{\mathbf{c}_k}(\xi_{k,q_k}) \Delta \xi_k \quad (6.11)$$

and

$$\check{\mathcal{H}}(\mathbf{c}_1, \dots, \mathbf{c}_K) = - \sum_{q_1, \dots, q_K=1}^Q \check{\rho}_{\mathbf{c}_1, \dots, \mathbf{c}_K}(\xi_{1,q_1}, \dots, \xi_{K,q_K}) \log \check{\rho}_{\mathbf{c}_1, \dots, \mathbf{c}_K}(\xi_{1,q_1}, \dots, \xi_{K,q_K}) \prod_{k=1}^K \Delta \xi_k \quad (6.12)$$

where the summation symbol denotes a multiple sum of q_1, \dots, q_K and $\Delta \xi_k$ is the spacing between the sampling points for the PDF. Using the approximated entropies, the MI can be estimated by

$$\check{I}(\mathbf{c}_1, \dots, \mathbf{c}_K) = \sum_{k=1}^K \check{\mathcal{H}}(\mathbf{c}_k) - \check{\mathcal{H}}(\mathbf{c}_1, \dots, \mathbf{c}_K). \quad (6.13)$$

6.2.3 The gradient of the mutual information

To find the most independent chromophores requires minimising the MI between the chromophores, which can be done efficiently using a gradient-based optimisation approach. The partial derivative of the MI with respect to the chromophore concentration at each voxel is given by [216]

$$\frac{\partial \check{I}(\mathbf{c}_1, \dots, \mathbf{c}_K)}{\partial c_{k,m}} = \frac{\partial \check{\mathcal{H}}(\mathbf{c}_k)}{\partial c_{k,m}} - \frac{\partial \check{\mathcal{H}}(\mathbf{c}_1, \dots, \mathbf{c}_K)}{\partial c_{k,m}}. \quad (6.14)$$

The first term in the right hand side of Eq. (6.14) is

$$\frac{\partial \check{\mathcal{H}}(\mathbf{c}_k)}{\partial c_{k,m}} = \frac{\partial \check{\mathcal{H}}(\mathbf{c}_k)}{\partial \check{\rho}_{\mathbf{c}_k}} \frac{\partial \check{\rho}_{\mathbf{c}_k}}{\partial c_{k,m}}, \quad (6.15)$$

where

$$\begin{aligned}
\frac{\partial \check{\mathcal{H}}(\mathbf{c}_k)}{\partial \check{\rho}_{\mathbf{c}_k}} &= - \sum_{q_k=1}^Q \frac{\partial}{\partial \check{\rho}_{\mathbf{c}_k}} [\check{\rho}_{\mathbf{c}_k}(\xi_{k,q_k}) \log \check{\rho}_{\mathbf{c}_k}(\xi_{k,q_k})] \Delta \xi_k \\
&= - \sum_{q_k=1}^Q \left[\check{\rho}_{\mathbf{c}_k}(\xi_{k,q_k}) \frac{\partial \log \check{\rho}_{\mathbf{c}_k}(\xi_{k,q_k})}{\partial \check{\rho}_{\mathbf{c}_k}} + \frac{\partial \check{\rho}_{\mathbf{c}_k}}{\partial \check{\rho}_{\mathbf{c}_k}} \log \check{\rho}_{\mathbf{c}_k}(\xi_{k,q_k}) \right] \Delta \xi_k \quad (6.16) \\
&= - \sum_{q_k=1}^Q [1 + \log \check{\rho}_{\mathbf{c}_k}(\xi_{k,q_k})] \Delta \xi_k
\end{aligned}$$

by the product rule, and

$$\frac{\partial \check{\rho}_{\mathbf{c}_k}}{\partial c_{k,m}} = \kappa'(\xi_{k,q_k} - c_{k,m}), \quad (6.17)$$

where κ' denotes the derivative of κ , given by

$$\kappa'(\xi_{k,q_k} - c_{k,m}) = \frac{\xi_{k,q_k} - c_{k,m}}{h^2} \kappa(\xi_{k,q_k} - c_{k,m}) \quad (6.18)$$

for the Gaussian kernel. Similarly, the second term in Eq. (6.14) is

$$\frac{\partial \check{\mathcal{H}}(\mathbf{c}_1, \dots, \mathbf{c}_K)}{\partial c_{k,m}} = \frac{\partial \check{\mathcal{H}}(\mathbf{c}_1, \dots, \mathbf{c}_K)}{\partial \check{\rho}_{\mathbf{c}_1, \dots, \mathbf{c}_K}} \frac{\partial \check{\rho}_{\mathbf{c}_1, \dots, \mathbf{c}_K}}{\partial c_{k,m}}, \quad (6.19)$$

where

$$\frac{\partial \check{\mathcal{H}}(\mathbf{c}_1, \dots, \mathbf{c}_K)}{\partial \check{\rho}_{\mathbf{c}_1, \dots, \mathbf{c}_K}} = - \sum_{q_1, \dots, q_K=1}^Q [1 + \log \check{\rho}_{\mathbf{c}_1, \dots, \mathbf{c}_K}(\xi_{1,q_1}, \dots, \xi_{K,q_K})] \prod_{i=1}^K \Delta \xi_i \quad (6.20)$$

and

$$\frac{\partial \check{\rho}_{\mathbf{c}_1, \dots, \mathbf{c}_K}}{\partial c_{k,m}} = \kappa'(\xi_k - c_{k,m}) \prod_{i=1, i \neq k}^K \kappa(\xi_i - c_{i,m}). \quad (6.21)$$

6.2.4 Implementation

6.2.4.1 FFT for fast computation of the kernel estimator

The number of operations required to evaluate an equation is referred to as its complexity, and is often denoted with \mathcal{O} . The complexity of evaluating the PDF of a chromophore at Q points in an image of M voxels is $\mathcal{O}(QM)$ using the kernel estimator in Eq. (6.5). Since Q is typically chosen to be in the order of a few hundreds, and M can be approximately a million for high resolution 3D images, the number of operations required to

calculate the PDF can be as large as $\sim 10^8$. The high complexity means that the kernel estimator can become prohibitively slow. To increase the computational efficiency, we take advantage of the fact that Eqs. (6.5) and (6.6) can be evaluated using convolutions, which can be calculated efficiently using fast Fourier transforms (FFT) [217]. The convolution of two continuous functions $f(x)$ and $g(x)$ is given by

$$f(x) \star g(x) = \int_{-\infty}^{\infty} f(x-s)g(s)ds = \int_{-\infty}^{\infty} f(s)g(x-s)ds, \quad (6.22)$$

The convolution theorem states that the convolution of two functions can be found by performing the Fourier transform on each of the functions, then multiplying the results, and finally taking the inverse Fourier transform of the product:

$$f(x) \star g(x) = \mathcal{F}^{-1} \{ \mathcal{F} \{ f(x) \} \mathcal{F} \{ g(x) \} \}, \quad (6.23)$$

where \mathcal{F} and \mathcal{F}^{-1} denote the Fourier transform and the inverse Fourier transform. For discrete and evenly spaced signals, the FFT algorithm can be used to calculate the convolution, which has a complexity of $\mathcal{O}(L \log L)$, where L is number of points that x is defined at [217]. It is shown in Sec. 6.2.4.2–6.2.4.5 that using the FFT to evaluate the PDFs can reduce the complexity by several orders of magnitude. The implementation largely follows Ref. [218] and is described in detail in the following sections.

6.2.4.2 Estimation of the marginal PDF

As mentioned in the previous section, the FFT can be used to evaluate the convolution provided that the functions are defined at discrete equally spaced points – a uniform grid. However, the chromophore concentration at different voxels, $\mathbf{c}_k = [c_{k,1}, \dots, c_{k,M}]$, is continuous. (By this we mean that the *value* of the concentration at each voxel is continuous, as it may be any continuous number, and it must not be confused with the spatial discretisation by the equispaced voxels.) To obtain discrete functions, the continuous concentration $\mathbf{c}_k = [c_{k,1}, \dots, c_{k,M}]$ is re-sampled onto a uniform grid defined at a discrete set of Q equally spaced points, $\boldsymbol{\xi}_k = [\xi_{k,1}, \dots, \xi_{k,Q}]$ [216, 217]. These are the same points where the PDF will be evaluated, as described in Sec. 6.2.2. The re-sampled data is given by $\hat{\mathbf{c}}_k = [\hat{c}_{k,1}, \dots, \hat{c}_{k,Q}]$, where each sampled point is given by

$\hat{c}_{k,q_k} = w(\xi_{k,q_k})$. The weight $w(\xi_{k,q_k})$ for each sampling point is calculated using [216]

$$w(\xi_{k,q_k}) = \frac{1}{M} \sum_{m=1}^M \wedge(\xi_{k,q_k} - c_{k,m}) \quad (6.24)$$

where $\wedge(x)$ is a triangular kernel

$$\wedge(x) = \begin{cases} 1 - (|x|/\Delta\xi_k), & \text{if } |x| < \Delta\xi_k \\ 0, & \text{otherwise} \end{cases} \quad (6.25)$$

This re-sampling is analogous to the histogram binning method. In the histogram method, the binning process can be thought of as re-sampling using box functions, where a box of a fixed height is placed on a bin for each data point with a value that falls within the bin, and the final weight of the bin is the sum of the boxes. In Eq. (6.24), the re-sampling uses triangular functions instead of box functions, such that the contribution to the bin is dependent on the distance between values of the data point and the grid point. To clarify, the original \mathbf{c}_k represents the continuous concentrations of the k th chromophore at different voxels and has size M . The re-sampled $\hat{\mathbf{c}}_k$ represents the ‘‘density’’ of the concentration at different sampling values and has size Q . The re-sampling is illustrated in Fig. 6.3 with the concentration of the chromophore k at six pixels.

It is clear from Eq. (6.25) that each $c_{k,m}$ only contributes to the weight of its closest neighbouring sampling points ξ_{k,i_m} and ξ_{k,i_m+1} . The weights due to $c_{k,m}$ are given by $w(\xi_{k,i_m}) = (1 - b_m)/M$ and $w(\xi_{k,i_m+1}) = b_m/M$, where $b_m = (|c_{k,m} - \xi_{k,i_m}|/\Delta\xi_k)$ is the normalised distance to the neighbour. This is illustrated in Fig. 6.4. The index of the left neighbour for each $c_{k,m}$, $\mathbf{i} = [i_1, i_2, \dots, i_M]$, and their corresponding distances, $\mathbf{b} = [b_1, b_2, \dots, b_M]$, are stored for subsequent calculations [217].

Thus, using the re-sampled concentrations, the kernel estimator of the marginal PDF at the sampling point $\xi_{k,a}$ is given by [216]

$$\check{\rho}_{\hat{\mathbf{c}}_k}(\xi_{k,a}) = \frac{1}{Q} \sum_{q_k=1}^Q \kappa(\xi_{k,a} - \xi_{k,q_k}) w(\xi_{k,q_k}). \quad (6.26)$$

Calculating the PDF for all Q sampling points, $\check{\rho}_{\hat{\mathbf{c}}_k}(\boldsymbol{\xi}_k)$, would require $\mathcal{O}(Q^2)$ operations

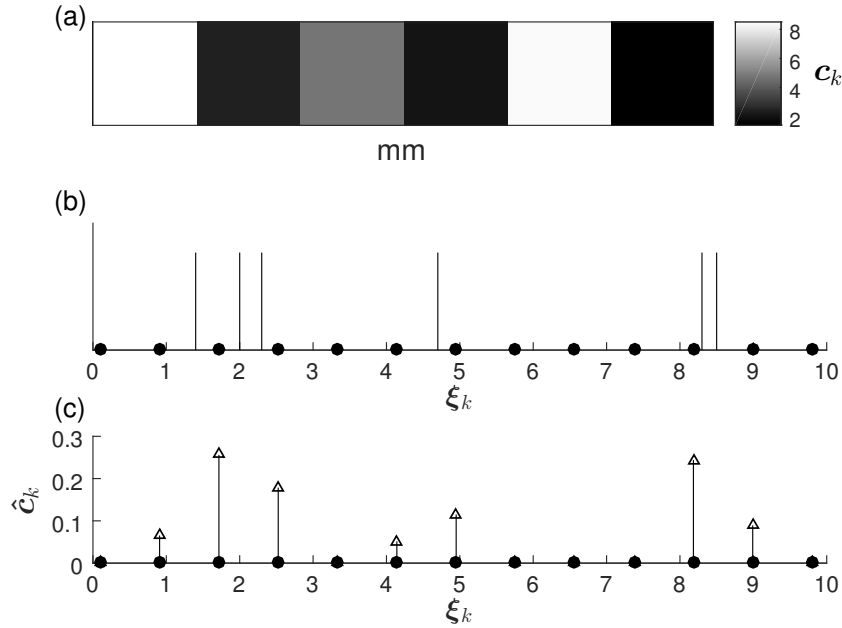


Figure 6.3: (a) The concentrations of the chromophore k at six voxels are $\mathbf{c}_k = [8.5, 2.3, 4.7, 2.0, 8.3, 1.4]$, as indicated with the colour scale. (b) The concentrations are shown using vertical lines along the uniform grid defined by 13 points at $\xi_k = [0.1, 0.9, 1.7, 2.5, 3.3, 4.1, 5.0, 5.8, 6.6, 7.4, 8.2, 9.0, 9.8]$, which are indicated with dots. (c) The re-sampled concentrations at the uniform grid, $\hat{\mathbf{c}}_k = [0, 0.07, 0.26, 0.18, 0.05, 0.12, 0, 0, 0, 0.24, 0.09, 0]$. Figure inspired by [217, 218].

using Eq. (6.26). To further reduce the complexity, the kernel estimator is expressed as a convolution, [216]

$$\begin{aligned} \check{\rho}_{\hat{\mathbf{c}}_k}(\xi_k) &= \kappa(\xi_k) \star \frac{1}{Q} w(\xi_k) \\ &= \mathcal{F}^{-1} \left\{ \mathcal{F} \{ \kappa(\xi_k) \} \mathcal{F} \left\{ \frac{1}{Q} w(\xi_k) \right\} \right\}, \end{aligned} \quad (6.27)$$

and evaluated efficiently using FFT, since both terms in the convolution are defined at equally spaced points. The practical details of the implementation are as follows [218]: The number of equidistant points where the PDF is sampled, Q , is chosen to be 500, which is considered enough for accurate estimation the PDF according to Refs. [219, 220]. The kernel κ is pre-calculated on a grid \mathbf{g} extending from $-6h$ to $6h$, where h is the kernel width defined in Eq. (6.9), such that $\mathbf{g} = [-\frac{Q_g-1}{2} \Delta \xi_k, \dots, -2\Delta \xi_k, -\Delta \xi_k, 0, \Delta \xi_k, 2\Delta \xi_k, \dots, \frac{Q_g-1}{2} \Delta \xi_k]$, where $\Delta \xi_k$ is the grid spacing and Q_g is the number of points on the grid. The convolution theorem assumes that the data is periodic when the FFT is used, which means that the points at the end of the grid wrap around and appear at the beginning

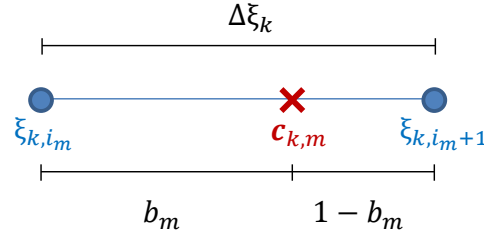


Figure 6.4: A graphic illustration of the normalised distances b_m , which are used to calculate the weights during the re-sampling. Figure inspired by [218].

of the grid. To avoid this wrapping effect, the functions $\kappa(\mathbf{g})$ and $w(\boldsymbol{\xi}_k)$ are zero-padded so that both have the size of $Q_{pad} = Q + Q_g$. The complexity of calculating the PDF in Eq. (6.27) with the padded functions is $\mathcal{O}(Q_{pad} \log Q_{pad})$. The total complexity including the re-sampling is then $\mathcal{O}(Q_{pad} \log Q_{pad} + M)$, which may be significantly smaller than the original $\mathcal{O}(QM)$ if M is large. The range in which the PDF is estimated is determined by the minimum and maximum \mathbf{c}_k . To also account for the width of the kernel, the range is increased by $6h$ at each extreme of values of \mathbf{c}_k . The spacing $\Delta \xi_k$ is determined by dividing the range with the pre-determined Q . The convolutions of the kernel and the discretised concentrations are illustrated in Fig. 6.5. The estimated PDFs are then used to calculate the entropies in Eq. (6.11).

6.2.4.3 Estimation of the entropy derivative

The derivative of the entropy with respect to the concentration of chromophore k at voxel m is given in Eqs. (6.15) to (6.18), and restated here

$$\frac{\partial \check{\mathcal{H}}(\mathbf{c}_k)}{\partial c_{k,m}} = - \sum_{q_k=1}^Q [1 + \log \check{\rho}_{\mathbf{c}_k}(\xi_{k,q_k})] \Delta \xi_k \frac{\partial \kappa(\xi_{k,q_k} - c_{k,m})}{\partial c_{k,m}}. \quad (6.28)$$

Equation (6.28) has a complexity of $\mathcal{O}(Q)$. However, the derivative needs to be calculated for all voxels to find the gradient of the error functional, so the total complexity is $\mathcal{O}(QM)$. Since the entropy derivative also has a convolution structure, the FFT can be utilised to reduce the complexity to $\mathcal{O}(Q_{pad} \log Q_{pad})$. Again, the functions need to be evaluated on a regular grid in order to apply the FFT. Therefore, instead of calculating the derivative with respect to the continuous concentrations $c_{k,m}$, it is calculated with

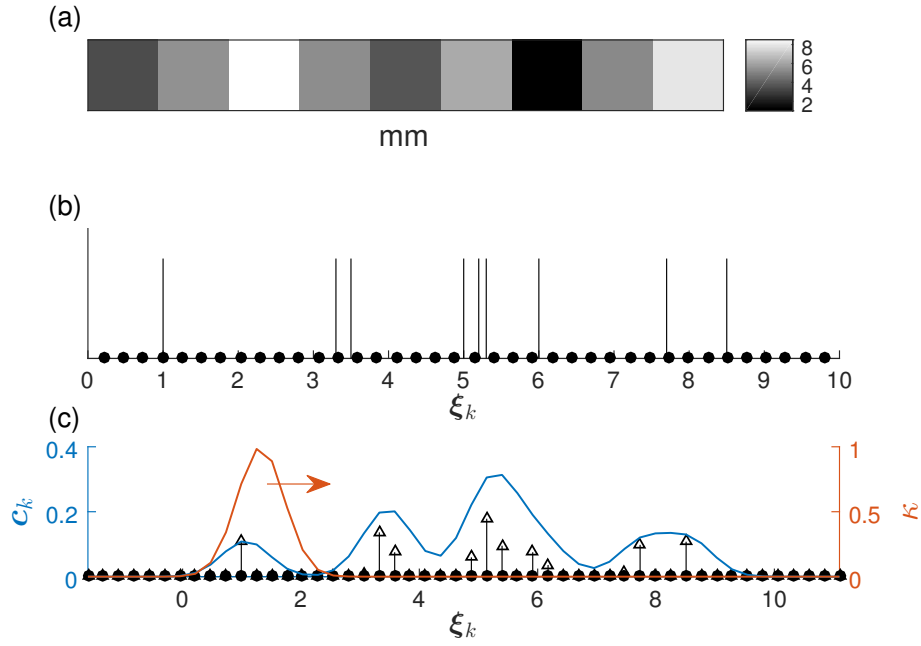


Figure 6.5: (a) An example of the concentrations of a chromophore at nine voxels. (b) The vertical lines indicate the concentrations along the uniform grid, which is defined at 50 points. The grid points are shown with dots. (c) The re-sampled concentrations are shown with black arrows. The Gaussian kernel κ with width $h = 0.4$ is shown with red curve. The kernel is convolved with the re-sampled concentrations to provide the kernel estimator of the PDF, which is shown with blue curve. Figure inspired by [217, 218].

respect to the regular grid ξ_k where the PDFs is evaluated. Thus the discrete version of Eq. (6.28) is given by [216]

$$\frac{\partial \check{\mathcal{H}}(\hat{\mathbf{c}}_k)}{\partial \xi_{k,j}} = - \sum_{q_k=1}^Q \left(1 + \log \check{\rho}_{\mathbf{c}_k}(\xi_{k,q_k}) \right) \Delta \xi_k \frac{\partial \kappa(\xi_{k,q_k} - \xi_{k,j})}{\partial \xi_{k,j}}. \quad (6.29)$$

The gradient of the entropy with respect to the grid ξ_k can then be expressed as a convolution [216]

$$\begin{aligned} \frac{\partial \check{\mathcal{H}}(\hat{\mathbf{c}}_k)}{\partial \xi_k} &= \left(1 + \log \check{\rho}_{\mathbf{c}_k}(\xi_k) \right) \star \left(-\Delta \xi_k \frac{\partial \kappa(\xi_k)}{\partial \xi_k} \right) \\ &= \mathcal{F}^{-1} \left\{ \mathcal{F} \{ 1 + \log \check{\rho}_{\mathbf{c}_k}(\xi_k) \} \mathcal{F} \left\{ -\Delta \xi_k \frac{\partial \kappa(\xi_k)}{\partial \xi_k} \right\} \right\}. \end{aligned} \quad (6.30)$$

and calculated efficiently using FFT. The derivative of $\kappa(\xi_k)$ is given by

$$\frac{\partial \kappa(\xi_k)}{\partial \xi_k} = \frac{\xi_k}{h^2} \kappa(\xi_k). \quad (6.31)$$

Equation (6.30) calculates the derivatives at the regular grid ξ_k in order to make use of the FFT. However, for the model-based inversion, the derivatives are required at the continuous values $c_{k,m}$. Therefore, the previously calculated re-sampling parameters \mathbf{b} and the indices \mathbf{i} are used to re-sample the derivative back to the continuous values $c_{k,m}$, using

$$\frac{\partial \check{\mathcal{H}}(\hat{\mathbf{c}}_k)}{\partial c_{k,m}} = (1 - b_m) \frac{\partial \check{\mathcal{H}}(\hat{\mathbf{c}}_k)}{\partial \xi_{k,i_m}} + b_m \frac{\partial \check{\mathcal{H}}(\hat{\mathbf{c}}_k)}{\partial \xi_{k,(i_m+1)}}. \quad (6.32)$$

6.2.4.4 Estimation of the joint PDF

To estimate the joint PDF between two chromophores, \mathbf{c}_1 and \mathbf{c}_2 , the concentrations are re-sampled onto a 2D regular grid defined by $\xi_1 = [\xi_{1,1}, \dots, \xi_{1,Q}]$ and $\xi_2 = [\xi_{2,1}, \dots, \xi_{2,Q}]$ with spacings $\Delta\xi_1$ and $\Delta\xi_2$, in analogous manner as for the marginal PDF in Sec. 6.2.4.2. The weight of each grid point is given by [216]

$$w(\xi_{1,q_1}, \xi_{2,q_2}) = \frac{1}{M} \sum_{m=1}^M \wedge(\xi_{1,q_1} - c_{1,m}, \xi_{2,q_2} - c_{2,m}), \quad (6.33)$$

where

$$\wedge(x, y) = \begin{cases} (1 - (|x|/\Delta\xi_1))(1 - (|y|/\Delta\xi_2)), & \text{if } |x| < \Delta\xi_1 \text{ and } |y| < \Delta\xi_2 \\ 0, & \text{otherwise} \end{cases} \quad (6.34)$$

Similarly to the 1D case for the marginal PDF, the set of two chromophore concentrations at each voxel, $(c_{1,m}, c_{2,m})$, only affects its four neighbouring sampling points $(\xi_{1,i_m}, \xi_{2,j_m})$, $(\xi_{1,i_m+1}, \xi_{2,j_m})$, $(\xi_{1,i_m}, \xi_{2,j_m+1})$ and $(\xi_{1,i_m+1}, \xi_{2,j_m+1})$, and the weight it contributes depends on the normalised distances, $b_m^x = (|c_{1,m} - \xi_{1,i_m}|/\Delta\xi_1)$ and $b_m^y = (|c_{2,m} - \xi_{2,j_m}|/\Delta\xi_2)$, as illustrated in Fig. 6.6. Again, the normalised distances and the indices associated with the continuous concentrations at each voxel, $\mathbf{i} = [i_1, \dots, i_M]$, $\mathbf{j} = [j_1, \dots, j_M]$, $\mathbf{b}^x = [b_1^x, \dots, b_M^x]$ and $\mathbf{b}^y = [b_1^y, \dots, b_M^y]$, are stored for subsequent re-sampling.

The re-sampled joint PDF at the sampling point $(\xi_{1,a}, \xi_{2,b})$ is given by [216]

$$\check{\rho}_{\hat{\mathbf{c}}_1, \hat{\mathbf{c}}_2}(\xi_{1,a}, \xi_{2,b}) = \frac{1}{Q} \sum_{q_1, q_2=1}^Q \kappa(\xi_{1,a} - \xi_{1,q_1}, \xi_{2,b} - \xi_{2,q_2}) w(\xi_{1,q_1}, \xi_{2,q_2}). \quad (6.35)$$

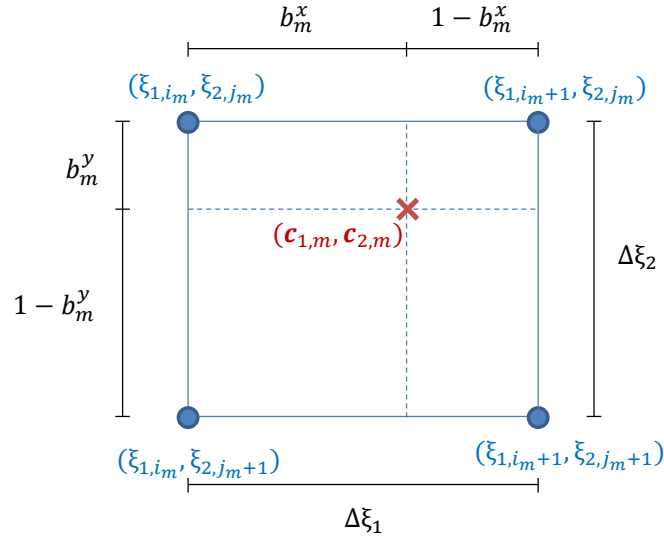


Figure 6.6: A graphic illustration of the normalised distances b_m^x and b_m^y , which are used to calculate the weights during the re-sampling in 2D. Figure inspired by [218].

where $\kappa(x, y)$ is the 2D Gaussian kernel given by

$$\kappa(x, y) = \frac{1}{2\pi h^2} \exp(-(x^2 + y^2)/2h^2). \quad (6.36)$$

The joint PDF for all sampling points, $\check{\rho}_{\hat{c}_1, \hat{c}_2}(\boldsymbol{\xi}_1, \boldsymbol{\xi}_2)$, can be calculated using a convolution [216]

$$\begin{aligned} \check{\rho}_{\hat{c}_1, \hat{c}_2}(\boldsymbol{\xi}_1, \boldsymbol{\xi}_2) &= \kappa(\boldsymbol{\xi}_1, \boldsymbol{\xi}_2) \star \star \frac{1}{Q} w(\boldsymbol{\xi}_1, \boldsymbol{\xi}_2) \\ &= \mathcal{F}^{-1} \left\{ \mathcal{F} \{ \kappa(\boldsymbol{\xi}_1, \boldsymbol{\xi}_2) \} \mathcal{F} \left\{ \frac{1}{Q} w(\boldsymbol{\xi}_1, \boldsymbol{\xi}_2) \right\} \right\} \end{aligned} \quad (6.37)$$

where $\star\star$ denotes the 2D convolution. The 2D kernel $\kappa(\boldsymbol{\xi}_1, \boldsymbol{\xi}_2)$ is calculated over a 2D grid of size Q_g^2 extending from $-6h$ to $6h$ in both dimensions. The kernel and the re-sampled concentrations are zero-padded in both dimensions, such that the size of each dimension is $Q_{pad} = Q + Q_g$. The total complexity of the re-sampling and evaluating Eq. (6.35) using FFT is $\mathcal{O}(Q_{pad}^2 \log Q_{pad} + M)$, which is typically several order of magnitude lower than the original $\mathcal{O}(Q^2 M)$ for high resolution 3D images.

6.2.4.5 Estimation of the joint entropy derivative

The derivative of the joint entropy was given in Eqs. (6.19)–(6.21), and restated here for the two chromophores, \mathbf{c}_1 and \mathbf{c}_2 :

$$\frac{\partial \check{\mathcal{H}}(\mathbf{c}_1, \mathbf{c}_2)}{\partial c_{k,m}} = - \sum_{q_1, q_2}^Q \left(1 + \log \check{\rho}_{\mathbf{c}_1, \mathbf{c}_2}(\xi_{1,q_1}, \xi_{2,q_2}) \right) \Delta \xi_1 \Delta \xi_2 \frac{\partial \kappa(\xi_{1,q_1} - c_{1,m}, \xi_{2,q_2} - c_{2,m})}{\partial c_{k,m}} \quad (6.38)$$

where $k = 1$ or 2 . In the same manner as for the marginal entropy derivative, the joint entropy derivative is evaluated at a 2D regular grid in order to apply the FFT [216]

$$\frac{\partial \check{\mathcal{H}}(\hat{\mathbf{c}}_1, \hat{\mathbf{c}}_2)}{\partial \xi_{k,(a,b)}} = - \sum_{q_1, q_2}^Q \left(1 + \log \check{\rho}_{\mathbf{c}_1, \mathbf{c}_2}(\xi_{1,q_1}, \xi_{2,q_2}) \right) \Delta \xi_1 \Delta \xi_2 \frac{\partial \kappa(\xi_{1,q_1} - \xi_{1,a}, \xi_{2,q_2} - \xi_{2,b})}{\partial \xi_{k,(a,b)}} \quad (6.39)$$

The subscript (a, b) is used to differentiate from the 1D case and should be interpreted as follows: for each a , the derivative is calculated for all b in the 2D grid, rather than just the one point a in the 1D case. Equation (6.39) has a convolution structure and can be calculated using FFT:

$$\begin{aligned} \frac{\partial \check{\mathcal{H}}(\hat{\mathbf{c}}_1, \hat{\mathbf{c}}_2)}{\partial \xi_k} &= \left(1 + \log \check{\rho}_{\mathbf{c}_1, \mathbf{c}_2}(\boldsymbol{\xi}_1, \boldsymbol{\xi}_2) \right) \star \star \left(-\Delta \xi_1 \Delta \xi_2 \frac{\partial \kappa(\boldsymbol{\xi}_1, \boldsymbol{\xi}_2)}{\partial \xi_k} \right) \\ &= \mathcal{F}^{-1} \left\{ \mathcal{F} \{ 1 + \log \check{\rho}_{\mathbf{c}_1, \mathbf{c}_2}(\boldsymbol{\xi}_1, \boldsymbol{\xi}_2) \} \mathcal{F} \left\{ -\Delta \xi_1 \Delta \xi_2 \frac{\partial \kappa(\boldsymbol{\xi}_1, \boldsymbol{\xi}_2)}{\partial \xi_k} \right\} \right\}, \end{aligned} \quad (6.40)$$

where the derivative of the 2D Gaussian kernel is

$$\frac{\partial \kappa(\boldsymbol{\xi}_1, \boldsymbol{\xi}_2)}{\partial \xi_k} = \frac{\xi_k}{h^2} \kappa(\boldsymbol{\xi}_1, \boldsymbol{\xi}_2). \quad (6.41)$$

The derivative is then re-sampled back into the continuous values using the stored \mathbf{b}^x , \mathbf{b}^y , \mathbf{i} and \mathbf{j} :

$$\begin{aligned} \frac{\partial \check{\mathcal{H}}(\mathbf{c}_1, \mathbf{c}_2)}{\partial c_{k,m}} &= (1 - b_m^x)(1 - b_m^y) \frac{\partial \check{\mathcal{H}}(\hat{\mathbf{c}}_1, \hat{\mathbf{c}}_2)}{\partial \xi_{k,(i_m, j_m)}} + \\ &\quad (b_m^x)(1 - b_m^y) \frac{\partial \check{\mathcal{H}}(\hat{\mathbf{c}}_1, \hat{\mathbf{c}}_2)}{\partial \xi_{k,(i_m+1, j_m)}} + \\ &\quad (1 - b_m^x)(b_m^y) \frac{\partial \check{\mathcal{H}}(\hat{\mathbf{c}}_1, \hat{\mathbf{c}}_2)}{\partial \xi_{k,(i_m, j_m+1)}} + \\ &\quad (b_m^x)(b_m^y) \frac{\partial \check{\mathcal{H}}(\hat{\mathbf{c}}_1, \hat{\mathbf{c}}_2)}{\partial \xi_{k,(i_m+1, j_m+1)}}. \end{aligned} \quad (6.42)$$

The joint entropy of three or more chromophores can be calculated in a similar manner by using multi-dimensional grids. The complexity of the FFT evaluation in n dimensions is $\mathcal{O}(Q_{pad}^n \log Q_{pad})$.

6.3 Generating multiwavelength images of tissue mimicking phantoms

The accuracy of the quantification using ε_{d+MI} compared to ε_d was investigated using experimental and numerical tissue mimicking phantoms. The phantoms consist of the same materials as the phantoms used in Chapter 5: aqueous solutions of CuCl_2 , NiCl_2 and black India ink are used to represent different absorbers in the tissue, and Intralipid is used to provide scattering in the medium. For both the numerical and the experimental phantom, the distributions of CuCl_2 and NiCl_2 are arranged such that they are statistically independent of each other.

6.3.1 Experimentally acquired images

A schematic of the experimental set-up is shown in Fig. 6.7. The tissue mimicking phantom consists of four polythene tubes with 0.58mm inner diameter and 0.19mm wall thickness (Scientific Laboratory Supplies Ltd, Nottingham, UK) submerged in a background solution of diluted India ink and 1% (w/v) Intralipid, which give rise to an absorption and scattering amplitude comparable to that of typical biological tissue [160]. The tubes are arranged in a line at depths of approximately 3.6, 6.1, 8.1 and 9.8mm from the top surface of the phantom, which are all within the diffusive regime. The first and third tube from the top contain 399gL^{-1} NiCl_2 and the second and the fourth tube contain 36gL^{-1} CuCl_2 . The absorption spectra of the chromophores and scattering spectrum of Intralipid are shown in Fig. 6.8. A photograph of the tubes is shown in Fig. 6.9. The CuCl_2 and NiCl_2 are statistically independent of each other in this phantom, which is clear from the fact that they are contained in distinct regions that are spatially separated. (However, the spatial separation is not a necessary criterion for statistical independence, as seen in Sec. 5.2.3.)

The phantom is imaged in a V-shaped photoacoustic imaging system [111, 223] consisting of two orthogonal Fabry-Perot interferometer sensors which are mounted in a

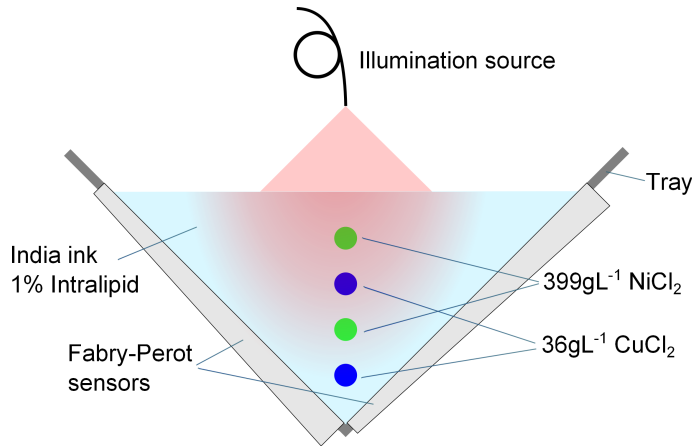


Figure 6.7: Experimental set-up and phantom structure. The four tubes containing CuCl_2 or NiCl_2 are fixed in a vertical line and submerged in the India ink and Intralipid solution. Two orthogonal Fabry-Perot interferometer sensors are used for increased detection aperture. The fibre tip at the top of the phantom delivers the pulsed excitation beam. Figure reprinted from [221] under [CC BY 4.0 License](#).

water-tight tray as illustrated Fig. 6.7. This sensor geometry increases the detection aperture compared to a single planar detector array and hence reduces the limited-view artefacts [223]. The fibre tip was positioned vertically above the phantom to deliver the pulsed excitation light from a Nd:YAG-pumped optical parametric oscillator (GWU, Spectra-Physics, Santa Clara, USA) with 10Hz repetition rate and a pulse energy of 15-19mJ depending on wavelength. The photoacoustic signals were detected at the two sensors using two interrogation laser systems. The imaging protocol was as follows: Prior to the main image acquisition, the V-shaped scanner was filled with deionised water and a registration phantom consisting of stretched polymer strands was positioned in the centre of the scanning region. The registration phantom was imaged using an excitation laser wavelength of 800nm. The image acquired by each sensor was reconstructed using the time reversal reconstruction algorithm [101, 224]. These two images were aligned using a registration algorithm [225] in order to find the rigid transformation that positions the two sensors in a common coordinate system. The registration phantom was then removed from the tray and replaced with the liquid phantom with capillary tubes. The phantom was imaged at 8 wavelengths with equal spacing between 750nm and 890nm by recording the photoacoustic time series at a $13 \times 13 \text{mm}^2$ area with $100 \mu\text{m}$ step size for both sensors. A small fraction of the light was directed to an inte-

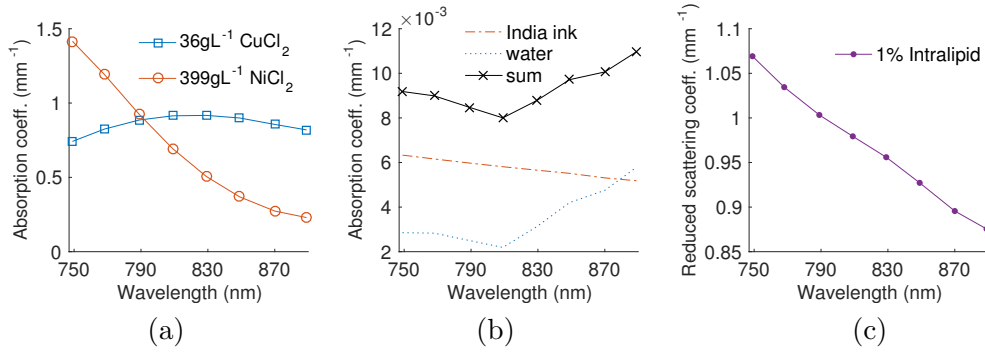


Figure 6.8: (a) The absorption coefficients of 36gL⁻¹ CuCl₂ (squares) and 399gL⁻¹ NiCl₂ (circles). (b) The absorption coefficient of the background solution (crosses), which is a sum of the absorption of water [50] (dotted) and the India ink (dashed). (c) The scattering amplitude of 1% Intralipid as a function of wavelength [222]. A spectrophotometer (Lambda 750S, Perkin Elmer) was used to measure the transmittance of CuCl₂, NiCl₂ and India ink in order to determine their absorption spectra. Figure reprinted from [221] under CC BY 4.0 License.

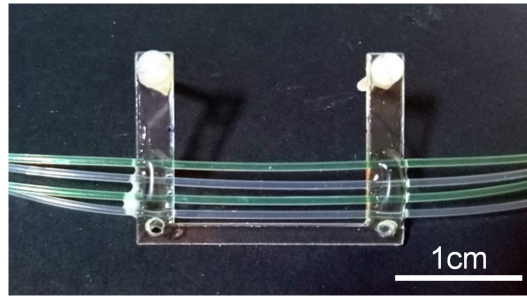


Figure 6.9: A photograph of the capillary tubes filled with solutions of CuCl₂ and NiCl₂ which are fixed onto a plastic holder.

grating sphere to measure the pulse energy, which was used to normalise the measured signals. After the main image acquisition, a transparent sheet with a printed grid of highly absorbing dots (with 1mm grid spacing) was placed in the tray such that it rests on the surface of the phantom. An image of the dotted sheet was acquired at 780nm with the purpose of measuring the beam position and the spatial distribution of the beam intensity. Based on the reconstruction of this image, the illumination source was approximated as a Gaussian beam with a 1/e diameter of 6.6mm.

The iterative time reversal acoustic reconstruction method [104, 226] was used to reconstruct 3D images from the measured pressure time series. The reconstruction involves first running the time reversal reconstruction (Sec. 3.1) using the detected time series at the sensors, p_{det}^{meas} , to obtain an initial reconstruction of the pressure

distribution, $p_0^{(0)}$. The time reversal operator is denoted with T , such that

$$p_0^{(0)} = T p_{det}^{meas}, \quad (6.43)$$

and subject to the constraints of positive initial pressure and zero initial particle velocity. An acoustic forward propagation model is then used to calculate the pressure time series at the sensor surfaces, $p_{det}^{(0)}$, based on the reconstructed initial pressure distribution $p_0^{(0)}$, such that

$$p_{det}^{(0)} = A p_0^{(0)}, \quad (6.44)$$

where A denotes the forward operator. The difference between $p_{det}^{(0)}$ and the measured times series p_{det}^{meas} is then used to reconstruct another map of the initial pressure with the time reversal algorithm. This pressure map is added to $p_0^{(0)}$ to find the next iteration of the reconstruction. Hence the iteration is given by

$$p_0^{(i+1)} = p_0^{(i)} + T(p_{det}^{meas} - p_{det}^{(i)}). \quad (6.45)$$

Both the forward and time reversal propagations of the acoustic pressures were numerically simulated using the k -space pseudospectral model implemented in the MATLAB toolbox k -Wave [70]. Seven iterations were used to reconstruct the 3D images of the tubes phantom. A 2D cross-sectional $12 \times 12 \text{mm}^2$ region of interest centred at the tubes was used for the optical inversion, and the dimension was reduced to 72×72 pixels to reduce the computational time and memory requirements. The 2D slices are shown for three wavelengths in Fig. 6.10.

6.3.2 Numerically simulated images

The numerical phantom has an element spacing of $100 \mu\text{m}$ and represents a $5 \times 5 \text{mm}^2$ area with six insertions arranged in two columns, as illustrated in Fig. 6.11. The left column of insertions represents solutions of CuCl_2 with concentrations 12, 24 and 36gL^{-1} in increasing order, where the top insertion has the lowest concentration. The right column of insertions contain solutions of NiCl_2 with concentrations 133, 266 and 399gL^{-1} , also in increasing order from the top insertion. The phantom is designed with increasing concentrations at the insertions with depth to improve the signal to noise ratio at the

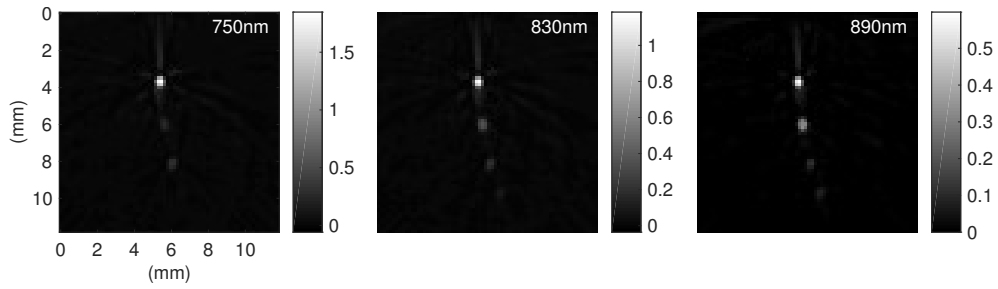


Figure 6.10: The 2D cross-sectional slices of the 3D reconstructed photoacoustic images at wavelengths 750, 830 and 890nm which are used for the optical inversion. The size of this region of interest is $12 \times 12 \text{mm}^2$ and the element spacing is $166 \mu\text{m}$. As expected, the intensity of the tubes decreases with depth for all wavelengths due to the decay of the fluence. Figure reprinted from [221] under [CC BY 4.0 License](#).

deeper insertions. The absorption of CuCl_2 and NiCl_2 are based on the measured spectra shown in Fig. 6.8(a) and assumed to follow linear dependence on concentration. The concentrations are chosen such that the average absorption of both columns is 0.52mm^{-1} over the wavelength range between 750nm to 890nm, which is similar to the absorption of blood over the same range of wavelengths. Water is present in the whole phantom and the background region outside the insertions represents a solution of India ink and Intralipid, which gives rise to the same absorption and scattering amplitude as shown in Fig. 6.8(b–c).

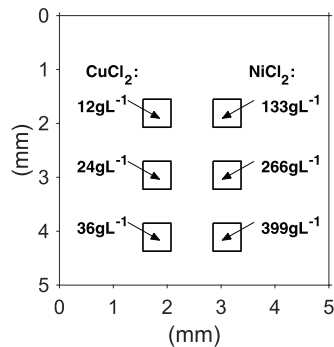


Figure 6.11: Diagram of the 2D numerical phantom. The phantom contains regions with different concentrations of CuCl_2 and NiCl_2 . The background region contains India ink and Intralipid. Figure reprinted from [221] under [CC BY 4.0 License](#).

The top surface of the domain was illuminated with a radially-symmetric light source with a Gaussian intensity profile with a $1/e$ width of 3mm. The light fluence distributions for the same 8 wavelengths as the experimental measurement in Sec. 6.3.1 were simulated

using the DA with the MATLAB software Toast++ [202]. The system calibration factor and the Grüneisen parameter are assumed to be known and equal to one, and the acoustic reconstruction is assumed to be perfect, such that the simulated photoacoustic images were equal to the product of the fluence and the absorption coefficient. Gaussian noise with a variance equal to 10% of the mean of the data, which was comparable to the magnitude of the noise in the experimental images (Sec. 6.3.1), was added to the simulated images.

6.4 Inverting for the chromophore concentrations

To investigate the effect of incorporating the MI term, the model-based inversion scheme was applied to the simulated and the experimentally acquired multiwavelength 2D photoacoustic images using both ε_d and ε_{d+MI} as error functionals. The known model parameters in the inversion are the absorption spectra, the scattering distribution, the system calibration factor, the Grüneisen parameter and the light source position and width. The unknown parameters are the chromophore concentrations of CuCl_2 , NiCl_2 , India ink and water. Thus, the error functionals are given by

$$\operatorname{argmin}_{\mathbf{c}_1, \dots, \mathbf{c}_{K_t}} \varepsilon_d(\mathbf{c}_1, \dots, \mathbf{c}_{K_t}) = \frac{1}{2} \sum_{n=1}^N \sum_{m=1}^M \left[H_{m, \lambda_n}^{\text{model}}(\mathbf{c}_1, \dots, \mathbf{c}_{K_t}) - H_{m, \lambda_n}^{\text{meas}} \right]^2 \quad (6.46)$$

and

$$\operatorname{argmin}_{\mathbf{c}_1, \dots, \mathbf{c}_{K_t}} \varepsilon_{d+MI}(\mathbf{c}_1, \dots, \mathbf{c}_{K_t}) = \frac{1}{2} \sum_{n=1}^N \sum_{m=1}^M \left[H_{m, \lambda_n}^{\text{model}}(\mathbf{c}_1, \dots, \mathbf{c}_{K_t}) - H_{m, \lambda_n}^{\text{meas}} \right]^2 + \gamma \check{I}(\mathbf{c}_1, \dots, \mathbf{c}_K), \quad (6.47)$$

where $K_t = 4$ and $K = 2$ denote the total number of unknown chromophores and the number of independent chromophores respectively. The MI is only calculated between the independent chromophores of interest, which are CuCl_2 and NiCl_2 in this phantom.

The error functionals were minimised with the limited-memory Broyden-Fletcher-Goldfarb-Shanno (BFGS) quasi-Newton algorithm [151] (Sec. 3.2.3.2), which searches for the optimal chromophore concentrations using the functional gradients of the data error term [154] and the MI term [216] (Sec. 6.2.3–6.2.4). The gradient of the data error

with respect to the concentration of the k^{th} chromophore is given by

$$\frac{\partial \varepsilon_d}{\partial \mathbf{c}_k} = \frac{\partial \varepsilon_d}{\partial \boldsymbol{\mu}_a} \frac{\partial \boldsymbol{\mu}_a}{\partial \mathbf{c}_k} = \frac{\partial \varepsilon_d}{\partial \boldsymbol{\mu}_a} \boldsymbol{\alpha}_k. \quad (6.48)$$

The gradient with respect to the absorption coefficient, $\frac{\partial \varepsilon_d}{\partial \boldsymbol{\mu}_a}$, can be calculated efficiently with the help of the adjoint equation, and is given by [227]

$$\frac{\partial \varepsilon_d}{\partial \boldsymbol{\mu}_a} = -\phi(H^{\text{meas}} - H^{\text{model}}) + \phi\phi^* \quad (6.49)$$

where ϕ^* is the solution to the to the adjoint equation

$$(\mu_a - \nabla \cdot D \nabla) \phi^* = \mu_a (H^{\text{model}} - H^{\text{meas}}). \quad (6.50)$$

The unknown chromophore concentrations were initialised with spatially homogeneous values equal to the true concentration at the background. The iterative update was run for 300 iterations for the inversion of both the simulated and the experimental images using ε_d or ε_{d+MI} . The difference in computation time for ε_{d+MI} and ε_d was negligible. As discussed in Sec. 6.2.1, the MI term in the error functional is non-convex. Therefore, the weight parameter γ of the MI term was set to zero for the first 200 iterations to avoid the algorithm being trapped in the local minima of the MI term when ε_{d+MI} is used.

6.4.1 Effect of model-mismatch

Two case studies were conducted using the simulated images to investigate the effect of the uncertainty in different model parameters on the quantification accuracy. In the first case, the beam diameter was set to be up to 75% smaller or larger than the true value in the inversion. In the second case, an error up to $\pm 75\%$ was included in the scattering amplitude. The average errors of the estimated concentrations of CuCl_2 and NiCl_2 at the insertions (region of interest, ROI) using the erroneous beam diameter are shown in Fig. 6.12(a), where the circles and asterisks correspond to the inversions using ε_d or ε_{d+MI} respectively. The results show that the increase in the percentage error in the beam diameter leads to larger quantification errors, as expected. The quantification errors for the simulated images are relatively small because only one model parameter

contains error at the time. In an experimental setting, there is likely to be a combination of modelling errors, resulting in larger quantification errors. Nonetheless, including the MI term results in a reduction in error compared to using only the standard data error for all data points.

The inaccuracies in the scattering amplitude used in the inversion resulted in similar trends for the quantification error, as shown in Fig. 6.12(b). The errors are generally larger in Fig. 6.12(b) than (a), which suggests that the changes in scattering amplitude have a larger impact on the fluence distribution than changes in the beam diameter for this numerical phantom. Using ε_{d+MI} is shown to provide more accurate estimations compared to using ε_d also for this case. The relative improvement in accuracy varied between 37% and 8% with an average of 22% over all data points for both cases.

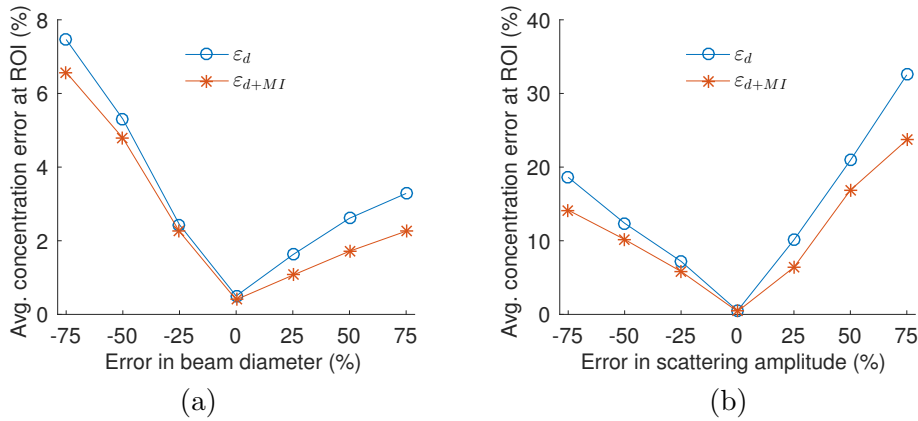


Figure 6.12: The average errors of the estimated concentrations of CuCl_2 and NiCl_2 at the insertions as a function of errors in (a) the beam diameter or (b) the scattering amplitude in the inversion. As expected, the quantification errors increase for larger errors in the beam diameter or scattering amplitude. However, the inversions using ε_{d+MI} (asterisks) result in smaller errors compared to using ε_d (circles) for all data points. The individual errors for CuCl_2 and NiCl_2 show similar general trends as the average of the two. The average errors outside the ROI are $<2\%$ for inversions using both ε_d and ε_{d+MI} . Figure reprinted from [221] under [CC BY 4.0 License](#).

6.4.2 Experimental results

The multiwavelength experimental images were divided by the calibration factor and the spatially varying Grüneisen parameter before the inversion. The calibration factor was determined using a forward simulation with the true concentrations. The Grüneisen parameter of aqueous solutions of CuCl_2 and NiCl_2 are calculated using the true con-

centrations and Eq. (5.11). In practical applications, where the true concentrations are unknown, the calibration factor can be obtained by measuring the acoustic sensitivity of the sensors [42], or included as an unknown parameter [41, 178], and the Grüneisen parameter can be included in the model as a parameter that is linearly dependent on the estimated chromophore concentrations [41, 42].

The results from the model-based inversion of the experimental data are presented in Fig. 6.13. The estimated concentrations of CuCl_2 (top row) and NiCl_2 (bottom row) using ε_d and ε_{d+MI} are shown in the left and centre columns respectively in Fig. 6.13(a), while the true concentrations are shown in the right column. The colour scale indicates the concentrations in units of gL^{-1} . Figure 6.13(b) compares the estimated with the true concentrations along a line profile across the tubes. The average estimated and expected concentrations for each tube are presented in Table 6.1. The inversions using ε_d resulted in high overestimation of CuCl_2 in the second tube and NiCl_2 in the first tube, where the estimated concentrations are 94% and 149% larger than the true values respectively. There are also large cross-talk errors in the estimation of both contrast agents. This is most clearly seen for the estimated CuCl_2 concentration, where the third tube shows a high false-positive concentration with comparable magnitude to the concentration in the fourth tube. The accuracy of the quantification is significantly improved when the MI term is included in the error functional. The cross-talk errors for both CuCl_2 and NiCl_2 are almost completely removed when ε_{d+MI} is used. The absolute concentrations of the CuCl_2 is estimated accurately with an error of 3gL^{-1} on average for the four tubes. The overestimation of the NiCl_2 concentration in the top tube remains present with ε_{d+MI} . However, this overestimation error is reduced when ε_{d+MI} is used compared to ε_d .

Table 6.1: The average estimated and true concentrations of CuCl_2 (left) and NiCl_2 (right) in gL^{-1} for each tube. The largest improvements using ε_{d+MI} are mostly seen for the tubes that are not expected to contain the relevant chromophore, as they suffer from significant cross-talk errors when ε_d is used. The average expected concentrations are lower than the true concentrations in the solutions due to the interpolation from the original images. Table reprinted from [221] under [CC BY 4.0 License](#).

CuCl_2	ε_d	ε_{d+MI}	Expected	NiCl_2	ε_d	ε_{d+MI}	Expected
Tube 1	-3	-1	0	Tube 1	860	698	345
Tube 2	60	35	31	Tube 2	185	-5	0
Tube 3	26	0	0	Tube 3	367	258	352
Tube 4	27	25	31	Tube 4	167	14	0

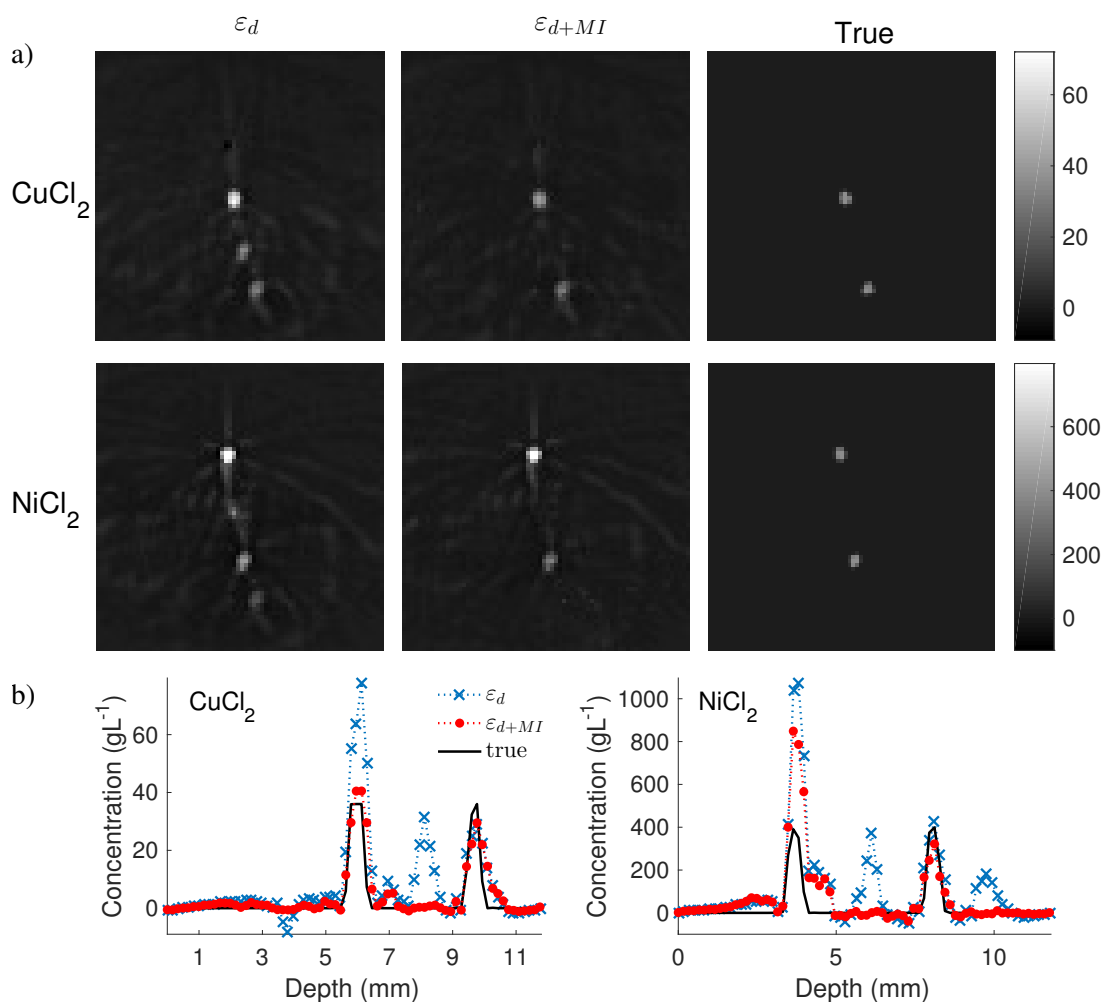


Figure 6.13: (a) The estimated concentrations of CuCl_2 (top row) and NiCl_2 (bottom row) in units of gL^{-1} . The results from the inversions using ε_d (left column) show over-estimation of the the upper tubes and large cross-talk errors, while using ε_{d+MI} results in more accurate quantification without cross-talk errors. The true concentrations are shown in the column to the right for comparison. (b) The estimated concentration of the CuCl_2 (top) and NiCl_2 (bottom) using ε_d (crosses) and ε_{d+MI} (circles) along a line across the tubes. The solid curves represent the true concentrations. Figure reprinted from [221] under [CC BY 4.0 License](#).

6.5 Summary and discussion

Minimising the MI as well as the data error led to improved quantification accuracy for both simulated and experimental multiwavelength photoacoustic images, compared to using the data error alone. In the numerical study, despite the significant fractional decrease of the quantification errors using ε_{d+MI} , in absolute terms, the error was decreased only by a few per cent. This was mainly due to the fact that only one model parameter was erroneous in each inversion, while all other assumptions in the model were accurate, which resulted in relatively small quantification errors, even when only ε_d was used. In the experimental study, on the other hand, a combination of different types of modelling errors was likely to have been present simultaneously, leading to poorer quantification results in the absence of the MI term. The main causes of model-mismatch may be due to the limited size of the modelled domain, which does not account for the backscattered light from outside of the domain, and the 2D modelling of the light fluence, which assumes that the light source is constant in the direction along the tubes, while in the experiment, the beam was of circular cross-section. Other possible errors may include uncertainty in the scattering spectra and amplitude, as different values have been reported in the literature [222, 228]. These errors in the model affect the calculation of $p_{0,m,\lambda_n}^{model}$, which consequently also affect ε_d . The MI is not affected by the fluence modelling errors, because MI is calculated based on only the distribution of the estimated chromophore concentrations in each iteration, and does not require the forward modelling of $p_{0,m,\lambda_n}^{model}$. Therefore, the quantification errors were greatly reduced when ε_{d+MI} was used in the experimental study. These results suggest that incorporating the statistical independence can improve the robustness of model-based inversion schemes for independent chromophores and thus potentially enhance their applicability to pre-clinical or clinical imaging studies.

Weight parameter In order to obtain accurate results with the inversion using ε_{d+MI} , it is necessary to use an appropriate weight parameter γ for the MI term. The weight was determined through manual trial and error. The same weight was used for all inversions of the simulated and the experimental data, despite the differences in the data and/or the model parameters. This suggests that the concentration estimates were not highly sensitive to small variations of the weighting of the MI term around this value

and, although non-trivial [229, 230], it may be possible to develop a general method for finding the optimal weight parameter for different types of applications.

Local minima In this study, the local minima in the MI term was avoided by adjusting the weight parameter depending on the iteration. The weight of the MI term was zero for the first 200 iterations such that initially, only the data error was minimised, which brings the unknown variables closer to the true solution. Then the MI term is introduced by setting the weight parameter to a positive number. In this way, the MI term is more likely to bring the solution to the local minimum closest to the true solution. Global optimisation methods such as simulated annealing could potentially provide alternative ways to allow the algorithm to escape from the local minima. However, since simulated annealing is a probabilistic optimisation technique, it may be extremely slow for large scale inverse problems with millions of unknowns.

Spatially overlapping chromophores The distributions of the chromophores of interest do not have any spatial overlap in the phantoms used in this chapter. This phantom design was chosen such that the independence criteria was clearly satisfied. However, the spatial overlap of chromophores is not expected to reduce the effectiveness of the proposed method, provided that it does not significantly reduce the statistical independence between the chromophores. For example, the CuCl_2 and NiCl_2 are completely overlapping with water, but they are still statistically independent from water, and therefore could be separated from water using the proposed method. A more interesting case of overlapping chromophores may arise when a probe is distributed within blood vessel. In this case, the probe overlaps spatially with blood, and the statistical independence may be reduced (Example C in Fig. 5.4). To simulate such a scenario, the inversion was performed on numerical phantom where both CuCl_2 and NiCl_2 are present in all six insertions in Appendix C. The results demonstrate that including the MI term can also improve the accuracy of the quantification when the chromophores overlap spatially.

Minimisation scheme There are alternative methods for incorporating the statistical independence in a minimisation scheme. For example, constrained minimisation algorithms can potentially be employed, where the data error term is minimised under

the constrained that MI must be smaller than a pre-defined value. Another potential approach could be to alternate between minimising the data error and the MI term. The algorithm could minimise one of the error terms for a pre-determined number of iterations, or until certain criteria have been met, before switching to minimising the other error term. It is also possible to explore using other measures of independence, such as normalised versions of the MI, which is commonly used in the field of image registration. Using the MI term in the error functional is also compatible with other regularisation methods such as the total-variation regulariser [83, 147, 231].

Extension to 3D The 2D fluence model based on the DA assumes that the features are constant in the third dimension and located at depths within the diffusive regime. These assumptions are appropriate for the phantom geometry used in this study. However, full 3D fluence modelling will be required for applications of the model-based inversion in biological tissue with complex structures. More accurate modelling of the fluence for the superficial layer can be achieved by incorporating the δ -Eddington approximation [41] or using the RTE [157]. The calculation of the MI can be straightforwardly extended to 3D without causing significant increase in computation time using the FFT calculations.

6.6 Conclusion

We proposed exploiting the statistical independence between certain chromophores in the model-based inversion method by minimising the MI between the independent chromophores in addition to the data error. The improvement in the accuracy of the estimated chromophore concentrations was demonstrated using both numerical simulations and an experimental phantom. The results suggest that the sensitivity of the model-based inversion to model-mismatch can be reduced by incorporating the additional information of statistical independence. Thus, the robustness and hence usefulness of the inversion scheme can potentially be improved for *in vivo* imaging experiments.

Chapter 7

Conclusions

The overarching aim of the work in this thesis is to bridge the gap between the simple linear methods that are routinely used in practice, but often without rigorous validation, and the more complex nonlinear methods that can be found in the theoretical literature, but are rarely implemented *in vivo*. This goal was approached from two perspectives:

1. The conditions under which approximate linear methods can achieve accurate quantification were investigated. The results provide guidance for selecting the appropriate methods and parameters, and thus help towards achieving the most accurate quantitative estimates based on simple linear models whenever possible.
2. The sensitivity of the nonlinear model-based inversion to model-mismatch errors were reduced by exploiting the intrinsic statistical properties of some chromophores. This improves the robustness of the method in experimental settings and hence provides a step towards bringing model-based inversion into practical use.

The performances of the linear and nonlinear QPAT methods were analysed under well-controlled conditions using numerical simulations and experimentally acquired images of tissue mimicking phantoms. The key findings and contributions of the thesis are:

Linear spectroscopic inversion (SI) Using numerically simulated photoacoustic images of a realistic mouse brain phantom, it was shown that the blood oxygenation, sO_2 , can be estimated with $<5\%$ error for a large range of depths and true sO_2 levels

using SI with 17 or more evenly spread wavelengths between 670nm and 1000nm. Increasing the number of wavelengths led to the estimated sO_2 converging to a constant value, provided that the spectral change in fluence is relatively small, which requires avoiding using wavelengths $<590\text{nm}$. It is possible to achieve low errors if optimal wavelength combinations were selected for each particular depth layer and true sO_2 level. However, it is difficult to predict these optimal wavelength combinations because the errors were shown to depend on a combination of the absorption spectra and its inverse, as well as the changes in fluence. Minimising the condition number of the spectral matrix is useful for eliminating wavelength combinations that give extremely large errors in sO_2 . However, it cannot be used to find wavelength combinations that lead to sO_2 estimates with an useful degree of accuracy, because it was shown that smaller condition numbers do not correlate with lower errors when the error is smaller than 25%.

Summary: SI can provide accurate sO_2 estimates if images at many evenly spread wavelengths within a certain wavelength range are available for tissue structures such as the vasculature in a mouse brain. It is difficult to identify wavelength combinations with reduced number of wavelengths that produce accurate sO_2 estimates for different depths and true sO_2 levels.

Independent component analysis (ICA) ICA is not suitable for estimating sO_2 , but it can provide more accurate estimates of the chromophore concentrations relative to other spatial locations than SI in certain scenarios, provided that a simple exponential fluence correction has been applied and the chromophores are statistically independent. Two such scenarios have been identified: 1) when the absorption coefficient of the vessel-like features of interest is approximately 0.5mm^{-1} and 2) when the condition number of the spectral matrix is high. This suggest that searching for the most independent chromophores and allowing the mixing matrix to vary, instead of inverting with a fixed spectral matrix, makes the inversion more tolerant towards spectral colouring and ill-conditioning. When the absorption exceeds a certain threshold, the spectral colouring is so severe that the estimated spectra become very different from the true absorption spectra. Consequently, the unmixed components can no longer be identified to the corresponding chromophores by comparing the estimated spectra with the known.

This results in large quantification errors unless the components are manually identified. The accuracy of the quantification also depends on the choice of dimension reduction, i.e. how many independent components the data will be decomposed into. Smaller dimensionality leads to easier identification of the estimated chromophores, while larger dimensionality ensures that a sufficient fraction of the total variance of the data is retained.

Summary: Provided that a first order fluence adjustment has been applied, ICA can quantify the relative concentration of independent chromophores under certain circumstances. ICA outperforms SI when the spectral matrix is ill-conditioned, and can be more robust to errors in the fluence correction than SI.

Statistical independence in nonlinear model-based inversion The nonlinear model-based inversion method has the potential to accurately estimate the absolute chromophore concentrations in arbitrary tissue structures. However, *in vivo* implementations of the method may suffer from its sensitivity to model-mismatch errors. In order to reduce these errors, we proposed exploiting the intrinsic statistical properties of the chromophore distributions which do not depend on the forward model. This involved including a mutual information (MI) term as measure of the statistical independence in the error functional in addition to the least-squares data error. The new error functional was minimised using a gradient-based algorithm. The MI term was estimated using a kernel density estimator such that the analytical gradients could be used, and evaluated efficiently using FFT, such that the increase in computational time was negligible. The results showed that including the MI term led to more accurate estimates of the chromophore concentrations in both a numerical and an experimental tissue mimicking phantom, compared to using the data error alone in the error functional. The improvements in accuracy were most evident for the experimental phantom, where cross-talk errors and over-estimations were significantly reduced. This was possible because statistical independence is an intrinsic property of the distribution of the chromophores alone, rather than a function of the forward modelling. This means that, unlike the data error, MI is not affected by errors in the fluence model. Hence, by incorporating MI in the error functional, the quantification errors due to model-mismatch in experimental settings can be reduced.

Summary: The errors due to model-mismatch in model-based inversion can be reduced by minimising the MI between the independent chromophores in addition to the data error. This improves the robustness of model-based inversion in experimental settings and thus can potentially enhance their applicability to in vivo imaging studies.

The ultimate goal is to be able to quantify the chromophore concentrations *in vivo* with sufficient accuracy such that clinically relevant functional information can be extracted reliably. The work in this thesis forms practically useful steps towards this goal. To build on these steps, we recommend further investigations and discuss a number of issues that need to be addressed:

If SI can be shown to be accurate for sO_2 measurements, it would be an extremely attractive method that is readily available. Therefore, it is of urgent interest to experimentally validate the accuracy of SI using the wavelengths recommended in Chapter 4. It is straightforward to apply SI on *in vivo* images, but it is difficult, or even arguably impossible, to validate its accuracy *in vivo*, due to the lack of other techniques that can provide *in vivo* sO_2 measurements with comparable spatial resolution. Instead, tube phantoms similar to the ones used in Chapter 5 and 6 where the concentration ratio of the chromophores can be controlled could be used. Since the results are highly dependent on the particular shape of the oxy- and deoxyhaemoglobin the absorption spectra, it would be necessary to use *in vitro* blood instead of surrogate chromophores like $CuCl_2$ and $NiCl_2$. The oxygenation of the *in vitro* blood inside the capillary tubes can be controlled using a blood oxygenator and monitored using a CO-oximeter [161, 232].

Both ICA and the model-based inversion using MI require that the chromophores are statistically independent. In practice, there may be many cases where the chromophores are not completely independent but have some dependence. It would be useful to investigate how the level of independence of the true chromophore distributions affects the accuracy of the methods. This work was initiated with the numerical phantom with spatially overlapping chromophores in Appendix C. Further work could be dedicated to more systematic investigations.

The realisation of accurate *in vivo* quantification requires dealing with practical challenges as well as developing theoretical solutions. The analyses of both ICA and the model-based inversion with MI are based on 2D images rather than 3D, which

is due to the practical issues of large computational memory demands or long image acquisition times. The extension to quantification in 3D could potentially be enabled by faster image acquisition, which is now possible with the recent developments in compressed sensing for photoacoustic imaging [83, 84] and parallel interrogation of the Fabry-Perot sensor [82, 233]. Large 3D inversions (with 1589764 unknowns) were recently demonstrated experimentally in Ref. [42], and were run on a computer with 256GB RAM and a 2.7GHz CPU with 12 cores, which took approximately 12h. This shows some promise of the practical feasibility of model-based inversion in 3D despite the higher computational demands and longer run-time. Provided that these practical issues can be overcome, both ICA and the addition of the MI term in model-based inversion are readily applicable in 3D, since both of them are fast to compute and computationally inexpensive.

Dealing with the spatially varying Grüneisen parameter and improving the accuracy of the acoustic reconstruction are two issues that require further theoretical or methodological developments. The Grüneisen parameter cancels out for the sO_2 estimate but poses a challenge to both linear and nonlinear quantification methods of the relative or absolute chromophore concentrations. As many other QPAT studies, the Grüneisen parameter was assumed to be known in Chapters 5 and 6. As discussed in Sec 3.2, potential solutions have been proposed in the theoretical literature, but their practical feasibility needs to be tested. The accuracy of the acoustic reconstruction of the initial pressure distribution was greatly improved using the V-shaped scanner compared to the single planar scanner, due to the increased detection aperture. There are however other issues that may cause errors in the acoustic reconstruction *in vivo*. For example, the sound speed was near homogeneous in the liquid phantom, but in biological tissue, the sound speed is likely to be spatially inhomogeneous, as it varies for different tissue types. The spatial variations in sound speed, which may not be known accurately, may cause blurring and artefacts in the acoustic reconstruction if unaccounted for. Therefore, reconstruction algorithms that can incorporate spatially heterogeneous sound speeds, or inversion methods where the sound speed can be included as an unknown parameter, may be required for accurate acoustic reconstruction *in vivo*.

Appendix A

Linear spectroscopic inversion with different spectral ranges

The figures in this appendix show the average error, δ_{sO_2} , of the estimated blood oxygenation, sO_2 , at the foreground vessel using linear spectroscopic inversion (SI) with evenly spread wavelengths between different wavelength ranges. Figure [A.1](#) shows that using wavelengths between 650nm and 1000nm results in higher errors for the deeper depths and lower true sO_2 levels compared to the errors in Fig. [4.4](#), which is based on using the wavelength range 670–1000nm. Figure [A.2](#) shows that increasing the shortest wavelength to $\lambda_{min} = 690\text{nm}$ leads to the opposite trend where the shallower depths and higher true sO_2 levels have higher errors.

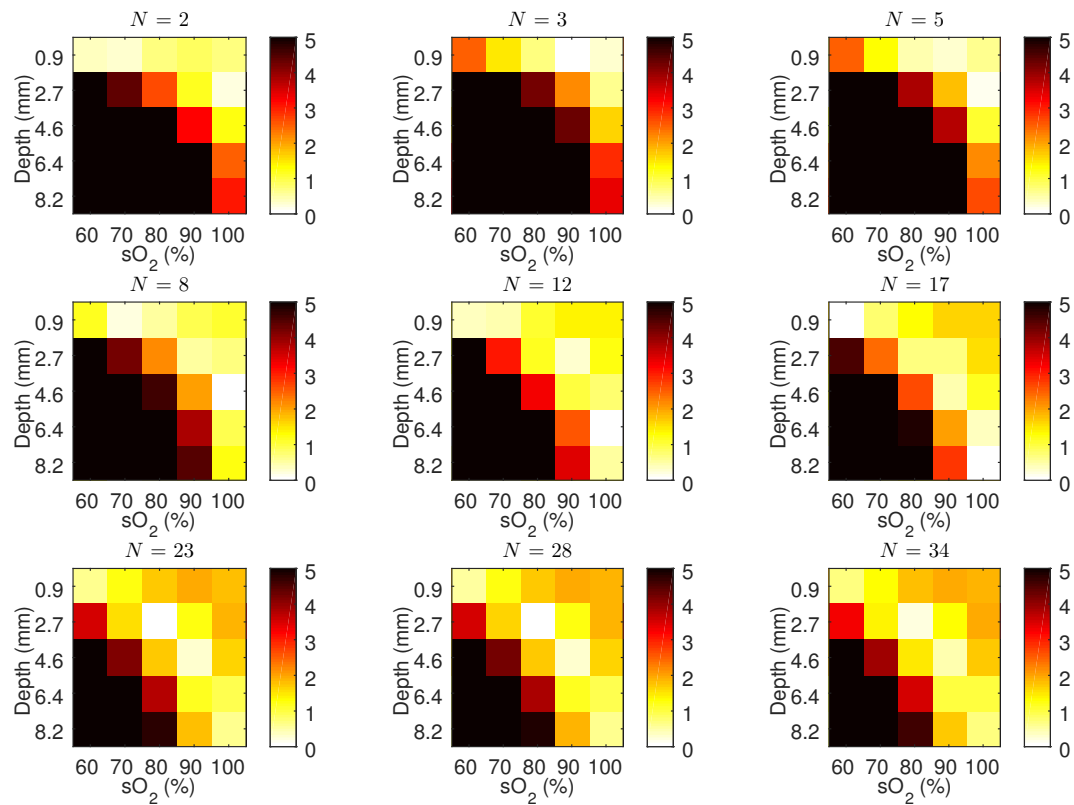


Figure A.1: The average error, δ_{sO_2} , using evenly spread wavelengths between $\lambda_{min} = 650\text{nm}$ and $\lambda_{max} = 1000\text{nm}$. The errors at the deeper depths and lower true sO_2 are higher compared to when $\lambda_{min} = 670\text{nm}$ in Fig. 4.4.

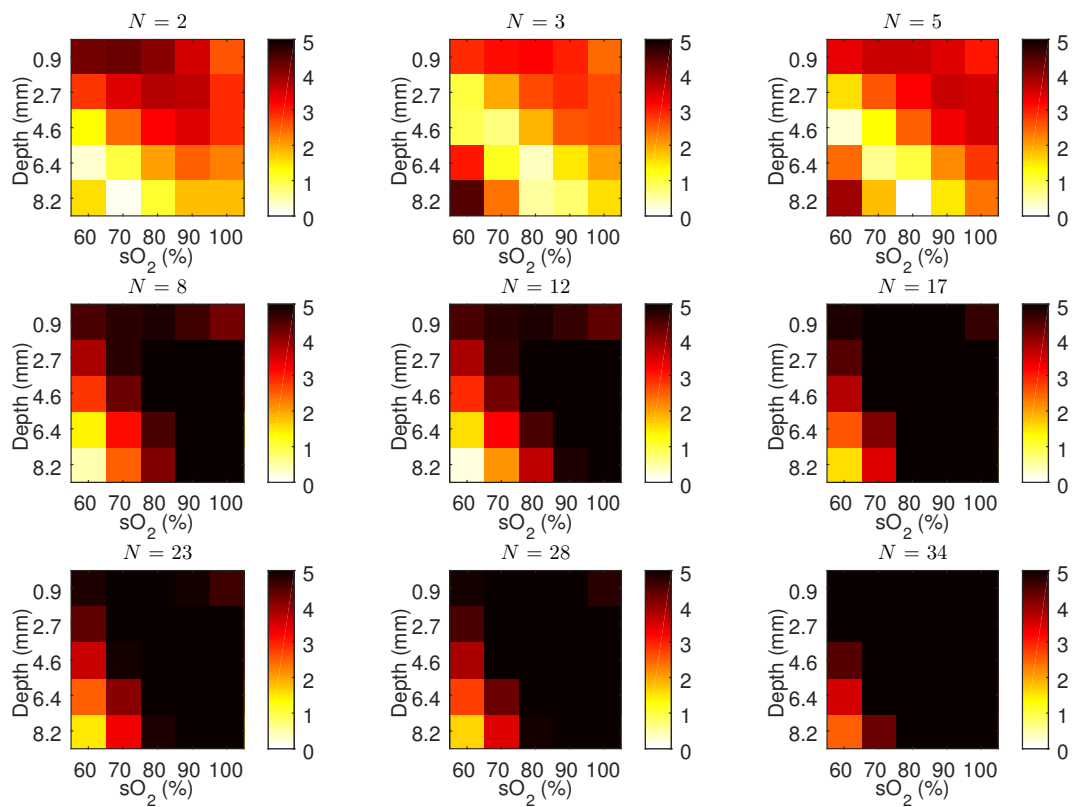


Figure A.2: Using $\lambda_{min} = 690\text{nm}$ generally leads to the opposite trend of shallower depths and higher true sO_2 having higher average errors.

Appendix B

Linear spectroscopic inversion with a different phantom

To demonstrate the generalisability of the results in Chapter 4, linear spectroscopic inversion (SI) is performed on numerically simulated images of a second phantom that has different structures to the mouse brain phantom. This phantom consists of a flat skin layer at the surface and 7 straight blood vessels arranged in a vertical line, as shown in Fig. B.1. All blood vessels have the same blood oxygenation, sO_2 , which varies between 60% to 100% in steps of 10% in five data sets. The absorption and scattering spectra for the blood, the background tissue and the skin are the same as those used for the mouse brain phantom in Chapter 4. The numerically simulated images were generated for the same 51 wavelengths between 500nm and 1000nm as in Chapter 4.

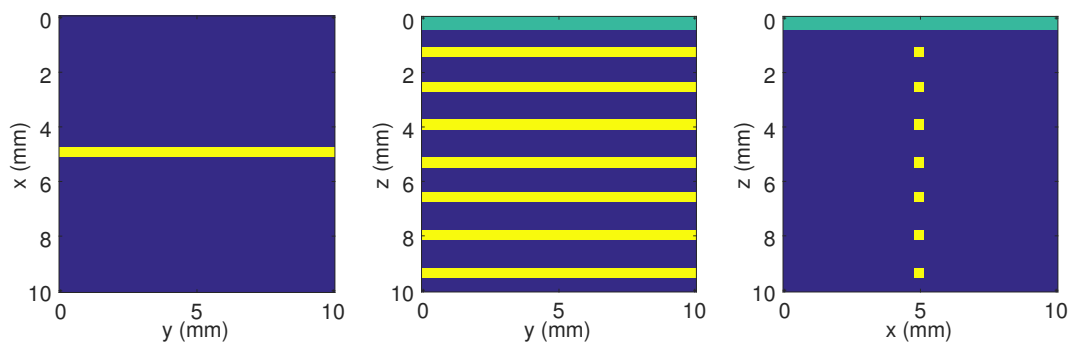


Figure B.1: The structure of the blood vessel phantom viewed from the x, y and z directions. The excitation beam is incident on the x-y plane. The phantom consists of a skin layer (green) and 7 blood vessels (yellow) surrounded by the background tissue (blue).

Figure B.2 shows the average error of the sO_2 estimation, δ_{sO_2} , for each depth layer (which contains one blood vessel) and true sO_2 level using evenly spread wavelengths with $\lambda_{min} = 670\text{nm}$ and $\lambda_{max} = 1000\text{nm}$. The errors are higher compared to the equivalent plot for the mouse brain phantom (Fig. 4.4), which is expected, because of the vertical alignment of the blood vessels is likely to lead to more spectral colouring of the deeper vessels. However, the increase in δ_{sO_2} does not exceed 5% for comparable depths and true sO_2 levels. The general trends of the errors are the same as in Fig. 4.4, where the errors are typically higher for larger depth and lower true sO_2 , and increasing N generally leads to lower errors, except for when the sO_2 is high.

Figure B.3 shows the δ_{sO_2} at a single voxel in the centre of the blood vessel at 4mm depth for increasing N and for various λ_{min} , while the λ_{max} is fixed at 1000nm. These errors are very similar to those in the equivalent plot for the mouse brain phantom in Fig. 4.12, where the errors converge smoothly to a constant value provided that wavelengths shorter than 590nm are excluded.

Overall, the comparable errors trends for the blood vessel phantom and the mouse brain phantom suggest that the results in Chapter 4 are not highly sensitive to the specific geometry of the blood vessels.

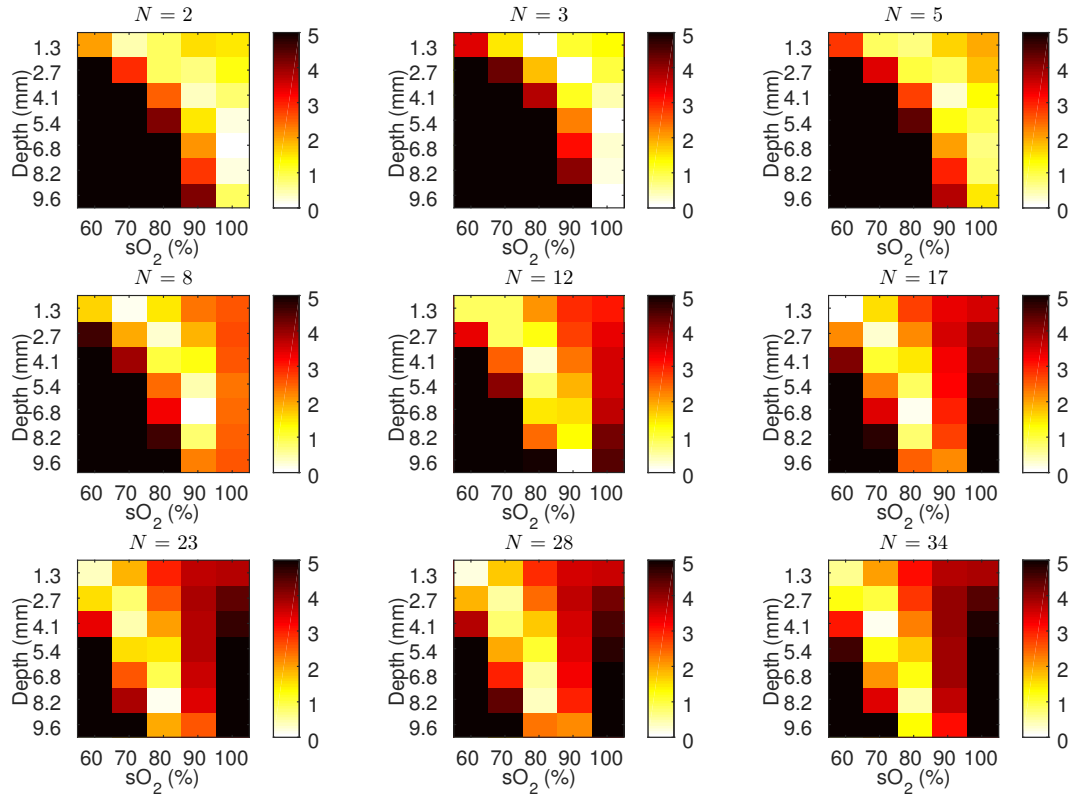


Figure B.2: The average error, δ_{sO_2} , at the blood vessels for different depths (y-axis) and true sO_2 levels (x-axis) using evenly spread wavelengths with $\lambda_{min} = 670\text{nm}$ and $\lambda_{max} = 1000\text{nm}$. The total number of wavelengths is indicated by N . The colour map indicate the errors in percentage points (%). The errors differs to that of the mouse brain phantom by $<5\%$ for comparable depths and true sO_2 levels. The equivalent error plot for the mouse brain phantom can be found in Fig. 4.4 for comparison.

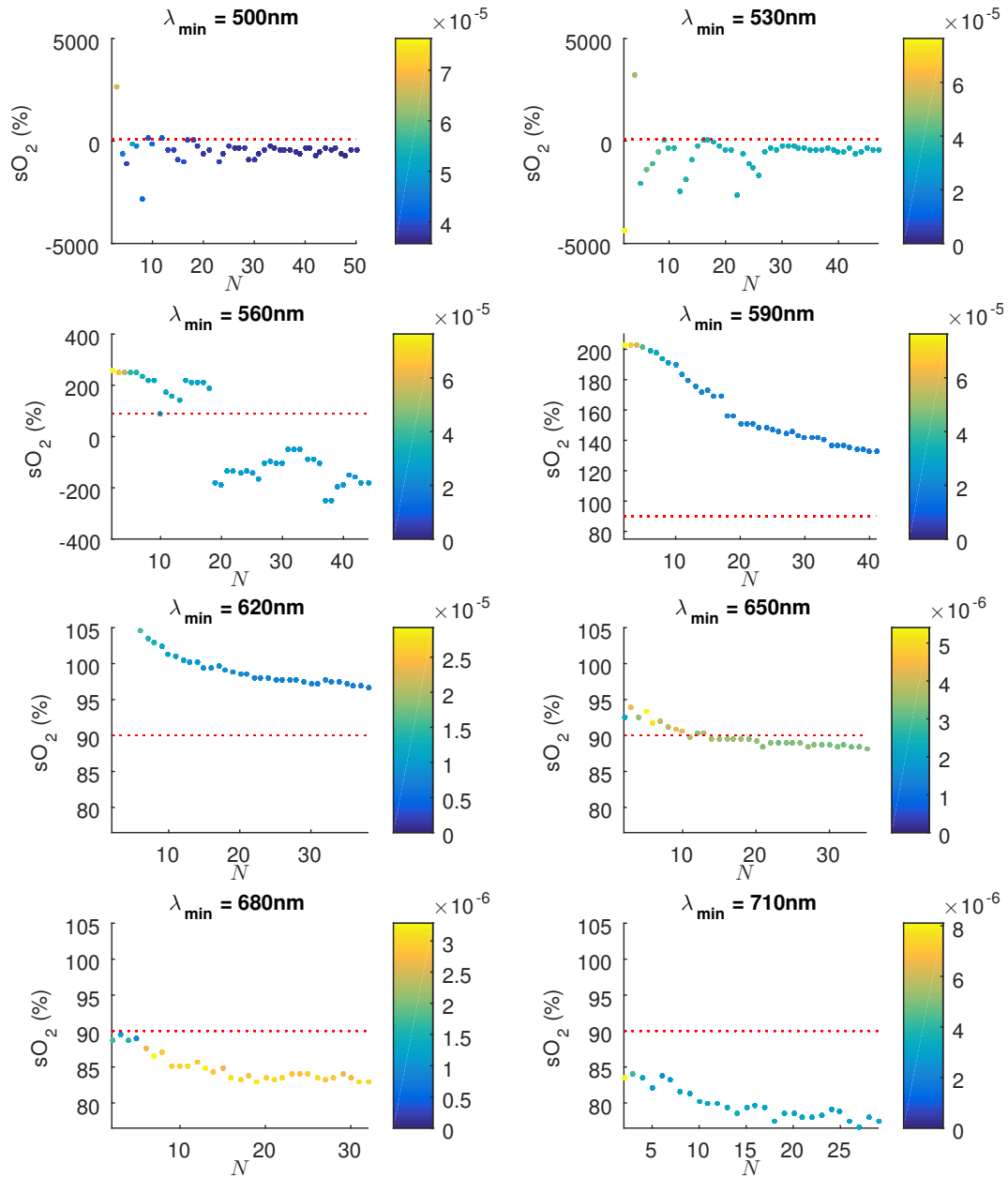


Figure B.3: Each plot shows the estimated sO_2 at a single voxel using increasing number of wavelengths, N , with a different λ_{\min} . Similarly to the equivalent plot for the mouse brain phantom (Fig. 4.12), the estimated sO_2 are shown to converge to a constant value as more wavelengths are added. The true sO_2 is 90%, as indicated with red dashed lines.

Appendix C

Model-based inversion with mutual information for spatially overlapping chromophores

The main aim of Chapter 6 is to demonstrate that statistical independence can be exploited to reduce model-mismatch errors in the model-based inversion. To clearly satisfy the independence criterion, the phantoms were designed such that the chromophores distributions did not overlap each other spatially. In this appendix, we demonstrate that improved quantification accuracy can also be obtained in cases where there is spatial overlap between the chromophores, provided that their statistical independence is not significantly reduced.

Numerically simulated photoacoustic images were generated based on a phantom with the same structure and chromophores as the numerical phantom in Chapter 6, but unlike in Chapter 6, both CuCl_2 and NiCl_2 are present in all six insertions in the new phantom. This phantom simulates a situation similar to Example C in Fig. 5.4, where a probe is distributed within the blood vessel. The concentration of CuCl_2 is constant in each column of insertions (simulating the “oxy-” or “deoxyhaemoglobin”) and the concentration of NiCl_2 varies for the different rows of insertions (simulating the “probe”). For comparison, the normalised mutual information (NMI) between CuCl_2 and NiCl_2 in this phantom is $\text{NMI}=0.12$, while $\text{NMI}=0$ when CuCl_2 and NiCl_2 were completely spatially separate in Chapter 6. The inversion was run with both the error

functional including MI, ε_{d+MI} (Eq. 6.3), and with the data error alone, ε_d (Eq. 6.2), for comparison. The beam diameter was set to be 50% larger than the true value in the inversions. The estimated CuCl_2 and NiCl_2 concentrations are shown at the top two rows of plots in Fig. C.1 for inversions using ε_d and ε_{d+MI} , and the true concentrations are shown to the right. The errors, which are the absolute differences between the estimated and the true concentrations, are shown in units of gL^{-1} in the bottom two rows. These results show that the errors are smaller using ε_{d+MI} compared to using ε_d . The most significant improvements are seen in the bottom right insertion in the phantom, where the errors are reduced by approximately 8 and 100gL^{-1} for CuCl_2 and NiCl_2 respectively in some pixels. This demonstrates that incorporating the MI in the inversion can reduce the model-mismatch errors also when there is spatial overlap between the independent chromophores, which is important for the broad applicability of the method.

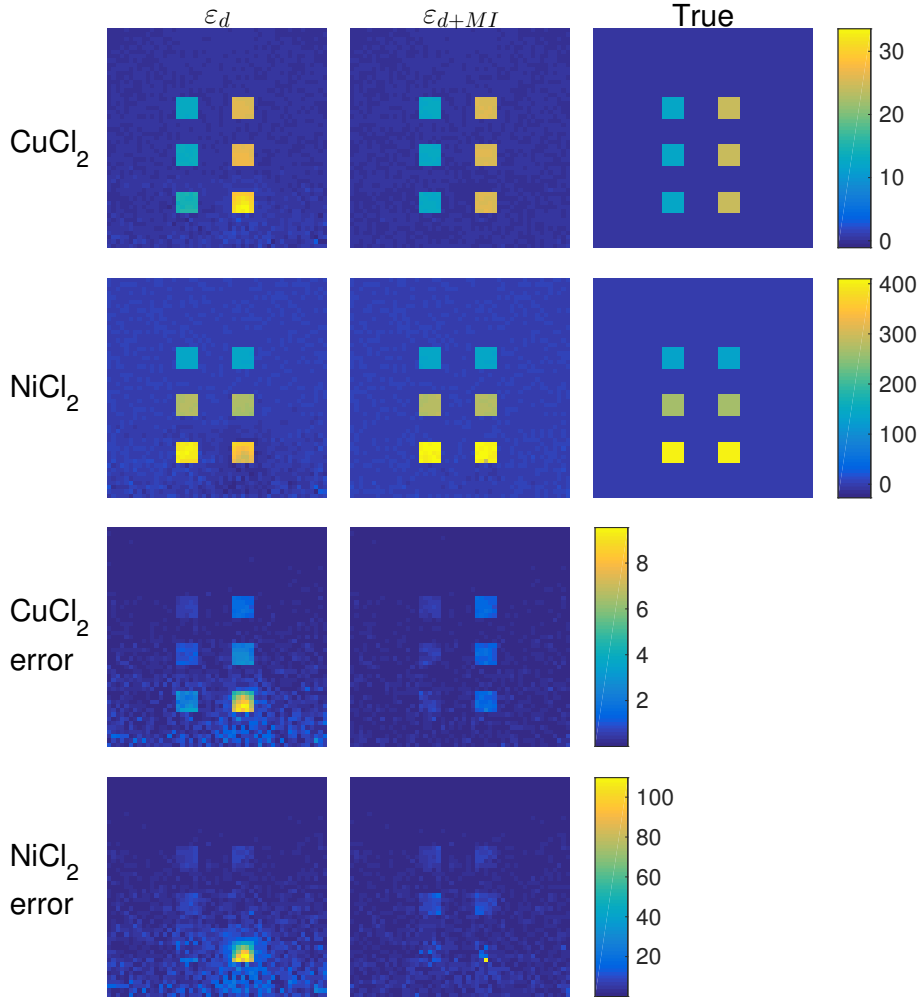


Figure C.1: The estimated concentrations of CuCl_2 and NiCl_2 using ε_d and ε_{d+MI} , and the true concentrations are shown in the top two rows. The true concentrations of CuCl_2 are 12 and 24 gL^{-1} in the left and right columns of insertions respectively, and the concentrations of NiCl_2 are 133 , 266 and 399 gL^{-1} for the top, centre and bottom rows respectively. The bottom two rows show the errors of the estimations, which are defined as the absolute difference between the estimated and the true concentrations. The colour maps indicate concentration in the units of gL^{-1} . The errors are smaller using ε_{d+MI} compared to ε_d , which demonstrates the including the MI term can improve the quantification accuracy for spatially overlapping chromophores.

Bibliography

- [1] A. G. Bell, "Upon the production and reproduction of sound by light," *Journal of the Society of Telegraph Engineers*, vol. 9, no. 34, pp. 404–426, 1880.
- [2] P. Beard, "Biomedical photoacoustic imaging," *Interface focus*, vol. 1, pp. 602–631, 2011.
- [3] R. A. Kruger, R. B. Lam, D. R. Reinecke, S. P. Del Rio, and R. P. Doyle, "Photoacoustic angiography of the breast," *Med. Phys.*, vol. 37, no. 11, pp. 6096–6100, 2010.
- [4] S. Manohar, A. Kharine, J. C. van Hespren, W. Steenbergen, and T. G. van Leeuwen, "The Twente Photoacoustic Mammoscope: system overview and performance," *Phys. Med. Biol.*, vol. 50, no. 11, p. 2543, 2005.
- [5] T. J. Allen, A. Hall, A. P. Dhillon, J. S. Owen, and P. C. Beard, "Spectroscopic photoacoustic imaging of lipid-rich plaques in the human aorta in the 740 to 1400 nm wavelength range," *J. Biomed. Opt.*, vol. 17, no. 6, pp. 0612091–06120910, 2012.
- [6] B. Wang, A. Karpouk, D. Yeager, J. Amirian, S. Litovsky, R. Smalling, and S. Emelianov, "In vivo intravascular ultrasound-guided photoacoustic imaging of lipid in plaques using an animal model of atherosclerosis," *Ultrasound Med. Biol.*, vol. 38, no. 12, pp. 2098–2103, 2012.
- [7] K. Jansen, A. F. Van Der Steen, H. M. van Beusekom, J. W. Oosterhuis, and G. van Soest, "Intravascular photoacoustic imaging of human coronary atherosclerosis," *Opt. Lett.*, vol. 36, no. 5, pp. 597–599, 2011.
- [8] J.-T. Oh, M.-L. Li, H. F. Zhang, K. Maslov, G. Stoica, and L. V. Wang, "Three-dimensional imaging of skin melanoma in vivo by dual-wavelength photoacoustic microscopy," *J. Biomed. Opt.*, vol. 11, no. 3, pp. 034032–034032–4, 2006.
- [9] C. P. Favazza, L. A. Cornelius, and L. V. Wang, "In vivo functional photoacoustic microscopy of cutaneous microvasculature in human skin," *J. Biomed. Opt.*, vol. 16, no. 2, pp. 026004–026004, 2011.
- [10] J.-M. Yang, K. Maslov, H.-C. Yang, Q. Zhou, K. K. Shung, and L. V. Wang, "Photoacoustic endoscopy," *Opt. Lett.*, vol. 34, no. 10, pp. 1591–1593, 2009.
- [11] T.-J. Yoon and Y.-S. Cho, "Recent advances in photoacoustic endoscopy," *World J. Gastrointest. Endosc.*, vol. 5, no. 11, p. 534, 2013.

- [12] X. Wang, Y. Pang, G. Ku, X. Xie, G. Stoica, and L. V. Wang, "Noninvasive laser-induced photoacoustic tomography for structural and functional in vivo imaging of the brain," *Nat. Biotechnol.*, vol. 21, no. 7, pp. 803–806, 2003.
- [13] J. Laufer, E. Zhang, G. Raivich, and P. Beard, "Three-dimensional noninvasive imaging of the vasculature in the mouse brain using a high resolution photoacoustic scanner," *Appl. Opt.*, vol. 48, no. 10, pp. D299–D306, 2009.
- [14] E. W. Stein, K. Maslov, and L. V. Wang, "Noninvasive, in vivo imaging of blood-oxygenation dynamics within the mouse brain using photoacoustic microscopy," *J. Biomed. Opt.*, vol. 14, no. 2, pp. 020502–020502–3, 2009.
- [15] G. Ku, X. Wang, X. Xie, G. Stoica, and L. V. Wang, "Imaging of tumor angiogenesis in rat brains in vivo by photoacoustic tomography," *Appl. Opt.*, vol. 44, no. 5, pp. 770–775, 2005.
- [16] Y. Lao, D. Xing, S. Yang, and L. Xiang, "Noninvasive photoacoustic imaging of the developing vasculature during early tumor growth," *Phys. Med. Biol.*, vol. 53, no. 15, p. 4203, 2008.
- [17] J. Laufer, P. Johnson, E. Zhang, B. Treeby, B. Cox, B. Pedley, and P. Beard, "In vivo preclinical photoacoustic imaging of tumor vasculature development and therapy," *J. Biomed. Opt.*, vol. 17, no. 5, pp. 0560161–0560168, 2012.
- [18] A. De La Zerda, C. Zavaleta, S. Keren, S. Vaithilingam, S. Bodapati, Z. Liu, J. Levi, B. R. Smith, T.-J. Ma, O. Oralkan, *et al.*, "Carbon nanotubes as photoacoustic molecular imaging agents in living mice," *Nat. Nanotechnol.*, vol. 3, no. 9, pp. 557–562, 2008.
- [19] P.-C. Li, C.-R. C. Wang, D.-B. Shieh, C.-W. Wei, C.-K. Liao, C. Poe, S. Jhan, A.-A. Ding, and Y.-N. Wu, "In vivo photoacoustic molecular imaging with simultaneous multiple selective targeting using antibody-conjugated gold nanorods," *Opt. Express*, vol. 16, no. 23, pp. 18605–18615, 2008.
- [20] L. Li, R. J. Zemp, G. Lungu, G. Stoica, and L. V. Wang, "Photoacoustic imaging of lacZ gene expression in vivo," *J. Biomed. Opt.*, vol. 12, no. 2, pp. 020504–020504–3, 2007.
- [21] C. Qin, K. Cheng, K. Chen, X. Hu, Y. Liu, X. Lan, Y. Zhang, H. Liu, Y. Xu, L. Bu, *et al.*, "Tyrosinase as a multifunctional reporter gene for Photoacoustic/MRI/PET triple modality molecular imaging," *Sci. Rep.*, vol. 3, 2013.
- [22] B. Cox, J. G. Laufer, S. R. Arridge, and P. C. Beard, "Quantitative spectroscopic photoacoustic imaging: a review," *J. Biomed. Opt.*, vol. 17, no. 6, pp. 0612021–0612022, 2012.
- [23] C. Menon and D. L. Fraker, "Tumor oxygenation status as a prognostic marker," *Cancer Lett.*, vol. 221, no. 2, pp. 225 – 235, 2005.
- [24] B. Venkatesh, R. Meacher, M. J. Muller, T. J. Morgan, and J. Fraser, "Monitoring tissue oxygenation during resuscitation of major burns," *J. Trauma*, vol. 50, no. 3, pp. 485–494, 2001.

- [25] A. A. Tandara and T. A. Mustoe, "Oxygen in wound healing more than a nutrient," *World J. Surg.*, vol. 28, no. 3, pp. 294–300, 2004.
- [26] F. Gottrup, "Oxygen in wound healing and infection," *World J. Surg.*, vol. 28, no. 3, pp. 312–315, 2004.
- [27] I. Vanzetta and A. Grinvald, "Increased cortical oxidative metabolism due to sensory stimulation: Implications for functional brain imaging," *Science*, vol. 286, no. 5444, pp. 1555–1558, 1999.
- [28] B. Wang, J. L. Su, J. Amirian, S. H. Litovsky, R. Smalling, and S. Emelianov, "Detection of lipid in atherosclerotic vessels using ultrasound-guided spectroscopic intravascular photoacoustic imaging," *Opt. Express*, vol. 18, no. 5, pp. 4889–4897, 2010.
- [29] K. Jansen, M. Wu, A. F. W. van der Steen, and G. van Soest, "Lipid detection in atherosclerotic human coronaries by spectroscopic intravascular photoacoustic imaging," *Opt. Express*, vol. 21, no. 18, pp. 21472–21484, 2013.
- [30] K. Jansen, A. F. van der Steen, M. Wu, H. M. van Beusekom, G. Springeling, X. Li, Q. Zhou, K. K. Shung, D. P. de Kleijn, and G. van Soest, "Spectroscopic intravascular photoacoustic imaging of lipids in atherosclerosis," *J. Biomed. Opt.*, vol. 19, pp. 19 – 19 – 10, 2014.
- [31] J.-T. Oh, M.-L. Li, H. F. Zhang, K. Maslov, G. Stoica, and L. V. Wang, "Three-dimensional imaging of skin melanoma in vivo by dual-wavelength photoacoustic microscopy," *J. Biomed. Opt.*, vol. 11, no. 3, pp. 034032–034032, 2006.
- [32] Y. Zhou, G. Li, L. Zhu, C. Li, L. A. Cornelius, and L. V. Wang, "Handheld photoacoustic probe to detect both melanoma depth and volume at high speed in vivo," *J. Biomed. Opt.*, vol. 8, no. 11-12, pp. 961–967, 2015.
- [33] J. Weber, P. Beard, and S. Bohndiek, "Contrast agents for molecular photoacoustic imaging," *Nat. Methods*, vol. 13, no. 8, p. 639, 2016.
- [34] A. Krumholz, D. M. Shcherbakova, J. Xia, L. V. Wang, and V. V. Verkhusha, "Multicontrast photoacoustic in vivo imaging using near-infrared fluorescent proteins," *Sci. Rep.*, vol. 4, 2014.
- [35] Z. Deng and C. Li, "Noninvasively measuring oxygen saturation of human finger-joint vessels by multi-transducer functional photoacoustic tomography," *J. Biomed. Opt.*, vol. 21, no. 6, pp. 061009–061009, 2016.
- [36] M. R. Tomaszewski, I. Q. Gonzalez, J. P. O'Connor, O. Abeyakoon, G. J. Parker, K. J. Williams, F. J. Gilbert, and S. E. Bohndiek, "Oxygen enhanced optoacoustic tomography (OE-OT) reveals vascular dynamics in murine models of prostate cancer," *Theranostics*, vol. 7, no. 11, p. 2900, 2017.
- [37] W. J. Akers, C. Kim, M. Berezin, K. Guo, R. Fuhrhop, G. M. Lanza, G. M. Fischer, E. Daltrozzo, A. Zumbusch, X. Cai, L. V. Wang, and S. Achilefu, "Noninvasive photoacoustic and fluorescence sentinel lymph node identification using dye-loaded perfluorocarbon nanoparticles," *ACS Nano*, vol. 5, no. 1, pp. 173–182, 2011.

- [38] A. N. Elayadi, K. N. Samli, L. Prudkin, Y.-H. Liu, A. Bian, X.-J. Xie, I. I. Wistuba, J. A. Roth, M. J. McGuire, and K. C. Brown, "A peptide selected by biopanning identifies the integrin $\alpha v\beta 6$ as a prognostic biomarker for nonsmall cell lung cancer," *Cancer Research*, vol. 67, no. 12, pp. 5889–5895, 2007.
- [39] A. Buehler, E. Herzog, A. Ale, B. D. Smith, V. Ntziachristos, and D. Razansky, "High resolution tumor targeting in living mice by means of multispectral optoacoustic tomography," *EJNMMI Research*, vol. 2, no. 1, pp. 1–6, 2012.
- [40] A. Taruttis, M. Wildgruber, K. Kosanke, N. Beziere, K. Licha, R. Haag, M. Aichler, A. Walch, E. Rummeny, and V. Ntziachristos, "Multispectral optoacoustic tomography of myocardial infarction," *Photoacoustics*, vol. 1, no. 1, pp. 3 – 8, 2013.
- [41] J. Laufer, B. Cox, E. Zhang, and P. Beard, "Quantitative determination of chromophore concentrations from 2D photoacoustic images using a nonlinear model-based inversion scheme," *Appl. Opt.*, vol. 49, no. 8, pp. 1219–1233, 2010.
- [42] M. Fonseca, E. Malone, F. Lucka, R. Ellwood, L. An, S. Arridge, P. Beard, and B. Cox, "Three-dimensional photoacoustic imaging and inversion for accurate quantification of chromophore distributions," in *Photons Plus Ultrasound: Imaging and Sensing 2017*, vol. 10064, p. 1006415, International Society for Optics and Photonics, 2017.
- [43] D. Razansky, M. Distel, C. Vinegoni, R. Ma, N. Perrimon, R. W. Köster, and V. Ntziachristos, "Multispectral opto-acoustic tomography of deep-seated fluorescent proteins in vivo," *Nature Photon.*, vol. 3, no. 7, pp. 412–417, 2009.
- [44] S. Kim, Y.-S. Chen, G. P. Luke, and S. Y. Emelianov, "In vivo three-dimensional spectroscopic photoacoustic imaging for monitoring nanoparticle delivery," *Biomed. Opt. Express*, vol. 2, no. 9, pp. 2540–2550, 2011.
- [45] S. Mallidi, K. Watanabe, D. Timerman, D. Schoenfeld, and T. Hasan, "Prediction of tumor recurrence and therapy monitoring using ultrasound-guided photoacoustic imaging," *Theranostics*, vol. 5, no. 3, p. 289, 2015.
- [46] V. Ermolayev, X. L. Dean-Ben, S. Mandal, V. Ntziachristos, and D. Razansky, "Simultaneous visualization of tumour oxygenation, neovascularization and contrast agent perfusion by real-time three-dimensional optoacoustic tomography," *Eur. Radiol.*, vol. 26, no. 6, pp. 1843–1851, 2016.
- [47] C. L. Bayer, B. J. Wlodarczyk, R. H. Finnell, and S. Y. Emelianov, "Ultrasound-guided spectral photoacoustic imaging of hemoglobin oxygenation during development," *Biomed. Opt. Express*, vol. 8, no. 2, pp. 757–763, 2017.
- [48] S. Prahl, "Optical Absorption of Hemoglobin." Oregon Medical Laser Center, <http://omlc.org/spectra/hemoglobin/summary.html>. (Accessed: 10 January 2016).
- [49] R. M. Pope, *Optical Absorption of Pure Water and Sea Water Using the Integrating Cavity Absorption Meter*. PhD thesis, Texas A&M University, 1993.

- [50] L. Kou, D. Labrie, and P. Chylek, "Refractive indices of water and ice in the 0.65-to 2.5- μm spectral range," *Appl. Opt.*, vol. 32, no. 19, pp. 3531–3540, 1993.
- [51] R. L. van Veen, H. Sterenborg, A. Pifferi, A. Torricelli, and R. Cubeddu, "Determination of vis- nir absorption coefficients of mammalian fat, with time- and spatially resolved diffuse reflectance and transmission spectroscopy," in *Biomedical Topical Meeting*, p. SF4, Optical Society of America, 2004.
- [52] M. I. Mishchenko, "Multiple scattering, radiative transfer, and weak localization in discrete random media: Unified microphysical approach," *Rev. Geophys.*, vol. 46, no. 2, pp. n/a–n/a, 2008.
- [53] J. Ripoll, "Derivation of the scalar radiative transfer equation from energy conservation of maxwell's equations in the far field," *J. Opt. Soc. Am. A*, vol. 28, no. 8, pp. 1765–1775, 2011.
- [54] S. R. Arridge, "Optical tomography in medical imaging," *Inverse Probl.*, vol. 15, no. 2, p. R41, 1999.
- [55] W. F. Cheong, S. A. Prahl, and A. J. Welch, "A review of the optical properties of biological tissues," *IEEE J. Quant. Electron*, vol. 26, no. 12, pp. 2166–2185, 1990.
- [56] J. H. Joseph, W. Wiscombe, and J. Weinman, "The delta-eddington approximation for radiative flux transfer," *J. Atmos. Sci.*, vol. 33, no. 12, pp. 2452–2459, 1976.
- [57] D. Contini, F. Martelli, and G. Zaccanti, "Photon migration through a turbid slab described by a model based on diffusion approximation. I. Theory," *Appl. Opt.*, vol. 36, no. 19, pp. 4587–4599, 1997.
- [58] S. R. Arridge, M. Schweiger, M. Hiraoka, and D. T. Delpy, "A finite element approach for modeling photon transport in tissue," *Med. Phys.*, vol. 20, no. 2, pp. 299–309, 1993.
- [59] B. Cox and P. Beard, "Fast calculation of pulsed photoacoustic fields in fluids using k-space methods," *J. Acoust. Soc. Am.*, vol. 117, no. 6, pp. 3616–3627, 2005.
- [60] G. Paltauf, H. Schmidt-Kloiber, and H. Guss, "Light distribution measurements in absorbing materials by optical detection of laser-induced stress waves," *Appl. Phys. Lett.*, vol. 69, no. 11, pp. 1526–1528, 1996.
- [61] K. P. Köstli and P. C. Beard, "Two-dimensional photoacoustic imaging by use of fourier-transform image reconstruction and a detector with an anisotropic response," *Appl. Opt.*, vol. 42, no. 10, pp. 1899–1908, 2003.
- [62] G. J. Diebold and P. J. Westervelt, "The photoacoustic effect generated by a spherical droplet in a fluid," *J. Acoust. Soc. Am.*, vol. 84, no. 6, pp. 2245–2251, 1988.
- [63] G. J. Diebold, T. Sun, and M. I. Khan, "Photoacoustic monopole radiation in one, two, and three dimensions," *Phys. Rev. Lett.*, vol. 67, pp. 3384–3387, 1991.
- [64] G. Diebold and T. Sun, "Properties of photoacoustic waves in one, two, and three dimensions," *Acta Acust. united Ac.*, vol. 80, no. 4, pp. 339–351, 1994.

- [65] M. Khan and G. Diebold, "The photoacoustic effect generated by laser irradiation of an isotropic solid cylinder," *Ultrasonics*, vol. 34, no. 1, pp. 19 – 24, 1996.
- [66] D.-H. Huang, C.-K. Liao, C.-W. Wei, and P.-C. Li, "Simulations of optoacoustic wave propagation in light-absorbing media using a finite-difference time-domain method," *J. Acoust. Soc. Am.*, vol. 117, no. 5, pp. 2795–2801, 2005.
- [67] Y.-L. Sheu and P.-C. Li, "Simulations of photoacoustic wave propagation using a finite-difference time-domain method with berengers perfectly matched layers," *J. Acoust. Soc. Am.*, vol. 124, no. 6, pp. 3471–3480, 2008.
- [68] M. Kasai, S. Fukushima, Y. Gohshi, T. Sawada, M. Ishioka, and M. Kaihara, "A basic analysis of pulsed photoacoustic signals using the finite elements method," *Journal of Applied Physics*, vol. 64, no. 3, pp. 972–976, 1988.
- [69] H. Jiang, Z. Yuan, and X. Gu, "Spatially varying optical and acoustic property reconstruction using finite-element-based photoacoustic tomography," *J. Opt. Soc. Am. A*, vol. 23, no. 4, pp. 878–888, 2006.
- [70] B. E. Treeby and B. T. Cox, "k-Wave: MATLAB toolbox for the simulation and reconstruction of photoacoustic wave fields," *J. Biomed. Opt.*, vol. 15, p. 021314, 2010.
- [71] J. Yao and L. V. Wang, "Photoacoustic microscopy," *Laser Photon. Rev.*, vol. 7, no. 5, pp. 758–778, 2013.
- [72] Y. Xu, L. V. Wang, G. Ambartsoumian, and P. Kuchment, "Reconstructions in limited-view thermoacoustic tomography," *Med. Phys.*, vol. 31, no. 4, pp. 724–733, 2004.
- [73] H.-P. Brecht, R. Su, M. Fronheiser, S. A. Ermilov, A. Conjusteau, and A. A. Oraevsky, "Whole-body three-dimensional optoacoustic tomography system for small animals," *J. Biomed. Opt.*, vol. 14, no. 6, pp. 064007–064007–8, 2009.
- [74] R. A. Kruger, C. M. Kuzmiak, R. B. Lam, D. R. Reinecke, S. P. Del Rio, and D. Steed, "Dedicated 3D photoacoustic breast imaging," *Med. Phys.*, vol. 40, no. 11, pp. 113301–n/a, 2013.
- [75] M. Toi, Y. Asao, Y. Matsumoto, H. Sekiguchi, A. Yoshikawa, M. Takada, M. Kataoka, T. Endo, N. Kawaguchi-Sakita, M. Kawashima, *et al.*, "Visualization of tumor-related blood vessels in human breast by photoacoustic imaging system with a hemispherical detector array," *Sci. Rep.*, vol. 7, p. 41970, 2017.
- [76] V. N. Alexander Dima, Neal C. Burton, "Multispectral optoacoustic tomography at 64, 128, and 256 channels," *J. Biomed. Opt.*, vol. 19, pp. 19 – 19 – 11, 2014.
- [77] X. Wang, X. Xie, G. Ku, L. V. Wang, and G. Stoica, "Noninvasive imaging of hemoglobin concentration and oxygenation in the rat brain using high-resolution photoacoustic tomography," *J. Biomed. Opt.*, vol. 11, pp. 11 – 11 – 9, 2006.
- [78] E. Zhang, J. Laufer, and P. Beard, "Backward-mode multiwavelength photoacoustic scanner using a planar Fabry-Perot polymer film ultrasound sensor for high-resolution three-dimensional imaging of biological tissues," *Appl. Opt.*, vol. 47, pp. 561–577, 2008.

- [79] G. Paltauf, R. Nuster, M. Haltmeier, and P. Burgholzer, "Photoacoustic tomography using a mach-zehnder interferometer as an acoustic line detector," *Appl. Opt.*, vol. 46, no. 16, pp. 3352–3358, 2007.
- [80] S.-W. Huang, S.-L. Chen, T. Ling, A. Maxwell, M. O'Donnell, L. J. Guo, and S. Ashkenazi, "Low-noise wideband ultrasound detection using polymer microring resonators," *Appl. Phys. Lett.*, vol. 92, no. 19, p. 193509, 2008.
- [81] A. Rosenthal, D. Razansky, and V. Ntziachristos, "High-sensitivity compact ultrasonic detector based on a pi-phase-shifted fiber bragg grating," *Opt. Lett.*, vol. 36, no. 10, pp. 1833–1835, 2011.
- [82] N. Huynh, O. Ogunlade, E. Zhang, B. Cox, and P. Beard, "Photoacoustic imaging using an 8-beam Fabry-Pérot scanner," in *Photons Plus Ultrasound: Imaging and Sensing 2016*, vol. 9708, p. 97082L, 2016.
- [83] S. Arridge, P. Beard, M. Betcke, B. Cox, N. Huynh, F. Lucka, O. Ogunlade, and E. Zhang, "Accelerated high-resolution photoacoustic tomography via compressed sensing," *Phys. Med. Biol.*, vol. 61, no. 24, p. 8908, 2016.
- [84] N. Huynh, F. Lucka, E. Zhang, M. Betcke, S. Arridge, P. Beard, and B. Cox, "Sub-sampled Fabry-Perot photoacoustic scanner for fast 3D imaging," in *Photons Plus Ultrasound: Imaging and Sensing 2017*, vol. 10064, p. 100641Y, International Society for Optics and Photonics, 2017.
- [85] A. Rosenthal, V. Ntziachristos, and D. Razansky, "Acoustic inversion in optoacoustic tomography: A review," *Curr. Med. Imaging. Rev.*, vol. 9, no. 4, pp. 318–336, 2013.
- [86] K. P. Köstli, M. Frenz, H. Bebie, and H. P. Weber, "Temporal backward projection of optoacoustic pressure transients using fourier transform methods," *Phys. Med. Biol.*, vol. 46, no. 7, p. 1863, 2001.
- [87] M. Xu, Y. Xu, and L. V. Wang, "Time-domain reconstruction algorithms and numerical simulations for thermoacoustic tomography in various geometries," *IEEE Trans. Biomed. Eng.*, vol. 50, no. 9, pp. 1086–1099, 2003.
- [88] M. Xu and L. V. Wang, "Universal back-projection algorithm for photoacoustic computed tomography," *Phys. Rev. E*, vol. 71, p. 016706, 2005.
- [89] B. E. Treeby, E. Z. Zhang, and B. T. Cox, "Photoacoustic tomography in absorbing acoustic media using time reversal," *Inverse Probl.*, vol. 26, no. 11, p. 115003, 2010.
- [90] K. Wang and M. A. Anastasio, "Photoacoustic and thermoacoustic tomography: Image formation principles," in *Handbook of Mathematical Methods in Imaging* (O. Scherzer, ed.), pp. 781–815, New York, NY: Springer New York, 2011.
- [91] P. Kuchment and L. Kunyansky, "Mathematics of photoacoustic and thermoacoustic tomography," in *Handbook of Mathematical Methods in Imaging* (O. Scherzer, ed.), pp. 817–865, New York, NY: Springer New York, 2011.
- [92] R. A. Kruger, P. Liu, Y. . Fang, and C. R. Appledorn, "Photoacoustic ultrasound (PAUS)–reconstruction tomography," *Med. Phys.*, vol. 22, no. 10, pp. 1605–1609, 1995.

- [93] A. A. Oraevsky, V. A. Andreev, A. A. Karabutov, D. R. Fleming, Z. Gatalica, H. Singh, and R. O. Esenaliev, "Laser optoacoustic imaging of the breast: detection of cancer angiogenesis," in *Optical Tomography and Spectroscopy of Tissue III*, vol. 3597.
- [94] D. Finch and R. Sarah K. Patch, "Determining a function from its mean values over a family of spheres," *SIAM Journal on Mathematical Analysis*, vol. 35, no. 5, pp. 1213–1240, 2004.
- [95] D. Finch, M. Haltmeier, and Rakesh, "Inversion of spherical means and the wave equation in even dimensions," *SIAM Journal on Applied Mathematics*, vol. 68, no. 2, pp. 392–412, 2007.
- [96] F. Natterer, "Photo-acoustic inversion in convex domains," *Inverse Probl. Imaging*, vol. 6, no. 2, pp. 1–6, 2012.
- [97] Y. Xu, D. Feng, and L. V. Wang, "Exact frequency-domain reconstruction for thermoacoustic tomography. I. Planar geometry," *IEEE Trans. Med. Imag.*, vol. 21, no. 7, pp. 823–828, 2002.
- [98] L. A. Kunyansky, "A series solution and a fast algorithm for the inversion of the spherical mean radon transform," *Inverse Probl.*, vol. 23, no. 6, p. S11, 2007.
- [99] Y. Xu, M. Xu, and L. V. Wang, "Exact frequency-domain reconstruction for thermoacoustic tomography. ii. cylindrical geometry," *IEEE Trans. Med. Imag.*, vol. 21, no. 7, pp. 829–833, 2002.
- [100] K. Wang and M. A. Anastasio, "A simple fourier transform-based reconstruction formula for photoacoustic computed tomography with a circular or spherical measurement geometry," *Phys. Med. Biol.*, vol. 57, no. 23, p. N493, 2012.
- [101] P. Burgholzer, G. J. Matt, M. Haltmeier, and G. Paltauf, "Exact and approximative imaging methods for photoacoustic tomography using an arbitrary detection surface," *Phys. Rev. E*, vol. 75, no. 4, p. 046706, 2007.
- [102] Y. Hristova, P. Kuchment, and L. Nguyen, "Reconstruction and time reversal in thermoacoustic tomography in acoustically homogeneous and inhomogeneous media," *Inverse Probl.*, vol. 24, no. 5, p. 055006, 2008.
- [103] B. Cox, S. Kara, S. Arridge, and P. Beard, "k-space propagation models for acoustically heterogeneous media: Application to biomedical photoacoustics," *J. Acoust. Soc. Am.*, vol. 121, no. 6, pp. 3453–3464, 2007.
- [104] P. Stefanov and G. Uhlmann, "Thermoacoustic tomography with variable sound speed," *Inverse Probl.*, vol. 25, no. 7, p. 075011, 2009.
- [105] J. Qian, P. Stefanov, G. Uhlmann, and H. Zhao, "A new numerical algorithm for thermoacoustic and photoacoustic tomography with variable sound speed," *UCLA CAM Report*, pp. 10–81, 2010.
- [106] Z. Yuan and H. Jiang, "Three-dimensional finite-element-based photoacoustic tomography: Reconstruction algorithm and simulations," *Med. Phys.*, vol. 34, no. 2, pp. 538–546, 2007.

- [107] X. L. Dean-Ben, A. Buehler, V. Ntziachristos, and D. Razansky, “Accurate model-based reconstruction algorithm for three-dimensional optoacoustic tomography,” *IEEE Trans. Med. Imag.*, vol. 31, no. 10, pp. 1922–1928, 2012.
- [108] J. Provost and F. Lesage, “The application of compressed sensing for photoacoustic tomography,” *IEEE Trans. Med. Imag.*, vol. 28, no. 4, pp. 585–594, 2009.
- [109] K. Wang, R. Su, A. A. Oraevsky, and M. A. Anastasio, “Investigation of iterative image reconstruction in three-dimensional optoacoustic tomography,” *Phys. Med. Biol.*, vol. 57, no. 17, p. 5399, 2012.
- [110] A. Rosenthal, D. Razansky, and V. Ntziachristos, “Fast semi-analytical model-based acoustic inversion for quantitative optoacoustic tomography,” *IEEE Trans. Med. Imag.*, vol. 29, no. 6, pp. 1275–1285, 2010.
- [111] R. Ellwood, O. Ogunlade, E. Zhang, P. Beard, and B. Cox, “Orthogonal Fabry-Pérot sensors for photoacoustic tomography,” in *Photons Plus Ultrasound: Imaging and Sensing 2016*, vol. 9708, pp. 9708 – 9708 – 6, International Society for Optics and Photonics, 2016.
- [112] F. A. Duck, *Physical properties of tissues: a comprehensive reference book*. Academic Press, 1990.
- [113] D. Modgil, M. A. Anastasio, and P. J. La Rivière, “Image reconstruction in photoacoustic tomography with variable speed of sound using a higher-order geometrical acoustics approximation,” *J. Biomed. Opt.*, vol. 15, no. 2, pp. 021308–021308, 2010.
- [114] E. Hysi, L. A. Wirtzfeld, J. P. May, E. Undzys, S.-D. Li, and M. C. Kolios, “Photoacoustic signal characterization of cancer treatment response: Correlation with changes in tumor oxygenation,” *Photoacoustics*, vol. 5, no. Supplement C, pp. 25 – 35, 2017.
- [115] M. Schwarz, A. Buehler, J. Aguirre, and V. Ntziachristos, “Three-dimensional multispectral optoacoustic mesoscopy reveals melanin and blood oxygenation in human skin in vivo,” *J. Biophotonics*, vol. 9, no. 1-2, pp. 55–60, 2016.
- [116] N. Beziere, N. Lozano, A. Nunes, J. Salichs, D. Queiros, K. Kostarelos, and V. Ntziachristos, “Dynamic imaging of PEGylated indocyanine green (ICG) liposomes within the tumor microenvironment using multi-spectral optoacoustic tomography (MSOT),” *Biomaterials*, vol. 37, no. Supplement C, pp. 415 – 424, 2015.
- [117] E. Herzog, A. Taruttis, N. Beziere, A. A. Lutich, D. Razansky, and V. Ntziachristos, “Optical imaging of cancer heterogeneity with multispectral optoacoustic tomography,” *Radiology*, vol. 263, no. 2, pp. 461–468, 2012.
- [118] X. L. Deán-Ben, N. C. Deliolanis, V. Ntziachristos, and D. Razansky, “Fast unmixing of multispectral optoacoustic data with vertex component analysis,” *Opt. Laser. Eng.*, vol. 58, pp. 119–125, 2014.

- [119] S. Tzoumas, N. Deliolanis, S. Morscher, and V. Ntziachristos, “Unmixing molecular agents from absorbing tissue in multispectral optoacoustic tomography,” *IEEE Trans. Med. Imag.*, vol. 33, no. 1, pp. 48–60, 2014.
- [120] J. Glatz, N. C. Deliolanis, A. Buehler, D. Razansky, and V. Ntziachristos, “Blind source unmixing in multi-spectral optoacoustic tomography,” *Opt. Express*, vol. 19, no. 4, pp. 3175–3184, 2011.
- [121] X. L. Deán-Ben, A. Buehler, D. Razansky, and V. Ntziachristos, “Estimation of optoacoustic contrast agent concentration with self-calibration blind logarithmic unmixing,” *Phys. Med. Biol.*, vol. 59, p. 4785, 2014.
- [122] K. Maslov, M. Sivaramakrishnan, H. F. Zhang, G. Stoica, and L. V. Wang, “Technical considerations in quantitative blood oxygenation measurement using photoacoustic microscopy in vivo,” in *Photons Plus Ultrasound: Imaging and Sensing 2006*, vol. 6086, p. 60860R, International Society for Optics and Photonics, 2006.
- [123] H. F. Zhang, K. Maslov, M. Sivaramakrishnan, G. Stoica, and L. V. Wang, “Imaging of hemoglobin oxygen saturation variations in single vessels in vivo using photoacoustic microscopy,” *Appl. Phys. Lett.*, vol. 90, no. 5, 2007.
- [124] J. R. Rajian, P. L. Carson, and X. Wang, “Quantitative photoacoustic measurement of tissue optical absorption spectrum aided by an optical contrast agent,” *Opt. Express*, vol. 17, no. 6, pp. 4879–4889, 2009.
- [125] D. Razansky and V. Ntziachristos, “Hybrid photoacoustic fluorescence molecular tomography using finite-element-based inversion,” *Med. Phys.*, vol. 34, no. 11, pp. 4293–4301, 2007.
- [126] W. L. Kiser Jr, R. A. Kruger, D. R. Reinecke, G. A. Kruger, and K. D. Miller, “Thermoacoustic in vivo determination of blood oxygenation,” in *Photons Plus Ultrasound: Imaging and Sensing 2004*, vol. 5320, p. 5320, 2004.
- [127] J. C. Ranasinghesagara and R. J. Zemp, “Combined photoacoustic and oblique-incidence diffuse reflectance system for quantitative photoacoustic imaging in turbid media,” *J. Biomed. Opt.*, vol. 15, no. 4, pp. 046016–046016, 2010.
- [128] S.-P. Lin, L. Wang, S. L. Jacques, and F. K. Tittel, “Measurement of tissue optical properties by the use of oblique-incidence optical fiber reflectometry,” *Appl. Opt.*, vol. 36, no. 1, pp. 136–143, 1997.
- [129] L. Yin, Q. Wang, Q. Zhang, and H. Jiang, “Tomographic imaging of absolute optical absorption coefficient in turbid media using combined photoacoustic and diffusing light measurements,” *Opt. Lett.*, vol. 32, no. 17, pp. 2556–2558, 2007.
- [130] A. Q. Bauer, R. E. Nothdurft, T. N. Erpelding, L. V. Wang, and J. P. Culver, “Quantitative photoacoustic imaging: correcting for heterogeneous light fluence distributions using diffuse optical tomography,” *J. Biomed. Opt.*, vol. 16, no. 9, p. 096016, 2011.
- [131] J. Ripoll and V. Ntziachristos, “Quantitative point source photoacoustic inversion formulas for scattering and absorbing media,” *Phys. Rev. E*, vol. 71, no. 3, p. 031912, 2005.

- [132] R. J. Zemp, “Quantitative photoacoustic tomography with multiple optical sources,” *Appl. Opt.*, vol. 49, no. 18, pp. 3566–3572, 2010.
- [133] P. Shao, B. Cox, and R. J. Zemp, “Estimating optical absorption, scattering, and grüneisen distributions with multiple-illumination photoacoustic tomography,” *Appl. Opt.*, vol. 50, no. 19, pp. 3145–3154, 2011.
- [134] B. Banerjee, S. Bagchi, R. M. Vasu, and D. Roy, “Quantitative photoacoustic tomography from boundary pressure measurements: noniterative recovery of optical absorption coefficient from the reconstructed absorbed energy map,” *J. Opt. Soc. Am. A*, vol. 25, no. 9, pp. 2347–2356, 2008.
- [135] G. Bal and G. Uhlmann, “Inverse diffusion theory of photoacoustics,” *Inverse Probl.*, vol. 26, no. 8, p. 085010, 2010.
- [136] G. Bal and K. Ren, “Multi-source quantitative photoacoustic tomography in a diffusive regime,” *Inverse Probl.*, vol. 27, no. 7, p. 075003, 2011.
- [137] B. T. Cox, S. R. Arridge, K. P. Köstli, and P. C. Beard, “Two-dimensional quantitative photoacoustic image reconstruction of absorption distributions in scattering media by use of a simple iterative method,” *Appl. Opt.*, vol. 45, no. 8, pp. 1866–1875, 2006.
- [138] Z. Yuan and H. Jiang, “Quantitative photoacoustic tomography: Recovery of optical absorption coefficient maps of heterogeneous media,” *Appl. Phys. Lett.*, vol. 88, no. 23, p. 231101, 2006.
- [139] Y. Sun and H. Jiang, “Quantitative three-dimensional photoacoustic tomography of the finger joints: phantom studies in a spherical scanning geometry,” *Phys. Med. Biol.*, vol. 54, no. 18, p. 5457, 2009.
- [140] Y. Sun, E. Sobel, and H. Jiang, “Quantitative three-dimensional photoacoustic tomography of the finger joints: an in vivo study,” *J. Biomed. Opt.*, vol. 14, no. 6, p. 064002, 2009.
- [141] Y. Sun, E. S. Sobel, and H. Jiang, “First assessment of three-dimensional quantitative photoacoustic tomography for in vivo detection of osteoarthritis in the finger joints,” *Med. Phys.*, vol. 38, no. 7, pp. 4009–4017, 2011.
- [142] Y. Sun, E. Sobel, and H. Jiang, “Noninvasive imaging of hemoglobin concentration and oxygen saturation for detection of osteoarthritis in the finger joints using multispectral three-dimensional quantitative photoacoustic tomography,” *J. Opt.*, vol. 15, no. 5, p. 055302, 2013.
- [143] B. Cox, S. Arridge, and P. Beard, “Quantitative photoacoustic image reconstruction for molecular imaging,” in *Photons Plus Ultrasound: Imaging and Sensing 2006*, vol. 6086, p. 60861M, International Society for Optics and Photonics, 2006.
- [144] L. Yao, Y. Sun, and H. Jiang, “Quantitative photoacoustic tomography based on the radiative transfer equation,” *Opt. Lett.*, vol. 34, no. 12, pp. 1765–1767, 2009.
- [145] L. Yao, Y. Sun, and H. Jiang, “Transport-based quantitative photoacoustic tomography: simulations and experiments,” *Phys. Med. Biol.*, vol. 55, no. 7, p. 1917, 2010.

- [146] A. Tikhonov and V. Arsenin, *Solutions of Ill-Posed Problems*. Winston and Sons, Washington DC., 1977.
- [147] L. I. Rudin, S. Osher, and E. Fatemi, “Nonlinear total variation based noise removal algorithms,” *Physica D.*, vol. 60, no. 1, pp. 259 – 268, 1992.
- [148] M. Haltmeier, L. Neumann, and S. Rabanser, “Single-stage reconstruction algorithm for quantitative photoacoustic tomography,” *Inverse Probl.*, vol. 31, no. 6, p. 065005, 2015.
- [149] A. D. Cezaro, F. T. D. Cezaro, and J. S. Suarez, “Regularization approaches for quantitative photoacoustic tomography using the radiative transfer equation,” *J. Math. Anal. Appl.*, vol. 429, no. 1, pp. 415 – 438, 2015.
- [150] H. Gao, H. Zhao, and S. Osher, “Bregman methods in quantitative photoacoustic tomography,” *UCLA CAM Report*, vol. 10, p. 42, 2010.
- [151] J. Nocedal and S. Wright, *Numerical Optimization*. Springer Science & Business Media, 2006.
- [152] R. Fletcher, *Practical methods of optimization*. John Wiley & Sons, 2013.
- [153] A. Chambolle and T. Pock, “An introduction to continuous optimization for imaging,” *Acta Numer.*, vol. 25, pp. 161–319, 2016.
- [154] B. T. Cox, S. R. Arridge, and P. C. Beard, “Estimating chromophore distributions from multiwavelength photoacoustic images,” *J. Opt. Soc. Am. A*, vol. 26, no. 2, pp. 443–455, 2009.
- [155] J. Laufer, D. Delpy, C. Elwell, and P. Beard, “Quantitative spatially resolved measurement of tissue chromophore concentrations using photoacoustic spectroscopy: application to the measurement of blood oxygenation and haemoglobin concentration,” *Phys. Med. Biol.*, vol. 52, no. 1, p. 141, 2007.
- [156] T. Tarvainen, B. T. Cox, J. P. Kaipio, and S. R. Arridge, “Reconstructing absorption and scattering distributions in quantitative photoacoustic tomography,” *Inverse Probl.*, vol. 28, no. 8, p. 084009, 2012.
- [157] T. Saratoon, T. Tarvainen, B. T. Cox, and S. R. Arridge, “A gradient-based method for quantitative photoacoustic tomography using the radiative transfer equation,” *Inverse Probl.*, vol. 29, no. 7, p. 075006, 2013.
- [158] G. Bal and K. Ren, “On multi-spectral quantitative photoacoustic tomography in diffusive regime,” *Inverse Probl.*, vol. 28, no. 2, p. 025010, 2012.
- [159] A. V. Mamonov and K. Ren, “Quantitative photoacoustic imaging in the radiative transport regime,” *Commun. Math. Sci.*, vol. 12, no. 2, pp. 201–234, 2014.
- [160] S. L. Jacques, “Optical properties of biological tissues: a review,” *Phys. Med. Biol.*, vol. 58, pp. R37–R61, 2013.
- [161] J. Laufer, C. Elwell, D. Delpy, and P. Beard, “In vitro measurements of absolute blood oxygen saturation using pulsed near-infrared photoacoustic spectroscopy: accuracy and resolution,” *Phys. Med. Biol.*, vol. 50, no. 18, p. 4409, 2005.

- [162] F. M. Brochu, J. Brunker, J. Joseph, M. R. Tomaszewski, S. Morscher, and S. E. Bohndiek, "Towards quantitative evaluation of tissue absorption coefficients using light fluence correction in optoacoustic tomography," *IEEE Trans. Med. Imag.*, vol. 36, no. 1, pp. 322–331, 2017.
- [163] R. Hochuli, *Monte Carlo methods in quantitative photoacoustic tomography*. PhD thesis, UCL (University College London), 2016.
- [164] R. Hochuli, S. Powell, S. Arridge, and B. Cox, "Quantitative photoacoustic tomography using forward and adjoint monte carlo models of radiance," *J. Biomed. Opt.*, vol. 21, pp. 21 – 21 – 9, 2016.
- [165] B. Kaplan, J. Buchmann, S. Prohaska, and J. Laufer, "Monte-carlo-based inversion scheme for 3D quantitative photoacoustic tomography," in *Photons Plus Ultrasound: Imaging and Sensing 2017*, vol. 10064, pp. 10064 – 10064 – 13, International Society for Optics and Photonics, 2017.
- [166] J. Buchmann, B. Kaplan, S. Prohaska, and J. Laufer, "Experimental validation of a monte-carlo-based inversion scheme for 3D quantitative photoacoustic tomography," in *Photons Plus Ultrasound: Imaging and Sensing 2017*, vol. 10064, p. 100645J, International Society for Optics and Photonics, 2017.
- [167] P. Shao, T. Harrison, and R. J. Zemp, "Iterative algorithm for multiple illumination photoacoustic tomography (MIPAT) using ultrasound channel data," *Biomed. Opt. Express*, vol. 3, no. 12, pp. 3240–3249, 2012.
- [168] Z. Yuan and H. Jiang, "A calibration-free, one-step method for quantitative photoacoustic tomography," *Med. Phys.*, vol. 39, no. 11, pp. 6895–6899, 2012.
- [169] T. Ding, K. Ren, and S. Vallian, "A one-step reconstruction algorithm for quantitative photoacoustic imaging," *Inverse Probl.*, vol. 31, no. 9, p. 095005, 2015.
- [170] A. Pulkkinen, B. T. Cox, S. R. Arridge, H. Goh, J. P. Kaipio, and T. Tarvainen, "Direct estimation of optical parameters from photoacoustic time series in quantitative photoacoustic tomography," *IEEE Trans. Med. Imag.*, vol. 35, no. 11, pp. 2497–2508, 2016.
- [171] T. Tarvainen, A. Pulkkinen, B. T. Cox, J. P. Kaipio, and S. R. Arridge, "Bayesian image reconstruction in quantitative photoacoustic tomography," *IEEE Trans. Med. Imag.*, vol. 32, no. 12, pp. 2287–2298, 2013.
- [172] A. Pulkkinen, B. T. Cox, S. R. Arridge, J. P. Kaipio, and T. Tarvainen, "A bayesian approach to spectral quantitative photoacoustic tomography," *Inverse Probl.*, vol. 30, no. 6, p. 065012, 2014.
- [173] E. Malone, S. Powell, B. T. Cox, and S. Arridge, "Reconstruction-classification method for quantitative photoacoustic tomography," *J. Biomed. Opt.*, vol. 20, pp. 20 – 20 – 10, 2015.
- [174] A. Rosenthal, D. Razansky, and V. Ntziachristos, "Quantitative optoacoustic signal extraction using sparse signal representation," *IEEE Trans. Med. Imag.*, vol. 28, no. 12, pp. 1997–2006, 2009.

- [175] S. Tzoumas, A. Nunes, I. Olefir, S. Stangl, P. Symvoulidis, S. Glasl, C. Bayer, G. Multhoff, and V. Ntziachristos, “Eigenspectra optoacoustic tomography achieves quantitative blood oxygenation imaging deep in tissues,” *Nat. Commun.*, vol. 7, 2016.
- [176] S. Choi, A. Mandelis, X. Guo, B. Lashkari, S. Kellnberger, and V. Ntziachristos, “Wavelength-Modulated Differential Photoacoustic Spectroscopy (WM-DPAS) for noninvasive early cancer detection and tissue hypoxia monitoring,” *J. Biophotonics*, vol. 9, no. 4, pp. 388–395, 2016.
- [177] T. Jetzfellner, D. Razansky, A. Rosenthal, R. Schulz, K.-H. Englmeier, and V. Ntziachristos, “Performance of iterative optoacoustic tomography with experimental data,” *Appl. Phys. Lett.*, vol. 95, no. 1, p. 013703, 2009.
- [178] M. Fonseca, T. Saratoon, B. Zeqiri, P. Beard, and B. Cox, “Sensitivity of quantitative photoacoustic tomography inversion schemes to experimental uncertainty,” in *Photons Plus Ultrasound: Imaging and Sensing 2016*, vol. 9708, p. 97084X, International Society for Optics and Photonics, 2016.
- [179] D.-K. Yao, C. Zhang, K. Maslov, and L. V. Wang, “Photoacoustic measurement of the Gruneisen parameter of tissue,” *J. Biomed. Opt.*, vol. 19, no. 1, p. 017007, 2014.
- [180] R. Hochuli, P. C. Beard, and B. Cox, “Accuracy of approximate inversion schemes in quantitative photoacoustic imaging,” in *Photons Plus Ultrasound: Imaging and Sensing 2014*, vol. 8943, p. 89435V, International Society for Optics and Photonics, 2014.
- [181] A. Needles, A. Heinmiller, J. Sun, C. Theodoropoulos, D. Bates, D. Hirson, M. Yin, and F. S. Foster, “Development and initial application of a fully integrated photoacoustic micro-ultrasound system,” *IEEE Trans. Ultrason. Ferroelectr. Freq. Control.*, vol. 60, no. 5, pp. 888–897, 2013.
- [182] L. M. Yamaleyeva, Y. Sun, T. Bledsoe, A. Hoke, S. B. Gurley, and K. B. Brosnihan, “Photoacoustic imaging for in vivo quantification of placental oxygenation in mice,” *The FASEB Journal*, 2017.
- [183] C. J. Arthuis, A. Novell, F. Raes, J.-M. Escoffre, S. Lerondel, A. Le Pape, A. Bouakaz, and F. Perrotin, “Real-time monitoring of placental oxygenation during maternal hypoxia and hyperoxygenation using photoacoustic imaging,” *PLOS ONE*, vol. 12, no. 1, pp. 1–11, 2017.
- [184] E. Fakhrejehani, M. Torii, T. Kitai, S. Kanao, Y. Asao, Y. Hashizume, Y. Mikami, I. Yamaga, M. Kataoka, T. Sugie, M. Takada, H. Haga, K. Togashi, T. Shiina, and M. Toi, “Clinical report on the first prototype of a photoacoustic tomography system with dual illumination for breast cancer imaging,” *PLOS ONE*, vol. 10, no. 10, pp. 1–13, 2015.
- [185] J. R. Eisenbrey, D. A. Merton, A. Marshall, J.-B. Liu, T. B. Fox, A. Sridharan, and F. Forsberg, “Comparison of photoacoustically derived hemoglobin and oxygenation measurements with contrast-enhanced ultrasound estimated vascularity and immunohistochemical staining in a breast cancer model,” *Ultrasonic Imaging*, vol. 37, no. 1, pp. 42–52, 2015.

- [186] J. P. May, E. Hysi, L. A. Wirtzfeld, E. Undzys, S.-D. Li, and M. C. Kolios, "Photoacoustic imaging of cancer treatment response: Early detection of therapeutic effect from thermosensitive liposomes," *PLOS ONE*, vol. 11, no. 10, pp. 1–21, 2016.
- [187] J. Jo, G. Xu, M. Cao, A. Marquardt, S. Francis, G. Gandikota, and X. Wang, "A functional study of human inflammatory arthritis using photoacoustic imaging.," *Sci. Rep.*, vol. 7, no. 1, p. 15026, 2017.
- [188] L. J. Rich and M. Seshadri, "Photoacoustic monitoring of tumor and normal tissue response to radiation," *Sci. Rep.*, vol. 6, p. 21237, 2016.
- [189] L. M. Smith, J. Varagic, and L. M. Yamaleyeva, "Photoacoustic imaging for the detection of hypoxia in the rat femoral artery and skeletal muscle microcirculation," *Shock*, vol. 46, no. 5, pp. 527–530, 2016.
- [190] S. Lee, J. H. Kim, J. H. Lee, J. H. Lee, and J. K. Han, "Non-invasive monitoring of the therapeutic response in sorafenib-treated hepatocellular carcinoma based on photoacoustic imaging," *Eur. Radiol.*, 2017.
- [191] A. Shah, N. Bush, G. Box, S. Eccles, and J. Bamber, "Value of combining dynamic contrast enhanced ultrasound and optoacoustic tomography for hypoxia imaging," *Photoacoustics*, vol. 8, no. Supplement C, pp. 15 – 27, 2017.
- [192] R. Hochuli, P. C. Beard, and B. Cox, "Effect of wavelength selection on the accuracy of blood oxygen saturation estimates obtained from photoacoustic images," in *Photons Plus Ultrasound: Imaging and Sensing 2015*, vol. 9323, p. 93231V, International Society for Optics and Photonics, 2015.
- [193] G. P. Luke, S. Y. Nam, and S. Y. Emelianov, "Optical wavelength selection for improved spectroscopic photoacoustic imaging," *Photoacoustics*, vol. 1, no. 2, pp. 36 – 42, 2013.
- [194] J. Xiao, Z. Yuan, J. He, and H. Jiang, "Quantitative multispectral photoacoustic tomography and wavelength optimization," *X-ray Sci. Technol.*, vol. 18, no. 4, pp. 415–427, 2010.
- [195] L. S. Hansen, J. E. Cogle, J. Wells, and M. W. Charles, "The influence of the hair cycle on the thickness of mouse skin," *Anat. Rec.*, vol. 210, no. 4, pp. 569–573, 1984.
- [196] A. J. Lin, M. A. Koike, K. N. Green, J. G. Kim, A. Mazhar, T. B. Rice, F. M. La Ferla, and B. J. Tromberg, "Spatial frequency domain imaging of intrinsic optical property contrast in a mouse model of alzheimers disease," *Ann. Biomed. Eng.*, vol. 39, no. 4, pp. 1349–1357, 2011.
- [197] A. Bashkatov, E. Genina, V. Kochubey, and V. Tuchin, "Optical properties of human skin, subcutaneous and mucous tissues in the wavelength range from 400 to 2000 nm," *J. Phys. D*, vol. 38, no. 15, p. 2543, 2005.
- [198] A. N. Bashkatov, E. A. Genina, V. I. Kochubey, and V. V. Tuchin, "Optical properties of human cranial bone in the spectral range from 800 to 2000 nm," in

- Saratov Fall Meeting 2005: Optical Technologies in Biophysics and Medicine VII*, vol. 6163, p. 616310, International Society for Optics and Photonics, 2006.
- [199] M. Firbank, M. Hiraoka, M. Essenpreis, and D. T. Delpy, “Measurement of the optical properties of the skull in the wavelength range 650-950 nm,” *Phys. Med. Biol.*, vol. 38, no. 4, p. 503, 1993.
- [200] D. Abookasis, C. C. Lay, M. S. Mathews, M. E. Linskey, R. D. Frostig, and B. J. Tromberg, “Imaging cortical absorption, scattering, and hemodynamic response during ischemic stroke using spatially modulated near-infrared illumination,” *J. Biomed. Opt.*, vol. 14, no. 2, pp. 024033–024033–9, 2009.
- [201] A. C. Silva, W. Zhang, D. S. Williams, and A. P. Koretsky, “Estimation of water extraction fractions in rat brain using magnetic resonance measurement of perfusion with arterial spin labeling,” *Magn. Reson. Med.*, vol. 37, no. 1, pp. 58–68, 1997.
- [202] M. Schweiger and S. Arridge, “The Toast++ software suite for forward and inverse modeling in optical tomography,” *J. Biomed. Opt.*, vol. 19, p. 040801, 2014.
- [203] G. P. Luke and S. Y. Emelianov, “Optimization of in vivo spectroscopic photoacoustic imaging by smart optical wavelength selection,” *Opt. Lett.*, vol. 39, no. 7, pp. 2214–2217, 2014.
- [204] P. Comon and C. Jutten, *Handbook of Blind Source Separation: Independent component analysis and applications*. Academic press, 2010.
- [205] N. C. Deliolanis, A. Ale, S. Morscher, N. C. Burton, K. Schaefer, K. Radrich, D. Razansky, and V. Ntziachristos, “Deep-tissue reporter-gene imaging with fluorescence and optoacoustic tomography: A performance overview,” *Mol. Imaging Biol.*, vol. 16, no. 5, pp. 652–660, 2014.
- [206] A. Hyvärinen and E. Oja, “Independent component analysis: algorithms and applications,” *Neural Netw.*, vol. 13, pp. 411–430, 2000.
- [207] A. Hyvärinen, J. Karhunen, and E. Oja, *Independent Component Analysis*. Toronto: John Wiley & Sons, 2004.
- [208] C. Kim, K. H. Song, F. Gao, and L. V. Wang, “Sentinel lymph nodes and lymphatic vessels: Noninvasive dual-modality in vivo mapping by using indocyanine green in rats - volumetric spectroscopic photoacoustic imaging and planar fluorescence imaging,” *Radiology*, vol. 255, no. 2, pp. 442–450, 2010.
- [209] A. P. Jathoul, J. Laufer, O. Ogunlade, B. Treeby, B. Cox, E. Zhang, P. Johnson, A. R. Pizzey, B. Philip, T. Marafioti, *et al.*, “Deep in vivo photoacoustic imaging of mammalian tissues using a tyrosinase-based genetic reporter,” *Nature Photon.*, vol. 9, no. 4, pp. 239–246, 2015.
- [210] T. Cover and J. Thomas, *Elements of Information Theory*. 1991.
- [211] A. Papoulis, “Random variables and stochastic processes (3rd ed.),” 1991.

- [212] L. An and B. Cox, “Independent component analysis for unmixing multi-wavelength photoacoustic images,” in *Photons Plus Ultrasound: Imaging and Sensing 2016*, vol. 9708, p. 970851, International Society for Optics and Photonics, 2016.
- [213] J. Laufer, E. Zhang, and P. Beard, “Evaluation of absorbing chromophores used in tissue phantoms for quantitative photoacoustic spectroscopy and imaging,” *IEEE J. Sel. Top. Quantum Electron.*, vol. 16, no. 3, pp. 600–607, 2010.
- [214] L. V. Wang and H.-I. Wu, *Biomedical Optics: Principles and Imaging*. John Wiley & Sons, Inc., 2009.
- [215] B. W. Silverman, *Density estimation for statistics and data analysis*. CRC press, 1986.
- [216] C. Panagiotou, S. Somayajula, A. P. Gibson, M. Schweiger, R. M. Leahy, and S. R. Arridge, “Information theoretic regularization in diffuse optical tomography,” *J. Opt. Soc. Am. A*, vol. 26, no. 5, pp. 1277–1290, 2009.
- [217] S. Shwartz, M. Zibulevsky, and Y. Y. Schechner, “ICA using kernel entropy estimation with NlogN complexity,” in *Independent Component Analysis and Blind Signal Separation*, pp. 422–429, Springer, 2004.
- [218] C. Panagiotou, *Information Theoretic Regularization in Diffuse Optical Tomography*. PhD thesis, UCL (University College London), 2010.
- [219] P. Hall and M. Wand, “On the accuracy of binned kernel density estimators,” *J. Multivariate Anal.*, vol. 56, no. 2, pp. 165 – 184, 1996.
- [220] M. P. Wand, “Fast computation of multivariate kernel estimators,” *Journal of Computational and Graphical Statistics*, vol. 3, no. 4, pp. 433–445, 1994.
- [221] L. An, T. Saratoon, M. Fonseca, R. Ellwood, and B. Cox, “Statistical independence in nonlinear model-based inversion for quantitative photoacoustic tomography,” *Biomed. Opt. Express*, vol. 8, no. 11, pp. 5297–5310, 2017.
- [222] H. J. van Staveren, C. J. M. Moes, J. van Marie, S. A. Prahl, and M. J. C. van Gemert, “Light scattering in Intralipid-10% in the wavelength range of 400–1100 nm,” *Appl. Opt.*, vol. 30, no. 31, pp. 4507–4514, 1991.
- [223] R. Ellwood, O. Ogunlade, E. Zhang, P. Beard, and B. Cox, “Photoacoustic tomography using orthogonal Fabry-Pérot sensors,” *J. Biomed. Opt.*, vol. 22, no. 4, p. 041009.
- [224] Y. Xu and L. V. Wang, “Time reversal and its application to tomography with diffracting sources,” *Phys. Rev. Lett.*, vol. 92, p. 033902, 2004.
- [225] A. Myronenko, X. Song, and M. . Carreira-perpin, “Non-rigid point set registration: Coherent point drift,” in *Advances in Neural Information Processing Systems 19*, MIT Press, 2006.
- [226] G. Paltauf, J. A. Viator, S. A. Prahl, and S. L. Jacques, “Iterative reconstruction algorithm for optoacoustic imaging,” *J. Acoust. Soc. Am.*, vol. 112, no. 4, pp. 1536–1544, 2002.

- [227] B. Cox, S. Arridge, and P. Beard, “Gradient-based quantitative photoacoustic image reconstruction for molecular imaging,” in *Photons Plus Ultrasound: Imaging and Sensing 2007*, vol. 6437, p. 64371T, International Society for Optics and Photonics, 2007.
- [228] S. T. Flock, S. L. Jacques, B. C. Wilson, W. M. Star, and M. J. van Gemert, “Optical properties of intralipid: a phantom medium for light propagation studies,” *Lasers Surg. Med.*, vol. 12, no. 5, pp. 510–519, 1992.
- [229] C. R. Vogel, *Computational methods for inverse problems*. Philadelphia, PA: Society for Industrial and Applied Mathematics (SIAM), 2002.
- [230] A. M. Thompson, J. C. Brown, J. W. Kay, and D. M. Titterington, “A study of methods of choosing the smoothing parameter in image restoration by regularization,” *IEEE Trans. Pattern Anal. Mach. Intell.*, vol. 13, no. 4, pp. 326–339, 1991.
- [231] C. Huang, K. Wang, L. Nie, L. V. Wang, and M. A. Anastasio, “Full-wave iterative image reconstruction in photoacoustic tomography with acoustically inhomogeneous media,” *IEEE Trans. Med. Imag.*, vol. 32, no. 6, pp. 1097–1110, 2013.
- [232] R. O. Esenaliev, I. V. Larina, K. V. Larin, D. J. Deyo, M. Motamedi, and D. S. Prough, “Optoacoustic technique for noninvasive monitoring of blood oxygenation: a feasibility study,” *Appl. Opt.*, vol. 41, no. 22, pp. 4722–4731, 2002.
- [233] A. A. Plumb, N. T. Huynh, J. Guggenheim, E. Zhang, and P. Beard, “Rapid volumetric photoacoustic tomographic imaging with a Fabry-Perot ultrasound sensor depicts peripheral arteries and microvascular vasomotor responses to thermal stimuli,” *Eur. Radiol.*, 2017.